UNIVERSITAT DE BARCELONA

Evolution of the lithospheric mantle in NE Angola: implications for diamond exploration

Montgarri Castillo i Oliver

UNIVERSITAT DE BARCELONA
DEPARTAMENT DE MINERALOGIA, PETROLOGIA i GEOLOGIA APLICADA

EVOLUTION OF THE LITHOSPHERIC MANTLE IN NE ANGOLA: IMPLICATIONS FOR DIAMOND EXPLORATION

Tesi doctoral presentada per

MONTGARRI CASTILLO I OLIVER

Memòria presentada per optar al títol de doctora per la Universitat de Barcelona amb Menció Internacional

Tesi realitzada dins del Programa de Doctorat de Ciències de la Terra per la Universitat de Barcelona i en règim de cotutela per la Macquarie University sota la direcció de:

SALVADOR GALÍ MEDINA (UB)
JOAN CARLES MELGAREJO DRAPER (UB)

WILLIAM L. GRIFFIN (Macquarie Univ.)
SUZANNE Y. O'REILLY (Maquarie Univ)

Barcelona, setembre del 2016

Evolution of the lithospheric mantle in NE Angola: implications for diamond exploration

BY

MONTGARRI CASTILLO I OLIVER

B.Sc. Universitat de Barcelona (2009)
M.Sc. Universitat de Barcelona (2010)

Directed by

SALVADOR GALÍ MEDINA
JOAN CARLES MELGAREJO DRAPER
WILLIAM L. GRIFFIN
SUZANNE Y. O'REILLY

A THESIS SUBMITTED TO UNIVERSITAT DE BARCELONA
FOR THE DEGREE OF DOCTOR OF PHILOSOPHY
DEPARTAMENT DE MINERALOGIA, PETROLOGIA I GEOLOGIA APLICADA

AUGUST 2016

A l'Oleguer, la Núria i en Janot.

A la Pilar, en Joan, en Quim i l'Antonieta.

TABLE OF CONTENTS

RESUM

Angola és actualment el vuitè major productor de diamants del món. Tanmateix, degut al seu particular context històric, el mantell litosfèric subcontinental (SCLM) del cratón del Congo-Kasai encara és poc estudiat. Tot i així, comprendre'n l'estructura, la composició i l'evolució, així com les característiques dels propis magmes kimberlítics, és essencial per al futur de l'exploració diamantífera d'aquesta zona.

Un estudi detallat de la textura i la composició de la perovskita ($CaTiO_3$) de la matriu en 6 intrusions kimberítiques de la província de Lunda Norte (NE Angola) ha posat de manifest un procés complex que s'ha interpretat com a *mingling* de magmes composicionalment diferents. La datació isotòpica d'aquest mineral mitjançant el mètode d'U-Pb ha indicat que les erupcions van tenir lloc durant el Cretaci Inferior (116-133 Ma). Aquests resultats suggereixen que el magmatisme kimberlític a Lunda Norte probablement va tenir lloc fruit de la reactivació de profundes falles translitosfèriques (>300km) durant la ruptura de Gondwana.

La caracterització de xenòlits i xenocristalls mantèl·lics transportats cap a la superfície per les kimberlites Cat115 i Catoca ha permès inferir una estratificació del SCLM al NE d'Angola. Aquesta estratificació ve definida per dues poblacions de peridotites granatíferes, separades per una zona rica en eclogites amb un baix contingut de Mg, situada aproximadament a 150km de profunditat. S'han proposat dos possibles orígens per a aquesta estructura (subducció *versus* ascens de plomall mantèl·lic), encara que cal noves dades per determinar quin dels dos escenaris és el més probable.

Complexos processos metasomàtics han modificat la composició d'un SCLM que ja havia estat prèviament empobrit. En el model proposat en aquesta tesi, les capes més superficials del mantell haurien estat ser inicialment afectades per un metasomatisme de tipus silicatat, del qual en resultà la incorporació de granat (± clinopiroxè). Posteriorment, magmes de

composició sílico-carbonatítica refertilitzarien el SCLM més profund, introduïnt tant clinopiroxè i granat. La cristal·lització fraccionada d'aquests magmes explicaria la formació tardana –o un metasomatisme críptic- de clinopiroxè de signatura carbonatítica, així com la cristal·lització de flogopita a la capa més somera del SCLM, poc abans de l'erupció kimberlítica. Finalment, la interacció amb el magma kimberlític hauria donat lloc a la cristal·lització d'una segona generació de flogopita i de piroxè de gra fi en fractures i vores de gra.

Els resultats presentat en aquesta tesi subratllen la complexitat dels processos que van tenir lloc al SCLM al NE d'Angola i com aquests poden haver modificat la composició dels minerals indicadors de diamant (ilmenita, clinopiroxè i granat) transportats per les kimberlites. Aquest fet és especialment rellevant en el cas de la ilmenita, ja que la interacció amb el magma kimberlític podria donar lloc a una evaluació errònia del potencial diamantífer de la kimberlita estudiada si no es tenen en compte criteris texturals i composicionals a nivell d'elements traça.

ABSTRACT

Angola is currently the 8th largest diamond producer in the world, but for historical reasons the subcontinental lithospheric mantle (SCLM) in the Congo-Kasai craton is still poorly studied. However, an understanding of the structure, composition and evolution of this SCLM, as well as the properties of the kimberlitic magmas themselves, is essential for the future of diamond exploration.

A detailed textural and compositional study of groundmass perovskite ($CaTiO_3$) in 6 kimberlitic intrusions in the Lunda Norte province (NE Angola) revealed a complex, multi-stage process that involved mingling of compositionally different melts. U-Pb dating of perovskite yielded Lower Cretaceous ages (116-133 Ma), which suggests that kimberlite magmatism resulted from reactivation of deep-seated translithospheric faults (>300km) during the break-up of Gondwana.

A layered structure of this SCLM was inferred from the characterisation of mantle xenoliths and xenocrysts sampled by the Cat115 and Catoca kimberlites. The layering is defined by two distinct garnet-peridotite suites, separated by a zone rich in low-Mg eclogite at ~150km depth. Two origins have been proposed to explain the current structure of the SCLM (stacking subduction vs plume upwelling), although more data are required to decide which is the most likely explanation.

Complex metasomatic processes have modified the composition of an originally depleted SCLM. In the model proposed in this thesis, the shallow SCLM was firstly affected by silicate melt metasomatism, which resulted in the introduction of garnet (± clinopyroxene). Subsequently, carbonatite-silicate melts refertilised the deep SCLM, introducing both clinopyroxene and garnet. Percolative fractional crystallisation of these melts would explain the late formation -or cryptic metasomatism- of clinopyroxene with a carbonatitic signature, as well as the

crystallisation of phlogopite, in the shallower layer of the SCLM, shortly prior to kimberlite eruption. Finally, interaction with the kimberlitic magma led to the crystallisation of a second generation of phlogopite and fine- grained pyroxene along fractures and grain boundaries.

The results presented in this thesis highlight the complexity of the processes that took place in the SCLM in NE Angola and how these may have modified the composition of the diamond indicator minerals (ilmenite, clinopyroxene and garnet) sampled by the kimberlites. This is especially relevant in the case of ilmenite, since interaction with a kimberlitic magma may lead to misinterpretation of the diamond potential of a prospective kimberlite if textures and trace-element composition are disregarded.

DECLARATION

This thesis is based on work carried out in the Departament de Mineralogia, Petrologia i Geologia Aplicada (MPGA) of Universitat de Barcelona (Spain) and the GEMOC National ARC centre, in the Department of Earth and Planetary Sciences of Macquarie University (Australia).

I hereby declare that all the data and interpretations presented in this thesis are my own work except for information cited from published or unpublished work or others that have been fully acknowledged.

I certify that the work in this thesis has not previously been submitted for any other degree at any university or education institution. This thesis is submitted to both Universitat de Barcelona (Spain) and Macquarie University (Australia) under the conditions of the Cotutelle agreement for this PhD program between these universities.

Montgarri Castillo i Oliver
Student ID (MQUni): 43537499
NIUB: 11318506

August 2016

ACKNOWLEDGEMENTS

A la meva família, pel seu suport incondicional durant tots aquests anys. Gràcies per resignar-vos a veure'm a través d'una pantalla d'ordinador durant mesos i mesos... i més mesos. I per haver-ho fet sempre amb un somriure. Pare, gràcies per fer-me estimar la ciència des de ben petita, per haver-me fet créixer amb una curiositat constant per saber més i més del món que m'envolta. Mare, has estat el suport més gran que he tingut aquest temps, acompanyant-me en tots els alts i baixos propis d'una tesi. Crec que mai t'ho podré agrair prou. I sí, gràcies Oleguer perquè, encara que ara facis veure que estàs molt indignat perquè no m'he casat amb un cangur i torno a casa, sempre has aconseguit fer-me riure i treure ferro als moments més crítics.

And also to my Australian family, which now is almost as important as my Catalan one. Finishing a thesis far from home would not have been possible without all of you. Special thanks to Rosa, Sean and Angela for making my life "in exile" much easier. Thanks for your patience, your delicious meals that kept me going during the last days of my PhD and for understanding my mood swings. Thanks to SSS people as well as the other housemates: I will always remember the good moments that we shared and I really appreciated your support in stressful times.

Al despatx 119: la Cristina Villanova i en Thomas Aiglsperger. Perquè estic convençuda que no hauria pogut tenir uns millors companys de viatge. I perquè més enllà de les llarguíssimes discussions científiques, heu aconseguit que aquests anys hagin sigut molt bons, ja fos a còpia de pastissos per llepar-se'n els dits, sorpreses d'aniversari en majúscules, teràpies de xoc transhemisfèriques, purple days *o classes de salsa clandestines. Moltíssimes gràcies, de debò. I, Marc, de nou moltes gràcies per haver-me intentat convèncer durant hores (i per haver-ho aconseguit!) que era bona idea aquella bogeria d'apuntar-nos als "Jóvenes investigadores". Qui*

ho hauria dit quan vam començar? I sobretot gràcies per seguir-hi sent. I evidentment, a tots els altres doctorands, a en Lisard, la Sandra, l'Amaia, en Saleh i la Lídia.

And also to all my Australian friends at Macquarie University. Thank you for creating such a nice working environment, for being there to cheer me up when things were not going as planned and for making me smile with unexpected surprises on my desk when I was tired. *Arigato*. Merci beaucoup. *Eskerrik asko.* Grazie mille.

I would also like to thank all the institutions and projects who made this work possible by providing the financial support required for this thesis. This PhD was supported by an FPU scholarship (AP2009-4574) given by Ministerio de Ciencia e Innovación of Spain, as well as by a Cotutelle International Macquarie University Research Excellence Scholarship (iMQRES–No. 2014210). I would like to acknowledge everyone who made this cotutelle possible from both universities, since their efforts resulted in a very positive and enriching experience for me. This research was also supported by the projects CGL2006-12973 and CGL2009-13758 of the Ministerio de Ciencia e Innovación of Spain; the SGR 589, SGR 444 and 2014 SGR 1661 projects of the AGAUR-Generalitat de Catalunya; as well as funds from the ARC Centre of Excellence for Core to Crust Fluid Systems. I would also like to thank the logistic assistance for the field trips provided by the mining company CATOCA SL and Universidade Agostinho Neto (Luanda, Angola). Finally, I would like to acknowledge the funding received from the Fundació Pedro Pons (UB) and the Faculty of Geology from the Universitat de Barcelona to do part of the research overseas.

Thanks to everyone who helped me to carry out the analytical work of this thesis. First of all, I would like to acknowledge Dra. Dolors Barsó, Dra. Fadoua Oumada, Saleh Lehbib and Montserrat Sibil·la at the Thin Section Laboratory of the UB for preparing the thin sections that I used in my thesis. My most sincere thanks to Dr. Xavier Llovet and Dr. Eva Prats for their assistance with EMP and SEM analysis at the Serveis Científico-Tècnics (UB). Additionally, I would also like to thank Dr. José Ignacio Gil Ibarguchi, Dra. Sonia García, Aratz and Maru for their invaluable help with the LA-ICP-MS analysis at IBERCRON (UPV/EHU). And last, but not least, I really appreciated the kind and selfless help that I got from Dr. William Powell, Dr. Yoann Gréau, Dr. Rosanna Murphy and MSc. Sarah Gain when using the LA-ICP-MS and the MC-LA-ICP-MS at the GEMOC (MQUni). I would like to make a special mention for Dr. Norm Pearson, whose invaluable help and high expertise were essential both during the analytical work and the interpretation of the geochemical data. This thesis used

instrumentation funded by ARC LIEF and DEST Systemic Infrastructure Grants, Macquarie University, NCRIS AuScope and Industry.

Com no podia ser d'altra manera, vull acabar fent un especial agraïment als meus directors de tesi, en Joan Carles Melgarejo i en Salvador Galí. Caixa, moltíssimes gràcies per haver dibuixat el primer dia de classe aquell famós diagrama que ens va fer sortir a tots convençuts que els geòlegs ens podem menjar el món. Si no fos per l'enorme entusiasme que transmets per la geologia i la recerca -i que em va fer entrar en el món de la investigació- estic segura que aquesta tesi ara no existiria. Salvador, moltíssimes gràcies per ser-hi absolutament sempre, per posar unes quantes dosis de realitat i d'optimisme en aquesta tesi. Gràcies a tots dos pel vostre guiatge i per tot el que he après de vosaltres; per haver-me donat suport en els moments més difícils i alhora haver-me deixat la llibertat de fer la recerca que jo volia. Gràcies també a la resta del professorat del departament, per haver-me fet sentir com una més del vostre equip des del primer dia i pel vostre recolzament sempre que l'he necessitat.

And finally to my Australian supervisors, Bill Griffin and Sue O'Reilly. Thanks for giving me the opportunity of doing part of my PhD at GEMOC and using the facilities available at the GAU. I'm very thankful for your guidance over these years, for entrusting me and being so supportive. Bill, thanks for patiently tolerating absolutely all my impromptu visits to your office, which I typically started with "I have a really short question...", even if we both knew that this was far from the truth. Thanks for offering me your time and sharing your knowledge and enthusiasm for science with me.

To all who made this thesis possible, my most sincere thanks.

LIST OF PUBLICATIONS

Castillo-Oliver, M., Galí, S., Melgarejo, J.C., Griffin, W.L., Belousova, E., Pearson, N.J., Watangua, M., O'Reilly, S.Y., 2016. Trace-element geochemistry and U-Pb dating of perovskite in kimberlites of the Lunda Norte province (NE Angola): petrogenetic and tectonic implications. Chem. Geol. doi:10.1016/j.chemgeo.2015.12.014

Chapter 1
INTRODUCTION

1.1. Kimberlites: diamond mines

Kimberlites are K-rich, ultrabasic volcanic rocks, characterised by high contents of volatiles (CO_2 and H_2O). They are composed of a mixture of xenoliths, xenocrysts and groundmass minerals (Mitchell, 1986). Over 5000 kimberlite intrusions are known worldwide, grouped in provinces or clusters (Faure, 2010). Most of them are associated with cratons, areas which have been stable over a long period of time and which are characterised by a thick Archean and Paleoproterozoic lithosphere.

The occurrence of diamond as a xenocryst in some kimberlites and related rocks has made a mining target, being kimberlitic deposits the main source of diamonds, together with lamproites. However, kimberlite exploration and evaluation of its diamond grade is complicated, since most of the pipes have been covered by thick sedimentary layers and soils which make the exploration stage difficult. Commonly, a combination of aerial geophysics, mineralogy and cartography are necessary to locate new kimberlitic bodies. Additionally, diamond occurrence in kimberlites is usually very low and, as a result, not all the kimberlites contain enough diamonds to be considered economically viable. In fact, less than 5% of the kimberlites are thought to be diamondiferous (Janse and Sheahan, 1995) and, even in the richest ones, diamond contents rarely exceed 70 ppb (Carmody et al., 2014). Therefore, quick and cheap identification of the diamond grade of the kimberlites has become one of the biggest challenges for the mining companies.

One of the most important prospecting techniques is based on the chemical characterisation of the diamond indicator minerals (DIMs) which are also carried to the surface by the kimberlitic magmas. Among the DIMs, the most common ones have historically been magnesian ilmenite, Cr- rich and Ca-poor pyrope, Ti-poor chromite and Cr-rich diopside (e.g. Mitchell, 1973; Sobolev, 1977; Griffin et al., 1994, 1997; Fipke et al., 1995; Sobolev et al., 1997; Kaminsky and Belousova, 2009). In kimberlites these minerals can be found either in their original assemblage in mantle xenoliths, as discrete xenocrysts derived from xenolith disaggregation or even as inclusions in diamonds.

Apart from being significantly more abundant than diamond, DIMs are considered resistant to weathering, as well as to any diagenetic or subsolidus change that could take place after kimberlite eruption. As a consequence, they are thought to preserve their original composition, which is defined by the environmental conditions (P, T, X, fO_2, etc.) in which they crystallised. The study of the DIMs, commonly concentrated in placers, has thus become particularly useful in diamond exploration, since it allows the prospector to constrain whether or not the source of the kimberlite magma was located within the diamond stability field. Geochemical discriminatory diagrams are commonly used by the mining companies to represent the composition of the DIMs and proceed to the evaluation of the diamond potential of the prospected kimberlite (e.g. Fipke et al., 1995; Gurney and Zweistra, 1995; Grütter et al., 2004; Wyatt et al., 2004).

However, it has been repeatedly proven that these criteria are not globally applicable and that appropriate knowledge of the structure, composition and metasomatic evolution of lithospheric mantle sampled by the kimberlites is essential when assessing their diamond grade using DIMs (e.g. Jacques et al., 1986; Jago and Mitchell, 1989; Shee et al., 1989; Carlson and Marsh, 1989; Mitchell, 1991; Griffin and O'Reilly, 2005). Moreover, a recent study of ilmenite xenocrysts from the diamondiferous Catoca kimberlite (NE Angola) has shown that the study of the textures related to these indicator minerals cannot be neglected, since it could lead to misinterpretation of the diamond grade of the kimberlites (Robles-Cruz et al., 2009).

1.2. Kimberlites: windows into the SCLM

The deep source (>200 km) of the kimberlitic magmas and their high emplacement velocity (40-70km/h; Mercier, 1979) also turn them into exceptional carriers of fresh mantle samples.

Indeed, kimberlites are often seen as windows into the subcontinental lithospheric mantle (SCLM), since they can provide priceless information on its structure, composition and evolution.

The SCLM is mainly composed of peridotites, with significantly less abundance of pyroxenites and eclogites (<1%; Schulze, 1989). Typical peridotite compositions encompass lherzolites (olivine + orthopyroxene + clinopyroxene), harzburgites (olivine + orthopyroxene clinopyroxene) and dunites (olivine ± orthopyroxene ± clinopyroxene), with garnet and/or spinel as accessories (Griffin et al., 2009). Peridotites from the Archean SCLM are usually depleted in magmaphile elements (Ca, Al, Fe, LREE, Ti, Zr, Y) compared to the convecting asthenosphere (e.g. O'Reilly and Griffin, 2006). The primary melting events related to the formation and stabilisation of the lithospheric mantle are thought to be responsible for the progressive removal of these basaltic components from the SCLM (e.g. Boyd and Mertzman, 1987). However, subsequent introduction of mantle-derived magmas along fractures or channels may lead to refertilisation of the SCLM, enriching the upper mantle in incompatible elements (Dawson, 1984). These processes produce a heterogeneous and geochemically complex SCLM, composed of mantle domains differing in composition and thermal state. These depletion and refertilisation processes may not only significantly modify the composition of the SCLM, but also play a major role in diamond formation and preservation of diamond in the lithospheric mantle prior to entrainment in the kimberlite (e.g. Araújo et al., 2009, and references therein). Therefore, understanding the lithospheric structure and how these processes affected the SCLM is essential to assessing the diamond potential of a kimberlitic province.

The SCLM beneath most of the cratonic areas worldwide has been repeatedly studied, based on petrochemical characterisation of both mantle xenoliths and mantle xenocrysts mainly carried by kimberlites. In Africa, the research developed over the last decades in the Kaapvaal craton has resulted in a very good knowledge of the lithospheric structure, composition and mantle dynamics of this area (e.g. Griffin et al., 2003; Muller et al., 2009; Viljoen et al., 2009; Baptiste et al., 2012). Similarly, the composition and structure of the cratonic mantle beneath the Siberian craton (e.g. Ashchepkov et al., 2010; Ionov et al., 2010; Doucet et al., 2013; Pokhilenko et al., 2015) and the Slave craton (e.g. Griffin et al., 1999; Kopylova and Russell, 2000; Davis et al., 2003; Aulbach et al., 2004a) are now quite well constrained.

1.3. The SCLM in the Congo craton: the big unknown

In striking contrast with other cratons worldwide, the lithospheric mantle beneath Central Africa, and in particular the Congo Craton, is still poorly understood. The very few studies carried out in the Congo Craton have shown that it is significantly thicker and cooler than other cratons in Africa (e.g. Begg et al., 2009; O'Reilly et al., 2009; Robles-Cruz et al., 2012a). Similarly, the limited accessible data in the literature suggest that the composition of the SCLM beneath the Congo Craton differs from other African cratons (Batumike et al., 2009; Ashchepkov et al., 2012; Robles-Cruz et al., 2012a). However, most of these works are based on the study of xenocrysts and megacrysts derived from mineral concentrates, resulting in a lack of petrographic information of this area.

Additionally, it has been shown that different crustal terranes within the Archean cores are underlain by distinctly different types of SCLM (Griffin et al., 1999b; 2003). Comparable differences among the Archaean shields composing the same craton have also been reported in other locations (Griffin et al., 1999a; Kopylova and Russell, 2000; Ashchepkov et al., 2014). Therefore, the structure of the SCLM in the central part of the Congo Craton defined by Batumike et al. (2009) may not necessarily be comparable to other shields composing this craton, like the Kasai shield (NE Angola).

However, improving our current knowledge about the SCLM in this particular shield has become critical, since it contains the Lunda Norte kimberlitic province, one of the main diamondiferous kimberlite clusters in Africa. The controversial results of recent studies on DIMs in this province also emphasise the necessity of a better characterisation of the materials brought to the surface by the Angolan kimberlites.

1.4. Aims and structure of the thesis

As stated previously, the models that are applicable to one craton may not be necessarily useful to explain the distribution of the fertile and barren kimberlites in other cratons (Mitchell, 1991). As a consequence, this thesis aims to:

1. Characterise the petrogenesis of several kimberlite intrusions in the Lunda Norte province, mainly based on the study of groundmass perovskite. Additionally it aims to date these eruptions by using U-Pb isotope systematics in order to understand what triggered kimberlite magmatism in this area.

2. Define the structure and composition of the SCLM beneath the Lunda Norte province, from the petrographic and chemical characterisation of mantle xenoliths (peridotites, eclogites, garnet-pyroxenites) carried to the surface by Angolan kimberlites.

3. Identify the different metasomatic processes that took place in this lithosphere based on the mineralogical and chemical characterisation of mantle xenoliths and garnet xenocrysts.

4. Compare the structure, composition and evolution of the SCLM beneath the Lunda Norte province with that found in other cratons worldwide.

5. Evaluate the use of the two main diamond indicator minerals, garnet and ilmenite, found in Angolan kimberlites and its implications for diamond exploration.

To achieve these goals, this thesis has been divided into 10 chapters. The first two chapters are introductory and are meant to provide the reader with the necessary geological and chemical background to understand an unknown area such as the Lunda Norte province. Chapter 3 includes the methodology that was used to carry out all the analytical work, which is followed by a general petrographic description of the kimberlites (chapter 4). The petrogenesis of several Angolan kimberlitic bodies and the timing of their eruption is discussed in chapter 5. Chapter 6 is devoted to the characterisation of the mantle xenoliths and megacrysts sampled by the kimberlites, including a detailed petrographic description, as well as mineral chemistry (major- and trace-element analyses). In chapter 7, the lithospheric structure of the mantle beneath the Lunda Norte province is discussed by combining geothermobarometry and the results presented in the previous chapter. This compositional information is subsequently used to characterise the metasomatic processes registered by the mantle xenoliths and the xenocrysts (chapter 8). The use of the garnet and ilmenite as DIMs is evaluated in chapter 9, as well as its implications in diamond exploration. Finally, a brief summary and conclusions are found in chapter 10.

I hope you will enjoy the reading!

Chapter 2
GEOLOGICAL SETTING OF THE LUNDA NORTE PROVINCE

Angola records most of the main geological events and tectonic episodes that have occurred in the African continent. This chapter aims to provide a quick overview on the processes that lead to the current configuration of Africa, with special emphasis on the tectonic evolution of the Congo Craton. Likewise, a general description of the geology of the Lunda Norte province is outlined below, as well as the major tectonic events that affected this area. Finally, the current knowledge about the tectonic controls for kimberlite emplacement in Angola is summarised in the last section of the chapter.

2.1. African tectonic evolution

Like other continents, Africa is composed of several Archaean craton nuclei, welded by orogenic – or mobile - belts that represent the breakups, accretions and collisions that led to the current configuration of the continent (De Waele et al., 2008). However, defining the boundaries of these cratons and their constituent Archean blocks - or shields - is not a trivial issue and significant divergence can be found in the literature (i.e. Hanson, 2003; Johnson et al., 2005; De Waele et al., 2008; Begg et al., 2009). Detailed explanations of African geology and its tectonic evolution have been compiled by Begg et al. (2009) and Bambi (2015).

At least 8 orogenies were involved in the formation of the African continent and defined its current structure (De Waele et al., 2008): i. 3.5-3.0 Orogeny; ii. Shamvaian Orogeny (2.8-2.5Ga); iii. Limpopo-Liberian Orogeny (2.6 Ga); iv. Eburnean Orogeny and Huabianian Episode (1.85 ± 0.25 Ga); v. Kibarian Orogeny (1.1 ± 0.2 Ga); vi. Pan-African or Damaranian Orogeny (750 ± 100 Ma); vii. Acadian and Variscan Orogenies and viii. Alpine Orogeny (Atlas). Rifting processes, such as the separation of the Congo-Tanzania-Bangweulu, Kalahari and Mozambique cratons around 800 Ma or the break-up of Gondwana (120 Ma), also have

played a major role in the present configuration of the African continent. These extensional regimes are of special interest for this thesis, since they favoured the eruption of kimberlites, carbonatites and nephelinites in Africa.

The schematic reconstruction of the tectonic evolution of the African continent proposed by Begg et al. (2009) is presented in fig.2.1.

As shown in this cartoon, the Precambrian (>2.5 Ga) basement in Africa was composed of several relatively small granite-gneiss and greenstone belts as nuclei. Progressive cratonization

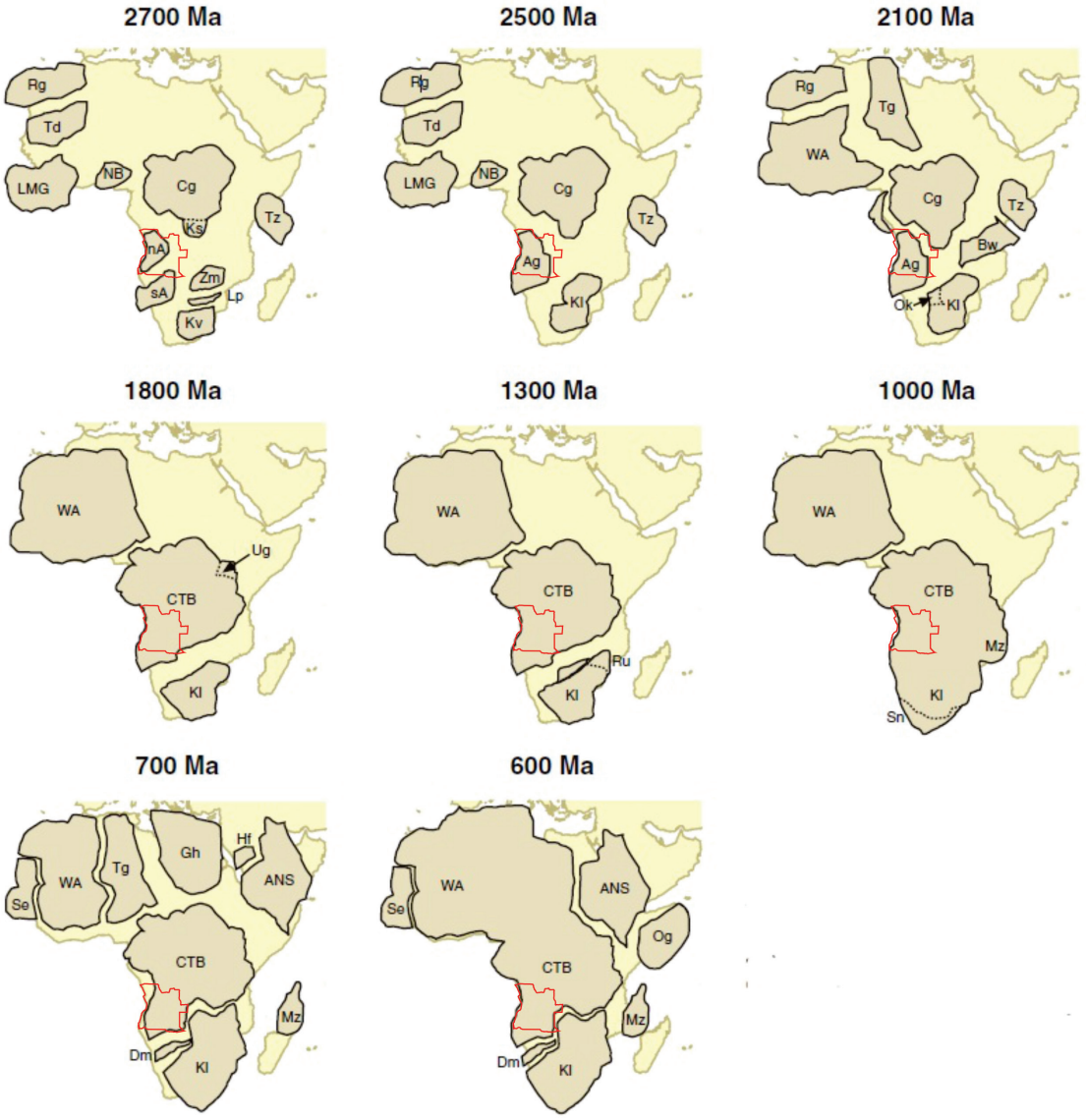

Figure 2.1. Simplified tectonic evolution of Africa, with the location of Angola, based on the upper lithosphere domains (adapted from Begg et al., 2009). As shown in this figure, the three main African cratons -the West African Craton (WA), the Congo-Tanzania-Bangweulu craton (CTB) and the Kalahari Craton (Kl)- resulted from tectonic assembly of smaller Archaean nuclei: Leo-Man-Ghana (LMG), Taoudeni (Td), Reguibat (Rg), (NB), Congo (Cg), Kasai (Ks), North Angolan (nA), South Angolan (sA), Tanzania (Tz), Zimbabwe (Zm), Limpopo (Lp), Kaapvaal (Kv), Taureg (Tg), Bangweulu (Bw), Okwa (Ok),Uganda (Ug), Rushinga (Ru), Saldania (Sn), Mozambique (Mz), Senegal (Se), Ghana (Gh), Arabian-Nubian Shield (ANS).

of the African continent led to the formation of three main Archaean cratons after the Eburnean Orogeny (1.85 ± 0.25 Ga): 1. West African Craton, 2. Congo Craton and 3. Kalahari Craton. Therefore, each of these cratons is actually composed of an amalgam of smaller cratons or blocks, such as the Tanzania Craton or the Uganda Craton, which differ from one another in their structure, composition and tectono-magmatic evolution (Begg et al., 2009 and references therein). The three main African cratons remained mostly unaffected by the Kibarian Orogeny (1.1 ± 0.2 Ga) and subsequent orogenies. In addition to these cratons, other old stable areas have been identified in Africa (e.g. Sahara Metacraton, or East Saharan Craton), although their boundaries and structure have not been totally defined yet.

2.2. Tectonic evolution of the Congo Craton

Angola is located at the south-western part of the Congo craton, which occupies a large part of central Africa, extending from Sudan through the Democratic Republic of Congo to Angola. Based on tomographic imaging, Begg et al. (2009) suggested that the core of this craton was already around 2000 km across ca 2.8 Ga ago. As shown in fig. 2.1, the Kasai craton was probably already accreted to the Congo craton in the Neoarchean, whereas the northern and southern Angolan cratons probably joined by 2.6 Ga. During the Eburnean orogeny, the Congo Craton collided with the Angolan, the Sao Francisco and the Gabon cratons. Over the same period, the Tanzania and the Bangwuelu cratons accreted and subsequently collided with the Ugandan microcontinent (1.85 Ga). Shortly later (~1.8 Ga), the formation of the Congo-Tanzania-Bangweulu craton (CTB) took place, consolidating the main structure of the current Congo Craton. During most of the Mesoproterozoic, little tectonic activity is registered in this craton and it was always restricted to its margins. However, convergence between the CTB and Kalahari cratons occurred in late Mesoproterozoic time. An extensional episode started around 800 Ma ago, which again separated the CTB and the Kalahari craton, accompanied by intrusion of basic magmas. Finally, the Panafrican orogeny (650-550 Ma) caused the convergence and suturing of most of the cratons (i.e. West African, Eastern Sahara, Tuareg, Senegal, Mozambique, Kalahari and CTB) and defined the current African continent.

The Eburnean event was the most important one, deforming most of the rocks of the basement of the Congo craton, while the Kibaran and Pan-African affected it only at local scales (Pereira et al., 2003). The superposition of these different tectono-magmatic events resulted in complex and intense deformation of the basement rocks, accompanied by high

grade metamorphism. On top of this basement, a thin and little deformed Phanerozoic sedimentary cover was deposited.

2.3. Current structure of the Congo Craton

As mentioned above, the boundaries of the Congo Craton changed significantly over time and they are still unclear. According to Begg et al. (2009) four main shields can be currently distinguished within it (fig. 2.2.): 1. Gabon-Cameroon Shield (NW, 3.2-2.99 Ga); 2. Bomu-Kibalian Shield (NE, 3.42-2.46 Ga); 3. Kasai Shield (SE, 3.01-2.1 Ga) and 4. Angolan Shield (SW Angola, 2.82-2.0 Ga). They are all composed of an old migmatitic-gneiss nucleus (3.5-2.8 Ga) with some remnants of younger greenstone belts, which have been later metamorphosed and/or intruded by younger granites (~2 Ga). The detailed composition, structure and evolution of the Congo Craton is still poorly understood, although the few published works demonstrate that the four shields show significant differences in terms of their composition and geological evolution (Cahen et al., 1984; Walraven and Rumvegeri, 1993; Goodwin, 1996; De Carvalho et al., 2000; Tchameni et al., 2000). As a consequence, they are usually considered as separate terranes (Begg et al., 2009). Amalgamation of these cratons is thought to have involved also their SCLM roots, creating cratonic nuclei large enough to survive later collisions (Griffin et al., 2004). Therefore, the cratonic roots of the current cratons are likely to represent a wide range of compositions inherited from the original Archean blocks, which emphasizes the necessity of an independent characterisation of each Archaean block (i.e. Kasai and Angola Shields). Some studies have been attempted to characterise the composition and structure of the northern and eastern part of the Congo craton (e.g. Batumike et al., 2009; Pivin et al., 2009). In contrast, there is very little information about the Kasai and Angola blocks, located in southern and central Angola, respectively. These two blocks are separated by the Congo Basin, an extensive and thick sedimentary cover that hinders correlation between the Kasai and Angola blocks (De Waele et al., 2008).

2.4. Geology of the Lunda Norte province

A very good description of the geology of Angola can be found in Gonçalves (2007) and a simplified map of the main geotectonic units is presented in fig. 2.3. In this thesis a general overview of the Angolan geology is included in appendix A2.1. However, because of its

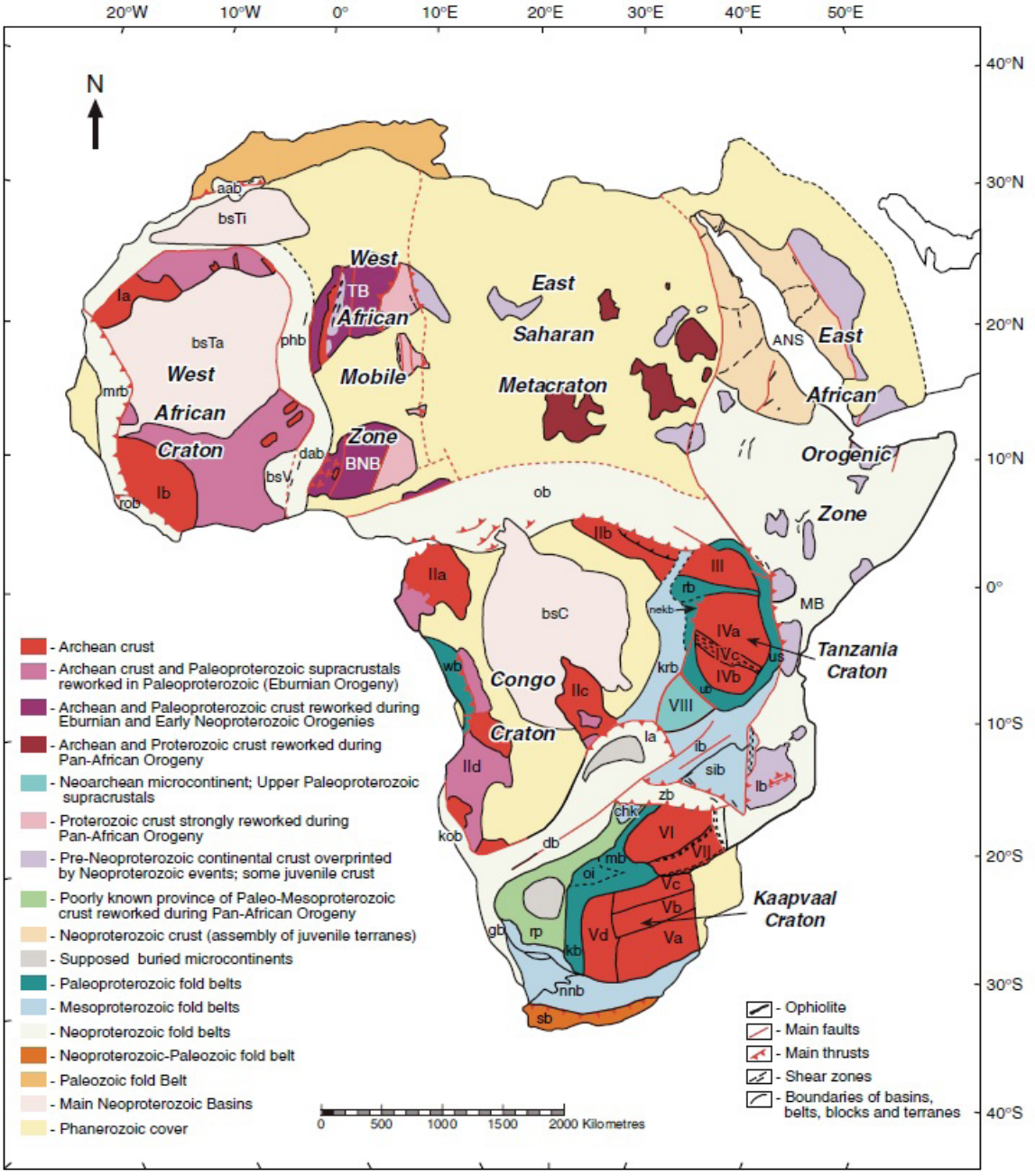

Figure 2.2. Map of the bedrock geology of Africa, outlining the major subdivisions of the crust (taken from Begg et al., 2009). Cratons and Microcontinents: West African Craton (Ia—Reguibat Shield; Ib—Man-Lèo Shield); Congo Craton (IIa—Gabon-Kamerun Shield; IIb— Bomu-Kibalian Shield; IIc—Kasai Shield; IId—Angolan Shield); Ugandan Craton—III; Tanzanian Craton (IVa—Northern Terrane; IVb—Southern Terrane; IVc—Dodoma Zone); Kaapvaal Craton (Va—Southern Terrane; Vb—Central Terrane; Vc—Pietersburg Terrane; Vd—Western Terrane); Zimbabwe Craton—VI; Limpopo Block—VII; Bangweleu Block—VIII. West African Mobile Zone: TB—Tuareg Block; BNB—Benin-Nigerian Block. East African Orogenic Zone: ANS—Arabian-Nubian Shield; MB—Mozambique Orogenic Belt. Fold Belts: Paleoproterozoic Belts: ub—Ubendian; us—Usagaran; rb—Ruwenzory; kb—Kheis; oi—Okwa inlier; mb—Magondi; wb—West Central African; nekb—North-Eastern Kibaran. Paleo-Mesoproterozoic Province: rp—Rehoboth. Mesoproterozoic Belts: krb—Kibaran; ib—Irumide; sib—Southern Irumide; chk—Chomo-Kolomo; nnb—Namaqua-Natal. Neoproterozoic Belts: zb—Zambezi; la—Lufi lian arc; db—Damara; kob—Kaoko; gb—Gariep; ob—Oubanguides; aab—Anti-Atlas; phb—Pharusian; dab—Dahomeyan; rob—Rockellides; mrb—Mauritanides; lb—Lurio; sb—Saldania. Neoproterozoic Basins: bsC—Congo; bsTa—Taoudeni; bsTi—Tindouf; bsV—Volta.

importance for the present work, a more detailed description of the geology of the Lundas region (NE Angola) is given here.

All the kimberlites studied in this thesis are located in the Lunda Norte province (NE Angola). Most of the kimberlite eruptions in Angola took place in the Lower Cretaceous (Davis, 1977; Haggerty et al., 1983; Eley et al., 2008; Robles-Cruz et al., 2012), and therefore they intruded an extremely wide range of materials, including the Precambrian basement and the Mesozoic cover. Figure 2.4 summarises the stratigraphic sequence as well as the main tectonic events reported in the Lundas province.

As shown in this table (fig. 2.4), in the Lundas area the crystalline Precambrian basement is mainly composed of Archaean charnockites, granites and gneisses, together with Proterozoic granitoids, BIF deposits and amphibolites. This province was extensively affected by both the Eburnean and the Kibaran orogenies and, as a result, most of these rocks register high metamorphic grade and strong deformation.

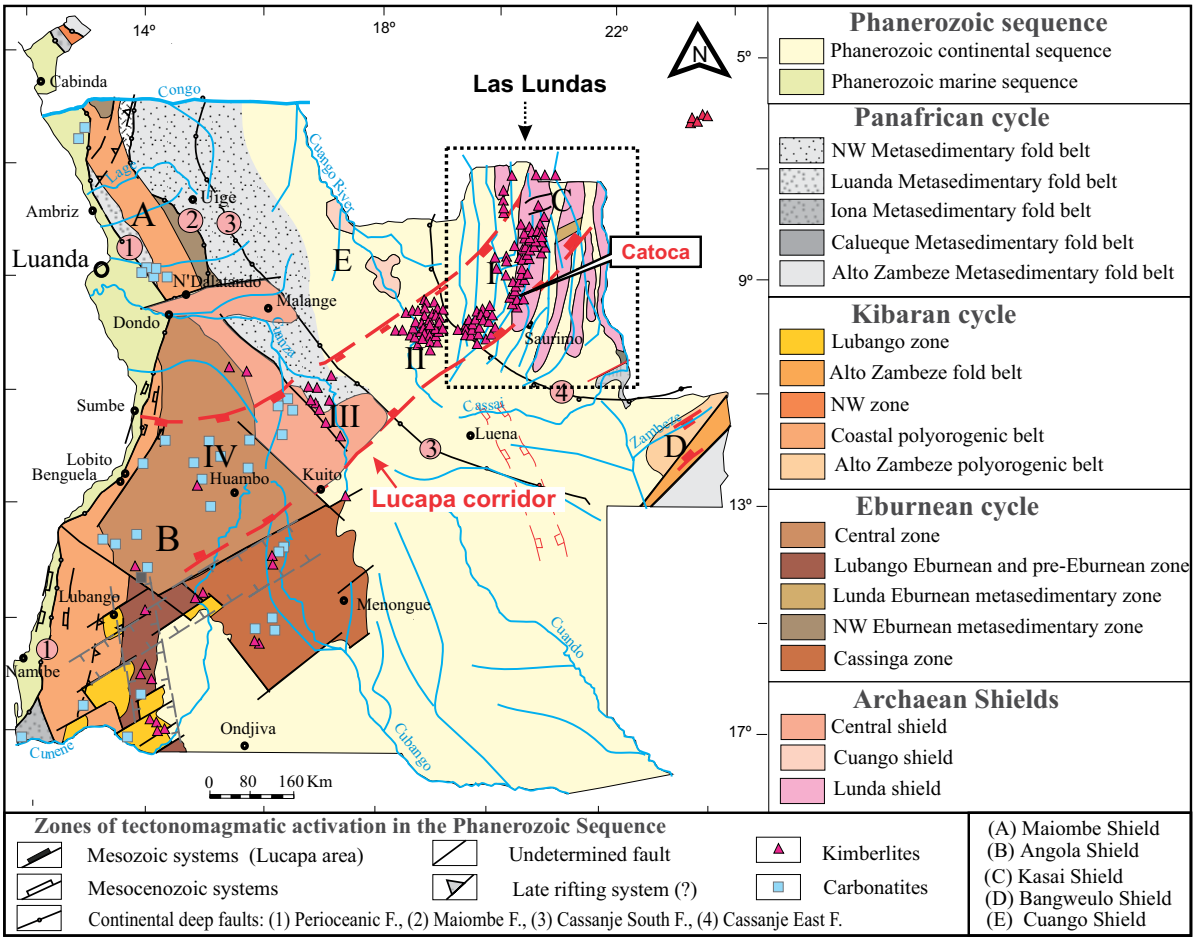

Figure 2.3. Map of the main geotectonic units found in Angola (modified from Araújo & Guimaraes (1995), Egorov et al. (2007), Robles-Cruz et al. (2009)). Note that most of the kimberlites (triangles) and carbonatites (blue squares) are located within the Lucapa corridor and define four main kimberlitic and carbonatitic provinces (I-IV). The study area, the Las Lundas province (I), is located on the NE part of Angola, in the Kasai Shield (C).

AGE		LITHOSTRATIGRAPHY	TECTONIC EVENTS
NEOGEN	Pliocene - Miocene	**Kalahari Group** Ochre sands and clays Fm	Erosion Erosion - hiatus
PALEOGENE	Eocene	Grés Polimorfos Fm	Erosion - hiatus
CRETACEOUS	Cenomanian	**Kwango Group** *Calonda Fm:* Sandstones and silcretes, mudstones; conglomerate interbeddings	Erosion
	Albian	Coloured sandstones and arkoses; reddish muddy arenites; basal conglomerates	**Kimberlite intrusions** Continental rifting
	Aptian	**Intercalar Continental Group** Mudstones and arenites, with conglomerate interbeddings White and reddish sandstones (caolonitized arkoses), interbedded with brownish clays Mudstones and sandstones, with fine-grained conglomerate interbeddings	W-E tectonic extension Erosion - hiatus
JURASSIC		**Karroo Supergroup** Continental tholeiites	Tectonic fracturing NNE-SSW
TRIASSIC		**Cassange Group** Beds with Phyllopodia Fm **Beds with Plant Fossils Fm** Beds with Fish Fossils Fm	
PERMIAN		**Lutôe Group** Glacio-fluvial conglomerates Fm Muddy-psammitic Fm Yellow mudstone Fm Violet sandstone Fm Tillite Fm	Tectonic fracturing NNW-SSE
CARBONIFEROUS			Tectonic extension W-E Erosion - hiatus
		Hyperalkaline granites of Lunda Basic rocks of Lunda	Tectonic fracturing WSW-ENE
CAMBRIAN		**West Congo Group** *Luana Fm:* Quartzites and red phyllites *Cartuchi-Camaungo Fm* Meta-arkoses and phyllites	Panafrican Orogeny
NEOPROTEROZOIC		Brown quartzites and conglomerates Meta-greywackes , quartzites and conglomerates	
PALAEOPROTEROZOIC		**Lulua Group (Upper metamorphic group)** Silicified meta-limestones and qtz-rich phyllites; phyllites and meta-sandstones with conglomerate interbeddings Phyllites and schists, fine-grained quartzites, black shales	Eburnean / Ubendian Orogeny
		Porphyry granites of Lunda	
		Lovua or Luiza Group (Lower metamorphic group) Micaschists, quartzites and itabirites Amphibolites, gneisses and gneissic granites	
ARCHAEAN		**Basal complex (undifferentiated) > 2.7 Ga** **Dibaya Group** Gneiss, migmatites and gneissic granitoids	Limpopo - Liberian Orogeny (?)
		Charnockite Complex Charnockite Quartzites Amphibolic gneiss, amphibolites and meta-gabbros	

Figure 2.4. Simplified lithostratigraphy of the Lundas area, including the major tectonic events, as summarised by Pereira et al. (2003).

In the Late Paleozoic, incipient rifting was accompanied by the sedimentation of large detrital continental series in the newly formed basins. As in other countries in Africa, the Karroo Supergroup is also present in Angola. In the Las Lundas area it includes the Lutôe (Carboniferous-Permian) and the Cassange (Late Permian-Triassic) groups, both mainly composed of red sandstones, with interbedded conglomerate and schist. Clear evidence of the Jurassic extensional regime, linked to the opening of the Atlantic Ocean, is found where the continental sedimentary rocks are interbedded with thick basaltic and tholeiitic flows.

On top of these rocks, the Intercalar Continental Group (ICG) was deposited, forming several subhorizontal detrital series differing in thickness. Detailed palaeontological studies yield Lower Cretaceous ages (Aptian) for most of the layers. The Angolan kimberlites usually intrude this unit, incorporating sandstone xenoliths of the ICG. Most of the kimberlitic bodies are in turn covered by the Calonda formation (Cenomanian). In this unit, made of continental alluvial materials, some diamond deposits have been identified as possible paleoplacers (Llusià et al., 2005).

Discordantly overlying the Cretaceous rocks, new continental series were deposited, forming thick layers of reddish sandstones. Among these Neogene sediments, the Kalahari Group is the most significant one in terms of its extension and thickness, resulting in an added difficulty for diamond exploration and mining. Finally Quaternary sediments, transported by the rivers, might also cover some of the kimberlitic bodies. However, in some cases this fluvial erosion can lead to the formation of new diamond deposits, as either alluvial or colluvial placers.

2.5. Tectonic control of the Angolan kimberlites

As shown in the synthetic geological map (fig. 2.3), most of the kimberlites and carbonatites found in Angola are located within the Lucapa corridor, an extensive tectonic structure that crosses the country from NE to SW. This major basement structure can be traced for more than 1600 km across Angola into the Democratic Republic of the Congo (Reis, 1972) and has a continuation to the southwest to the transform faults of the Mid Atlantic Ridge, with 300-km dextral offsets (Reis, 1972; Sykes, 1978) .

Four kimberlite and carbonatite provinces (I-IV) can be distinguished within the Lucapa Corridor. Province I, on the north-eastern area, represents the main Angolan kimberlite field. There is an increase in the number of carbonatite intrusions from northeast to southwest, so

that province IV is mainly carbonatitic with very few diamondiferous kimberlites (White et al., 1995). Even if the NE-SW fault and fracture corridors are largely predominant, two secondary fault systems (ENE-WSW and NNW-SSE) also play a major role in kimberlite emplacement in these provinces (White et al., 1995). These secondary corridors are particularly important in Provinces I and IV, whereas kimberlite emplacement in Provinces II and III is thought to be mostly driven by intersection of the conjugate (NW-SE) corridors (R'-shears) with the Lucapa Corridor (De Boorder, 1982).

The Lunda Norte kimberlitic cluster is located in Province I and thus kimberlite emplacement in this area is mainly controlled by fault-bounded compartments with WSW-ENE direction which are dislocated by NNW-SEE faults, giving an en echelon pattern (Pereira et al., 2003). Additional indicators of such corridors were given by Jelsma et al. (2004) , who suggested that the major crosscutting lineaments that could be defined using digital elevation data actually represent sets of faults at regional and/or subregional scale (fig. 2.5).

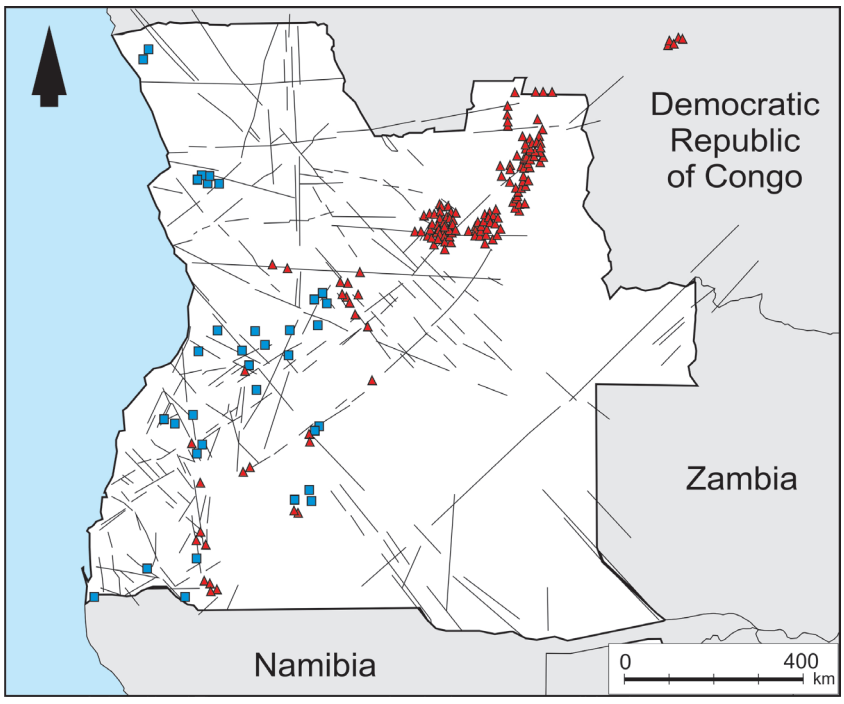

Figure 2.5. Lineaments defined from digital elevation data in Angola; these are interpreted to reflect deep fault systems that controlled kimberlite emplacement in the country. This map has been modified from Jelsma et al. (2004) and it includes the kimberlite (triangles) and carbonatite (squares) distributions compilated by Jelsma et al. (2004), Egorov et al. (2007) and Faure (2010).

Kimberlite emplacement in Southern Africa has been triggered by the reactivation of deep cryptic corridors (Jelsma et al., 2004), which is consistent with the conclusions of White et al. (1995) for Angola. Further evidence of such translithospheric (>300km) corridors has been provided by the global-scale tomographic studies carried out by Begg et al. (2009). They observed that carbonatite, nepheline syenite and kimberlite occurrences in Africa usually are

restricted to belts or linear arrays, following steep Vs gradients around the cold cratons. In Angola, the NE-SW distribution of kimberlites and carbonatites within the Lucapa corridor also coincides with strong gradients in Vs along the south-western edge of the Congo craton (fig. 2.6). Since the margins of cratonic blocks correspond to former tectonic sutures, they are prone to tectonic reactivation and thus to become channels for ascending asthenosphere-derived fluids.

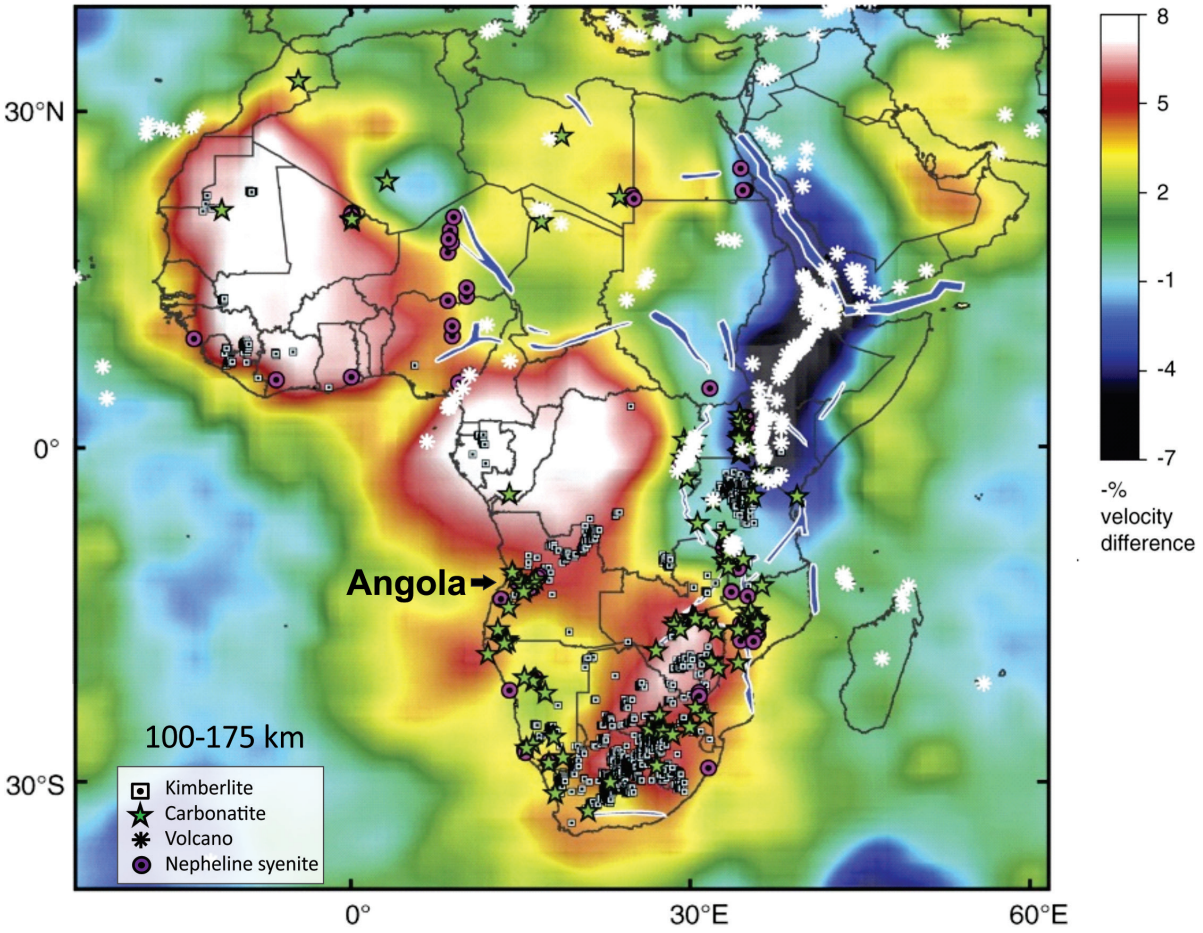

Figure 2.6. Tomographic S-wave velocity (Vs) image taken from Begg et al. (2009), coupled with the distribution of low-volume melts (alkaline rocks, carbonatites, and kimberlites) and Mesozoic to Cenozoic rifts (in blue). As seen in this slice, alkaline intrusions are preferently located along the boundaries of the cratonic blocks, defined by high-velocity areas (white colours).

2.6. Chemical background of the Congo craton

As noted in the introductory chapter, the lithospheric structure beneath Central Africa, and in particular the Congo Craton, is still poorly understood and only limited information can be found in the literature (Batumike et al., 2009; Pivin et al., 2009; Ashchepkov et al., 2012; Robles-Cruz et al., 2012a; Nikitina et al., 2014).

The few published results show that the thickness of the lithosphere in the Congo craton is not homogeneous, but it ranges between 175 km in the Kudelungu Plateau to 210 km in the Mubji Mayi region (Batumike et al., 2009). Moreover, regional tomographic surveys suggest that the lithosphere-asthenosphere boundary (LAB) in the core of the craton may be located up to 300 km deep (Begg et al., 2009; O'Reilly et al., 2009). This thick lithosphere is consistent with the cool geotherms (35 mW/m^2) calculated by Batumike and coauthors (2009). These authors also highlighted that the structure of the SCLM in the Congo Craton is heterogeneous, with provinces where harzburgitic garnets are almost absent and others where they define a ca. 80-km thick layer. Moreover, significant differences were observed in terms of the metasomatic processes affecting the SCLM beneath different kimberlitic provinces in this craton (Batumike et al., 2009; Pivin et al., 2009). Evidence of pronounced melt metasomatism was found in the thinner parts of the craton, whereas the thicker regions are characterised by a mixed type of metasomatism, involving both melt-related and phlogopite-related metasomatism (Batumike et al., 2009). These results point to a complex upper mantle, differing in composition, structure and type of metasomatism beneath each of the tectonic shields that make up the Congo Craton.

In the Kasai shield, the understanding of the SCLM is even more restricted than in other areas of the Congo Craton, because of the recent troubled history of the country, which has made it very difficult to get samples from the Angolan kimberlites. The few preliminary studies carried out only recently in the Kasai shield are mostly based on mineral concentrates from Cretaceous kimberlites (Ashchepkov et al., 2012; Robles-Cruz et al., 2012a). However, essential information from mantle xenoliths (i.e. microstructure, mineral assemblage, chemical equilibrium, textural relationship between minerals and metasomatic processes) is obliterated or wrongly simplified when using mineral concentrates. Robles-Cruz et al. (2012) carried out geothermobarometric studies on the SCLM beneath the Lundas using a limited number of mantle xenoliths from the Catoca pipe; neither petrographic nor metasomatic information was included in their work.

However, their research revealed similar low, cratonic-type conductive geotherms for all

the studied kimberlites (37-40 mW/m^2), although a slightly cooler geotherm was calculated beneath the Catoca kimberlite (Robles-Cruz et al., 2012a). These thermal conditions are cooler than those observed in other African cratons, which is in good agreement with a thicker lithosphere beneath the Congo craton as suggested from tomographic studies (Begg et al., 2009).

Based on the study of mineral concentrates, Ashchepkov et al. (2012) defined a layered structure of the SCLM beneath the Lunda Norte province, which included several eclogite lenses at different levels of the lithosphere. The occurrence of low-Mg eclogites at 130-170km depth was subsequently confirmed by a detailed characterisation of eclogite xenoliths sampled by the Catoca kimberlite (Nikitina et al., 2014). However, to date there is still no petrographic characterisation of other mantle xenoliths (spinel-peridodites, garnet-peridotites, highly metasomatised peridotites) in the Congo Craton.

Chapter 3
METHODOLOGY

All the analytical work included in this thesis was carried out using facilities located in three different laboratories: the Centres Científics i Tecnològics (CCiT) from the Universitat de Barcelona, the IBERCRON laboratory from the Universidad del País Vasco (UPV/EHU) and the Geochemical Analysis Unit (GAU) at Macquarie University.
In this chapter, the methodology used to characterise the different samples is explained in detail. After sample preparation, a preliminary characterisation of the main mineralogy and textures by means of petrographic and scanning electron microscopes was done. Data on mineral chemistry were subsequently acquired in situ, using both electron microprobe and LA-ICP-MS techniques, allowing spatial control on the different generations of minerals. Isotope analyses (U-Pb and Sr-Nd) were done on perovskites using LA-MC-ICP-MS.

3.1. Sample preparation

Most of the samples studied in this thesis come from the field work in July 2008 and the subsequent field campaigns carried out by members of the SGR444 Research Group from the University of Barcelona. The majority of the rock samples were taken from drill cores provided by the Catoca mine petrologist, Dr. Vladimir Pervov, and Dr. Antonio Olimpio Gonçalves from Universidade Agostinho Neto. Their size ranges between 4 and 15cm, and they weigh between 0.1 and 3.5kg. A descriptive catalogue with the main features of each sample is included in appendix A3.1.

Each sample was sawed into several sections (~1cm thick) in order to select its most representative and fresh (least serpentinised) portions. When necessary, more than one zone per sample was chosen to ensure a systematic study of all the features. Subsequently, thin (30-40 μm) and thick (~100 μm) polished sections and blocks were prepared at the Thin Section Laboratory in the Faculty of Geology of the Universitat de Barcelona. The ilmenite xenocrysts collected from the Tchiuzo kimberlite outcrops were set in epoxy mounts and

polished. Additional thin sections and mounts from previous studies were also examined for comparison and to complete the dataset. These include samples from the Catoca, Lucapa 1, Lucapa 2 and Tchiuzo kimberlites.

The kimberlite samples selected for X-Ray diffraction were taken from off-cuts of the original sawing of the rocks. After crushing, they were milled into powder using an agate mill. Subsequently, manual pressing of this powder material was done by means of a glass plate to get a flat surface, in cylindrical standard sample holders of 16 millimetres in diameter and 2.5 millimetres high.

3.2. Petrographic characterisation: SEM-EDS

A detailed characterisation of both the kimberlite rocks and the mantle xenoliths was initially carried out using a petrographic microscope. However, in order to identify the fine-grained phases, as well as to describe their complex textures, alteration and zoning patterns, and their textural relations, higher magnification and semi-quantitative analyses were required. For this purpose, two scanning electronic microscopes were used: a SEM Leica Cambridge S.36 and an ESEM Quanta 200 FEI XTE 325/D8395, both located at the Centres Científics i Tecnològics (CCiT) of the Universitat de Barcelona. A focused beam of 20 keV was used and semi-quantitative analyses were performed using the EDS detector coupled to these instruments. Identification of the small inclusions found in some ilmenite grains was carried out by means of a JEDL J-7100 field emission SEM located in the same facilities. Additional characterisation was also performed using the SEM facility coupled with semi-quantitative EDS analysis in the Geochemical Analysis Unit (GAU) facility of the ARC (Australian Research Council) Centre of Excellence for Core to Crust Fluid Systems (GEMOC, Macquarie University, Australia).

3.3. Major element analysis: Electron microprobe

Major- and minor-element contents of silicates, carbonates and oxides in carbon coated thin sections were analysed with a CAMECA SX50 electron microprobe with four wavelength dispersive spectrometers (WDS), at the CCiT of the Universitat de Barcelona. Additional analyses of garnet xenocrysts were done at the GAU facilities, using a CAMECA SX100 electron microprobe. The approximate diameter of the electron beam was 1-2 μm. Analytical

conditions were 20 KV accelerating potential, a beam current of 10 nA and a take off angle of 40º. Both for major and minor elements, counting times were 10s for the peak and 10s for the background. For most of the minerals, totals between 99 and 101% were accepted. Standards used for calibration in each instrument are included in appendix A3.2.

The raw data were corrected using the Pouchou and Pichoir (1984) reduction. A structural formula for each mineral was calculated using either a software included in the CAMECA SX50 electron microprobe or a home-made excel spreadsheet. In both cases, the structural formula was obtained according to Dana's mineralogical classification.

3.4. Trace-element analysis: LA-ICP-MS

Trace-element compositions of silicates (garnet, clinopyroxene, orthopyroxene, olivine, phlogopite and amphibole), ilmenite, chromite and perovskite were obtained by means of two different laser ablation inductively coupled plasma mass spectrometers (LA-ICP-MS). The first system used, a Thermo Fisher XSeries-II, located at the IBERCRON (Laboratorio de Geocronología y Geoquímica) of the Universidad del País Vasco (UPV/EHU). In this case, a second vacuum pump was added to the interphase system to increase the sensitivity of the instrument. The second mass spectrometer, set up at the GEMOC laboratories (Macquarie University), consists of an Agilent 4500 series 300 ICPMS. In both instruments, the laser ablation microsampling system was a New Wave Research UP-213. Data obtained at the IBERCRON laboratory (UPV/EHU) were processed using the Iolite 2.2 software (Paton et al., 2011; Paul et al., 2012), whereas the results obtained at the GAU facilities were subsequently treated using the GLITTER program (Griffin et al., 2008). An inter-laboratory comparison of the data showed very good agreement between the two instruments. The spatial control provided by this *in-situ* technique was crucial to characterising the variations in trace-element contents of the different generations of minerals in the mantle xenoliths. Likewise, it allowed resolution of the chemical signatures of the different textural populations of the diamond indicator minerals as they occur in the kimberlitic matrix, which would not have been possible if the samples were DIM concentrates or dissolution of the minerals was necessary.

Since the instrument settings for each mineral or group of minerals were different, a separate description of the analytical conditions for each case is included next. In all cases, the typical relative precision and accuracy for a laser microprobe analysis range from 1 to 10%.

3.4.1. Silicates

Trace-element (Sc, Ti, V, Cr, Mn, Co, Ni, Ga, Rb, Sr, Y, Zr, Nb, Cs, Ba, REE, Hf and Ta) contents of olivine, garnet, clinopyroxene and orthopyroxene grains were analysed on polished sections >100 microns thick using the LA-ICP-MS at the UPV/EHU. The relative sensitivity was calibrated against silicate glass standards (NIST 610 and NIST 612), using the values of Jochum et al. (2011). Each analysis was normalised to the Si values determined by the electron microprobe. The counting time for each sample was 90s (30s background and 60s signal) and the spot size was 55 μm. In order to ensure that no drilling through the phlogopite and amphibole crystals took place during the ablation, a 100-micron linear traverse was used. With the spot size still 55 microns, this procedure allowed a long acquisition time and good-quality signal. In all analyses, the repetition rate of the laser beam was 10Hz, and its energy density, 70% (6.5 J/cm^2). Samples were analysed in runs of 16 analyses comprising 12 analyses of unknowns bracketed by analyses of both standards at the beginning and the end of each run.

Additional analyses on garnet xenocrysts were performed at the GAU facility (GEMOC). The NIST 612 glass was used as internal standard, adopting the values from Norman et al., (1996). The Si contents given by the microprobe analyses were used to normalise each analysis. Samples were analysed in runs of 14-20 analyses comprising 8-14 analyses of unknowns bracketed by two analyses of the standard at the beginning and end of each run. Additionally, to monitor the accuracy of the measurements, two secondary standards (BCR-2 and Mongolian garnet) were included at the beginning of each run. The ablation or total counting time for each analysis was 120s, preceded by 30s of background analysis. The counting time for one sample was 120s, the spot size was 50 μm, the repetition rate of the laser beam was 10Hz and its energy density, 70% (6.5 J/cm^2).

3.4.2. Ilmenite

Trace-element compositions of the ilmenite grains were obtained by means of the LA-ICP-MS located at the IBERCRON of UPV/EHU. It has already been demonstrated that NIST glasses can be used to determine the trace-element composition of ilmenite with better than 10% accuracy (e.g. Donohue et al., 2012; Carmody et al., 2014). However, to further confirm the adequacy of the use of the NIST 610 and NIST 612 glasses as standards, a large and compositionally homogeneous ilmenite nodule of kimberlitic origin was cut and a piece was

analysed by dissolution using the Q-ICP-MS. Subsequently, the trace-element composition of the grain was analysed by ablation of the nodule and calibrating the instrument through the 610 and 612 NIST standards. The results obtained in both cases were consistent and, as a consequence, all analyses of the unknown samples were performed *in situ* using the NIST glasses as standards.

Fourteen trace elements (Sc, V, Cr, Mn, Co, Ni, Zn, Ga, Zr, Nb, Ta, Hf, W, U) in ilmenite grains were analysed both on thick polished sections and on polished epoxy mounts containing individual ilmenite grains. The counting time for each spot was 90s (30s background, 60s signal) and each analysis was normalised using the Ti values obtained by the electron microprobe. Samples were analysed in runs of 14 analyses comprising 10 analyses of unknowns bracketed by two analyses of the standards at the beginning and the end of each run. Additionally, two analyses of the ilmenite nodule were included in each run as an internal standard, to check the operation of the instrument. Typical theoretical detection limits are 6 ppm for Mn and V, from 1 to 4 ppm for Sc, Cr, Ni and Zn, from 100 ppb to 1 ppm for Co, Ga, Zr, Nb and Ta and from 10 to 100 ppb for Hf, W and U. The nominal spot size was 55 μm, although in the smaller grains it was reduced up to 10 μm. The repetition rate and the energy density of the laser beam was 10Hz and 65-75%, respectively.

3.4.3 Chromite

Chromite analyses were carried out at the GAU laboratories. For calibration two different standards were used (PGEA and NIST610 glass) and each analysis was normalised using the Cr values previously obtained by electron microprobe. A NIST610 glass was selected as standard to determine trace-element composition of the chromite found in xenoliths. PGEA is an in-house sulphide standard useful for the characterisation of the trace elements not included in the NIST glass (S, Fe, Ni, Cu, As, Se, Ru, Rh, Ag, Pd, Cd, Te, Re, Os, Ir, Pt, Au, Pb and Bi). In addition to these two standards, an external standard (BCR) was used to verify the proper operation of the LA-ICP-MS.

Chromite was usually analysed in runs of 15 analyses comprising 10 analyses of unknowns bracketed by two analyses of each standard (NIST610 and PGEA) at the beginning and the end of each run, as well as one analysis of the BCR external standard after the first set of analysis of the standards. The counting time for each analysis ranges from 50 to 120s; the acquisition of

data was stopped if the laser drilled through the grain. The spot size ranged between 15-40 μm.

3.4.4. Perovskite

Trace elements (Na, Mg, K, Sc, V, Fe, Rb, Sr, Y, Zr, Nb, Ba, REE, Hf, Ta, Th, U and Pb) of perovskite grains were analysed on polished sections >100 microns thick and on polished mounts using the LA-ICP-MS at the GAU (Macquarie University). For calibration the NIST 610 glass was used and each analysis was normalised using the Ca values determined by the electron microprobe. Samples were analysed in runs of 16 analyses comprising 12 analyses of unknowns bracketed by two analyses of the standard at the beginning and end of each run. Additionally, one analysis of the USGS BCR-2 standard was included in each run as a secondary standard to monitor the accuracy of the measurements. The ablation or total counting time for each analysis was 120s, except in cases where the crystal was totally ablated. Typical detection limits range from 5 to 50 ppb for V, Rb, Sr, Y, Zr, Nb, REE, Hf, Ta, Th, U and Pb, 100 ppb for Ba and Sc and <1 ppm for Na and Mg. The spot size ranged between 15-40 μm. Given the small size of the perovskite grains, only one spot was analysed on each grain.

3.5. U-Pb dating: LA-ICP-MS

Determination of U-Pb ratios in perovskite was done following the methods described by Batumike et al., (2008) for U-Pb dating of this mineral in kimberlites from the Congo Republic. The analyses were performed using a New Wave Research UP-213 laser ablation microsampling system coupled to an Agilent 7500 ICP-MS system at GEMOC (Macquarie University). Measurements of U-Pb were done in situ on thick (100 μm) polished sections and polished blocks, using a spot size ranging from 30 to 40 microns. Each analytical run consisted of 8-12 analyses of unknowns, bracketed by two analyses of a primary standard (zircon GJ-1, 609 Ma) at the beginning and the end of each run. Additionally, two near-concordant zircons (91500, 1065Ma,; Wiedenbeck et al., 1995); Mud Tank, 732±5Ma, (Black and Gulson, 1978)) were analysed as secondary standards after the first two GJ-1 analyses in order to assess the accuracy and precision of the method. As already suggested by Storey et al. (2007) for titanite, and demonstrated by Batumike et al. (2008) for perovskite, strict matrix matching of the sample and the external standard is not essential for U-Pb dating of this mineral by LA-ICP-MS. Typical acquisitions consisted of 60s background measurement followed by 120s of sample

ablation. The ablation was done in He instead of Ar, since it leads to efficient sample transport, signal stability and better reproducibility of U/Pb fractionation. The laser was set to give a 2.5 mJ/cm^2 energy, using 5 Hz repetition rate for all the analyses. Avoidance of cracks and inclusions was achieved by selecting the stable parts of the ablation signal, with data collected in time-resolved mode. This also enabled termination of the analysis if the laser drilled into the kimberlite matrix.

The U-Pb isotope ratios were obtained from raw signals using the software GLITTER (Griffin et al., 2008). The common-Pb correction was done using a regression technique, as described by Batumike et al. (2008). The upper intercept of the regression line defined by the raw data on a Tera-Wasserburg plot is taken as the $^{207}Pb/^{206}Pb$ of the common-Pb component. The lower intercept gives the crystallisation age of the perovskite population, and hence of the kimberlite. The slight scatter observed in some of the data may reflect heterogeneity in the composition of the common-Pb component due to intrinsic variations of the Pb composition of the mantle. Pb loss can also occur in highly altered perovskites (Donnelly et al., 2012), giving unrealistically young ages. However, as discussed later, these problematic ages can be identified by anchoring the upper intercept to the present-day $^{207}Pb/^{206}Pb$ terrestrial value. Therefore, the points that did not fit the initial correlation line within 1σ have been rejected in order to reduce the scatter of the data. The U-Pb plots and the regression calculations were done using the Isoplot 4.0 software of Ludwig (2003).

3.6. In situ Sr-Nd analyses by LA-MC-ICP-MS

The Sr-Nd isotopic analyses were conducted at the GEMOC laboratories (Macquarie University, Sydney) using a Nu Plasma MC-ICP-MS attached to a New Wave Research UP-213 laser ablation microsampling system. The detailed analytical procedure followed in this study can be found in Donnelly et al. (2012) and only a brief summary of the protocol is given here.

The laser was set to produce 30-50 micron diameter spots, with 5Hz repetition rate, and a fluence of 2.5 mJ/cm^2. Due to the small grain size of most of the perovskite crystals, only one analysis could be performed on each grain. Therefore, in this work the Nd-Sr isotope study has been carried out under the premise that all the perovskite grains of the same kimberlite were derived from the same source.

As in the U-Pb analyses, a time-resolved software was used in order to select the more

stable portions of the ablation signal, giving only the data strictly corresponding to perovskite and excluding contributions to the signal from inclusions, cracks or other phases.

The Nd isotopic data were acquired in static mode, measuring masses 142, 143, 144, 145, 146, 147, 148 and 150 simultaneously in Faraday collectors. To calibrate the instrument, as well as to monitor the reproducibility and evaluate the accuracy of the data, a standard 100ppb JMC321 Nd solution was used. Corrections for mass fractionation and the interference of ^{144}Sm on ^{144}Nd were made following the method described by Donnelly et al. (2012).

For the in situ Sr-isotope analyses, masses 83, 83.5, 84, 85, 85.5, 86, 86.5, 87 and 88, were measured simultaneously in Faraday collectors, in static mode. The interferences of ^{86}Kr on 86Sr and doubly-charged REE on the isotopes of interest, as well as the mass fractionation, were also corrected using the procedures given by Donnelly et al. (2012). No ^{87}Rb correction on ^{87}Sr was applied, in order to avoid overcorrection of the initial ^{87}Sr/^{86}Sr ratios, which would result from the very low Rb contents (close to the detection limit, and consequently with high uncertainties) of the analysed perovskite grains.

In order to verify the accuracy and external precision of the in situ LA-MC-ICP-MS data for both Nd and Sr, repeated measurements of the Ice River perovskite (^{143}Nd/^{144}Nd = 0.512598 ± 49; ^{87}Sr/^{86}Sr = 0.702870± 130; 2σ uncertainties; n= 57 and n=69, respectively) were carried out. These results are in good agreement with the values obtained by solution of the same standard (^{143}Nd/^{144}Nd =0.512581±32; 87Sr/86Sr = 0.702838±51; 2σ uncertainties; Tappe and Simonetti, 2012). Since in that work the isobaric interferences for Nd were negligible, the consistency between our measurements and their data for the same standard proves the adequacy of the interference corrections applied here to the LA-ICP-MS data. A total of 71 and 76 perovskite crystals were analysed for Nd and Sr, respectively.

3.7. Groundmass mineral identification: XRD

For the identification of the serpentine-group minerals in the kimberlitic matrix, as well as other groundmass minerals, X-ray diffraction was carried out. 14 samples were analysed at the CCiT of the Universitat of Barcelona using a PANalytical X'Pert PRO MPD Alpha1 powder diffractometer in Bragg-Brentano θ/2θ geometry with a 240mm radius. Analytical conditions were 45 kV and 40 mA, using a Ni filtered Cu Kα radiation (λ = 1.5418 Å). During the analysis, the sample was spun at 2 revolutions per second. A variable automatic divergence slit kept

the area illuminated at 10mm, with a mask limiting to 12mm the length of the beam over the sample in the axial direction. Axial divergence Soller slits of 0.04 radians were used. Samples were scanned from 4.2 to 80º 2θ with step size of 0.017º and measuring time of 50 seconds per step, using a X'Celerator detector (active length = 2.122º). Diffractograms were processed using the *Xpert Highscore* software.

Chapter 4
PETROGRAPHY OF THE ANGOLAN KIMBERLITES

This chapter contains a brief summary of the structure of the studied Angolan kimberlites and the main petrographic features observed in each one. The following descriptions were done by combining the information provided by the mine petrologists and collected during the field work, with petrographic observations using optical microscopes, SEM techniques on thin sections and polished blocks, and powder X-Ray diffraction (XRD) analysis of some of the minerals forming the kimberlitic groundmass.

4.1. Introduction

The main sampling work for this thesis was carried out between 19th and 27th July 2010. As shown in fig. 4.1, it involved collecting samples both from kimberlite outcrops and open-pit mines, as well as from drill cores provided by the CATOCA Company during our visit. All the other samples were either provided by the CATOCA mine petrologist, Dr. Vladimir Pervov, or by the head of the Departamento de Geologia from Universidade Agostinho Neto de Luanda, Dr. Antonio Olimpio Gonçalves.

Due to its troubled recent history, systematic diamond prospecting in Angola started in the 1950s; it stopped during the wars for 40 years and re-started around 15 years ago. Additionally, the fact that most of the kimberlites are covered by thick sedimentary layers not only makes it hard to correctly locate the pipes but might make them into expensive and thus non-viable mines, regardless of their diamond content. As a consequence, a detailed characterisation of the structure and composition of the Angolan pipes has only been carried out when there is the prospect of high profits. The CATOCA Company provided us with the detailed description of the structure of the only two kimberlites that fulfilled this premise at the time of our


a
b
c
d
e
f
g
h

sampling: the Catoca and the Cat115 pipes. All the other samples come from kimberlites that are either still in the exploration stage or whose cost of exploitation would not compensate the possible profits and, hence, no sketch can be included in this work. The location of the studied kimberlites can be found in the geological map of the Lundas area in fig. 4.2, and a summary of their main petrographic features is included in table 4.1 at the end of this chapter.

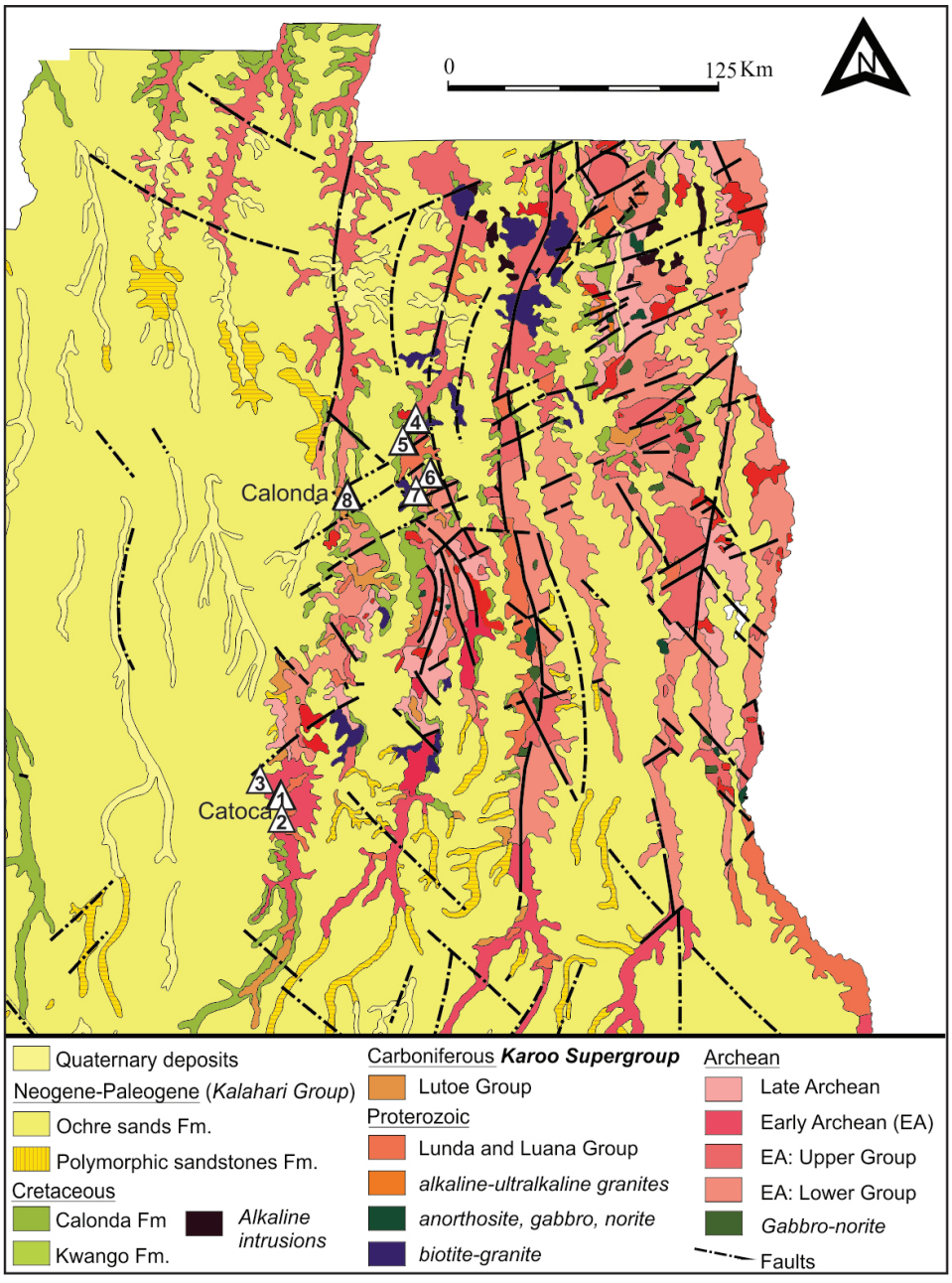

Figure 4.1 (left page) Images of the field work carried out in July 2010. (a-c) Visiting the open pit of the Catoca kimberlite and sampling its crater facies. Note the bedding in the uppermost part of the crater facies (b). (d-f) Sampling of the Cat115 kimberlite, mostly done from drill cores (f) since it is still in the exploration stage. (g-h) Doing field work in the Tchiuzo kimberlite. This kimberlite contains significant amounts of 0.1-1 cm ilmenite xenocrysts that can be handpicked in the open pit (h).

Figure 4.2 (top) Geological map of the Las Lundas province, including the location of the intrusions studied in this thesis: Cat115 (1), Catoca (2), Tchiuzo (3), Mulepe 1 (4), Mulepe 2 (5), Lucapa 1 (6), Lucapa 2 (7) and Calonda (8) kimberlites (modified from Perevalov et al. (1992); Guiraud et al. (2005); Egorov et al. (2007) and Robles-Cruz et al., 2012b)).

Characterisation of the kimberlitic rocks is complex, since there is a lack of consensus about the terminology and nomenclature that should be used to describe these deposits (e.g. Clement and Skinner, 1985; Mitchell, 1986; Field and Scott Smith, 1998). These classification schemes were mainly "model driven" and thus broadly used by the scientific community and the diamond producers for their utility and simplicity. However, they failed to separate descriptive and genetic terminology (Cas et al., 2008). In order to reconcile the nomenclature used in modern volcanology and kimberlite petrography, these authors suggested a new "descriptive to genetic" approach, which resulted in a descriptive lithological name. In this thesis, rock descriptions follow the terminology proposed by Cas and coauthors (2008) and are summarised in table 4.1. However, the names of the facies used currently by the Angolan mine petrologists are still used in the description of the Catoca and Cat115 kimberlites for comparative purposes.

4.2. Petrography and structure of the studied kimberlites

4.2.1. Catoca kimberlite

Catoca is one of the main diamondiferous kimberlites in the world and one of only two diamond deposits being currently mined in Angola. Several samples from the crater zone were taken during the field work (fig. 4.1. a-c), and were complemented by the study of mantle xenoliths sampled from drill cores. Additional research was done on thin sections and polished blocks already available at MPGA department (University of Barcelona).

Catoca is a group I kimberlite (Ganga et al., 2003) and, because of minimal erosion, the complete sequence of the crater (230-270m) and the diatreme (> 609m) facies can be identified (Pervov, personal communication). The upper part is composed of epiclastic sandstones, showing cross-stratification in the central part and coarse debris rimming the crater (fig. 4.3). There is a progressive increase of volcaniclastic material in the lower parts of the sequence, leading to a dominantly resedimented volcaniclastic kimberlite (RVK) rock in the lower half of the crater facies. This unit has a characteristic reddish colour, given by the almost ubiquitous presence of a ferruginous cement consolidating the sandstones. Xenocrysts of garnet, diopside and ilmenite are rare and usually show alteration along grain boundaries and cracks.

The diatreme zone is mainly characterised by tuffisitic kimberlite (TK), with the original olivine completely serpentinised and replaced by calcite and saponite (Kotel'nikov et al., 2005).

Xenoliths of the host rocks, including gneiss, amphibolite, granite, sandstone and shale are very common, and the mantle rocks (peridotite, eclogite, clinopyroxenite and carbonatite) are significantly less abundant. The xenocryst suite in the Catoca kimberlite comprises garnet, zircon, chromian diopside, amphibole, phlogopite and ilmenite. Robles-Cruz et al. (2009) characterised the matrix of the diatreme facies by means of PXRD, SEM and EMP and reported the occurrence of lizardite, apatite, calcite, ilmenite and chromite, as the main components, and titanite, zirconolite, baddeleyite, barite, dolomite, witherite, barytocalcite, strontianite and sulphides as accessory minerals. Following the classification of Cas et al. (2008), the majority of the samples taken from this zone were classified as fragmental, serpentine-altered, poorly sorted, crystal-rich, matrix-supported olivine kimberlites.

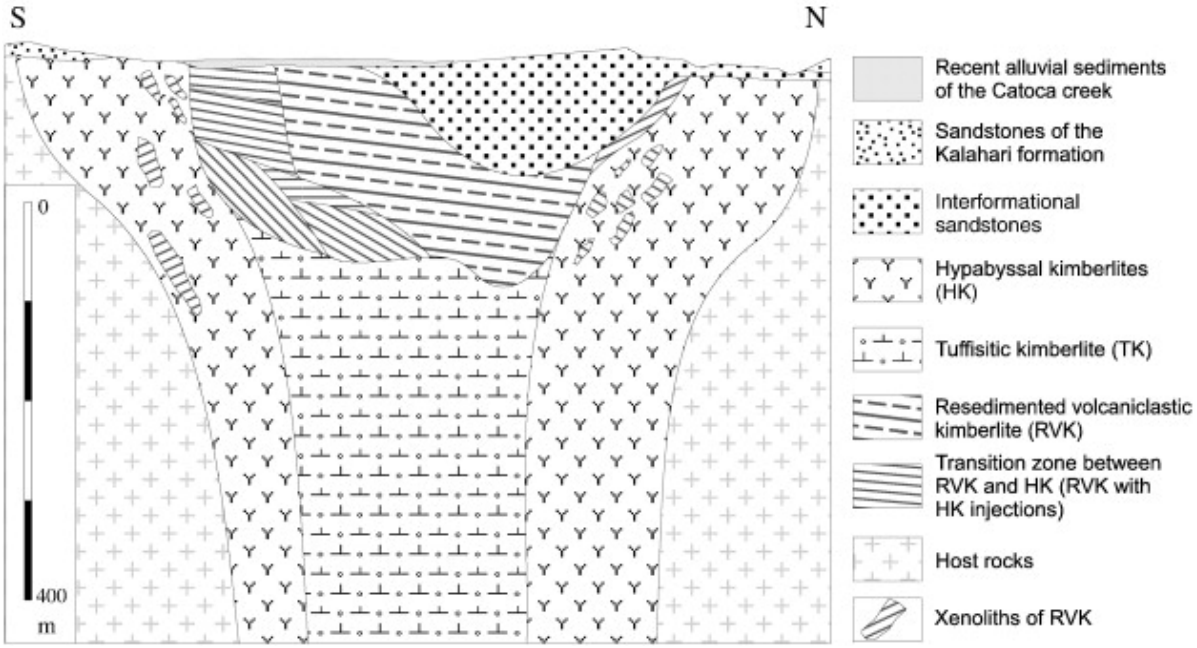

Figure 4.3 Cross section of the Catoca kimberlite (Robles-Cruz et al., 2009 after Kriuchkov et al., 2000)

4.2.2. CAT115

The CAT115 kimberlite (9°22'40"S, 20°17'47"E) is located 7.5km NE of the Catoca kimberlite. Most of the samples studied in this thesis were taken from drill cores of this kimberlite, which is still in exploration stage (fig. 4.2.d-f). It has a diamond-rich layer at 140-160m depth, although this is 2.5 times poorer than the Catoca kimberlite (Vladimir Pervov, personal communication). However, the very low erosion rates in this area have ruled it out as a potential diamond mine, since the costs of exploitation of such a deep layer made it non-viable despite its diamond

content. As it is shown in the cross section (fig.4.4), the Cat 115 pipe also preserves both the crater and the diatreme zones. The hypabyssal zone is probably located at greater depths, beyond the reach of the prospecting drill cores, so none of the samples belong to this zone.

The crater zone is composed of interbedded volcanoclastic breccias, sandstones, conglomerates and kimberlitic tuffs, with some lateral facies variations. Kimberlitic rocks are weathered to depths of 30-40 m. The boundary between the crater and diatreme zones is quite abrupt over the entire pipe, where pyroclastic (tuffisitic) kimberlites appear at 150-170m. The apparently two different pyroclastic kimberlite domains shown in the cross section are connected in the southern part of the pipe into a single body.

The rocks in the diatreme zone are generally altered, with separate olivine grains completely replaced by serpentine -mainly lizardite- and, to a significantly lesser extent, calcite. This zone is also characterized by the presence of mantle xenoliths differing in size (1-10 cm) and composition (Grt-peridotites, Spl-peridotite, Grt-pyroxenite, eclogite). In deep drill cores (180-295m) these xenoliths are usually fresh and, therefore, suitable for a geochemical, mineralogical and textural characterisation of the mantle below the Lunda Norte province. Additionally, abundant xenocrysts are encountered in the Cat115 kimberlite, including

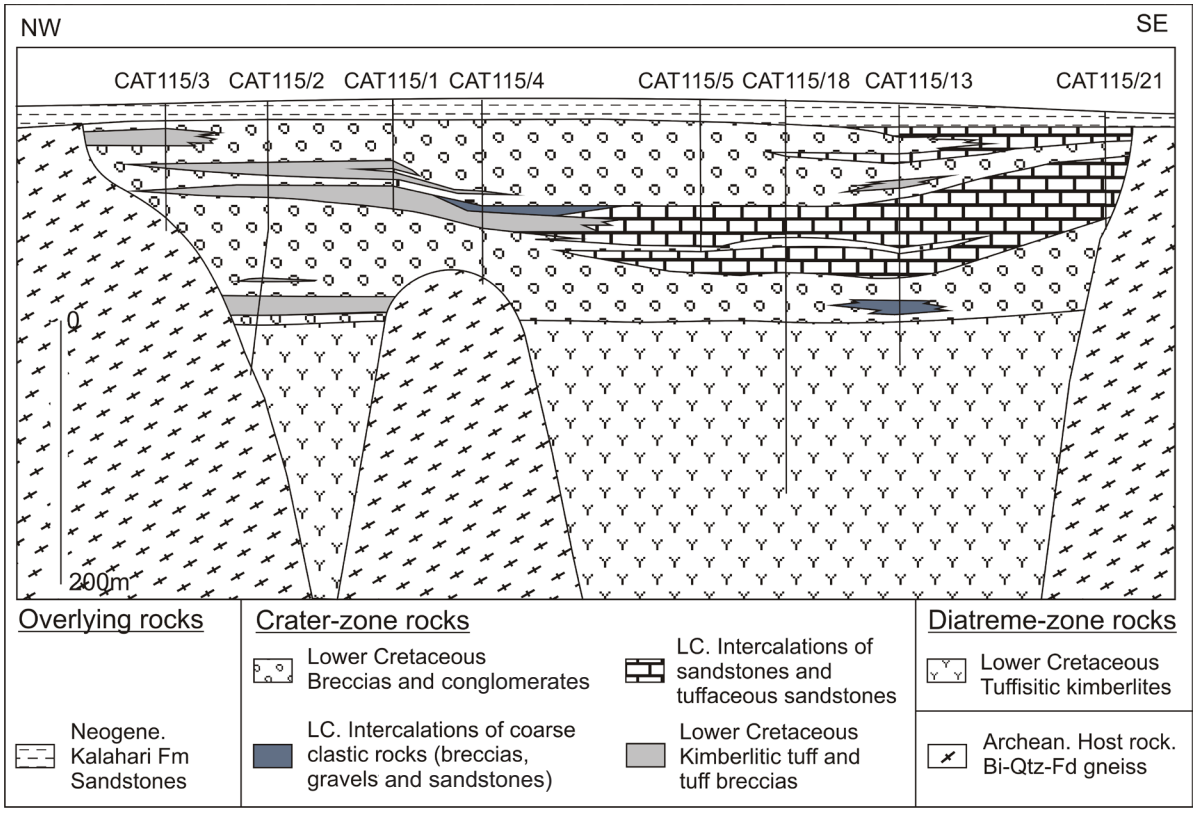

Figure 4.4 Cross section of the Cat115 kimberlite, modified from a section provided by Dr. Vladimir Pervov.

ilmenite, garnet, phlogopite, clinopyroxene and zircon, in order of abundance. As shown in the SEM images (fig. 4.5), the fine-grained matrix is mainly composed of serpentine, with only minor amounts of calcite, perovskite, apatite, barite, phlogopite, titanite and magnetite. As it happens in the Catoca kimberlite, groundmass chromite is very scarce in this pipe. Following the classification of Cas et al. (2008), the samples from the diatreme zone should be classified as fragmental, serpentine-altered, poorly sorted, moderately crystal-rich, matrix-supported olivine kimberlite.

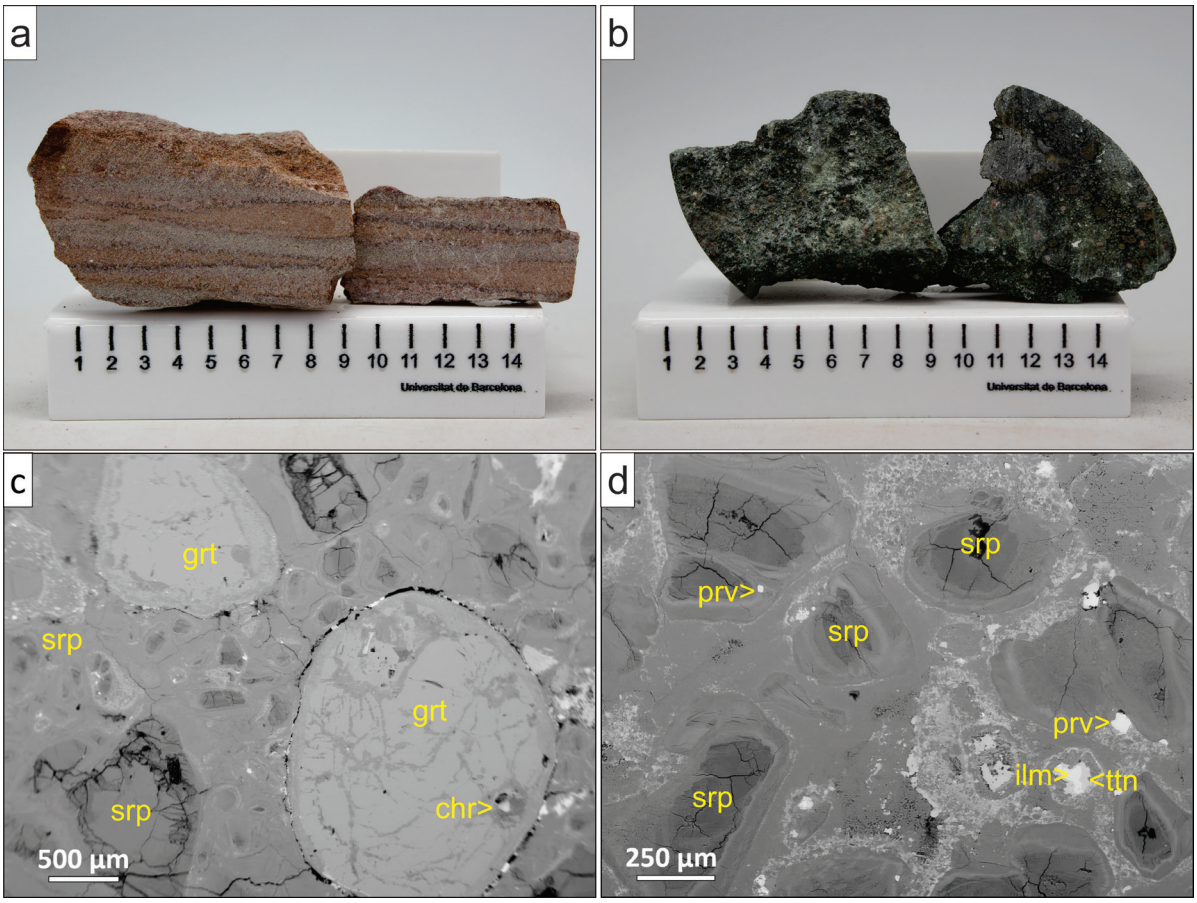

Figure 4.5 Samples collected from the drill cores of the Cat115 kimberlite: crater (a) and diatreme zones (b). (c-d) SEM images of the diatreme zone of the Cat115 kimberlite. Abbreviations: garnet (grt), serpentine (srp), chromite (chr), olivine altered to serpentine (srp), perovskite (prv), ilmenite (ilm) and titanite (ttn).

4.2.2. Tchiuzo kimberlite

This kimberlite is located 15 km north of the Catoca kimberlite (9°24'23"S; 20°18'7"E). The diamond content of this mine has not been defined yet.

A collection of thin sections were available at the MPGA department from previous projects, and some were selected as representative of the geological units seen in drill core samples. Most of them are classified as volcanoclastic, highly serpentinised, moderately sorted, moderately

crystal-rich, matrix supported olivine kimberlite. Significant amounts of ilmenite xenocrysts were found in this kimberlite, with subordinate amounts of garnet and Mg-rich spinel. The kimberlitic matrix is completely serpentinised and it contains magnetite, phlogopite and apatite, with only minor amounts of calcite.

In addition, a set of ilmenite xenocrysts was hand-picked from the outcrop of the Tchiuzo kimberlite during the field work carried out in 2010. As shown in fig. 4.2 and fig.4.6, abundant rounded to subrounded ilmenite xenocrysts are concentrated on the weathered crater facies of the kimberlite. Their grain size ranges from 0.2 cm to 2 cm; most of them are around 1cm in diameter. This unusual enrichment in ilmenite has not been found in any other kimberlite studied in this thesis.

Figure 4.6 Ilmenite xenocrysts from the Tchiuzo kimberlite.

4.2.3. Mulepe 1 and Mulepe 2 kimberlites

These two kimberlites are located near the Mulepe village, approximately 20 km NE of the Catoca mine. They are still at exploration stage and no information about their structure could be provided by the CATOCA Company. Therefore, this description relies only on the petrographic description that could be done from the drill core samples provided by the company.

Rock samples from the Mulepe 1 and Mulepe 2 kimberlites are usually dark grey and they have been classified as coherent, inequigranular olivine kimberlite. Olivine grains represent approximately between 10 and 35% of the rock and they are usually rounded. Their grain size ranges between 0.1 and 2 mm and they have been completely replaced by serpentine group minerals (lizardite).

The xenocryst suite in both kimberlites is dominantly composed of chromian garnet and ilmenite, although these minerals finally represent less than 3% of the whole rock.

The interstitial medium between olivine xenocrysts is composed of serpentine, carbonate –

mainly calcite-, titanite, perovskite, phlogopite and magnetite, which formed as a consequence of the late serpentinisation process (fig.4.7 and 4.8). Powder X-Ray diffraction analyses of the serpentine-group minerals shows a predominance of lizardite over antigorite and (clino-) chrysotile. Additionally, fluorapatite, zircon, chromite, rutile and members of the chlorite group were found as minor phases disseminated in the kimberlitic matrix.

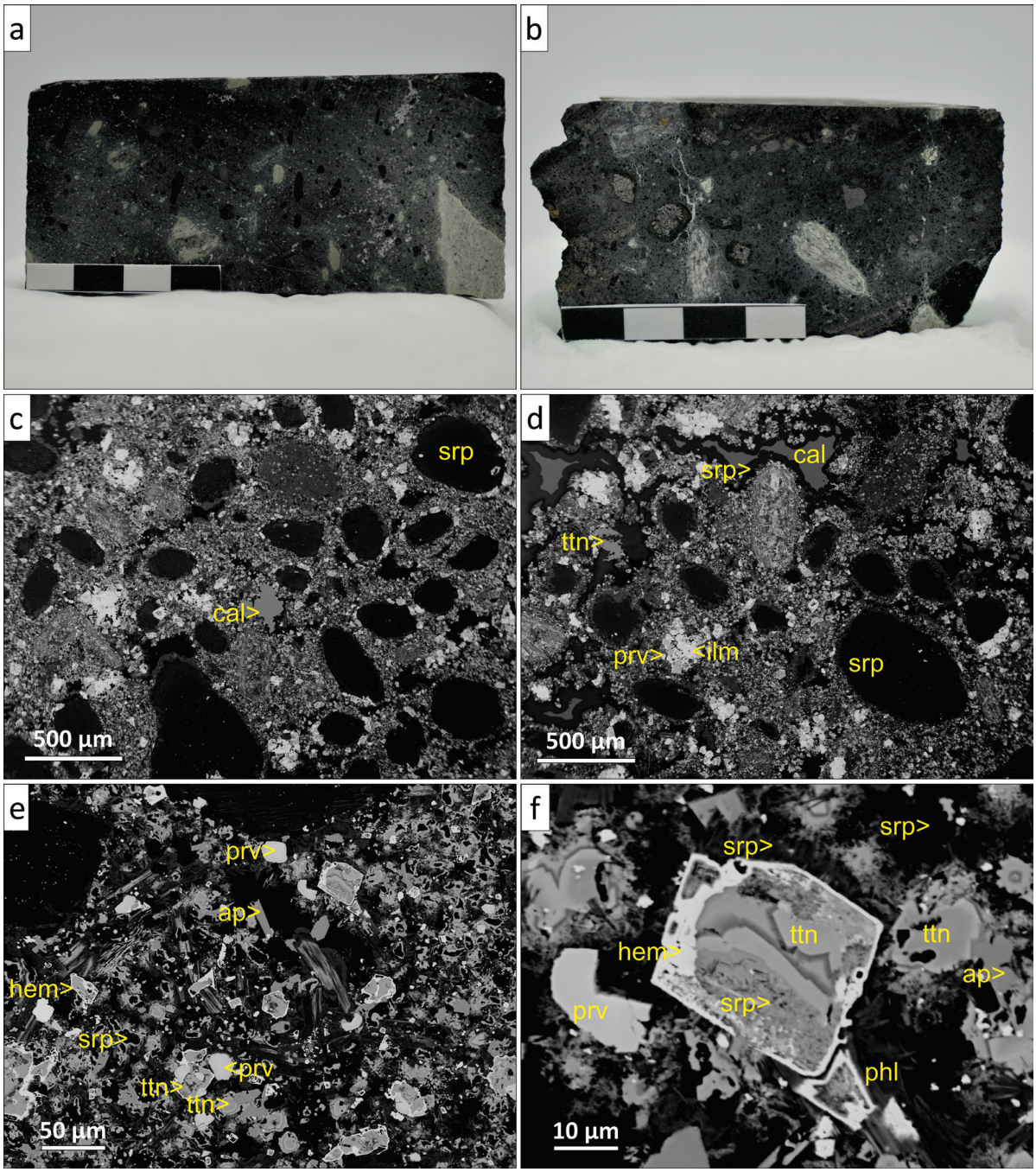

Figure 4.7 (a-b) Hand samples of the diatreme zone of the Mulepe 1 kimberlite. (c-f). BSE images of the matrix of the kimberlite. Note the abundance of titanite (ttn) replacing the original groundmass phases. Abbreviations for minerals: serpentine (srp), calcite (cal), perovskite (prv), hematite (hem), apatite (ap) and phlogopite (phl).

Compared to the Catoca and Cat115 kimberlites, the xenolith content in the Mulepe pipes is quite low (<5%) and shows a narrower compositional range. Apart from few crustal xenoliths (gneiss, amphibolites, sandstones), the mantle xenoliths sampled by the kimberlitic magma rarely exceed 1.5 cm in diameter and typically consist of coarse garnet lherzolites and dunites. Neither eclogitic nor carbonatitic xenoliths were found in the samples provided by the CATOCA company.

4.2.4. Calonda kimberlite

This intrusion is located near the Calonda village, only 20 km from the Mulepe kimberlites, but its petrography is significantly different. The studied samples are characterised by a yellowish-greenish colour, clearly lighter than the rocks from the Mulepe area (fig.4.9). The Calonda kimberlite typically shows an inequigranular to aphanitic texture, defined by small (<0.5 mm) olivine grains, which are totally replaced by lizardite. The groundmass is a mixture

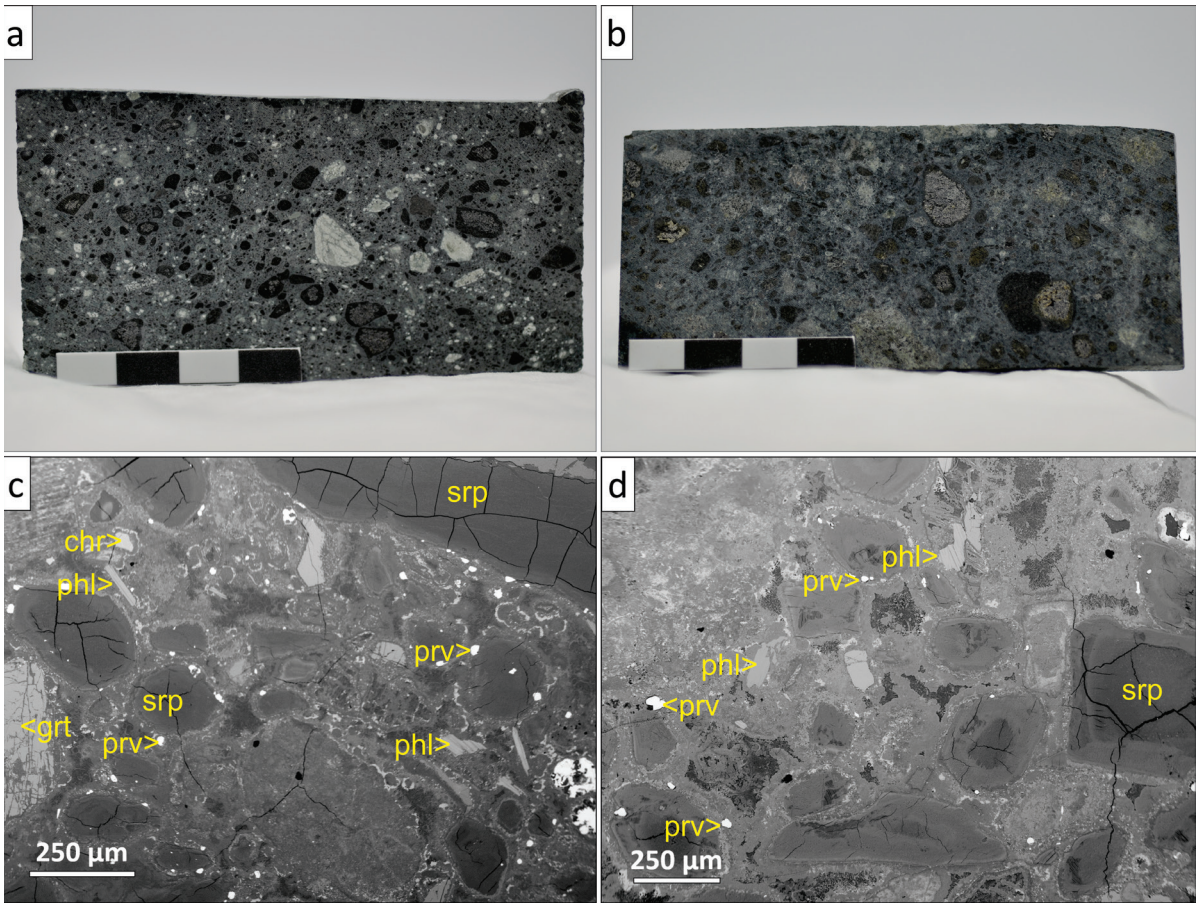

Figure 4.8 (a-b) Hand samples of the diatreme zone of the Mulepe 2 kimberlite. (c-d). BSE images of the matrix of the kimberlite. Abbreviations for minerals: serpentine (srp), chromite (chr), phlogopite (phl), garnet (grt), perovskite (prv) and apatite (ap).

of lizardite and antigorite, and abundant carbonate grains, which may have oscillatory zoning. The phlogopite content is higher (>5%) than in the other kimberlites described here, although it is not enough to classify it as a group II kimberlite or orangeite. Titanite and vermiculite are also abundant. By means of X-Ray diffraction, minor phases such as fluorapatite were identified. No xenoliths were found in the few samples recovered from this kimberlite.

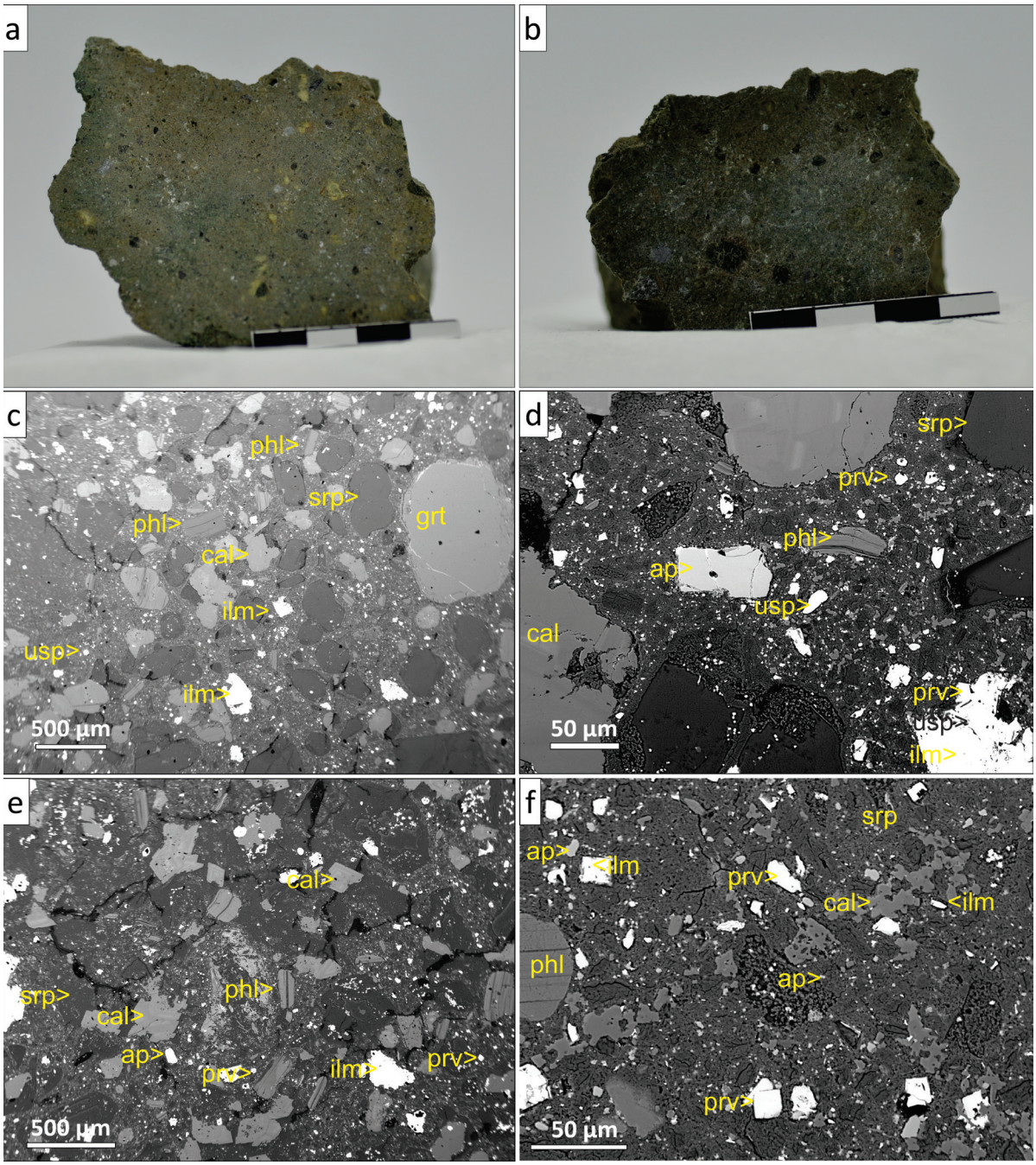

Figure 4.9 (a-b) Hand samples of the diatreme zone of the Calonda kmberlite. Samples from this kimberlite are significantly more altered to serpentine, contain no xenoliths and few macrocrysts. (c-f) BSE images of the matrix of the Calonda kimberlite. Calcite (cal) occurs also as subrounded grains and it is zoned . Abbreviations for minerals: serpentine (srp), phlogopite (phl), garnet (grt), perovskite (prv), ilmenite (ilm) and apatite (ap).

4.2.5. Lucapa 1 and Lucapa 2 "kimberlites"

These two intrusions are located near the Lucapa village (8°25'06"S, 20°44'31"E). All the characterisation was done on samples from the diatreme zone that were already available in the CMDM department, collected during previous field work. Although previous research classified them as kimberlites, some petrological evidence suggests that they are likely kimberlite-related rocks and not kimberlites *sensu strictu*. Samples from both intrusions are petrographically very similar and they are characterised by rounded olivine xenocrysts, which have been totally replaced by lizardite, representing up to 20% of the rock. A distinctive feature of these rocks is the occurrence of fresh clinopyroxene microlites (fig. 4.10). These occur as small (<5 μm), euhedral to subhedral grains, partially resorbed, disseminated in the matrix around the serpentinised olivine grains. Since the composition of the kimberlitic magma would not allow the crystallisation of clinopyroxene (Kamenetsky et al., 2009), these primary textures suggest that they are more likely to be meimechites like those defined in Siberia (Arndt et al., 1995, Sobolev et al., 2009) or Canada (Francis and Patterson, 2009). However, the high degree of alteration of these rocks prevents the characterization of the rock according to the geochemical criteria defined by the IUGS for the meimechites, picrites and related rocks (Le Bas, 2000; see also Williaams-Jones et al. 2004). Kimberlites and meimechites may in fact occur in a same igneous province (e.g., Carlson et al., 2006).Therefore, in this thesis the term "kimberlite" will still be used to describe all the studied intrusions.

Chromite is widely scattered across the groundmass; the crystals are skeletal with a typical atoll shape and have an ulvöspinel rim. Perovskite, partially altered to rutile or other TiO_2 polymorphs, serpentine, carbonate, titanite and apatite are the other constituents of the kimberlite matrix. The xenocryst suite is mainly composed of garnet and ilmenite, which can be replaced by titanite.

Although they are very rare, some small (<2cm) crustal (amphibolite, gneiss, carbonatite) and mantle (eclogite, garnet-peridotite) xenoliths are present in the studied sections.

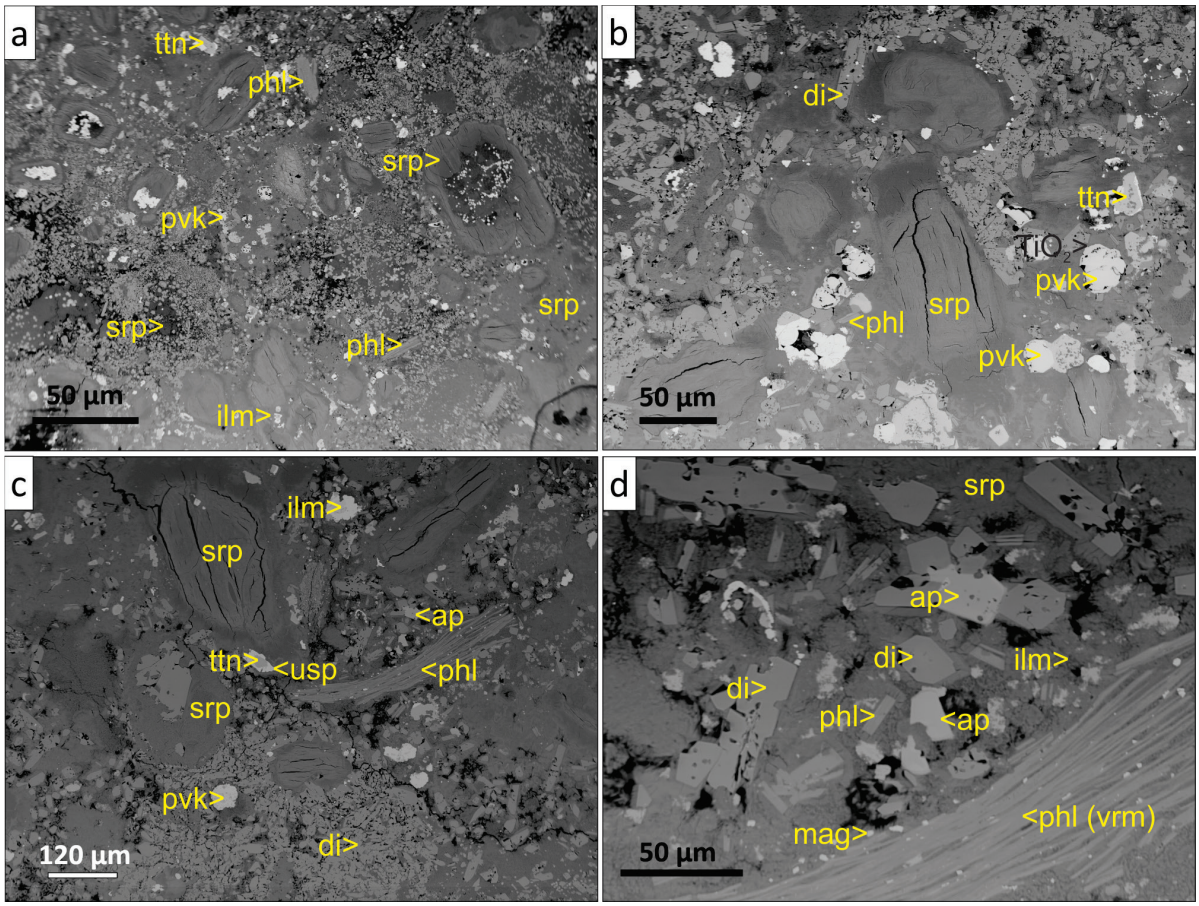

Figure 4.10 (a-d) BSE images of the matrix of the Lucapa 1 kimberlite. Note the distinctive abundance of diopside microlites in the matrix, surrounding the serpentinised olivine crystals. Abbreviations for minerals: serpentine (srp), phlogopite (phl) altered to vermiculite (vrm), titanite (ttn), perovskite (pvk) altered to titanium oxide (maybe rutile?), ilmenite (ilm) and apatite (ap).

Table 4.1 Petrography of the studied kimberlites. Abundance of each mineral phase is indicated with x, from very rare [(x)] to very abundant [xxx].

Kimberlite	Rock description	Olivine xenocrysts			Xenoliths (size)				Other xenocrysts				Groundmass minerals						
		vol %	Size	Alteration	Crustal		Mantle		Grt	Cpx	Ilm	Zr	Srp (ol)	Phl	Cb	Prv	Ap	Chr	Di
Cat115	Dark green. Fragmental. Serpentine-altered, poorly sorted, moderately crystal-rich, matrix-supported, olivine kimberlite	10-25 %	0.25-2 mm	Srp	gneiss, amphibolite, shales, sandstones	(1cm to >1m)	Grt and Spl-lherzolite, harzburgite, eclogite, wherlite	(1-8cm)	xxx	(x)	xx	(x)	xxx	(x)	(x)	x	(x)	x	-
Mulepe 1	Very dark green. Fragmental. Serpentine-carbonate altered, moderately crystal-rich, macrocrystic, coarse, non-vesicular, olivine kimberlite	10-20%	0.1-2 mm	Srp	granite, gneiss	(< 10 cm)	dunite, Grt-harzburgite	(<3 cm)	x		xx	(x)	xxx	x	x	xx	x	-	
Mulepe 2	Grey- dark green. Fragmental. Serpentine-carbonate altered, moderately crystal-rich, macrocrystic, coarse to very coarse, non-vesicular, olivine kimberlite	10-30 %	0.1-3 mm	Srp	gneiss	(<8 cm)	dunite, Grt-harzburgite	(<3 cm)	xx		x	(x)	xxx	x	x	xx	x	-	
Calonda	Grey to greenish-ochre aphanitic kimberlite. Coherent. Carbonate-serpentine altered, crystal rich, fine to medium, non-vesicular, olivine kimberlite	30-40%	0.1-0.5 mm	Cb-Srp	altered gneiss, shales	(1-4 cm)	-		x		xx	(x)	xxx	xx	xxx	x			
Lucapa 1	Dark green. Coherent. Olivine phenocrysts, serpentine-(carbonate) altered, abundant microlites of diopside. Meimechite?	10-25%	<0.5 mm	Srp	gneiss, shale, amphibolite, "granulite"	(1-8 cm)	carbonatite, eclogite, Grt-lherzolite	< 1cm	x		x	(x)	xx	x		x		x	xxx
Lucapa 2	Dark green. Coherent. Olivine phenocrysts, serpentine-(carbonate) altered, abundant microlites of diopside. Meimechite?	10-25%	<0.5 mm	Srp	gneiss, shale, amphibolite	(1-8 cm)	eclogite, Grt-lherzolite	< 1cm	x		x	(x)	xx	x		x		x	xxx

Chapter 5
AGE AND PETROGENESIS OF KIMBERLITES IN LUNDA NORTE

Perovskite ($CaTiO_3$) has become a very useful mineral for dating kimberlite eruptions, as well as for constraining the compositional evolution of a kimberlitic magma and its source. Despite the undeniable potential of such an approach, no similar study had been done in Angola. This chapter includes the results obtained from in situ U-Pb geochronology and Sr-Nd isotope analyses of perovskite in six Angolan kimberlites, supported by a detailed petrographic and geochemical study of their perovskite populations. Four types of perovskite were identified, differing in texture, major- and trace-element composition, zoning patterns, type of alteration and the presence or absence of inclusions. The occurrence of these four types within the Mulepe kimberlites is interpreted as an evidence of a complex, multi-stage process that involved mingling of compositionally different melts.

U-Pb dating of these perovskites yielded Lower Cretaceous ages for four of the studied kimberlites, thus indicating that kimberlite magmatism occurred in NE Angola likely due to reactivation of deep-seated translithospheric faults (>300km) during the break-up of Gondwana. Sr-Nd isotope analyses of four of these kimberlites indicate that they are Group I kimberlites, which is consistent with the petrological observations.

5.1. Introduction

Kimberlites are heterogeneous rocks, with variable contents of groundmass minerals, xenocrysts and xenoliths entrained by the magmas during their ascent towards the surface (Mitchell, 1986). As a consequence of their complex nature, dating kimberlites and characterising their source is challenging. Bulk-rock analyses cannot be used to constrain either the age of the kimberlite eruption or the isotopic signature of the original magma, since each rock represents a compositional spectrum resulting from a mixture of crystals and liquids of diverse origin (e.g. Paton et al., 2007; Donnelly et al., 2012). Crustal contamination and post-emplacement alteration also can have significant effects on the bulk-rock data (Le Roex

et al., 2003; Kjarsgaard et al., 2009), further complicating the understanding of kimberlite petrogenesis. These problems, coupled with the improvement of the in situ methods and incorporation of LA-ICP-MS as a routine technique, have led to an increasing interest in the geochemical and isotopic analysis of groundmass minerals as the best approach to characterise these rocks.

Angola is ranked fourth in Africa in terms of kimberlite abundances (Faure, 2010), but very little dating work has been carried out. A summary of published ages for Angolan kimberlites is given in table 5.1, including the method used to constrain the time of eruption of each pipe. Almost all the ages have been obtained by U-Pb dating of zircon (Davis, 1977; Haggerty et al., 1983; Eley et al., 2008; Robles-Cruz et al., 2012b). However, since zircon is always a xenocryst in the kimberlitic rocks, the measured age may pre-date the eruptive event, leading to misinterpretation of the links between kimberlite eruption and tectonic events. A few studies have been carried out to date kimberlite emplacement through direct analysis of groundmass minerals such as phlogopite (Creaser et al., 2004; Egorov et al., 2007; Tappe et al., 2014). However, in the Angolan kimberlites studied here, phlogopite is relatively scarce and it is usually altered by post-emplacement processes. Therefore, dating of phlogopite would not be reliable and more suitable groundmass minerals should be considered.

Over the last decade, perovskite ($CaTiO_3$) has become widely used for both age determination and characterisation of the source of kimberlitic magmas. Perovskite is a ubiquitous minor phase (<10%) in kimberlites and crystallises directly from the magma (Mitchell, 1986). It also is relatively resistant to weathering (Heaman, 1989) and a main carrier of U (>100ppm) and

Kimberlite	Age (Ma)	Author	Method
Alto Cuilo 1	145.1 ± 4	Eley et al., 2008	U-Pb perovskite
Alto Cuilo 139	135.7 ± 2.1	Eley et al., 2008	U-Pb perovskite
Alto Cuilo 197	113 ± 0.8	Eley et al., 2008	U-Pb zircon
Alto Cuilo 254	115.5 ± 1.1	Eley et al., 2008	Rb-Sr phlogopite
Alto Cuilo 55	113 ± 0.8	Eley et al., 2008	U-Pb zircon
Catoca	117.9 ± 0.7	Robles-Cruz et al., 2012	U-Pb zircon
Chicuatite	372 ± 8	Egorov et al., 2007	K-Ar phlogopite
Tchiuzo	121.2 ± 1	Robles-Cruz et al., 2012	U-Pb zircon
Val do Queve	134 ± 2	Davis, 1977	U-Pb zircon
Val do Queve	133.4 ± 11.5	Haggerty, 1983	fission track zircon

Table 7.1 Summary of published Angolan kimberlite eruptions.

Th (Heaman, 1989). Thus in situ LA-ICP-MS (laser ablation inductively coupled plasma mass spectrometry) U-Pb analysis of perovskite has turned out to be an excellent means to date the eruption of kimberlites (e.g. Batumike et al., 2008; Donnelly et al., 2012; Sun et al., 2014), lamprophyres and melilitites (Tappe et al., 2006; Corfu and Dahlgren, 2008) and carbonatites (Cox and Wilton, 2006; Reguir et al., 2010). This technique has some advantages over other instruments such as SIMS (e.g. Smith et al., 1989) and ID-TIMS (Heaman, 1989), since it is rapid, cost-efficient and allows spatial control on the analysed grains. However, to the authors' knowledge, in Angola only two pipes, from the Alto Cuilo kimberlite field, have been dated through U-Pb analysis of perovskite (Eley et al., 2008), and the article did not specify which technique was used to obtain these data.

In addition to its potential for U-Pb dating, Heaman (1989) envisaged that perovskite could also be used to assess the origin of the kimberlite magma based on Sr and Nd isotope studies. Perovskite usually has high Sr and low Rb contents, which leads to very low $^{87}Rb/^{86}Sr$ ratios (<0.001). Therefore, it is an ideal mineral for Sr isotope studies because Sr_i is insensitive to any age correction (Heaman, 1989; Paton et al., 2007). The use of groundmass perovskite therefore represents an improvement, in terms of constraining possible mantle reservoirs of the kimberlites, over the values obtained from bulk rock analyses, whose Sr-Nd isotopic signature is known to be modified by crustal contamination (e.g. Paton et al., 2007; Donnelly et al., 2012; Tappe et al., 2012; Chalapathi Rao et al., 2013; Sarkar et al., 2014).

This is the first work of in situ U-Pb geochronology and Sr-Nd isotope analysis of perovskite grains from Angolan kimberlites, based on a detailed petrographic and chemical study of this mineral from six pipes. These results can provide key information on the tectonic evolution of the Lundas kimberlitic province in Early Cretaceous time, which is still poorly understood, and also contribute to our knowledge of the sources of the Angolan kimberlites.

5.2. Sample description

In Angola, the erosion rate of the sedimentary cover is extremely low compared to other cratonic areas worldwide (Hawthorne, 1975; Pervov et al., 2011). Therefore, the diatreme and hypabyssal facies, where perovskite is expected to be better preserved, are rarely reached during the drilling work done at the exploration stage. As a consequence, only six out of 25 kimberlites available at the Crystallography, Mineralogy and Ore Deposits Department from

the Universitat de Barcelona are included in this study: Cat115, Mulepe 1 and Mulepe 2, Lucapa 1 and Lucapa 2 and Calonda kimberlites (see fig. 4.2). Each sample was sawed into slices and those showing the least alteration and the lowest abundance of xenoliths were selected. This material was then prepared either as thick (100 μm) polished sections or as polished blocks set in 25 mm epoxy mounts.

5.3. Perovskite occurrence

Perovskite represents up to 2 % by volume of the studied rocks. All samples are composed partly of rounded olivine crystals (20-35% volume) totally replaced by serpentine. The interstitial medium is mainly composed of serpentine, with variable amounts of calcite, ilmenite, phlogopite, spinel, apatite and sulphides. Perovskite belongs to the groundmass minerals and it occurs as primary euhedral, subhedral or rounded crystals scattered in the fine-grained matrix of the kimberlite. Based on textural observations two main textural types of perovskite may be defined: i) primary and ii) secondary.

5.3.1. Primary perovskite

This is the most common perovskite type and is present in all the studied kimberlites. This type of perovskite occurs as discrete single crystals, and can be interpreted as a primary phase crystallising directly from the magma. Two subtypes can be distinguished, based on the perfection of the crystals, their zoning pattern and the presence/absence of inclusions:

Ia. Anhedral perovskite

Crystals are rounded to sub-rounded and grain size typically ranges from 10 to 60 microns. The only exception are the Calonda perovskites, which are mostly euhedral and commonly smaller (<20 μm). They are usually scattered in the serpentinised groundmass of the kimberlite, together with calcite and apatite, as well as with some xenocrysts such as ilmenite and garnet. In some kimberlites, it can form “necklaces” around earlier-formed macrocrysts or phenocrysts of olivine, now replaced by serpentine (fig. 5.1a-e). This texture has been described in kimberlites from different geological settings (e.g. Chakhmouradian and Mitchell, 2000; Donnelly et al., 2012). A few crystals contain inclusions of unidentified

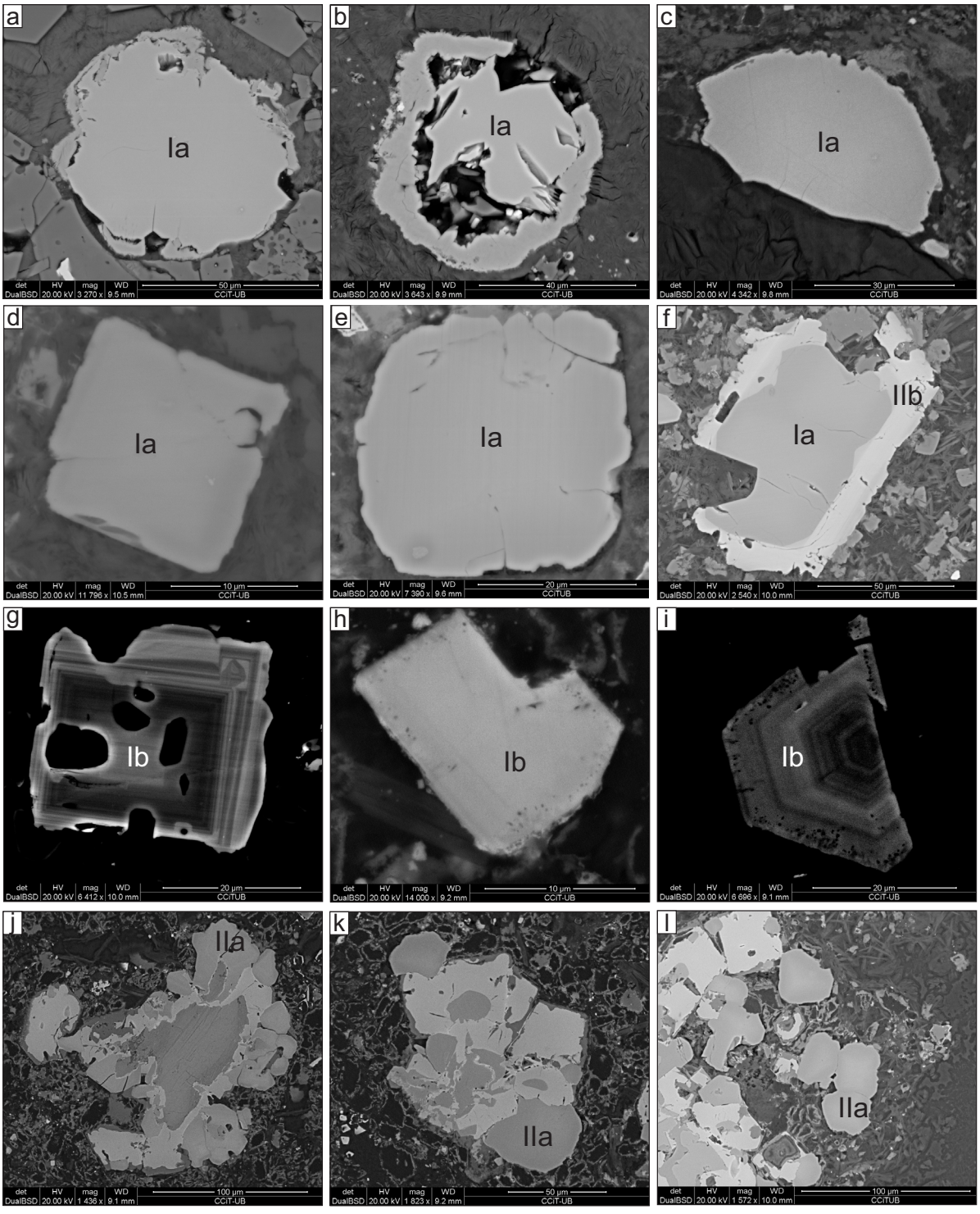

Figure 5.1 Back-scattered electron (BSE) images of perovskite showing the different textural types found in the studied kimberlites. (a) groundmass perovskite (Lucapa 1); (b) highly altered groundmass perovskite, with TiO2 rim (Lucapa 2); (c) groundmass perovskite as necklace around serpentinised olivine xenocryst (Cat115); (d) euhedral groundmass perovskite (Calonda); (e) subrounded groundmass perovskite (Mulepe 1); (f) groundmass perovskite with a Fe-Nb rich perovskite overgrowth (Mulepe 2); (g-i) euhedral perovskite with strong oscillatory zoning and inclusions and (j-l) reaction- induced rims of perovskite on ilmenite xenocrysts (Calonda and Mulepe kimberlites).

phases. Anhedral groundmass perovskite typically exhibits a slight zoning, with bright cores and darker rims under backscatter electron (BSE) imaging on the SEM. Perovskite from this group can be partially altered, developing rims of TiO_2 and titanite.

Ib. Euhedral perovskite

In this work, this type of perovskite is found exclusively in the Mulepe kimberlites, forming small groundmass crystals (up to 30 microns). As shown in figure 5.1 (g-i), they are always euhedral in shape, giving diamond or hexagonal sections with straight boundaries. Commonly they show neither replacement nor alteration to other minerals. This group usually has inclusions, which may be from <0.5 to 10 μm in diameter. The smallest inclusions are usually located near the grain boundaries, whereas the largest inclusions, when present, commonly occupy the centre of the grain. The latter could be identified as serpentinised olivine and apatite. Most of the crystals show a distinctive oscillatory zoning pattern in BSE images, which has not been reported in the other types of perovskite described here.

5.3.2. Secondary perovskite

IIa. Reaction-induced rims on ilmenite

In some kimberlites, perovskite is found as reaction-induced rims on earlier-crystallised Ti-bearing oxides belonging to the macrocryst suite, mainly Mg-ilmenite (fig. 5.1 j-l). This texture was described by Boctor and Boyd (1981), and it is interpreted as the result of interaction between ilmenite and the kimberlite magma (Chakhmouradian and Mitchell, 2000). Some of these ilmenite xenocrysts were altered to ulvöspinel before being coated by perovskite. The thickness of this coating ranges from few microns up to 15 μm in rare cases. Large (25-30 μm on average) and rounded crystals of perovskite commonly crystallised around the ilmenite xenocryst. A normal zoning pattern, defined by decrease in Na, Nb and LREE from core to rim, can be recognised in a few of these grains, which always remain unaltered. The presence of ilmenite inclusions is not unusual in this type of perovskite.

IIb. Nb-rich perovskite overgrowths

Some significantly larger (>100 μm) groundmass grains (Ia perovskite) in the Mulepe 2

kimberlite characteristically are overgrown by Nb-rich perovskite (up to 10.6 wt% Nb_2O_5) with sharp boundaries between the original grain and the late generation of perovskite (fig.5.1f). A similar overgrowth has also been described in Canadian and South African kimberlites (Chakhmouradian and Mitchell, 2001; Donnelly et al., 2011).

5.3.3. Alteration of perovskite

Resorption, cation leaching and replacement of perovskite by other minerals are common processes in hypabyssal and diatreme facies kimberlites (Chakhmouradian and Mitchell, 2000). Perovskite is unstable in a CO_2-rich, weakly acidic environment (Chakhmouradian and Mitchell, 1998). As a result, during the final stages of kimberlite evolution, perovskite is commonly replaced by other Ti-bearing minerals. In the kimberlites studied here, titanium dioxide (TiO_2) is the most common alteration product. It appears in the CAT115 kimberlite, as well as in both barren and diamondiferous kimberlites from Lucapa. The formation of TiO_2 at the expense of perovskite involves the crystallisation of calcite by leaching of Ca (Chakhmouradian and Mitchell, 2000). As shown in fig. 5.1b, this gives the TiO_2 rim a characteristic "spongy" appearance. In some cases, an atoll shape, similar to that observed in groundmass spinel, was recognised.

In the Cat115 kimberlite, perovskite has been replaced by titanite, which has been previously interpreted as an indicator of higher SiO_2 activity in the later stages of the crystallisation due to either crustal contamination (Chakhmouradian and Mitchell, 2000) or magma cooling (Carmichael Ise et al., 1970). No rims of late Mn-Nb-rich ilmenite have been found on any of the perovskite grains.

5.4. Major-element composition

Most of the perovskite analyses are close to the ideal composition ($CaTiO_3$), with lesser concentrations of LREE, Na, Sr, Nd, Al, Fe, Nb and Ta. Negative correlations of Ce, La, Nd, Nb and Na against Ca and Ti have been observed (fig.5.2). Na and Nb correlate positively in all the analysed grains, particularly significant in the Mulepe kimberlites, in which perovskite is more enriched in the lueshite component ($NaNbO_3$).

Based on their major-element compositions, three different groups are distinguished. Table

5.2 summarises the textures and compositions typical of perovskite in the studied Angolan kimberlites, whereas the average compositions of each group and for each kimberlite are reported in table 5.3. Major-element composition of the whole dataset can be found in the appendix A5.1.

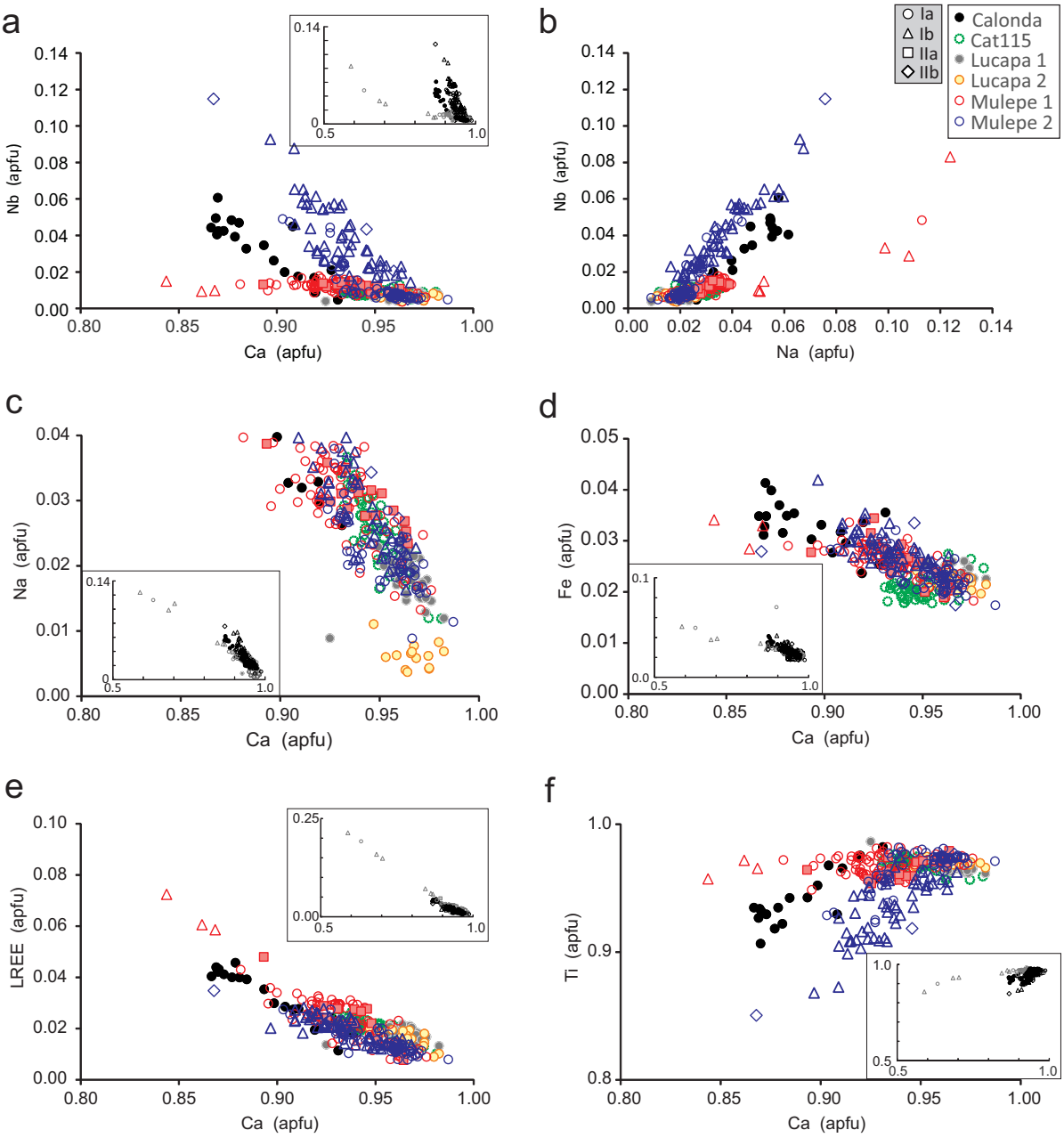

Figure 5.2 Binary diagrams representing the major-element chemistry of the perovskites, in atoms per formula unit (apfu). Symbols correspond to the different perovskite textures found in the kimberlites: type Ia (circles), type Ib (triangles), type IIa (squares) and type IIb (diamonds). The kimberlitic bodies are represented by different colours and lines (see legend in fig.3b). Calcium is represented against Nb (a), Na (c), Fe (d), REE (e) and Ti (f). The Na-Nb (b) diagram shows a positive correlation and significantly higher Na and Nb contents in subtype Ib perovskite. Conversely, a negative correlation is found between Ca and Nb, Na, REE and Fe.

Group 1

All the studied kimberlites contain this compositional group, which occurs both as groundmass perovskite (type Ia) and reaction-induced rims on ilmenite (type II). This is compositionally homogeneous and it is characterised by relatively low average contents of REE (mean 1.0 wt% ΣLREE) and Nb (0.4-4.6 wt% Nb_2O_5), and by low Na contents (0-1.0 wt% Na_2O). These values are in good agreement with those found in perovskite II as defined by Chakhmouradian and Mitchell (2001) in Canadian kimberlites. However, groundmass perovskite from Calonda kimberlite is enriched in these elements (mean 3.3 wt% ΣLREE and up to 5.7 wt% Nb_2O_5 and 1.3 wt% Na_2O).

Group 2

Only the Mulepe kimberlites contain this compositional group and it corresponds to type Ib perovskite, usually showing very strong zoning. This is significantly enriched in La, Ce and Nd (up to 22.5 wt% ΣLREE). Niobium (0.9-8.8 wt% Nb_2O_5) and sodium (0.4-2.4 wt% Na_2O) contents are also high compared to most of the grains from group I perovskite, thus indicating a high abundance of the lueshite component. However, due to its low content of Zr (165-2824 ppm) this perovskite type cannot be equated with the perovskite III group defined by Chakhmouradian and Mitchell (2001). Similar enrichments in LREE, Nb and Na

Type	**Ia**	**Ib**	**IIa**	**IIb**
Texture	primary, rounded subhedral	primary, euhedral	secondary, pseudomorphic after ilmenite	Nb-rich rims of perovskite on type Ia perovskite
Chemistry	Group 1: Low LREE (<5.58 wt% LREE), Na (<0.97, <1.45* wt% Na_2O) and Nb (<4.65; <5.68* wt% Nb_2O_5)	Group 2: High LREE (<25.55 wt% LREE), Na (2.49 wt% Na_2O) and Nb (<8.8 Nb_2O_5)	Group 1: Low LREE (<5.58 wt% LREE), Na (<0.85 wt% Na_2O) and Nb (<1.46 wt% Nb_2O_5)	Group 3: Low LREE (<3.99 wt% LREE), medium Na (<1.65 wt% Na_2O) and high Nb (10.6 wt% Nb_2O_5)
Zoning (core to rim)	*Normal* (decrease in Na, Nb, LREE) *Reverse* (increase in Fe and Nb, constant LREE) *Oscillatory* (very rare)	*Oscillatory* (very common, with main variations in Nb, Ce, Na)	Unzoned, only occasionally *normal* pattern	Unzoned
Alteration	when present: TiO_2, titanite	very rare	very rare	none
Inclusions	rare	very common (<0.5 µm,in the rims, to 10 µm, mainly serpentinised olivine, chromite)	ilmenite	none
Location	Cat 115, Calonda*, Mulepe, Lucapa	Mulepe	Calonda, Mulepe	Mulepe

Table 5.2. Main features of each perovskite type, defined by texture, major-element chemistry, zoning pattern, alteration mineral(s) and presence/absence of inclusions. Note that both Mulepe kimberlites contain all perovskite types.

Table 5.3 Averaged major-element (wt%) compositions and structural formula of each textural and compositional group in the six studied kimberlites

Compositional group	**Group 1**																**Group 2**				**Group 3**	
Textural group	**Ia**												**IIa**				**Ib**				**IIb**	
Kimberlite	**Cat115**		**Mulepe 1**		**Mulepe 2**		**Lucapa 1**		**Lucapa 2**		**Calonda**		**Mulepe 2**		**Calonda**		**Mulepe 1**		**Mulepe 2**		**Mulepe**	
oxides (wt%)	*av.*	1σ	*av.*	1σ	*av.*	1σ	*av.*	1σ	*av.*	1σ	*av.*	1σ	*av.*	1σ	*av.*	1σ	*av.*	1σ	*av.*	1σ	*av.*	1σ
TiO_2	55.91	0.37	55.60	0.76	56.04	1.13	55.86	0.35	56.40	0.17	53.45	1.72	55.63	0.86	56.62	0.43	50.70	4.15	53.56	1.75	49.81	3.66
Al_2O_3	0.26	0.05	0.10	0.03	0.18	0.04	0.20	0.02	0.17	0.03	0.06	0.02	0.08	0.05	0.06	0.01	0.08	0.04	0.12	0.05	0.11	0.02
FeO	1.20	0.13	1.55	0.33	1.36	0.17	1.35	0.10	1.27	0.09	1.84	0.27	1.46	0.23	2.00	0.08	2.00	0.33	1.63	0.20	1.73	0.25
CaO	38.39	0.61	37.61	0.97	38.72	0.92	39.08	0.49	39.48	0.49	35.57	1.30	38.08	1.08	37.57	0.43	28.91	5.54	37.57	0.93	35.84	2.86
SrO	0.12	0.06	0.11	0.07	0.11	0.06	0.12	0.04	0.13	0.05	0.16	0.10	0.14	0.08	0.31	0.04	0.60	0.31	0.16	0.08	0.12	0.13
Na_2O	0.57	0.12	0.67	0.13	0.51	0.13	0.41	0.08	0.42	0.09	1.03	0.22	0.66	0.10	0.63	0.06	1.67	0.63	0.79	0.27	1.20	0.62
Ta_2O_5	0.20	0.13	0.25	0.14	0.17	0.12	0.16	0.12	0.12	0.07	0.23	0.19	0.19	0.18	0.06	0.06	0.15	0.16	0.15	0.16	0.21	0.29
Nb_2O_5	0.86	0.17	1.13	0.26	1.29	1.06	0.62	0.11	0.61	0.19	3.26	1.27	1.13	0.21	0.65	0.27	2.61	2.32	3.70	1.74	7.37	4.59
La_2O_3	0.52	0.09	0.44	0.14	0.19	0.10	0.22	0.07	0.21	0.05	0.75	0.12	0.44	0.29	0.45	0.18	3.38	1.81	0.32	0.10	0.45	0.32
Ce_2O_3	1.88	0.28	1.80	0.46	1.27	0.23	1.35	0.14	1.23	0.23	2.40	0.48	1.70	0.59	1.13	0.54	7.61	3.81	1.46	0.31	1.77	0.71
Nd_2O_5	0.00	-	0.68	0.29	0.54	0.23	0.55	0.18	0.52	0.21	0.96	0.33	0.68	0.26	0.29	0.01	2.04	0.98	0.60	0.21	0.68	0.52
LREE	2.40	0.34	2.82	0.83	1.76	0.54	2.13	0.26	1.95	0.41	3.93	0.98	2.58	1.10	1.86	0.71	13.03	6.58	2.38	0.54	2.89	1.56
total	99.94	0.49	99.87	0.48	100.20	0.40	99.97	0.51	100.56	0.27	99.64	0.44	100.03	0.56	99.82	0.22	99.81	0.34	100.11	0.45	99.39	0.01
apfu (O=3)																						
Ti	0.97	0.00	0.97	0.01	0.97	0.01	0.97	0.00	0.97	0.00	0.94	0.02	0.97	0.01	0.98	0.00	0.94	0.04	0.93	0.02	0.88	0.05
Al	0.01	0.00	0.00	0.00	0.00	0.00	0.01	0.00	0.00	0.00	0.00	0.00	0.00	0.00	0.00	0.00	0.00	0.00	0.00	0.00	0.00	0.00
Fe	0.02	0.00	0.03	0.01	0.02	0.00	0.02	0.00	0.02	0.00	0.03	0.01	0.03	0.00	0.03	0.00	0.04	0.01	0.03	0.00	0.03	0.00
Ca	0.95	0.01	0.93	0.02	0.95	0.02	0.96	0.01	0.97	0.01	0.89	0.02	0.94	0.02	0.93	0.01	0.76	0.12	0.93	0.02	0.91	0.06
Sr	0.00	0.00	0.00	0.00	0.00	0.00	0.00	0.00	0.00	0.00	0.00	0.00	0.00	0.00	0.00	0.00	0.01	0.00	0.00	0.00	0.00	0.00
Na	0.03	0.01	0.03	0.01	0.02	0.01	0.02	0.00	0.02	0.00	0.05	0.01	0.03	0.00	0.03	0.00	0.08	0.03	0.04	0.01	0.06	0.03
Ta	0.00	0.00	0.00	0.00	0.00	0.00	0.00	0.00	0.00	0.00	0.00	0.00	0.00	0.00	0.00	0.00	0.00	0.00	0.00	0.00	0.00	0.00
Nb	0.01	0.00	0.01	0.00	0.01	0.01	0.01	0.00	0.01	0.00	0.03	0.01	0.01	0.00	0.01	0.00	0.03	0.03	0.04	0.02	0.08	0.05
La	0.00	0.00	0.00	0.00	0.00	0.00	0.00	0.00	0.00	0.00	0.01	0.00	0.00	0.00	0.00	0.00	0.03	0.02	0.00	0.00	0.00	0.00
Ce	0.02	0.00	0.02	0.00	0.01	0.00	0.01	0.00	0.01	0.00	0.02	0.00	0.01	0.01	0.01	0.00	0.07	0.04	0.01	0.00	0.02	0.01
Nd	0.00	0.00	0.00	0.00	0.00	0.00	0.00	0.00	0.00	0.00	0.01	0.00	0.00	0.00	0.00	0.00	0.02	0.01	0.00	0.00	0.01	0.00
LREE	0.02	0.00	0.02	0.01	0.01	0.00	0.02	0.00	0.02	0.00	0.03	0.01	0.02	0.01	0.02	0.01	0.12	0.06	0.02	0.00	0.03	0.01
cations	2.00	0.00	2.00	0.01	2.00	0.01	2.01	0.01	2.01	0.00	1.99	0.01	2.00	0.00	2.00	0.00	1.98	0.02	2.00	0.00	1.99	0.02

* Only Mulepe 1 and Mulepe 2 kimberlites have IIb subtype

in late crystallising perovskites have been observed in a wide range of alkaline-ultramafic and carbonatitic rocks (Platt, 1994; Chakhmouradian and Mitchell, 1998).

Group 3

In addition to these two main compositional groups, a third distinctively different composition is defined by the Nb-rich overgrowth on some perovskite crystals from the Mulepe2 kimberlite. These rims have very high Nb contents (up to 10.6 wt% Nb_2O_5), with only a slight enrichment of other minor elements such as LREE (1.8-4.0 wt% ΣLREE) or Na (0.8-1.6 wt% Na_2O).

Zoning is a very common feature in perovskite grains from kimberlites worldwide. Chakhmouradian and Mitchell (2000) defined the *normal pattern* as a decrease in LREE and Th in the outer part of the crystal, which may or may not be accompanied by a decrease in Na and Nb contents. These authors also found that it can be complicated by the presence of transitional zones characterised by intermediate LREE contents. Most of the perovskite grains from the kimberlites studied here exhibit this pattern, with a bright core and a darker rim in BSE images (fig. 5.3a), related to a decrease in Na, Nb and LREE towards the rim. The *reverse pattern*, with enrichment in LREE and Th towards the rim, is rare in perovskite crystallised from kimberlitic magmas. In the Angolan kimberlites this pattern is found only occasionally in type Ia perovskites and it is characterised by an increase in the Fe and Nb contents, although the LREE values remain constant or decrease slightly (fig. 5.3b). The reverse zoning has been previously interpreted as the result of a re-equilibration of the perovskite with a magma that has been compositionally modified by assimilation or contamination processes. *Oscillatory zoning* is quite rare in kimberlites worldwide and it typically reflects variation in Ca, Ti and LREE contents (Chakhmouradian and Mitchell, 2000). However, the oscillatory pattern (fig.5.3c-h) is very common in type Ib perovskite from the Mulepe samples and it is defined by significant variations in Nb, Na, Ce, Fe and Nd within a single grain. As shown in figure 5.4h, the brighter areas of the BSE images of this zoning have the highest LREE (11.9-20.3 wt% LREE), Sr (0.5-1.5wt% Sr_2O), Na (1.6-2.2 wt% Na_2O) and Nb (1.1-7.0 wt% Nb_2O_5) contents, while the darkest zones show lower contents of these elements but still higher than group 1 perovskite (1.4-8.3wt% LREE oxides, 0-0.6wt% Sr2O, 0.4-1.5 wt% Na_2O) with slightly higher Nb contents (0.9-8.8 wt% Nb_2O_5).

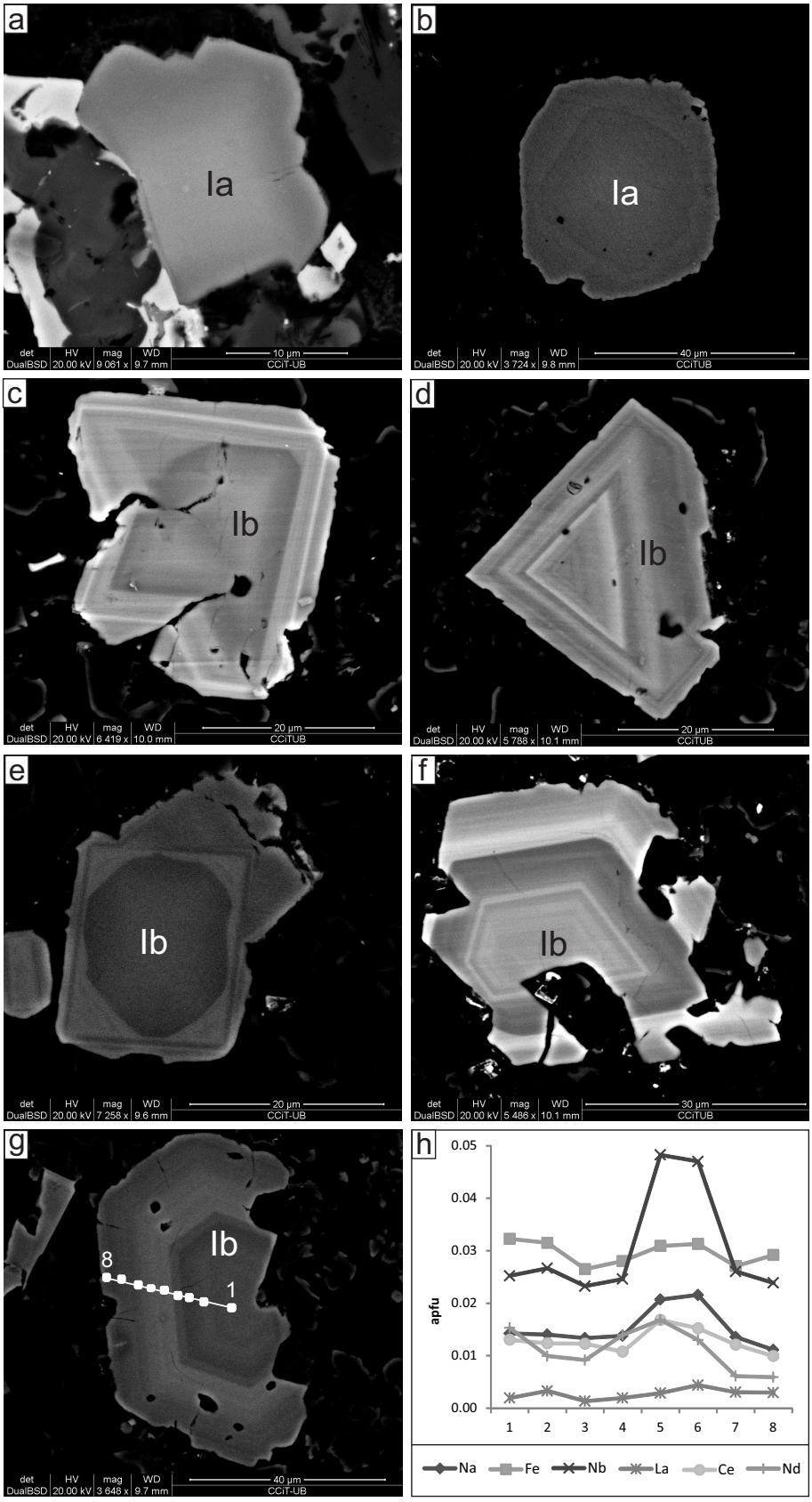

Figure 5.3 BSE images of the different zoning pattern found in the studied kimberlites. (a) Normal zoning pattern, with Na- and Nb-poor rim. (b) Inverse zoning pattern, given by a decrease in Fe and Nb rim-wards. (c-g) Complex oscillatory zoning patterns in subtype Ib perovskite from the Mulepe kimberlites. As shown in the major-element profile (h) corresponding to the crystal, the brighter areas are given by higher concentrations of Nb, Na and REE.

5.5. Trace-element composition

The complete set of trace-element analyses of the perovskites is included in appendix A5.2. The chondrite REE normalised patterns (fig. 5.4) have smooth negative slopes, reflecting the enrichment in LREE with respect to the MREE and HREE (La_N: 4350-7850 vs Lu_N: 8-12). This diagram also confirms that perovskite is a main carrier for REE and high field strength elements (Zr, Hf, Nb, Th and U). In contrast, perovskite is extremely depleted in Rb (usually <0.8ppm or below detection limit), Ba, K and Sc with respect to the average whole rock kimberlite composition, with compositions close to the chondritic values. As already observed by Chakhmouradian et al. (2013) and Beyer et al. (2013), perovskite shows higher affinity for Th, Ta, Hf, Ho and LREE relative to U, Nb, Zr, Y and HREE respectively. All perovskite types show a slight negative Y anomaly, giving strongly subchondritic Y/Ho ratios.

Despite the strong enrichment in La and Ce observed in EMP analyses of the bright areas of group II perovskite, both types have similar REE patterns when analysed by laser ablation techniques. This is because the spot size (> 20 microns) makes it impossible to analyse separately

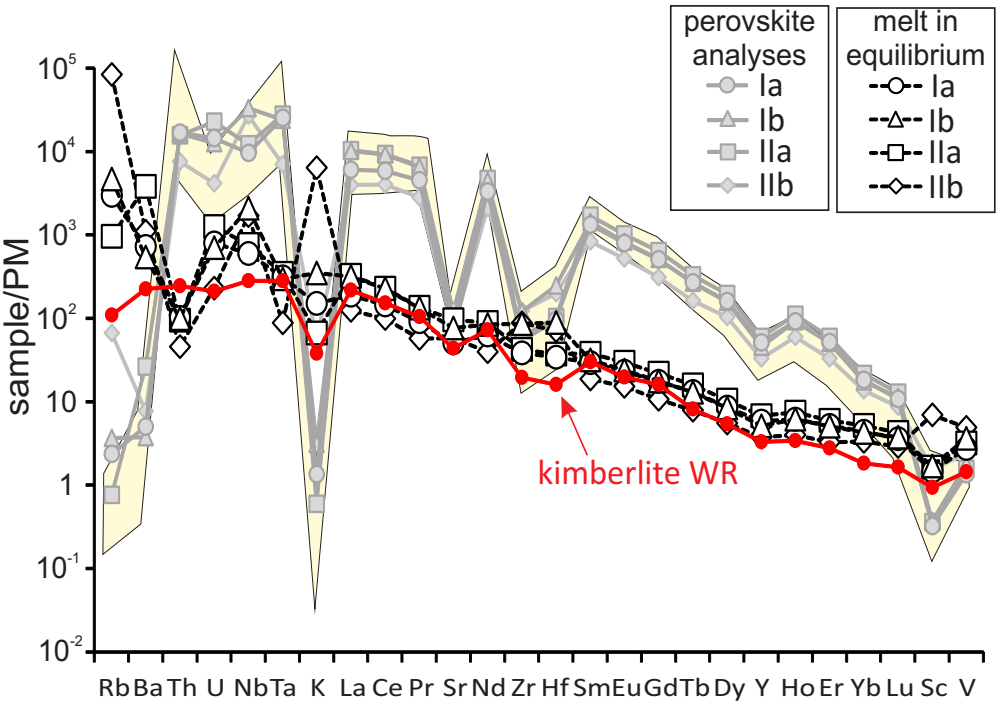

Figure 5.4 Average composition of each perovskite textural type normalised to the primitive mantle of McDonough and Sun (1995). The melt in equilibrium for each type of perovskite was calculated from the KD published by Chakhmouradian et al. (2013) and it is discussed further on in the text. The ochre field corresponds to data for perovskite from kimberlites worldwide (Chicken Park; Iron Mountain, Udachnaya and Grizzly kimberlites; from Chakhmouradian et al. (2013). The average whole rock kimberlite (WR) composition has also been taken from Chakhmouradian et al. (2013) calculated from 75 pipes worldwide. Given the small size of the type IIb perovskite, the high Rb, Ba and K values are probably an artefact caused by ablation of phlogopite.

Table 5.4. Averaged trace-element (ppm) compositions of the perovskites of the Angolan kimberlites

Kimberlite	Lucapa 1		Lucapa 2		Mulepe 1						Mulepe 2						Cat115		Calonda	
Type	Ia		Ia		Ia		Ib		IIa		Ia		Ib		IIb		Ia		Ia	
ppm	*av.*	*σ*	*av.*	*σ*	*av.*	*σ*	*av.*	*σ*	*av.*	*σ*	*av.*	*σ*	*av.*	*σ*	*av.*	*σ*	*av.*	*σ*	*av.*	*σ*
Na	2210	320	2290	120	3600	1300	8490	270	4230	870	2500	1100	4000	1400	5000	2100	3000	1100	5410	200
Mg	3400	6000	2410	780	5200	7400	4170	140	3100	3500	4700	9800	3000	570	37000	31000	5400	5900	28000	11000
K	101	43	69.2	2.9	170	150	256	8.4	140	120	170	170	320	200	13500	9400	130	110	2330	920
Sc	4.38	0.57	4.15	0.23	6.93	9.02	5.06	0.22	5.5	1.7	4.39	0.98	5.7	2.1	25	13	13	21	8.0	1.5
V	107.7	5.7	106	3.5	117	28	110.5	3.6	127	16	120	26	142	26	195	36	91	22	125.6	1.2
Fe	8700	3200	7046	35	13000	14000	9220	370	11000	4400	7300	3300	9400	4900	49000	12000	8900	3000	19900	5400
Rb	0.40	0.36	0.10	0.019	0.9	1.4	0.694	0.064	0.55	0.89	0.64	0.84	1.11	0.95	39	22	0.7	1.2	7.77	0.18
Sr	1220	63	1144	28	1450	560	6860	230	2100	1200	950	210	1290	310	1430	630	1250	310	1850	430
Y	222.7	9.1	222.1	2.4	234	46	49.8	1.7	257	32	179	38	213	40	140	45	244	61	277.0	1.4
Zr	490	130	405	21	528	97	950	32	630	120	430	280	1690	760	1265	64	980	440	1204	35
Nb	4510	280	4070	220	6800	2100	12130	400	8200	1200	6900	6000	29000	17000	17300	4600	6300	1700	16800	1000
Ba	19	21	8.43	0.25	23	25	30.7	1.4	22	22	12	26	13	16	53	35	9.3	6.3	118	71
La	3190	160	3280	100	4600	2900	31300	1000	7000	4800	2290	670	3590	570	2507	31	4800	1300	5930	140
Ce	8400	1200	8710	490	11500	6500	63100	2000	16100	8100	6300	2000	10100	1100	6590	110	11300	3600	13780	99
Pr	1000	150	1070	110	1330	740	6320	200	1770	730	760	250	1160	180	700	130	1320	460	1520	100
Nd	3820	610	4050	320	4700	2400	18010	570	6000	2000	2920	990	4250	760	2570	450	4700	1700	5330	130
Sm	517	67	548	30	590	240	976	32	710	120	400	120	571	90	332	26	610	200	671.0	7.1
Eu	121	15	126.5	2.8	133	45	144.7	4.7	159	18	93	26	133	22	78.6	7.7	138	41	156.3	5.7
Gd	278	27	285.1	9.2	297	95	308	10	351	37	214	58	294	41	166	7.9	310	91	344.50	0.71
Tb	27.1	2.8	28.32	0.13	28.6	8.3	17.2	0.59	32.4	3.4	21.0	5.3	29.3	5.4	15.78	0.93	29.3	8.1	33.9	2.0
Dy	110	12	109.8	3.0	116	30	43.1	1.6	132	14	87	22	124	16	69	13	117	31	137.2	5.7
Ho	13.93	0.90	14.13	0.31	14.5	3.3	4.30	0.18	16.6	2.0	11.1	2.5	16	2	8.8	2.6	14.7	3.8	17.460	0.014
Er	23.5	1.8	22.6	1.3	24.1	5	7.07	0.34	26.3	3.9	18.8	3.9	26.1	3.7	14.2	4.9	24.2	6.2	28.70	0.99
Tm	2.10	0.28	1.936	0.091	2.04	0.41	0.351	0.034	2.3	0.38	1.60	0.33	2.24	0.3	1.26	0.54	2.11	0.54	2.52	0.20
Yb	8.2	1.1	7.72	0.54	8.4	1.6	1.390	0.14	9.4	1.5	10	13	8.8	1.6	5.9	4.1	8.9	2.4	10.1	1.0
Lu	0.74	0.17	0.747	0.013	0.76	0.17	0.1110	0.019	0.86	0.17	0.64	0.16	0.93	0.16	0.58	0.33	0.78	0.21	0.884	0.067
Hf	21.5	2.3	17.3	1.5	24.9	5.7	56.5	2.0	30.0	6.3	20	14	97	59	55.6	7.1	53	23	57.9	9.1
Ta	740	160	752	39	1140	720	1548	50	1110	640	740	380	860	490	260	160	860	410	730	250
Th	790	440	760	100	1800	1500	3270	110	1500	1400	790	600	1150	720	590	250	1400	1200	1260	730
U	185	34	180.2	7.3	400	170	67.5	2.3	460	120	251	92	291	84	83	14	131	46	365	45

each zoning band (<5 microns wide). As a result, the results given by the LA-ICP-MS reflect the average composition of the whole perovskite grain. Besides a significant enrichment in LREE, the main differences between type Ia and Ib are in terms of Na, Sr, Zr, Nb and Hf (table 5.4, and fig.5.5). In contrast, Ta, Th and U contents are quite similar in both textural types. Consequently, type Ib perovskites are characterised by higher Nb/Ta and Th/U ratios (fig.5.5b). Perovskite crystallising as reaction rims on ilmenite is significantly enriched in U, Sr and Nd (180 ppm, 460 ppm, 2100 ppm and 6000 ppm, respectively) compared to the other textural types of perovskite (see table 5.4), although its REE contents are systematically lower than those of the other types.

Significant differences can be identified in terms of the trace-element compositions of perovskites in the different kimberlites (table 5.4 and fig. 5.6). Perovskite in the Calonda kimberlite is typically enriched in Nb (mean 16800 ppm), Zr (mean 1200 ppm), U (mean 370), Th (mean 1260 ppm) and Na (mean 5410 ppm), showing similar compositions to type Ib perovskite from the Mulepe kimberlites. Cat115 kimberlite pipe has also high Zr (up to

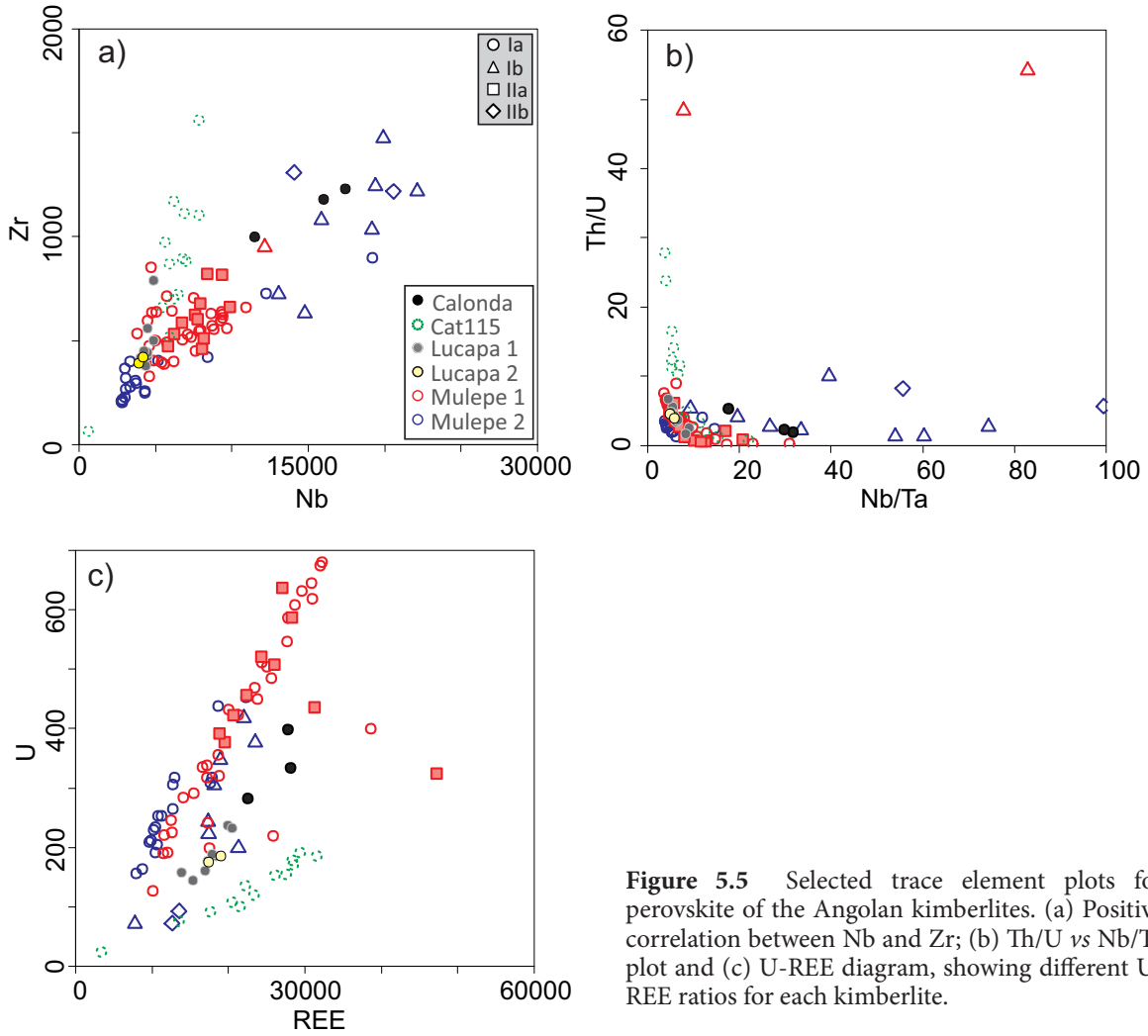

Figure 5.5 Selected trace element plots for perovskite of the Angolan kimberlites. (a) Positive correlation between Nb and Zr; (b) Th/U *vs* Nb/Ta plot and (c) U-REE diagram, showing different U/REE ratios for each kimberlite.

1560ppm) and extremely high Th contents (up to 4520 ppm), which leads to high Th/U ratios (fig.6b). Finally each kimberlite field shows a distinctive REE/U ratio, translated into different trends in the REE-U diagram (fig. 5.5c).

5.6. Oxygen fugacity

Major-element contents of perovskite can be used to estimate the oxygen fugacity (fO_2) during kimberlite emplacement. Bellis and Canil (2007) developed an oxybarometer, independent of temperature and bulk composition, based on the Fe and Nb content of perovskite. Since the fO_2 of kimberlite magmas changes during their ascent, the values given by different perovskite generations within a single pipe can shed light on the evolution of this magma from the mantle to the surface. Therefore, this oxybarometer could be useful to unravel not only differences at local or regional scale, by comparing different kimberlites, but also to identify discrete emplacement episodes or magma batches in a single pipe.

As shown in table 5.5 and figure 5.6a, most of the type Ia perovskites display a narrow range of Fe and Nb contents, giving a relative fO_2 commonly ranging between ΔNNO -3.0 and -1.0. These fO_2 values are similar to those from other kimberlites worldwide calculated using the same oxybarometer (fig. 5.6b). However, the high values reported for the Lac de Gras kimberlites (Canil and Bellis, 2007) were not observed in any of the analysed grains. The results presented here are also consistent with those obtained by the use of other oxybarometers in kimberlites, such as spinel-olivine pairs (Fedortchouk and Canil, 2004; Tappe et al., 2006) and

Kimberlite	*Type*	fO_2			
		av	σ	*min*	*max*
Cat115	***Ia***	-3.4	0.5	-4.3	-1.7
Mulepe 1	***Ia***	-2.3	0.6	-3.8	-0.6
	Ib	-1.9	1.7	-5.1	-0.5
	IIa	-2.6	0.9	-4.0	-0.4
Mulepe 2	***Ia***	-3.3	0.9	-6.6	-1.6
	Ib	-5.3	1.9	-10.3*	-2.4
	IIb	-9.3 *	7.9	-14.9*	-3.8
Calonda	***Ia***	-3.5	1.6	-5.9	0.8
Lucapa 1	***Ia***	-2.4	0.5	-3.2	-0.7
Lucapa 2	***Ia***	-2.8	0.4	-3.6	-1.8

Table 5.5 Averaged, minimum and maximum oxygen fugacities of perovskites, calculated using the oxybarometer of Bellis and Canil (2007)

Fe-in-monticellite (Le Pioufle and Canil, 2012) (fig. 5.6b), although these yield narrower fO_2 ranges. Oxybarometry of most of type Ib perovskite grains indicates slightly more reducing conditions in the kimberlitic magma from which they crystallised. The large spectrum of

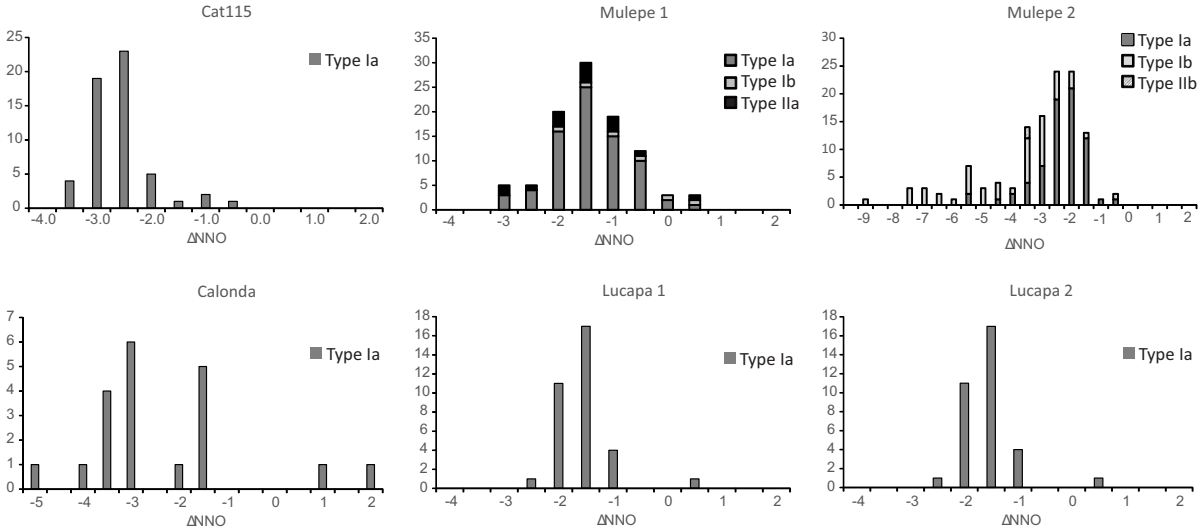

Figure 5.6 (a) Frequency histograms of log fO_2 expressed relative to the NNO buffer (ΔNNO) calculated using the perovskite oxybarometer developed by Bellis and Canil (2007). The wider fO_2 range observed in the Mulepe 2 kimberlite results from the higher type 2 perovskite content in this kimberlite.

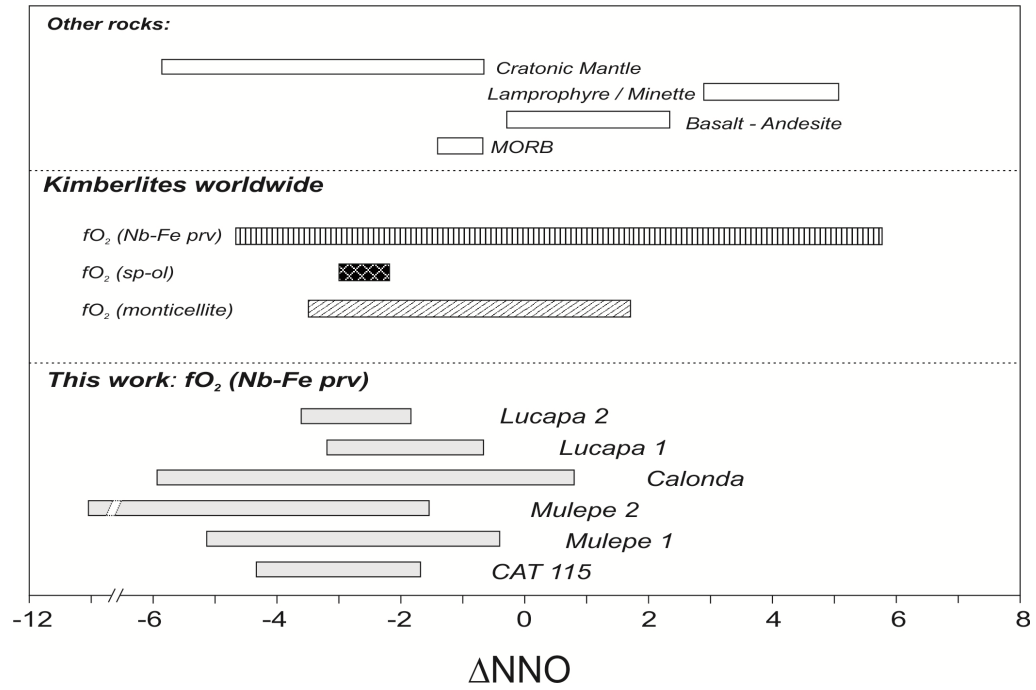

Figure 5.6 (b) Comparison of the ΔNNO conditions recorded by the perovskite grains of the Angolan kimberlites with the data obtained from the literature and compilated by Canil and Bellis (2007) and Chalapathi Rao et al. (2013), including worldwide kimberlites, cratonic lithospheric mantle and mantle-derived magmas. With the exception of the Mulepe 2 pipe, in which some type Ib perovskite yield more reducing conditions, all kimberlites recorded oxygen fugacities within the range of the kimberlites from the literature. Additionally, the oxygen fugacities calculated by other oxybarometers are also included for comparison: spinel-olivine oxybarometer (Fedortchouk and Canil, 2004) and monticellite oxybarometer (Le Pioufle and Canil, 2012).

ΔNNO observed in this type of perovskite undoubtedly stems from its oscillatory zoning, as well as its strong enrichment in Nb in relation to its medium-low Fe content. Reaction rims of perovskite on ilmenite (type IIa) show relative fO_2 similar to that calculated for groundmass perovskite, but reflect slightly more reducing conditions (ΔNNO down to -4.0) than other perovskite grains in the same kimberlite. In any case, the extremely low values (ΔNNO = -14.9) calculated for Nb-rich overgrowths (type IIb) are unlikely to be real and thus the use of this oxybarometer is not recommended for such compositions. The simplistic approach of this oxybarometer was also mentioned by Chakhmouradian et al. (2013), who considered that it neglects the influence of other highly compatible elements in perovskite (i.e. Ta, REE).

5.7. U-Pb DATING

The complete set of U-Pb dating results is presented in appendix A5.3 and they are summarised in table 5.6. Trace element analyses reveal a significant difference in the U contents of perovskite between Calonda and the other studied kimberlites. Perovskite has very similar U contents (125-730 ppm and 125-680 ppm) in the two kimberlites from Mulepe and these values are very similar to those from Calonda (280-400 ppm). In contrast, kimberlites located near Lucapa have systematically lower values (50-240 U ppm) in perovskite. These differences among the pipes have also been observed in terms of Th content, although in this case the variation within a single kimberlite can also be very important (Mulepe1 20-2400ppm; Mulepe2 15-5150 ppm; Calonda 630-1770 ppm; CAT115 10-4520 ppm; Lucapa1 230-1580 ppm and Lucapa2 680-830 ppm).

After common-Pb correction of the LA-ICP-MS datasets, the age of eruption of each kimberlite was calculated using ISOPLOT. The results are presented in fig. 5.7. Perovskite analyses on the two Mulepe kimberlites, the Calonda kimberlite and the CAT115 kimberlite yield U-Pb ages identical within error (116.2 ± 6.5 Ma, 123.0 ± 3.6 Ma, 119.5±4.3 Ma and 133± 10 Ma, respectively).

Previous work by Yang et al. (2009) and Donnelly et al. (2012) found that alteration of perovskite could produce a spread in U-Pb isotopic composition and give anomalous younger ages as a result of Pb loss. To better constrain the influence of Pb loss on the calculated ages, the composition of the common-Pb component was fixed at the present-day $^{207}Pb/^{206}Pb_{terrestrial}$ value of 0.835722. The same procedure was applied using a value of 0.83110, which is the

Kimberlite	Age (Ma)	MSWD
CAT115	133 ± 10	2.2
Mulepe 1	116.2 ± 6.5	4.1
Mulepe 2	123 ± 3.6	5.9
Mulepe 2 (Ia)	*121 ± 10*	*4.2*
Mulepe 2 (Ib)	*121.6 ± 5.5*	*6.7*
Calonda	119.5 ± 4.3	6
Lucapa 1 *	156.1 ± 9.7	1.4
Lucapa 2 *	87 ± 10	3.9

Table 5.6 Summary of U-Pb age of perovskites from the studied Angolan kimberlites. As shown in the table, the crystallisation age of type Ia and Ib perovskites of the Mulepe kimberlites was also calculated separately, but the values are still identical within uncertainty. * The ages reported for the Lucapa kimberlites are not reliable (see text for a better approximation).

$^{207}Pb/^{206}Pb$ value of the convecting-mantle source at 240 Ma [both values are calculated from Stacey and Kramers, 1975]. With the exception of the Lucapa kimberlites, the ages from the anchored regression lines coincide with those obtained without anchoring the common-Pb composition, giving the same emplacement ages within the errors. Therefore, the calculated ages probably represent the time of the eruptions and cannot be ascribed to a higher degree of alteration of the perovskite.

The ages calculated for the Lucapa pipes are not reliable, since they turn out to be either too old (Lucapa 1: 155.6±6 Ma) or too young (Lucapa 2: 83.1±4.6Ma) compared to those obtained when the composition of the common-Pb component was fixed at the actual $^{207}Pb/^{206}Pb$ value (135.7±6.9Ma and 152±11 Ma, respectively). In the former kimberlite, the low dispersion of the data, coupled with large uncertainties on individual analyses, can explain the low accuracy of the originally calculated age. The Lucapa 2 kimberlite, in turn, does not represent a younger eruptive episode; its age is a consequence of Pb loss during the alteration of perovskite. In an attempt to estimate the possible intrusion age of these kimberlites, a regression line was drawn through the grains with the least Pb loss, using the present-day $^{207}Pb/^{206}Pb$ value (0.83572) as the upper intercept. By comparing the values obtained by SIMS and LA-ICP-MS Donnelly et al. (2012) showed that this approach can give a good approximation to the actual age of the eruption. However, in our case this approach did not give acceptable values, due to the small number of data points having low Pb loss and their high intrinsic errors. We therefore have calculated provisional ages for each kimberlite, using the $^{238}U/^{206}Pb$ and $^{207}Pb/^{206}Pb$ ratios of the least altered perovskite grain in each pipe, regardless of their error (thus it is not possible to determine the age uncertainty). The best estimated age for the Lucapa 1 kimberlite would be 135 Ma, whereas the Lucapa 2 kimberlite would have intruded around 127 Ma. These ages are at least consistent with the few published data on kimberlitic eruptions in the area (Eley et al., 2008; see table 5.1).

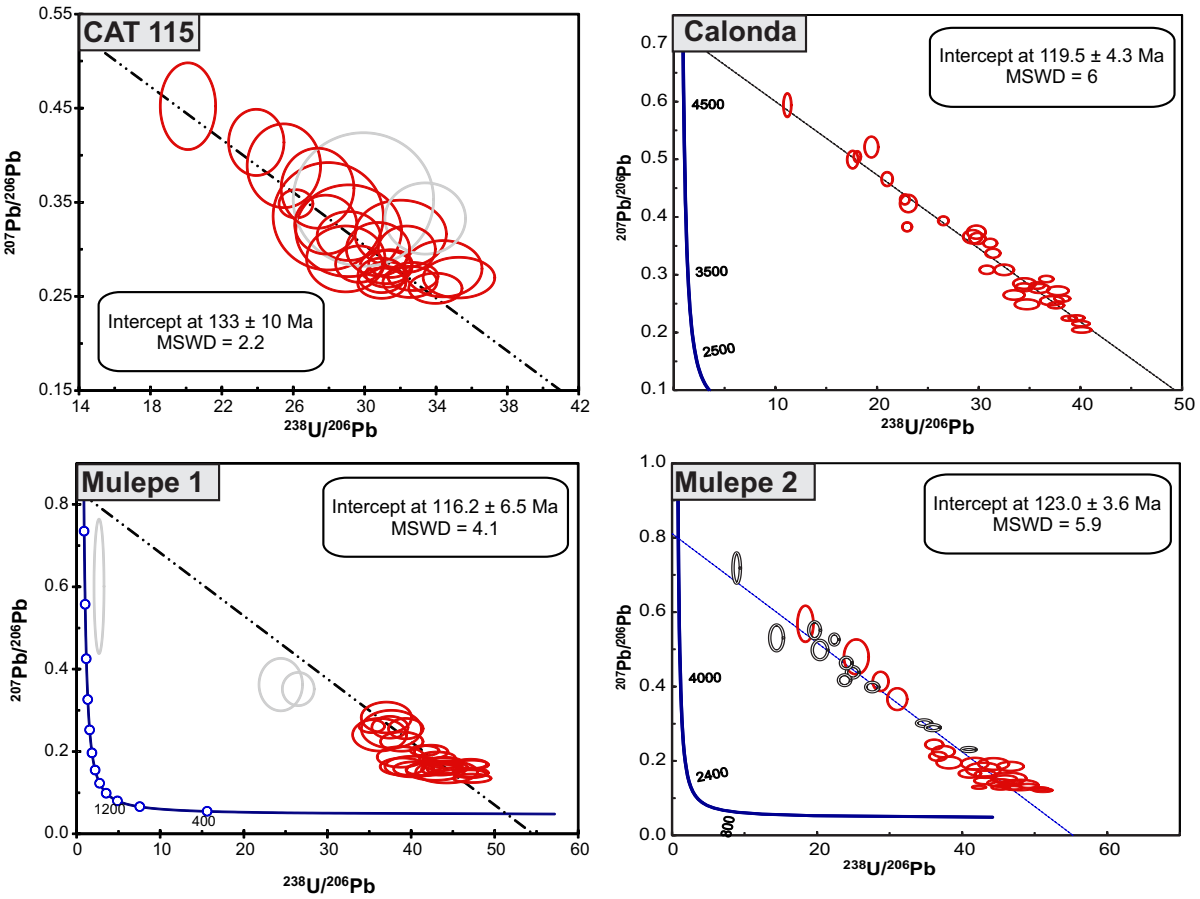

Figure 5.7. Cat115, Calonda and Mulepe perovskite U-Pb data in inverse-Concordia (Tera-Wasserburg) plots. The lower intercept gives the age recorded by the perovskite grains of each pipe. Errors are shown as ellipses at 1σ. In the Mulepe 2 kimberlite, analysis corresponding to subtype Ib perovskite are represented by two concentric circles.

5.8. Sr-Nd ISOTOPES

Sr and Nd contents of the perovskites were obtained by laser ablation techniques (mean values: Lucapa1, 1220 ± 65 ppm Sr and 3820 ± 610 ppm Nd; Mulepe1, 1450 ± 560 ppm Sr and 4700 ± 2400 ppm Nd; Mulepe2, 950 ± 210 ppm Sr and 2920 ± 990 ppm Nd; and Cat115, 1250 ± 31 ppm Sr and 4700 ± 1700 ppm Nd). To ensure the best signal quality in the Sr and Nd isotope analyses, only the kimberlites with perovskite completely lacking alteration and >30 microns were characterised (Cat115, Lucapa 1, Mulepe1 and Mulepe2). For the same reason, type Ib and secondary perovskite from the Mulepe kimberlites were excluded from this study. Despite the aforementioned precautions, large uncertainties and dispersion are still found in the dataset and interpretation should be taken with caution. The small size of the grains, coupled with instability of the instrument during data acquisition, limited the quality of the presented results. A summary of the Sr and Nd isotope compositions is shown in table 5.7; the whole dataset is included in appendix A5.4.

The $^{87}Sr/^{86}Sr$ ratios in perovskites derived from these four kimberlites overlap, giving isotope compositions identical within their uncertainties: 0.70361±43 (Mulepe 1), 0.70308±31 (Mulepe2), 0.70323±66 (Lucapa1) and 0.70405±74 (Cat115). As shown in supplementary files, these values correspond to initial Sr isotopic ratios ranging between 0.70118 and 0.70567. Only analyses with $^{145}Nd/^{144}Nd$ within uncertainty of the canonical value were accepted for further interpretation As seen in table 5.7, there is significant dispersion in the $^{143}Nd/^{144}Nd$ values of the remaining dataset, even in perovskite grains derived from the same kimberlite. As a result, large uncertainties are linked to the average $^{143}Nd/^{144}Nd$ perovskite compositions for each pipe: 0.51241±27 (Mulepe 1); 0.51264±8 (Mulepe2); 0.51270±23 (Lucapa1) and 0.51265±21 (Cat115). The U-Pb ages of each kimberlite were used in order to obtain an average εNd at the time of the eruption (εNd_i), yielding the following values: $\varepsilon Nd_{116.2}$=-2.6±5.4 (Mulepe1), εNd_{123}=1.9±1.6 (Mulepe2), $\varepsilon Nd_{135.7}$=3.1±4.5 (Lucapa1) and εNd_{133}=2.2±4.1 (Cat115).

The $^{87}Sr/^{86}Sri$ - $\varepsilon Nd_{(i)}$ diagram (fig.5.8) is conventionally used to distinguish the isotopic reservoirs of the sources of the kimberlites and other mantle magmas (Becker and Le Roex, 2006; Tappe et al., 2011; Donnelly et al., 2012;). This figure shows that the average initial Sr and εNd isotopic compositions of 3 out of the 4 analysed kimberlites plot within the Group I

Kimberlite	**Mulepe1**	**Mulepe2**	**Lucapa1**	**Cat115**
Age (Ma)	116.2	123	135.7	133
n:	*20*	*35*	*12*	*9*
$^{87}Sr/^{86}Sr$	0.70361 ± 43	0.70308 ± 31	0.70323 ± 66	0.70405 ± 74
$^{87}Rb/^{86}Sr$	0.00043 ± 24	0.00070 ± 31	0.00033 ± 43	0.00099 ± 63
$^{87}Sr/^{86}Sr_i$	0.70361 ± 43	0.70308 ± 31	0.70323 ± 66	0.70405 ± 74
n:	*14*	*34*	*9*	*14*
$(^{143}Nd/^{144}Nd)$	0.51241 ± 27	0.51264 ± 8	0.51270 ± 23	0.51265 ± 21
$(^{147}Sm/^{144}Nd)$	0.0799 ± 18	0.08620 ± 49	0.08336 ± 71	0.07958 ± 47
$(^{143}Nd/^{144}Nd)_T$	0.51235 ± 28	0.51256 ± 8	0.51262 ± 23	0.51258 ± 21
$\varepsilon Nd_{(0)}$	-4.3 ± 5.4	0.1 ± 1.6	1.1 ± 4.5	0.2 ± 4.1
$\varepsilon Nd_{(T)}$	-2.6 ± 5.4	1.9 ± 1.6	3.1 ± 4.5	2.2 ± 4.1

n: number of analyses

$\varepsilon Nd_{(t)} = ((^{143}Nd/^{144}Nd)_s - (^{147}Sm/^{144}Nd)_s \times (e^{\lambda t}-1))/((^{143}Nd/^{144}Nd)_{CHUR} - (^{147}Sm/^{144}Nd)_{CHUR} \times (e^{\lambda t}-1)) - 1) \times 10000$

where s=sample; $(^{143}Nd/^{144}Nd)_{CHUR}$ = 0.512638; and $(^{147}Sm/^{144}Nd)_{CHUR}$=0.1967; λ=0.00654/Ga for ^{147}Sm; t=age (in Ga) calculated for each kimberlite in this study

$Sr_i = {}^{87}Sr/^{86}Sr_s - (^{87}Rb/^{86}Sr_s \times e^{\lambda t}-1)$

where s=sample; λ=0.01420/Ga; t=age (in Ga) calculated for each kimberlite in this study

Table 5.7 Summary of Sr-Nd results of perovskites from the studied Angolan kimberlites

kimberlite field, which is consistent with the petrography of the studied pipes. The Mulepe 1 kimberlite shows negative mean εNd values, although the results still plot in the field of Group I kimberlites within the errors.

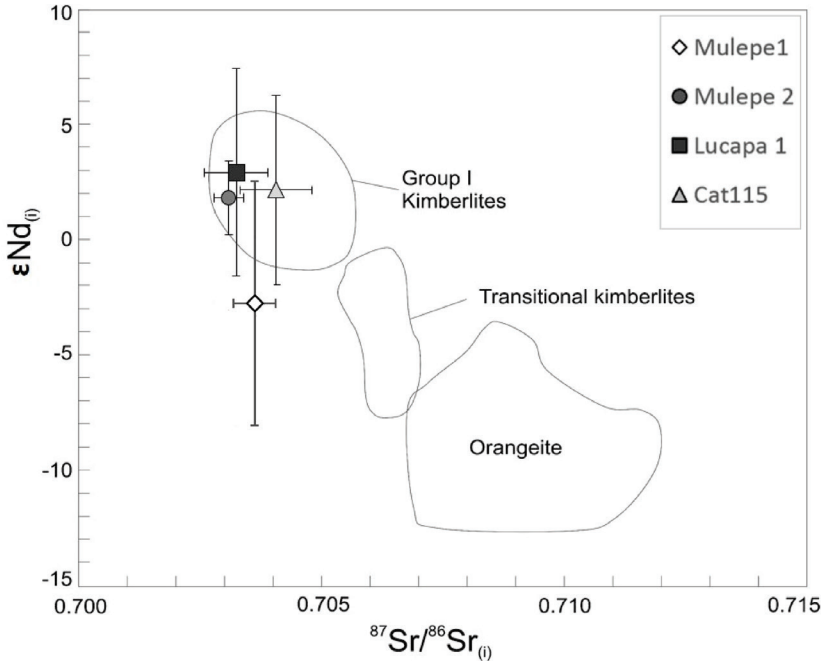

Figure 5.8 εNd_i vs. $^{87}Sr/^{86}Sr_i$ average composition of groundmass perovskite from the Mulepe 1 and 2, Cat115 and Lucapa1 kimberlites. Kimberlite, orangeite and transitional kimberlite fields from Donnelly et al. (2012) and references therein.

5.9. Discussion

5.9.1. Kimberlite petrogenesis: the Mulepe case

The occurrence of two discrete perovskite populations (type Ia and Ib) in the Mulepe kimberlites, even within the same thin section, suggests that the petrogenesis of these pipes is more complex than that of other kimberlites. As previously shown, these two types of perovskite differ not only in texture (fig.5.1), but also in their major- and trace-element composition (fig.5.2, fig.5.4 and fig.5.5), their zoning patterns and the presence or absence of inclusions. When considering all these features together, it seems reasonable to suggest that type Ia perovskite was the first population to grow, sometimes developing necklaces around the previously crystallised olivine. Subsequently, a second magma led to the formation of type Ib perovskite, crystallising as discrete grains in the kimberlitic groundmass. The fact that Ib perovskite is typically euhedral and shows no evidences of alteration also supports its

late formation, in equilibrium with the last kimberlitic melt. In contrast, type Ia perovskite usually occurs as rounded and partially corroded crystals, indicating partial assimilation as a consequence of its interaction with a late melt under non-equilibrium conditions.

The coexistence of these two completely different populations of perovskite could be either explained by i) reworking of kimberlite facies that underwent different crystallisation processes; ii) degassing of the kimberlite magma or iii) mingling of two compositionally different magmas.

Chakhmouradian and Mitchell (2000) observed that enrichment in LREE, Th and Nb in perovskites is correlated neither with a particular facies of the kimberlite nor with a specific mineral paragenesis. Therefore it seems unlikely that coexistence of type Ia and Ib is just a consequence of mixing of facies within the same kimberlite. Degassing processes have been invoked previously to explain the occurrence of different populations of perovskite within the same kimberlite (Sarkar et al., 2011). In our work, it could be argued that the petrography supports a hypothetical two-stage crystallisation process in a degassing magma, in which type Ia perovskite would have crystallised prior to degassing, whereas type Ib perovskite would be the post-degassing phase. However, the lack of TiO_2 rims on type Ia perovskite, expected from devolatilization processes, as well as the composition of the type Ib perovskite (i.e. enriched in HFSE and REE) argue against the explanation by Sarkar et al. (2011). Moreover, Fe-Nb oxybarometry shows that the magma from which type Ib perovskite crystallised was slightly more reducing than that which crystallized type Ia. This is not consistent with a degassing process, which would typically lead to more oxidised conditions in the remaining magma (Sarkar et al., 2011). Instead, it is more likely that the wide range of the oxygen fugacity displayed by groundmass perovskite of the Mulepe kimberlites resulted from the mingling of compositionally distinct magmas or multiple intrusion events (Eccles et al., 2004; Ogilvie-Harris et al., 2009).

The differences in composition between both types of perovskite also support a late incorporation of a more evolved melt previously enriched in these elements. Most grains of type Ia perovskite exhibit the “normal” zoning pattern described by Chakhmouradian and Mitchell (2001). The rimward sodium loss, coupled with a significant decrease in REE, Th and Ta, could be explained by progressive depletion in the kimberlitic melt during perovskite crystallisation (Chakhmouradian et al., 2013). Therefore, the high Na, REE and Nb contents reported in type Ib perovskite require the presence of a compositionally different magma from

which type Ia perovskite crystallised.

Since perovskite crystallisation plays an important role in the fractionation of trace elements in kimberlite and carbonatite magmas during cooling (e.g. Beyer et al., 2013; Chakhmouradian et al., 2013), the trace element composition of each population of perovskite could be used to infer the nature of the different melts in equilibrium at the moment of perovskite crystallisation. An inversion modelling of the perovskite trace element data was carried out, using the perovskite/kimberlite partition coefficients (D) proposed by Chakhmouradian et al. (2013). These coefficients are generally consistent with those obtained experimentally by Beyer et al. (2013). The composition of the melt in equilibrium with each perovskite type is represented in fig. 5.4. The patterns of the resulting melts are very similar to that defined by whole rock analyses of kimberlite (Chakhmouradian et al., 2013), characterised by a 10x to 100x enrichment in incompatible elements (LILE and HFSE) relative to the primitive mantle. In general, the calculated melts are slightly further enriched in these incompatible elements compared to the whole rock analyses. This enrichment is significantly more important for some elements such as U, Nb, Zr and Hf, whereas the Th contents are lower than those found by whole-rock analysis. As expected from their trace-element composition, the composition of the calculated melt in equilibrium with type Ib perovskite is more enriched in HFSE than that from which type Ia crystallised. The most relevant divergence between the calculated melt and the whole rock analyses is observed in type IIb perovskite, although given its small grain size the high Rb and K values are probably an artefact resulting from the ablation of groundmass phlogopite.

There is also some evidence of a third melt that reacted with the groundmass minerals already crystallised. The Nb-rich perovskite (IIb) found rimming some type Ia perovskite in the Mulepe kimberlites is compositionally identical to those found in Lac de Gras (Canada) and in Kuruman (South Africa) kimberlites (Donnelly et al., 2012; Chakhmouradian et al., 2013). These rims have been previously interpreted as due to an interaction with an evolved kimberlite melt, without contribution of a hydrous fluid. The early loss of fluid from the kimberlite magma could result in an increase of fluid-incompatible elements in the melt, which would explain the secondary formation of Nb-rich rims on the original groundmass perovskite (Chakhmouradian et al., 2013). Interestingly, the Nb-rich overgrowth in the Mulepe kimberlites is compositionally different to the average values for the type Ib perovskites found in the same pipes. These differences further support the hypothesis that the euhedral perovskites

correspond to a completely different and independent magma, indicating that crystallisation of perovskite in Mulepe kimberlites was a multi-stage process. Additionally, the oscillatory zoning typical of the Mulepe kimberlites can be overprinted by more evolved compositions related to late processes. This supports a magmatic origin of the oscillatory zoning, related to the rapid crystallisation of the perovskite grain, regardless of further long-term interaction with a later more evolved kimberlitic magma. Our observations are consistent with several examples of mixing, mingling or scavenging in kimberlites, carbonatites and alkaline rocks (e.g. Ivanikov et al., 1998; Chakhmouradian and Mitchell, 2001; Zurevinski and Mitchell, 2004; Ogilvie-Harris et al., 2009; Tappe et al., 2009).

In any case, the ages calculated by U-Pb methods for both type Ia and Ib perovskite are identical within error and all the analyses fit the same regression line in the inverse Concordia diagram, regardless of their texture (fig. 5.7). Therefore, the lapse of time between the crystallisation of these two perovskite types should be less than 3My.

5.9.2. Age and tectonic implications

Structural control of kimberlite emplacement has been a matter of study for many years. There is a broad consensus that kimberlites are linked either to extensional episodes or reactivation of previous fault systems well after the main tectonic activity. Three different mechanisms are known to provide favourable conditions for kimberlite emplacement, always related to complex fault networks: i) supercontinent formation, ii) continental rifting and iii) late strain accommodation (Dawson, 1970; White et al., 1995; Jelsma et al., 2009; Tappe et al., 2014).

The ages reported for kimberlites in Angola, both in this study and in previously published work (table 5.1), are not temporally linked to supercontinent assembly, but rather point to incipient rifting and strain accommodation. Continental break-up entails creation of a network of rift and fault zones as a consequence of extensional strain propagation into the supercontinent. During this stage pre-existing lithospheric discontinuities can also be reactivated and favour kimberlite emplacement. This seems to be the case for the studied kimberlites, which yield Early Cretaceous ages (115-130 Ma), coinciding with the break-up of Gondwana and the opening of the South Atlantic Ocean. The main eruptive age peak (120 Ma) correlates with the onset of spreading. This is also in very good agreement with other kimberlite magmatism

in Africa, which is also related to NE-SW fault systems (Jelsma et al., 2004). Therefore as De Boorder (1982) suggested, deep-seated faults in Central Angola apparently played a major role in the emplacement of kimberlite and alkaline rocks. These structures delimit relatively narrow (50-90 km width) hidden corridors, or aulacogens, which are both chemically and physically different from the surrounding material. Jelsma et al. (2004) defined them as cryptic continental corridors and found that they are collinear with fracture zones along the Atlantic and Indian continental margins of Southern Africa; and are major features of the African lithospheric architecture (Begg et al., 2009).

The calculated U-Pb ages for the Angolan kimberlites are older than most of the Group I kimberlites in South Africa (Jelsma et al., 2004; Griffin et al., 2014), which would be consistent with a stress propagation and melt migration along deep fracture zones, related with the opening of the South Atlantic Ocean.

5.10. Preliminary conclusions

1. Perovskite is usually homogeneous in terms of major-element composition, but notable differences in trace-element patterns were observed among the Angolan kimberlites. This suggests that either the kimberlite source was heterogeneous at local scale and the magma composition changed through time, or that magma fractionation was significantly different between the kimberlites within the same area.

2. The Mulepe perovskites show a complex petrogenetic history. At least three different compositional and textural types of perovskite were identified within the same kimberlite, which has been explained by mingling of magmas differing in composition or in degree of evolution.

3. The kimberlite magmatism in the Lundas province (115-130 Ma) had the main eruptive peak around 120 Ma, coinciding with the Gondwana breakup. Kimberlite emplacement is explained by reactivation of NE-SW deep-seated faults, or cryptic continental corridors, which represent the continuation of the oceanic fracture zones.

4. The Sr_i and εNd_i values reported for the perovskites are in good agreement with the published data for on- and off-craton South African Group I kimberlites.

Chapter 6
PETROGRAPHY AND MINERAL COMPOSITION OF MANTLE XENOLITHS OF THE LUNDA NORTE SCLM

Kimberlites are important carriers of mantle xenoliths, bringing to the surface fresh rocks from depths which are commonly not accessible to scientists. This chapter includes the petrographic description of the mantle xenoliths carried out by Catoca and Cat115 kimberlites, as well as their mineralogical composition, based on the analysis performed using EMP and LA-ICP-MS. Garnet-peridotite xenoliths are the most important lithology sampled by these kimberlites, which were subsequently divided into coarse and porphyroclastic peridotites according to their microstructure. The compositional differences between these two suites is also discussed in this chapter. Petrography and composition of bi-mineral clinopyroxene-garnet xenoliths (eclogites and garnet-pyroxenites) is followed by the description of large clinopyroxene megacrysts and highly metasomatised xenoliths.

6.1. Introduction

The xenolith samples were obtained from several drill cores during the prospection stage of the Cat115 kimberlite and exploitation of the Catoca pipe. They are up to 8 cm in maximum dimension, although most of them have diameters between 2 and 5 cm. They usually are rounded and show little serpentinisation, with the original assemblage well preserved. Most of the fresh xenoliths are classified as peridotites (fig. 6.1), although eclogites, garnet-clinopyroxenites and clinopyroxene megacrysts are also abundant. The main features of each xenolith studied here are summarized in table 6.1, and a detailed petrographic description is included in appendix A6.1.

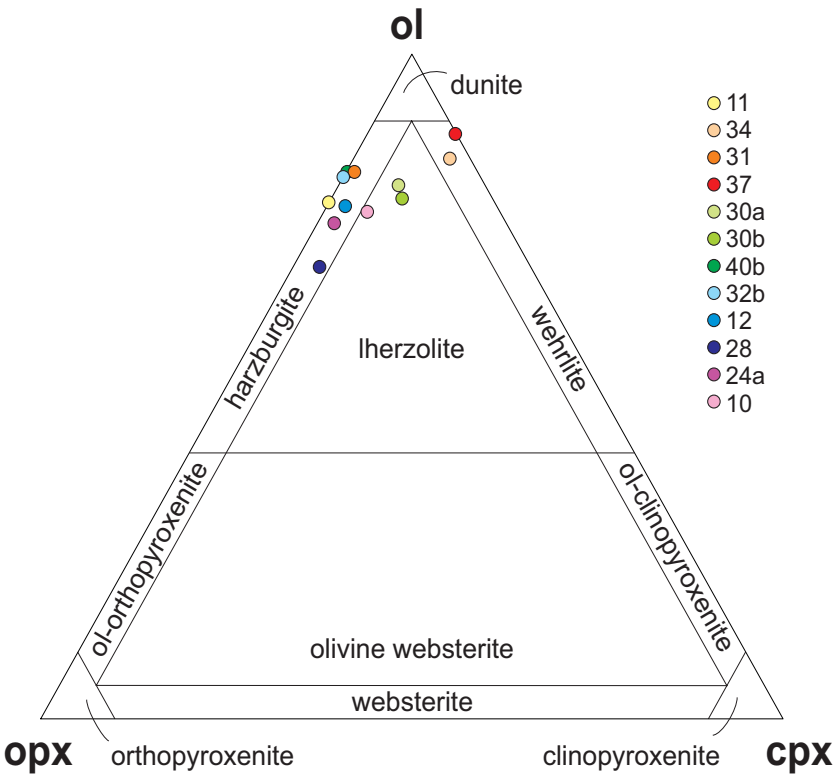

Figure 6.1 Modal classification of the ultramafic xenoliths sampled by the Cat115 kimberlite

6.2. Ultramafic rocks

6.2.1. Petrography

Spinel harzburgite

Only one spinel peridotite was recovered from the drill cores (fig.6.2a). This sample is composed of rounded olivine grains (70% modal) which have undergone partial serpentinisation. Orthopyroxene (20% modal) forms subhedral prismatic grains (2-3mm) and it is in textural equilibrium with olivine. Anhedral primary spinel is randomly distributed in the interstitial spaces, representing around 2% of the xenolith. Clinopyroxene is absent in this rock.

Garnet peridotites

Garnet peridotites are the most abundant mantle xenoliths collected during the field work, and represent more than half of the whole sampling. As shown in fig. 6.1, these peridotites encompass three rock types: harzburgite, lherzolite and wehrlite, harzburgite being the most abundant.

Two garnet-peridotite suites were distinguished, based on their microstructure: coarse garnet peridotites and porphyroclastic garnet peridotites.

I. Coarse garnet peridotites

These peridotites typically show an equant microstructure (fig. 6.2). Only one generation of olivine is observed; it is in textural equilibrium with orthopyroxene and garnet, with triple point grain-grain contact (120º). Coarse (1-5mm) olivine crystals usually represent between 65 and 75% of the whole xenolith and they have straight to slightly curved boundaries.

Orthopyroxene is always present in low amounts (7-15%) or even absent in this suite. When present, it is euhedral to subhedral (2-10 mm) and shows no evidence of preferred orientation.

Sample	Pipe	Size (cm)	Rock type	Microstructure	Modal abundances
MGR-11	Cat 115	1.5	spl-Hz	coarse	ol (70), opx (20), spl (<2), srp (8)
MGR-34	Cat 115	3	grt-Wehr	coarse	ol (70), grt (10), Cr-di (8), opx (<2), srp (10)
MGR-31	Cat 115	4	grt-Hz	coarse	ol (70), opx (12), grt (7), Cr-di (<1), cb? (<5), srp (6)
MGR-37	Cat 115	4	grt-Wehr	coarse	ol (75), Cr-di (10), grt (10), phl (<2), srp (4)
MGR-30A	Cat 115	5	grt-Lhz	coarse	ol (65), opx (9), grt (10), Cr-di (8), phl (3), srp (5)
MGR-30B	Cat 115	4	grt-Lhz	coarse	ol (70), opx (10), grt (7), Cr-di (7), phl (<1), srp (5)
MGR-40A	Cat 115	2	Hz	coarse	ol (70), opx (20), srp (10)
MGR-40B	Cat 115	5	grt-Hz	coarse	ol (70), opx (15), grt (10), phl (<1), srp (5)
MGR-32B	Cat 115	6	grt-Hz	porphyroblastic	ol (75), opx (17), grt (3), srp (5)
MGR-12	Cat 115	5	grt-Hz	porphyroblastic	ol (65), opx (17), grt (8), Cr-di (<2), srp (8)
MGR-28	Cat 115	6	grt-Hz	porphyroblastic	ol (60), opx (25), grt (8), Cr-di (<3), srp (5)
MGR-24A	Cat 115	6	grt-Hz	porphyroblastic	ol (65), opx (20), grt (3), Cr-di (<2), srp (10)
MGR-10	Cat 115	2	grt-Lhz	porphyroblastic	ol (65), opx (15), grt (10), Cr-di (5), srp (5)
Cat-18	Catoca	9	Ecl	coarse	omp (50), gt (45), phl (<3), rut (<1), srp (<2)
Cat-34	Catoca	6	Ecl	coarse	grt (70), omp (30)
Cat-41	Catoca	4	Ecl	coarse	grt (50), omp (50)
Cat-26	Catoca	6	grt-px	coarse	grt (50), cpx (45), phl (4), rt (<2%)
MGR-13	Cat 115	4	grt-px	coarse	cpx (65), grt (35)
MGR-35	Cat 115	4	granulite?	coarse	grt (45), cpx (40), ol (3), ilm (<2), srp (10)
MGR-1	Catoca	8	Px	megacryst	cpx (100)
Cat-84	Catoca	5	Px	megacryst	cpx (100)
Cat-86	Catoca	5	Px	megacryst	cpx (100)
Cat-94	Catoca	2.5	Px	megacryst	cpx (100)
Cat-95	Catoca	3	Px	megacryst	cpx (100)
Cat-97	Catoca	4	Px	megacryst	cpx (100)
MGR-20A	Cat 115	4	Px	megacryst	cpx (100)
MGR-20B	Cat 115	4	Px	megacryst	cpx (100)
MGR-44	Cat 115	6	H metasom.	coarse	ol-srp (45), cpx (40), ilm (15)
MGR-27	Cat 115	8	H metasom.	coarse	srp (45), cpx (30), cal (15), krs (8), ilm (<3), ap (<1)
MGR-15A	Cat 115	1.5	H metasom.	coarse	srp (50), phl (35), ol (10), di (4), chr (<2)
MGR-24B	Cat 115	5	H metasom.	coarse	phl (60), di (35), chr (<5)

Table 6.1 List of the studied xenoliths, including the kimberlite pipe, their diameter, rock type, microstructure and modal abundances. Mineral abbreviations: olivine (ol), orthopyroxene (opx), clinopyroxene (cpx), garnet (grt), spinel (spl), phlogopite (phl), omphacite (omp), chromian diopside (Cr-di), serpentine (srp), carbonate (cb), rutile (rut), calcite (cal), kaersutite (krs), diopside (di), apatite (ap). Rock type abbreviations: harzburgite (Hz), Wehrlite (wehr). Lherzolite (Lhz), eclogite (Ecl), garnet pyroxenite (grt-px), pyroxene megacryst (px), highly metasomatised xenolith (H metam.)

Garnet (7-10%) is commonly rounded and its size usually ranges from 2 to 4 mm, although in some peridotites it might reach 10 mm in diameter. In one of the wehrlite xenoliths (sample MGR-37) garnet occurs only in the diopside-phlogopite rich zones and equilibrium between garnet and olivine cannot be guaranteed. Instead, this assemblage may indicate that this garnet has a metasomatic origin, linked to the formation of the other two typical metasomatic

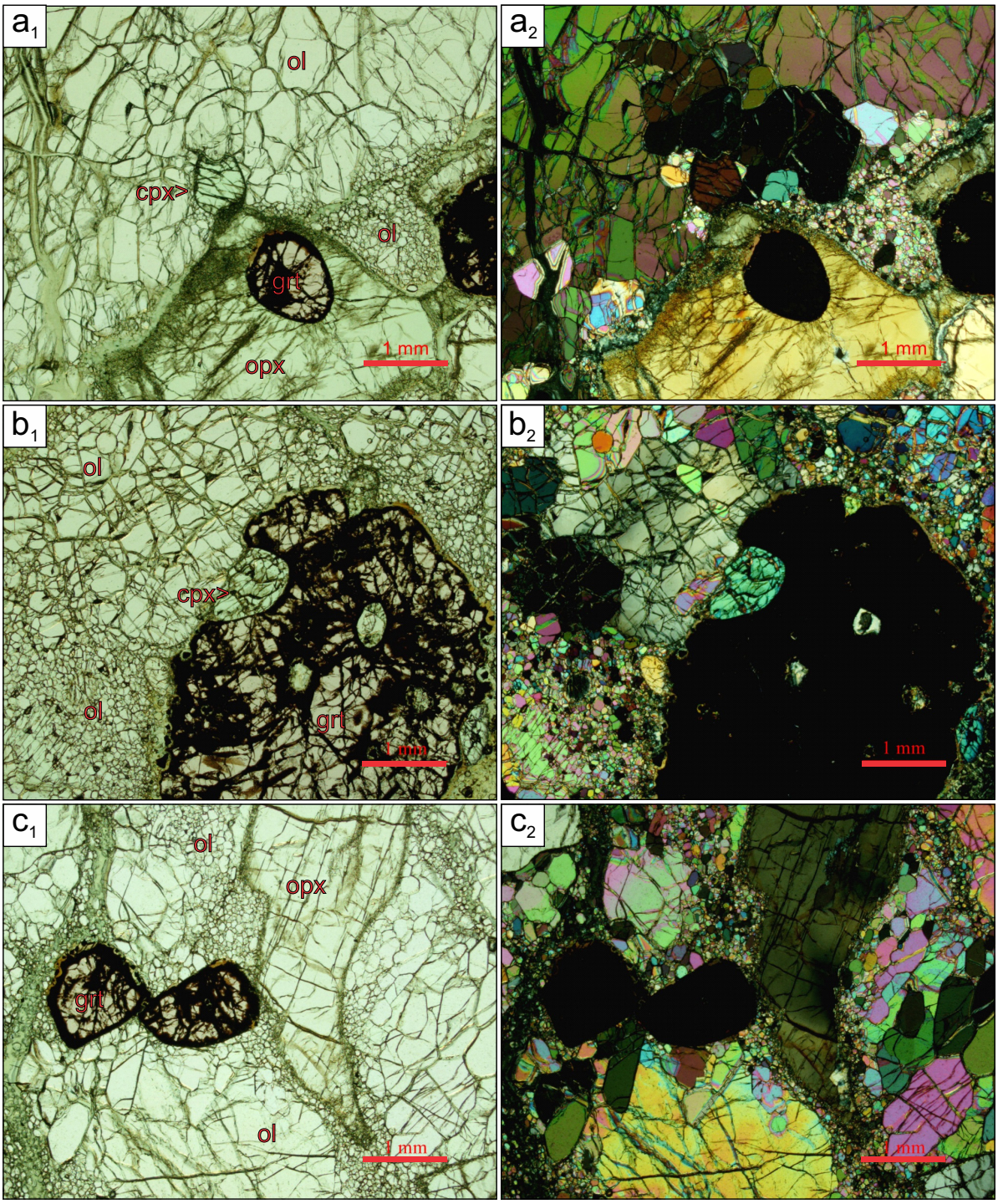

Figure 6.2 Petrographic microscope images of the coarse peridotites as seen in transmitted light. (a) Spl-harzburgite, (b) Grt-lherzolite and (c) Grt-harzbugite. Mineral abbreviations: spinel (spl), olivine (ol), orthopyroxene (opx), diopside (di), garnet (grt). Note serpentinisation along grain boundaries and within fractures of the silicates. Garnet grains have reaction rims of phlogopite and chromite.

phases. In almost all xenoliths, garnet has a thin reaction rim of biotite, locally accompanied by secondary small (< 50 μm) euhedral chromite grains, which are typically zoned, with an enricment in Mg towards the rims, coupled with a depletion in Cr.

Anhedral Cr-rich diopside (usually 7-10%) commonly occupies the intergranular space between the other mineral phases.

In some garnet peridotites, tabular (<1cm) euhedral crystals of phlogopite (<3%) have formed. As shown in fig. 6.3, these crystals may show thin (10-100 μm) zoning near the grain boundaries. Crystallisation of phlogopite is always directly related to the formation of anhedral clinopyroxene and sometimes is accompanied by crystallization of chromite (fig.6.3). Slight serpentinization has been observed in these peridotites, which occurs as thin veinlets along fractures and grain boundaries of olivine.

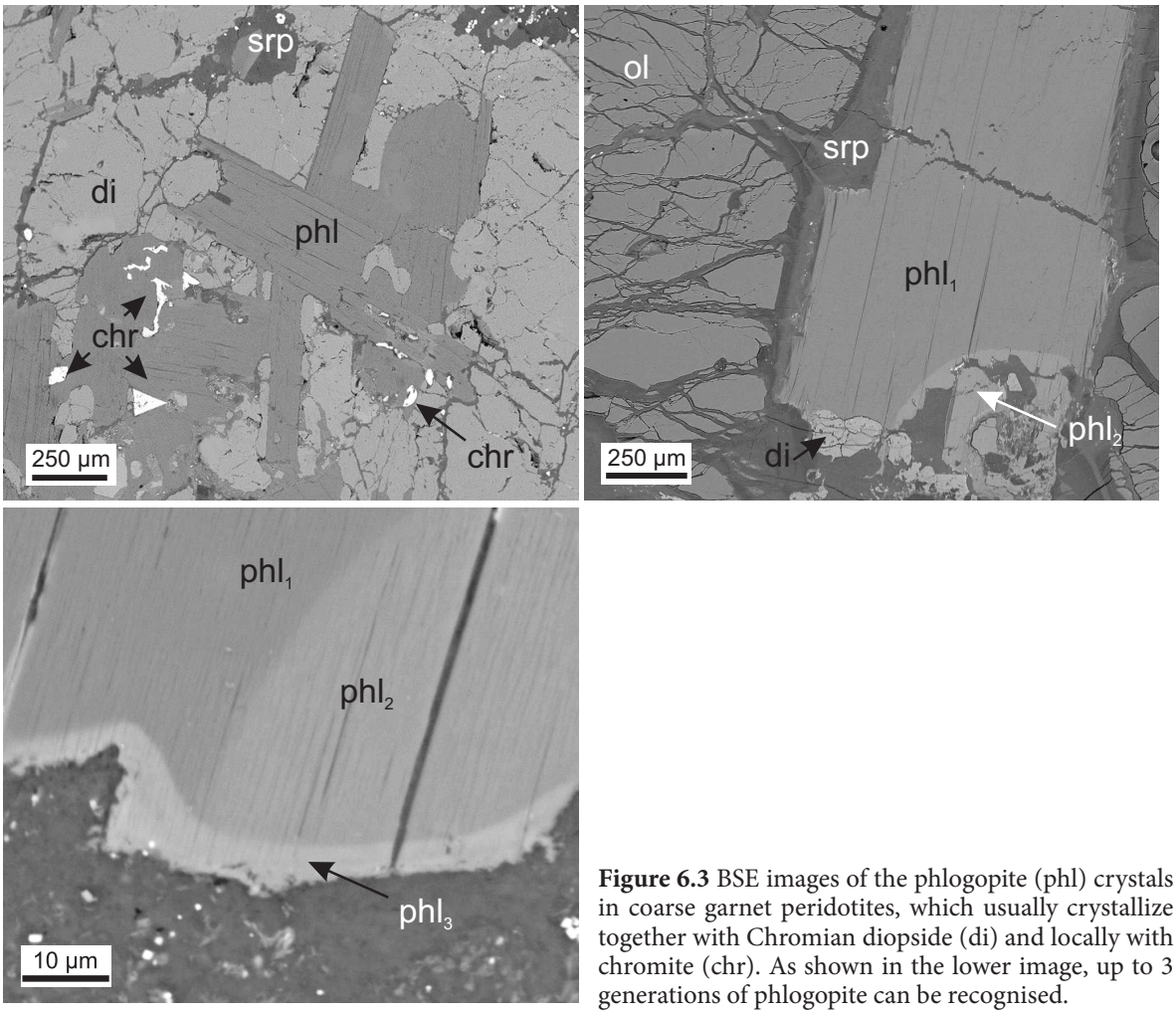

Figure 6.3 BSE images of the phlogopite (phl) crystals in coarse garnet peridotites, which usually crystallize together with Chromian diopside (di) and locally with chromite (chr). As shown in the lower image, up to 3 generations of phlogopite can be recognised.

II. Porphyroclastic garnet peridotites

Garnet peridotites belonging to this suite have a porphyroclastic (sheared) microstructure, defined by coarse olivine grains and elongated pyroxenes surrounded by interstitial, rounded olivine neoblasts, which are up to 0.2 mm in diameter (fig. 6.4). The large (1-3 mm) olivine crystals from these peridotites usually show undulose extinction, which indicates deformation, although neither olivine nor pyroxene show any preferred orientation. In these rocks, coarse olivine grains constitute between 30 and 45 modal % of the xenolith, whereas the neoblasts are between 20 and 25 modal %.

Orthopyroxene is significantly more abundant than in the other suite, representing in some xenoliths up to 25% of the volume of the rock, with maximum grain lengths typically ranging between 5 and 10 mm. Kink bands and undulose extinction are observed in most of the orthopyroxene grains (fig. 6.4c). Additionally, in some peridotites of this suite a second generation of orthopyroxene has been observed on the boundaries of the coarser grains. It is interpreted as peripheral recrystallization of the primary pyroxene into small (< 100 μm) neoblasts. Neoblasts of pyroxene and olivine are free of dislocations and fluid inclusions.

Garnet (3-10%) is in microstructural equilibrium with olivine and orthopyroxene. In general, rounded garnet grains from the sheared peridotite suite are significantly smaller than those in coarse peridotites. With only one exception (sample MGR-10), the typical grain size is 1mm. The larger grains may contain small (0.2-0.5μm) diopside inclusions (fig. 6.4b). Most of the garnet crystals have developed a reaction rim of phlogopite coupled with the formation of euhedral chromite crystals. The alteration of garnet is usually more important than that observed in garnet from coarse peridotites (fig.6.5).

As in the coarse suite, clinopyroxene (chromian diopside) mostly occurs interstitially to the other minerals, although it is significantly less abundant than in the first suite, usually below 2% of the whole rock. The boundaries of these clinopyroxenes are fine-grained, showing a characteristic spongy appearance already described in other xenoliths worldwide. Another generation of diopside appears locally as small (< 100 μm) tabular grains in contact with the primary coarser grains of the xenoliths. As shown in fig. 6.5, crystallisation of this chromian diopside occurred after the formation of the olivine and orthopyroxene neoblasts, thus indicating that it postdates deformation. The large euhedral phlogopite crystals observed in coarse garnet peridotites are absent in all the porphyroclastic samples.

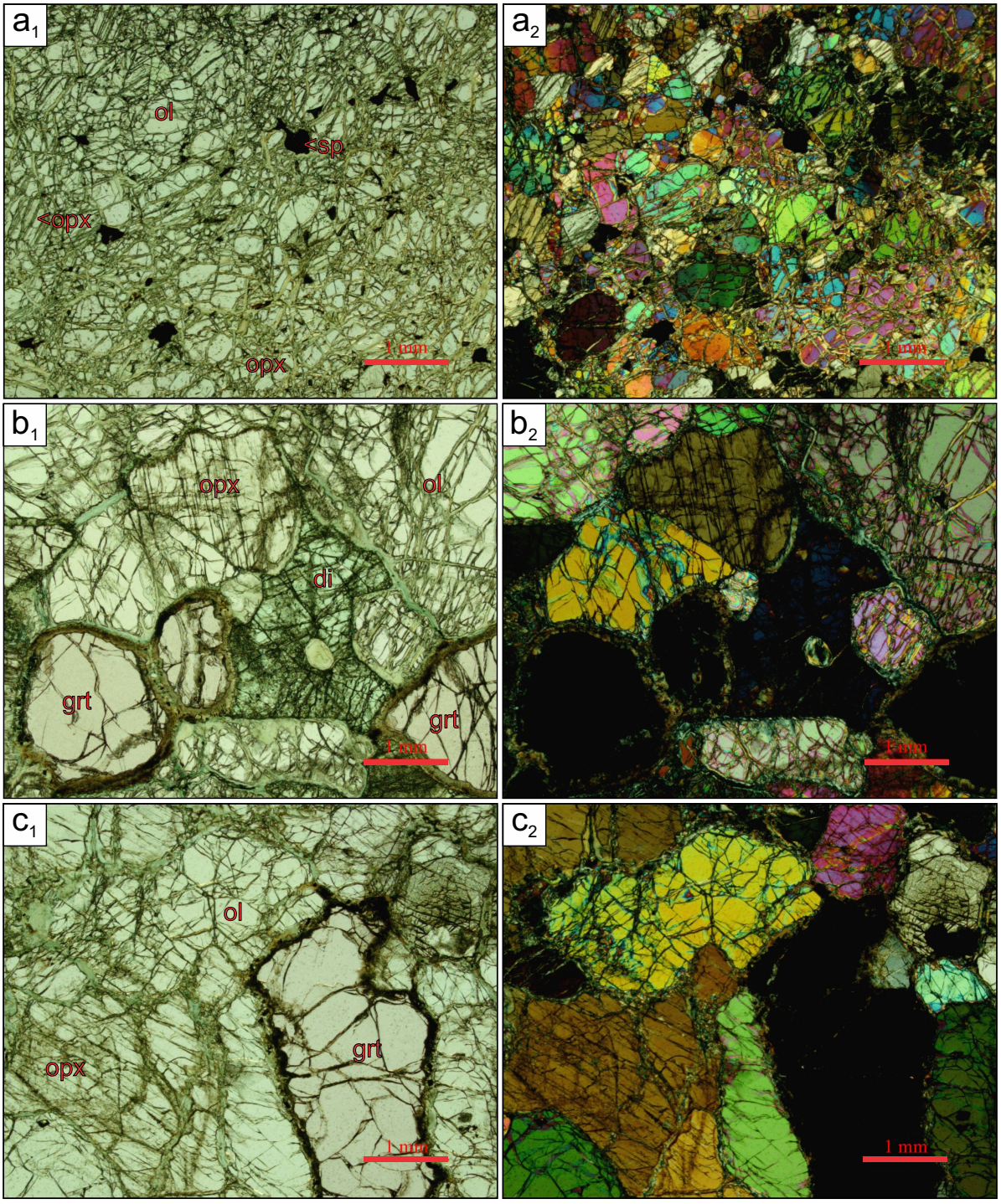

Figure 6.4 Petrographic microscope images of the porphyroclastic peridotites as seen in transmitted light. Mineral abbreviations: olivine (ol), orthopyroxene (opx), diopside (di), garnet (grt). Note that olivine neoblasts occur in all of them. Undulose extinction in both olivine and orthopyroxene can be seen in these pictures.

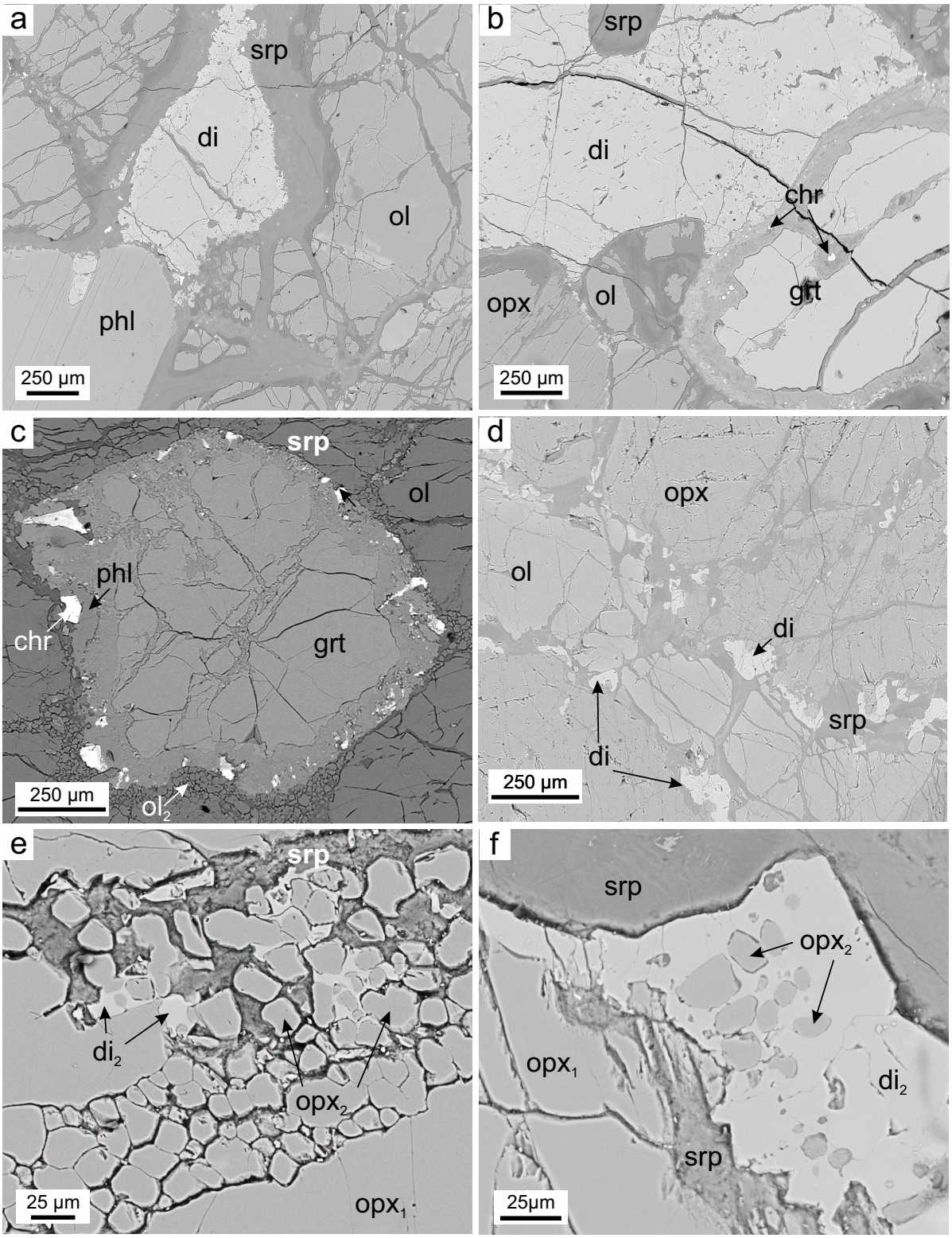

Figure 6.5 BSE images of coarse and porphyroclastic garnet peridotites. (a) Anhedral clinopyroxene occurs at the boundaries of the anhedral chromian diopside, interstitial to olivine grains. (b-c) Garnet in porphyroclastic garnet peridotites is highly altered, leading to the crystallization of chromite grain. (d-f) Interstitial clinopyroxene replaces previously formed orthopyroxene neoblasts.

6.2.2. Mineral composition

Olivine

Average olivine compositions for each xenolith are reported in table 6.2. The range of the Mg number in all samples is very narrow (Fo_{91-93}). However, Fo content of olivine is slightly different depending on the mineralogical assemblage of each xenolith and its microstructure, which is consistent with what it has been observed in other cratons (e.g. Kopylova et al., 1999). The most magnesian olivine occurs in spinel peridotite ($Fo_{92.5-93}$), followed by the coarse Grt-peridotite, which shows a wider range of values (Fo_{91-93}). Olivine from porphyroclastic Grt-peridotites has slightly lower magnesium contents (Fo_{91-92}). Olivine grains within each xenolith are always very homogeneous in composition. This homogeneity also applies to the porphyroclastic garnet peridotites, in which no significant differences were found between the coarse olivine grains and the surrounding neoblasts (table 6.2).

Trace element analysis also shows some differences between the lithologies. Olivine from Grt-porphyroclastic peridotites typically shows an enrichment in Ni, Ti and Cr, compared to the coarse garnet peridotite suite and to the Spl-peridotite. This results in a negative correlation between Ni, Ca, Cr and Mn with the Fo content, which has already been observed in other cratons (e.g. Arndt et al., 2010).

Orthopyroxene

Orthopyroxene appears in most of the xenoliths, in all cases being a high-Mg enstatite, with #Mg of 92-94 (table 6.3). There are no significant differences in the #Mg between orthopyroxenes from the different peridotite suites. The lowest #Mg is found in the Spl-peridotite (#Mg up to 92) and the highest #Mg in the porphyroclastic peridotite (#Mg=92-94), having the porphyroclastic Grt-peridotites intermediate values of #Mg (#Mg=92-93). Orthopyroxene in these peridotites shows no compositional zonation and displays a wide range of CaO (0.1-1.05wt%). There are positive correlations between Ca and Cr, Ti and Ni. The contents of these elements also vary as a function of the microstructure; the coarse grt-peridotites are those with lower Cr, Ni and Ca contents. Aluminum content in orthopyroxene of the Spl-peridotite is markedly higher (1.53-2.42 Al_2O_3 wt%) than that in Grt-peridotites. Additionally, Al is slightly higher in orthopyroxene of the porphyroclastic peridotites (0.62-0.78wt% Al_2O_3) relative to that of the coarse peridotites (0.4-0.68 wt% Al_2O_3). Its composition

Label	11	34	31	37	30	40	32B	32B
Rock type	spl-Hz	grt-Whr	grt-Lhz	grt-Whr	grt-Lhz	grt-Hz	grt-Hz	grt-Hz
Microst.	coarse	coarse	coarse	coarse	coarse	coarse	porphy.	porphy.
Grain size	coarse	coarse	coarse	coarse	coarse	coarse	coarse	fine
N	*9*	*7*	*10*	*8*	*20*	*10*	*9*	*6*
SiO_2	40.60	41.06	40.79	40.79	40.64	40.45	39.90	40.63
TiO_2	0.01	0.02	0.02	0.03	0.04	0.03	0.02	0.04
Al_2O_3	0.00	0.00	0.00	0.00	0.01	0.01	0.01	0.02
Cr_2O_3	0.02	0.04	0.03	0.03	0.03	0.04	0.08	0.10
FeO	7.40	7.42	8.80	8.03	7.95	8.91	8.72	8.52
MnO	0.12	0.09	0.09	0.10	0.08	0.12	0.12	0.15
MgO	51.58	51.54	50.54	51.71	51.88	50.92	50.95	50.65
CaO	0.00	0.01	0.01	0.01	0.01	0.02	0.05	0.07
NiO	0.40	0.43	0.39	0.39	0.39	0.41	0.43	0.39
Sum Ox%	100.13	100.61	100.66	101.11	101.03	100.90	100.30	100.55
Fa	0.074	0.075	0.089	0.080	0.079	0.089	0.088	0.086
Fo	0.926	0.925	0.911	0.920	0.921	0.911	0.912	0.914
LA-ICP-MS (ppm)								
N	*5*	*4*	*5*	*4*	*7*	*4*	*2*	*6*
Sc	4.4	3.1	3.3	3.2	3.0	3.6	3.8	4.4
Ti	21	34	29	78	136	93	121	132
V	39.3	2.6	2.2	3.2	4.1	7.1	11.8	13.0
Cr	257	62.1	60.0	124.3	73.2	198.6	447	539
Co	111.6	129.5	149.9	142.0	122.9	167.3	147.7	153.1
Ni	2130	2960	3060	3140	2540	3450	3670	3110

Label	10	10	28	28	24A	12	12
Rock type	grt-Lhz	grt-Lhz	grt-Hz	grt-Hz	grt-Hz	grt-Hz	grt-Hz
Microst.	porphy.	porphy.	porphy.	porphy.	porphy.	porphy.	porphy.
Grain size	coarse	fine	coarse	fine	coarse	coarse	fine
N	*13*	*9*	*12*	*8*	*11*	*6*	*1*
SiO_2	40.72	40.82	40.47	40.51	39.88	39.93	40.63
TiO_2	0.04	0.03	0.04	0.03	0.01	0.03	0.00
Al_2O_3	0.01	0.01	0.01	0.01	0.01	0.02	0.00
Cr_2O_3	0.05	0.04	0.07	0.09	0.08	0.07	0.09
FeO	8.69	8.75	8.83	8.76	8.43	8.41	8.01
MnO	0.10	0.12	0.11	0.09	0.11	0.13	0.12
MgO	49.89	50.03	50.29	50.00	51.01	50.80	49.35
CaO	0.05	0.05	0.05	0.06	0.06	0.05	0.06
NiO	0.41	0.42	0.42	0.43	0.42	0.39	0.36
Sum Ox%	99.95	100.27	100.29	99.98	100.01	99.84	98.62
Fa	0.089	0.089	0.090	0.090	0.085	0.085	0.083
Fo	0.911	0.911	0.910	0.911	0.915	0.915	0.917
LA-ICP-MS (ppm)							
N	*4*	*3*	*4*	*6*	*9*	*4*	*5*
Sc	4.2	3.8	4.0	3.9	4.6	7.1	7.0
Ti	185	163	154	137	43	197	140
V	12.3	11.3	11.8	10.7	9.2	12.0	9.8
Cr	316	296	618	482	369	657	453
Co	180.6	163.2	180.4	164.0	138.8	182.4	152.5
Ni	3630	3240	8020	2690	3040	3600	3160

Table 6.2 Average major- and trace-element compositions of olivine. Oxides in wt% and trace-element in ppm. Abbreviations: spinel (spl), garnet (grt), harzburgite (Hz), wehrlite (Whr), lherzolite (Lhz); porphyroclastic (porphy.). Number of analysis (N)

is nearly identical to that of the orthopyroxenes from both Spl-peridotites and Grt-peridotites from the Kaapvaal craton (Gregoire et al., 2005 and references therein).

Label	**11**	**34**	**31**	**30a**	**40A**	**40B**	**32B**	**10**	**28**	**24a**	**12**
Rock type	spl-Hz	grt-Whr	grt-Hz	grt-Lhz	grt-Hz	grt-Hz	grt-Hz	grt-Lhz	grt-Hz	grt-Hz	grt-Hz
Microstr.	coarse	coarse	coarse	coarse	coarse	coarse	coarse	porphy.	porphy.	porphy.	porphy.
N	*5*	*4*	*8*	*10*	*5*	*10*	*9*	*13*	*15*	*8*	*6*
SiO_2	56.28	57.95	57.82	58.00	57.58	57.85	56.74	57.65	57.37	57.29	56.09
TiO_2	0.01	0.06	0.02	0.07	0.08	0.07	0.16	0.18	0.17	0.06	0.14
Al_2O_3	2.14	0.54	0.43	0.46	0.64	0.63	0.69	0.68	0.70	0.59	0.69
Cr_2O_3	0.37	0.35	0.25	0.26	0.25	0.23	0.48	0.30	0.45	0.42	0.44
FeO	5.35	4.70	5.47	4.79	5.16	5.33	5.19	5.19	5.24	5.08	5.06
MnO	0.15	0.13	0.10	0.09	0.11	0.12	0.14	0.14	0.11	0.14	0.12
MgO	35.41	36.42	36.15	36.73	35.23	35.70	35.17	34.82	34.85	35.51	35.48
CaO	0.35	0.25	0.22	0.29	0.56	0.56	0.99	0.84	0.99	0.99	0.95
Na_2O	0.04	0.08	0.07	0.07	0.25	0.27	0.24	0.22	0.25	0.15	0.27
K_2O	0.01	0.00	0.00	0.00	0.00	0.00	0.01	0.00	0.00	0.00	0.01
Sum Ox%	100.11	100.46	100.54	100.77	99.86	100.74	99.80	100.01	100.12	100.23	99.42
Wo(Ca)	0.65	0.46	0.40	0.52	1.05	1.02	1.82	1.57	1.84	1.81	1.74
En(Mg)	91.39	92.66	91.67	92.58	91.29	91.17	90.48	90.65	90.38	90.70	90.82
Fs(Fe^{2+})	7.96	6.88	7.93	6.90	7.66	7.81	7.70	7.77	7.78	7.48	7.44
XMg	0.92	0.93	0.92	0.93	0.92	0.92	0.92	0.92	0.92	0.93	0.93
LA-ICP-MS (ppm)											
N	*4*	*NA*	*3*	*3*	*NA*	*NA*	*3*	*3*	*2*	*NA*	*NA*
Sc	12.1		4.6	5.1			5.9	6.3	6.5		
Ti	29		111	340			645	928	894		
V	51.5		26.4	27.2			56.0	59.4	56.6		
Cr	2030		1485	847			2780	2160	4870		
Co	38.0		53.3	50.2			59.1	71.4	67.6		
Ni	374		643	721			927	1034	b.d.l.		
Ga	0.7		2.4	2.0			1.8	3.4	3.3		
Rb	b.d.l.		b.d.l.	b.d.l.			b.d.l.	0.47	b.d.l.		
Sr	7.00		0.0730	0.876			0.628	2.44	b.d.l.		
Y	b.d.l.		b.d.l.	0.07			0.08	0.12	0.27		
Zr	b.d.l.		b.d.l.	0.26			0.28	0.45	b.d.l.		
Nb	b.d.l.		0.06	0.16			b.d.l.	0.17	0.07		

Table 6.3 Average major- and trace-element compositions of orthopyroxene. Oxides in wt% and trace-element in ppm. Abbreviations: spinel (spl), garnet (grt), harzburgite (Hz), wehrlite (Whr), lherzolite (Lhz); porphyroclastic (porphy.). Number of analysis (N) . *NA* stands for "Not analysed" and *bdl* for below detection limit.

Clinopyroxene

Clinopyroxene in garnet peridotites is commonly Cr-rich diopside, with Cr_2O_3 contents up to 4.3 wt% Cr_2O_3 and Mg-numbers clustering between 89 and 94. Differences in composition in terms of Mg, Cr, Na and Al between clinopyroxene from coarse and porphyroclastic garnet peridotites can be significant (table 6.4). As shown in fig. 6.5, coarse garnet peridotite usually contains diopside with higher Cr, Na and Al contents than that found in porphyroclastic garnet

Label	**34**	**31**	**37**	**30**	**10**	**24B**	**28**	**28**	**12**
Rock type	grt-Whr	grt-Hz	grt-Whr	grt-Lhz	grt-Lhz	grt-Hz	grt-Hz	grt-Hz	grt-Hz
Texture	coarse	coarse	coarse	coarse	porphy.	porphy.	porphy.	porphy.	porphy.
Min. text.	anhedral	anhedral	anhedral	anhedral	anhedral	anhedral	anhedral	fine	anhedral
N	*4*	*11*	*3*	*24*	*15*	*8*	*9*	*4*	*6*
SiO_2	54.95	54.53	54.87	54.69	54.73	54.38	54.96	54.02	54.74
TiO_2	0.09	0.26	0.06	0.23	0.42	0.11	0.28	0.90	0.26
Al_2O_3	3.30	3.04	2.21	2.75	1.90	0.61	1.69	2.01	1.46
Cr_2O_3	3.02	3.95	1.79	1.87	1.27	1.95	1.64	1.28	1.23
FeO	1.82	2.49	1.85	2.30	3.23	2.68	3.34	3.81	3.69
MnO	0.04	0.08	0.05	0.07	0.12	0.04	0.12	0.17	0.12
MgO	14.59	14.54	16.27	15.86	18.29	16.17	19.02	18.30	23.78
CaO	18.69	17.26	21.00	19.26	17.79	22.32	17.18	18.49	12.33
Na_2O	3.32	3.90	2.18	2.77	1.79	1.69	1.73	1.21	1.34
K_2O	0.01	0.02	0.01	0.01	0.03	0.01	0.03	0.01	0.02
Sum Ox%	99.81	100.07	100.29	99.82	99.57	99.94	99.99	100.18	98.98
Wo(Ca)	46.21	43.68	46.54	44.59	38.79	47.55	37.06	39.38	26.57
En(Mg)	50.21	51.22	50.19	51.12	55.51	47.93	57.09	54.03	67.34
Fs(Fe^{2+})	3.58	5.10	3.28	4.29	5.70	4.52	5.84	6.59	6.10
XMg	0.93	0.91	0.94	0.93	0.91	0.92	0.91	0.90	0.92
LA-ICP-MS (ppm)									
N	*3*	*3*	*10*	*13*	*7*	*2*	*8*	*3*	*3*
Sc	35.0	21.0	38.3	32.9	22.7	16.5	20.6	46.2	26.1
Ti	403	284	1254	1730	1813	310	1881	4680	1576
V	610	334	276	398	330	192.7	290	192.5	329
Cr	20200	11500	23800	9780	10410	5700	10840	6840	8170
Co	15.0	16.6	17.6	20.9	33.6	31.4	37.5	22.5	34.8
Ni	283	288	272	293	540	560	639	233	612
Ga	7.0	6.4	4.4	7.6	7.3	1.7	6.1	4.5	4.3
Rb	0.14	bdl	0.23	1.49	0.50	0.02	0.66	0.68	0.11
Sr	470	216	205	319	150.1	116.2	143.8	113.8	128.7
Y	1.41	1.44	7.16	4.80	3.28	0.52	3.64	7.68	2.75
Zr	26.0	9.23	111.9	66.6	13.23	1.18	15.29	89.4	8.77
Nb	0.18	0.16	0.52	8.35	0.29	0.10	2.58	9.76	0.19
Ba	0.86	0.52	1.61	10.02	1.74	0.31	13.47	7.12	0.66
La	27.7	8.81	3.58	11.11	2.40	1.437	2.87	5.59	2.06
Ce	76.5	28.3	15.36	37.1	9.30	6.08	10.78	17.71	8.32
Pr	8.24	3.45	2.62	5.25	1.512	1.027	1.680	2.95	1.451
Nd	28.0	12.53	13.83	23.4	7.76	5.35	8.51	14.56	7.44
Sm	3.37	1.603	3.65	4.48	1.916	0.990	2.07	3.57	1.838
Eu	0.839	0.404	1.184	1.209	0.583	0.228	0.626	1.063	0.525
Gd	2.00	1.045	3.43	3.27	1.650	0.442	1.807	2.74	1.513
Tb	0.155	0.107	0.409	0.334	0.189	0.038	0.195	0.368	0.167
Dy	0.514	0.440	2.03	1.457	0.891	0.155	0.928	2.02	0.751
Ho	0.056	0.059	0.297	0.202	0.128	0.019	0.138	0.312	0.099
Er	0.109	0.107	0.620	0.415	0.280	0.042	0.296	0.682	0.208
Tm	0.008	0.009	0.060	0.038	0.029	0.003	0.032	0.082	0.017
Yb	0.037	0.045	0.287	0.190	0.142	0.018	0.177	0.480	0.100
Lu	0.002	0.004	0.033	0.021	0.015	0.001	0.023	0.066	0.009
Hf	0.611	0.294	5.74	2.84	0.764	0.065	0.707	3.93	0.507
Ta	0.018	0.014	0.048	0.320	0.020	0.003	0.077	0.664	0.009
Th	1.060	0.379	0.071	0.385	0.041	0.009	0.156	0.610	0.016
U	0.222	0.100	0.020	0.086	0.010	0.002	0.015	0.026	0.003

peridotites. Additionally, clinopyroxene from coarse Grt-peridotites usually has higher #Mg (#Mg=91-94) than that of porphyroclastic Grt-peridotites (#Mg=89-93) (see Appendix A6.2).

The REE distribution patterns of the clinopyroxene are slightly convex in shape, with smooth negative slopes, reflecting the enrichment in LREE with respect to the MREE and HREE (fig. 6.7 and fig. 6.8). As shown in these patterns, clinopyroxene of the coarse garnet peridotites is typically x10 more enriched in REE than that of the porphyroclastic suite. Additionally, the later usually shows a small hinge at Pr and Nd, which is also observed in one of the wehrlite xenoliths (MGR-37).

The boundaries of the anhedral clinopyroxene, showing spongy appearance, are compositionally identical to the core of the crystals, which indicates that they result from recrystallisation of the same grain. However, the diopside found between the olivine and orthopyroxene neoblasts (see fig. 6.5f) is more enriched in Ti, Ca and Al, with lower Mg and Cr contents (fig. 6.6). This generation of clinopyroxene has also significantly higher REE contents than the anhedral clinopyroxene in the same xenolith (fig 6.8).

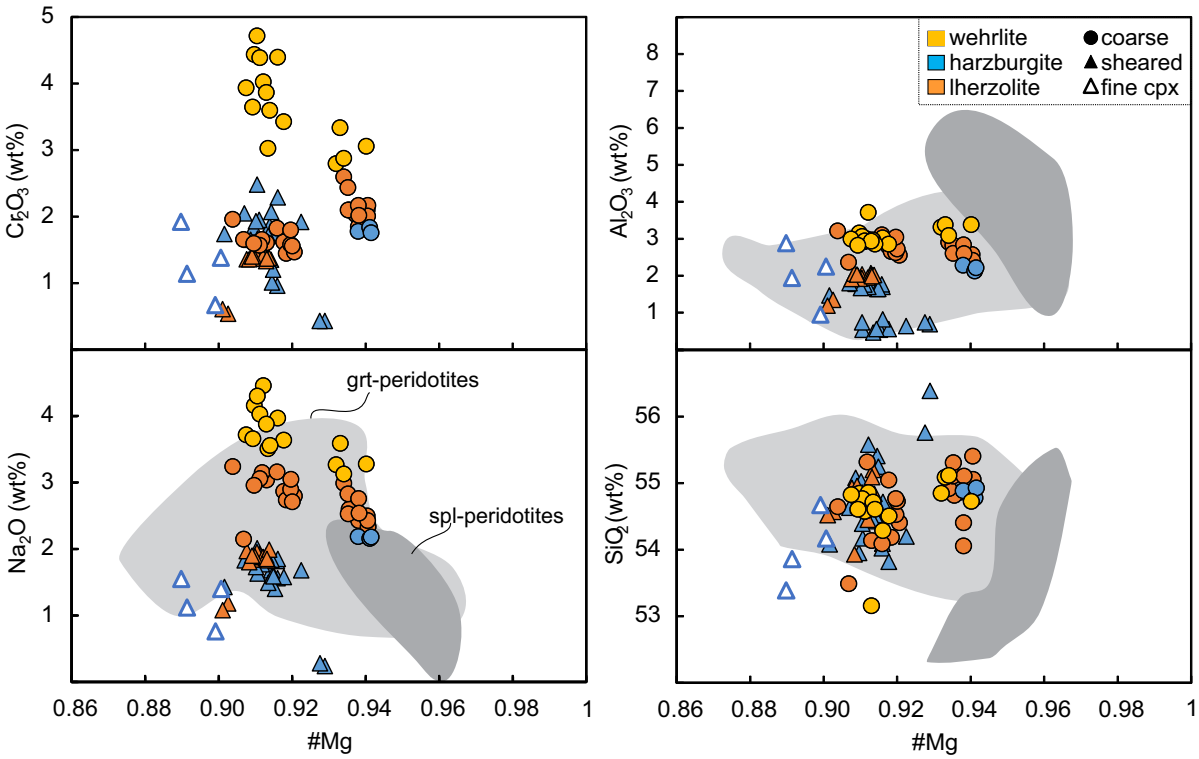

Figure 6.6 Bivariate diagrams of clinopyroxene in ultramafic rocks. Circles represent data for coarse garnet peridotites, whereas triangles are data from porphyroclastic garnet peridotites. Open triangles correspond to the fine grained clinopyroxene. Fields represent data from the Kaapvaal craton (data collected by Gregoire et al., 2005).

Table 6.4 (left page) Averaged major element (in wt% oxide) composition and trace element (in ppm) composition of clinopyroxene in the peridotite xenoliths. The number of analyses averaged is indicated by N.

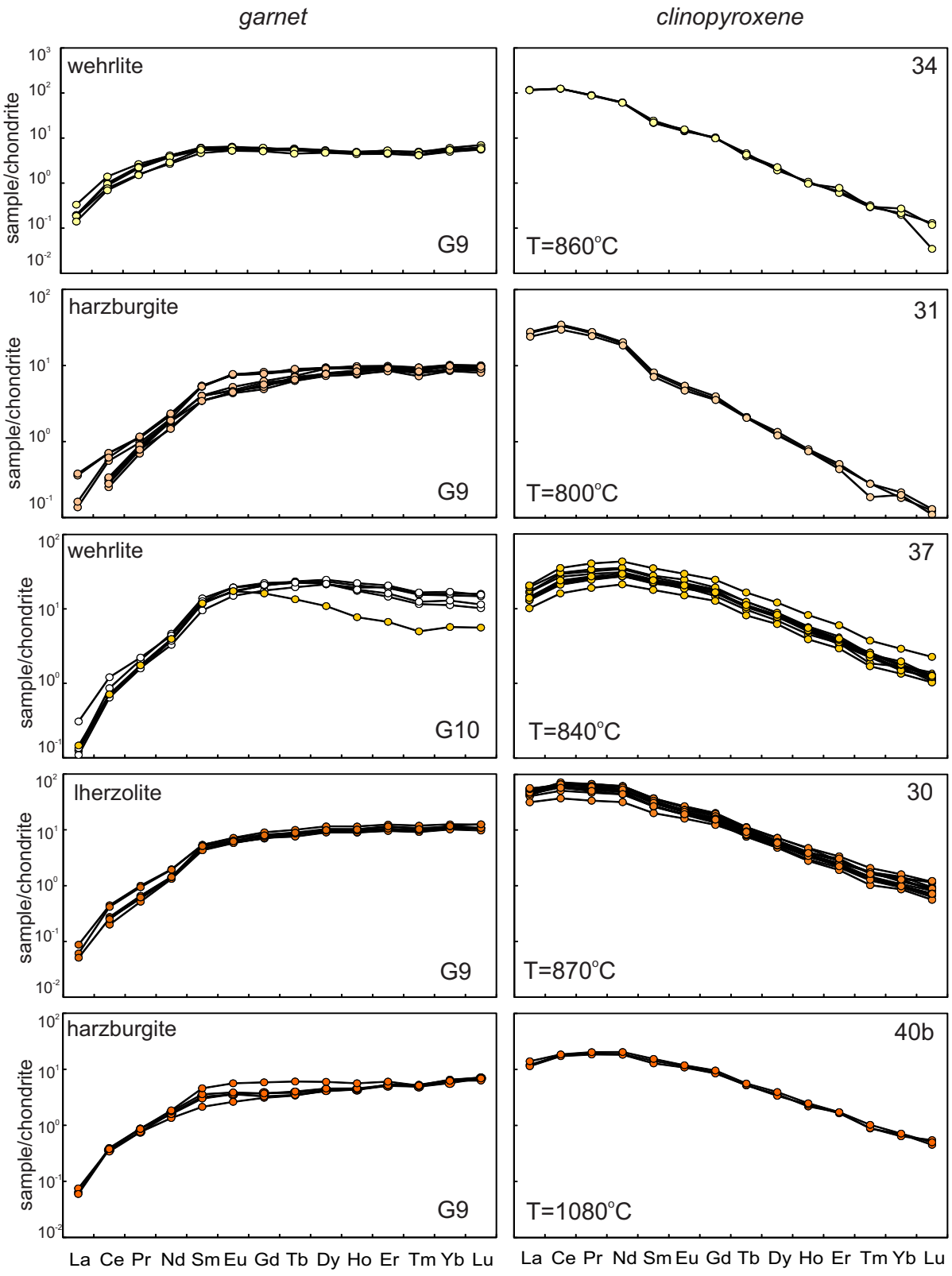

Figure 6.7 REE patterns of garnet and clinopyroxene of the coarse garnet peridotites. Note that in sample 37, the cores of the garnet grains show positive patterns, whereas one analysis on the rim has a sinusoidal REE_N pattern. Garnet types are also included, following the classification by Grütter et al. (2004): lherzolitic garnet (G9) and harzburgitic garnet (G10). Temperatures were obtained from two-mineral thermobarometry (see chapter 7).

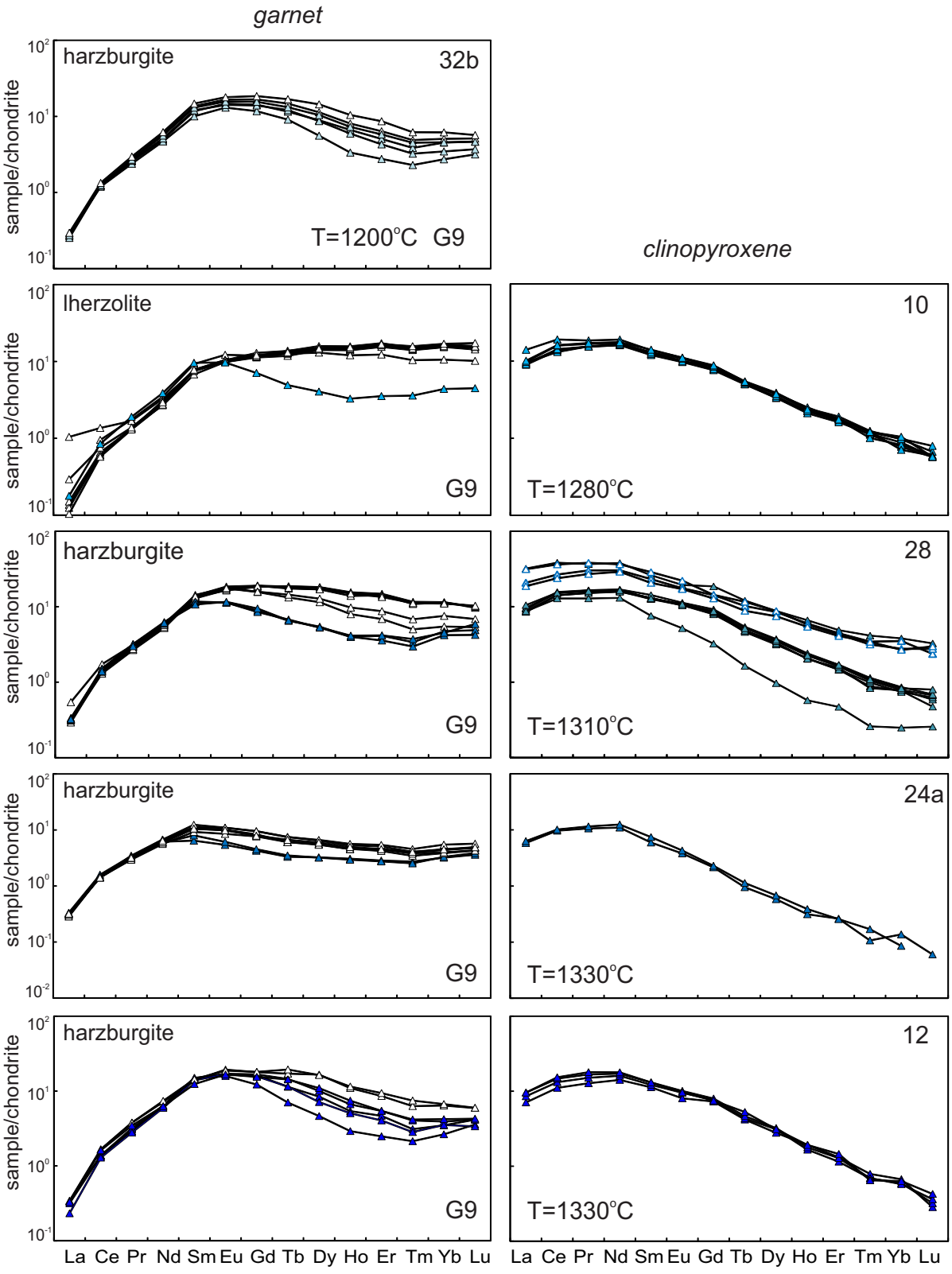

Figure 6.8 REE patterns of garnet and clinopyroxene in the porphyroclastic garnet peridotites. Open symbols represent analyses on the rims of the garnet grains. Garnet types are also included, following the classification by Grutter et al. (2004) (G9= lherzolitic garnet). Temperatures were obtained from two-mineral thermobarometry (see chapter 7). Note the compositional differences of the two generations of clinopyroxene found in sample 28, being the first generation represented by filled triangles and the second one, by open triangles.

Garnet

In terms of major elements, garnet of the Cat115 xenolith suite is homogeneous in composition, without any evidence of zoning or core-rim variations. Those of peridotitic origin are predominantly chromian pyropes and display a wide range of Cr (3.00-8.88 wt% Cr_2O_3) and a narrower Ca (4.15-6.5 wt% CaO) contents (fig.6.9). Based on the relationship between Ca and Cr (Grütter et al., 2004), most of them can be classified as G9 -or lherzolitic- garnets, with only minor examples of G4 garnets also present. Even though Cat115 has a diamond -rich layer, only two xenoliths contain garnets that plot in the harzburgitic "G10" garnet field, and none of them is represented above the "graphite-diamond constrain" of Grütter and Sweeney (2000). These two G10 garnets where found in the two xenoliths that were petrographically defined as wehrlites. The averaged compositions are included in table 6.5.

Garnet from coarse peridotites is compositionally different from garnet found in porphyroclastic peridotites, which generally shows higher Cr content. Additionally, garnet in coarse peridotites is slightly enriched in Al and Fe compared to the porphyroclastic ones (~19.54wt% Al_2O_3 and ~6.79 wt% FeO *vs* ~16.49 wt% Al_2O_3 and ~5.58 wt% FeO). More significant differences between these two textural types have been observed in terms of Ti, Ni and Zr (670-1970ppm Ti, 16-69 ppm Ni and 9-116 ppm Zr in coarse garnet-peridotites; 1840-9420ppm Ti, 80-145 ppm Ni and 18- 116 ppm Zr in porphyroclastic garnet-peridotites).

All the analysed garnets from peridotites are characterised by depletion in LREE and enrichment in HREE with respect to the chondritic values. Nevertheless, it is possible to identify different REE patterns, directly related to the type of xenolith and its microstructure.

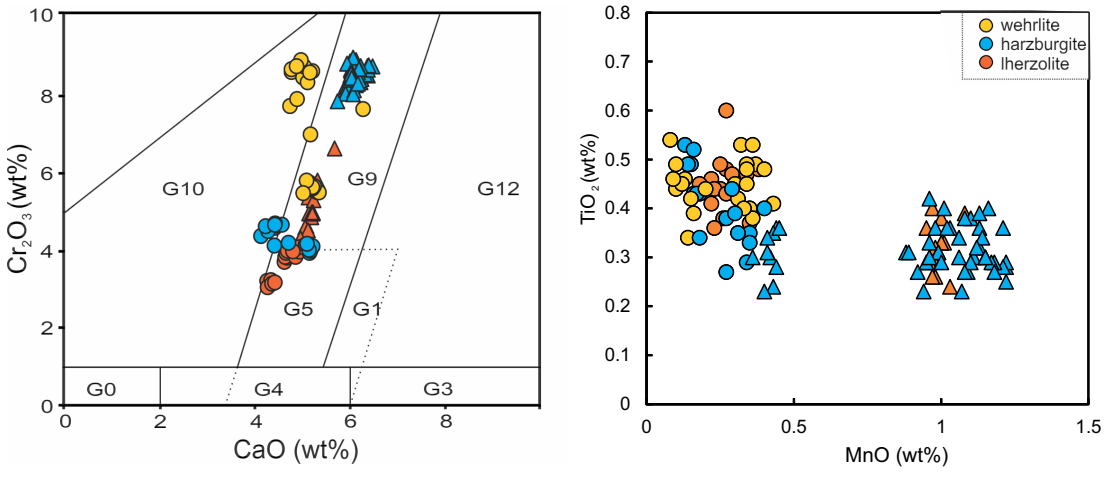

Figure 6.9 (a) Classification of garnet based on the Cr_2O_3-CaO content proposed by Grutter et al. (2009). (b) TiO_2-MnO diagram. With the exception of sample 24, garnet of the porphyroclastic garnet peridotites (triangles) is enriched in TiO_2, whereas Mn content is usually higher in coarse garnet peridotites (circles).

Garnets from coarse garnet peridotites are characterised by a smooth positive slope in the LREE and MRRE, with a relatively flat pattern from Eu to the highest HREE, showing a progressive enrichment in the HREE (fig. 6.7). MREE and HRRE are usually les than 10x the chondrite values (McDonough et al, 1995). The only exception to this pattern is defined by one of the wehrlites (MGR-37), which not only is slightly more enriched in MREE and HREE compared to the other coarse garnet peridotites, but it also presents one analysis which shows a sinusoidal pattern. This analysis corresponds to the rim of the grain, showing disequilibrium between the core and the rim.

Garnets of porphyroclastic peridotites typically show a slight depletion in the HREE, with the hinge at Eu_N~16 (fig. 6.8). This gives the pattern a sinusoidal shape , which was also found in harzburgitic garnets from the Congo Craton (Batumike et al., 2009). Additionally, these REE patterns show that no chemical equilibrium was achieved in terms of trace elements, since different degrees of enrichment in HREE are found among the grains in the same xenolith. As shown in these REE_N patterns, the different degrees of enrichment can be correlated with the area of the garnet that was analysed; the cores are significantly more depleted in HREE than the rims of the grains. These compositional differences are very clear in the porphyroclastic garnet lherzolite (sample 10), where the core presents a characteristic sinusoidal pattern and the rim a flat pattern for MREE and HREE.

Label	**34**	**31**	**37**	**30**	**40B**	**32**	**10**	**28**	**24a**	**12**
Rock	grt-Whr	grt-Hz	grt-Whr	grt-Lhz	grt-Hz	grt-Hz	grt-Lhz	grt-Hz	grt-Hz	grt-Hz
Microstr.	coarse	coarse	coarse	coarse	coarse	porph.	porph.	porph.	porph.	porph.
N	*10*	*7*	*13*	*15*	*10*	*12*	*12*	*21*	*10*	*9*
SiO_2	41.53	41.31	40.57	41.50	41.35	40.70	41.39	40.76	40.39	40.80
TiO_2	0.13	0.16	0.35	0.27	0.33	0.91	0.99	1.08	0.42	1.14
Al_2O_3	19.49	20.40	17.14	20.83	19.87	16.48	18.45	15.63	16.20	15.70
Cr_2O_3	5.53	4.00	8.21	3.59	4.53	7.64	5.06	8.33	8.51	8.40
$Fe_2O_{3(c)}$	0.34	1.32	2.24	1.67	2.14	2.19	0.82	1.49	3.27	1.32
FeO	7.67	8.08	5.71	6.61	5.86	5.29	6.68	5.94	4.18	5.84
MnO	0.44	0.47	0.45	0.45	0.37	0.34	0.32	0.30	0.31	0.33
MgO	19.61	19.28	20.27	20.66	21.25	20.39	20.58	20.00	20.22	19.99
CaO	5.23	5.16	5.10	4.63	4.39	5.87	5.23	6.09	6.36	6.06
Sum Ox%	99.97	100.18	100.04	100.20	100.08	99.80	99.52	99.61	99.84	99.57
Pyrope	70.23	69.38	74.01	73.91	76.19	73.47	72.82	71.75	74.06	71.90
Almandin	15.41	16.31	11.67	13.28	11.76	10.65	13.25	11.93	8.57	11.77
splessartine	0.90	0.97	0.94	0.91	0.75	0.68	0.65	0.61	0.64	0.67
Andradite	0.93	3.53	6.00	4.38	5.67	5.95	2.28	4.17	8.82	3.60
Uvarovite	15.84	11.30	23.24	10.04	12.67	22.31	14.87	24.72	24.15	24.99
Grossulaire	0.00	0.04	0.00	0.21	0.00	0.00	0.00	0.00	0.00	0.00
X_{Mg}	0.82	0.81	0.86	0.85	0.87	0.87	0.85	0.86	0.90	0.86

Table 6.5 Averaged major element (in wt% oxide) composition of garnet in the peridotite xenoliths, as well as their endmembers. The number of analyses averaged is indicated by N.

Label	34	31	37	30	40B	32	10	28	24a	12
Rock	Grt-Whr	Grt-Hz	Grt-Whr	Grt-Lhz	Grt-Hz	Grt-Hz	Grt-Lhz	Grt-Hz	Grt-Hz	Grt-Hz
Microstr.	coarse	coarse	coarse	coarse	coarse	porph.	porph.	porph.	porph.	porph.
N	*6*	*6*	*6*	*7*	*5*	*8*	*6*	*9*	*8*	*7*
Sc	100.1	91.5	118.9	75.1	117.3	125.6	117.2	133.8	162.4	169.4
Ti	728	772	1788	1690	1420	4530	5770	6850	2360	7180
V	220	206	137.6	239	334	409	378	501	482	526
Cr	28700	25200	56400	18920	30700	36400	37200	73400	53800	65100
Co	33.5	42.1	41.2	39.5	47.6	43.3	49.1	51.7	44.1	53.7
Ni	18	20	30	33	66	96	100	299	100	130
Ga	4.2	7.4	5.0	10.6	9.8	7.2	13.5	12.6	6.0	8.3
Rb	b.d.l.	b.d.l.	0.04	b.d.l.	b.d.l.	0.05	0.85	0.66	0.05	b.d.l.
Sr	0.25	0.12	0.81	0.17	0.29	0.75	1.24	1.04	0.76	0.99
Y	7.10	12.55	26.7	15.01	7.03	9.55	18.31	15.74	6.65	11.66
Zr	9.31	10.48	102.1	35.4	18.02	66.8	75.4	95.3	39.0	101.8
Nb	0.11	0.08	0.24	0.07	0.26	0.36	0.28	0.51	0.54	0.45
Ba	0.01	b.d.l.	0.05	0.01	b.d.l.	0.02	0.46	0.19	0.03	0.01
La	0.046	0.011	0.038	0.013	0.015	0.057	0.043	0.081	0.074	0.075
Ce	0.577	0.184	0.495	0.185	0.227	0.665	0.445	0.892	0.892	0.903
Pr	0.190	0.075	0.169	0.066	0.077	0.213	0.140	0.276	0.299	0.305
Nd	1.609	0.797	1.814	0.711	0.750	2.11	1.407	2.64	2.84	2.98
Sm	0.818	0.549	1.778	0.729	0.490	1.553	1.198	1.898	1.464	2.09
Eu	0.323	0.261	0.990	0.358	0.217	0.711	0.583	0.867	0.506	0.974
Gd	1.115	1.109	3.92	1.541	0.785	2.43	2.18	2.95	1.486	3.19
Tb	0.191	0.241	0.748	0.312	0.150	0.376	0.415	0.480	0.211	0.490
Dy	1.219	1.950	5.07	2.44	1.133	2.01	3.09	3.02	1.296	2.60
Ho	0.255	0.454	0.960	0.542	0.254	0.332	0.679	0.541	0.244	0.389
Er	0.785	1.422	2.58	1.730	0.858	0.825	2.15	1.495	0.679	0.914
Tm	0.111	0.202	0.317	0.251	0.126	0.106	0.302	0.183	0.090	0.106
Yb	0.883	1.460	2.09	1.803	1.002	0.766	2.14	1.277	0.669	0.710
Lu	0.147	0.218	0.301	0.273	0.169	0.123	0.323	0.184	0.112	0.110
Hf	0.184	0.186	1.182	0.582	0.353	1.368	1.698	1.969	0.835	1.950
Ta	0.002	0.002	0.019	0.001	0.023	0.030	0.021	0.040	0.053	0.034
Th	0.028	0.005	0.006	0.006	0.001	0.010	0.008	0.017	0.020	0.013
U	0.109	0.030	0.027	0.039	0.009	0.026	0.017	0.040	0.045	0.029

Table 6.5 (continued) Averaged trace element (in ppm) composition of garnet in the peridotite xenoliths. The number of analyses averaged is indicated by N and values below detection limit, by "bdl".

Spinel

The anhedral spinel found in the spinel-bearing harzburgite is characterised by low Cr (#Cr=0.30) and high Mg contents (#Mg=0.68). As described in the petrography section, spinel also occurs in the reaction rims on some garnet grains, accompanied by the formation of phlogopite, as well as inside of these grains, also related to alteration of garnet. The newly-formed grains are usually euhedral to subhedral. Spinel in Grt-peridotites displays a very wide range in Mg (7.13-20.13%MgO) and Cr (14.03-56.91 wt% Cr_2O_3) contents. This wide compositional range reflects the zoning observed in most of the analysed spinels, with the sole exception of those in the Spl-harzburgite (table 6.6). This zoning is defined by an increase in

Label	**11**	**34**	**34**	**37**	**37**	**40b**	**40b**	**32b**	**32b**	**28**	**10**	**10**	**12**
Rock type	spl-Hz	grt-Whr	grt-Whr	grt-Whr	grt-Whr	grt-Hz	grt-Hz	grt-Hz	grt-Hz	grt-Hz	grt-Lhz	grt-Lhz	grt-Hz
Area	core	core	rim	core	rim	core	rim	core	rim	core	core	rim	core
N	*7*	*3*	*4*	*4*	*4*	*2*	*1*	*3*	*1*	*2*	*2*	*3*	*3*
SiO_2	0.03	0.10	0.14	0.63	0.30	0.40	0.85	0.17	0.12	0.39	0.16	0.14	0.63
TiO_2	0.01	1.39	0.80	1.87	0.68	1.67	0.48	1.06	0.62	1.69	1.79	1.20	1.47
Al_2O_3	41.03	15.03	44.78	11.98	35.56	33.60	48.49	33.78	40.11	37.12	31.50	41.12	29.87
Cr_2O_3	25.42	47.18	18.31	51.00	22.74	27.19	14.24	30.58	25.60	25.59	30.35	22.50	32.89
$Fe_2O_{3(c)}$	3.34	6.27	5.87	5.18	8.17	6.28	5.36	4.77	3.62	4.33	5.52	4.83	6.16
FeO	13.47	17.25	11.35	14.81	7.50	13.99	10.04	11.05	10.72	12.58	13.21	11.31	10.46
V_2O_3	0.10	0.19	0.11	0.11	0.07	0.19	0.06	0.19	0.09	0.13	0.21	0.18	0.15
MnO	0.20	0.43	0.27	0.29	0.25	0.30	0.32	0.30	0.27	0.31	0.33	0.21	0.36
MgO	15.99	11.62	18.49	13.71	20.00	16.30	20.13	17.61	18.11	17.53	16.33	18.37	18.33
ZnO	0.26	0.04	0.06	0.08	0.05	0.01	0.00	0.04	0.14	0.00	0.04	0.05	0.02
NiO	0.17	0.11	0.05	0.19	0.06	0.07	0.00	0.04	0.06	0.07	0.06	0.04	0.08
Sum Ox%	100.02	99.61	100.22	99.82	95.39	99.99	99.99	99.60	99.47	99.71	99.47	99.94	100.41
XCr	29.37	67.78	21.61	75.03	30.20	36.25	16.46	37.94	29.98	31.63	39.68	26.86	42.57
XFe^{2+}	32.09	45.42	25.68	38.21	17.09	32.72	21.87	26.10	24.92	28.70	31.32	25.66	24.50
YFe^{3+}	3.54	7.89	6.16	6.71	10.10	7.24	5.57	5.30	3.88	4.84	6.38	5.20	6.90
#Mg	0.68	0.55	0.74	0.62	0.83	0.67	0.78	0.74	0.75	0.71	0.69	0.74	0.75
#Cr	0.29	0.68	0.22	0.75	0.30	0.36	0.16	0.38	0.30	0.32	0.40	0.27	0.43
LA-IPC-MS (ppm)													
N	*8*	*1*	*NA*	*4*	*NA*	*NA*	*NA*	*3*	*NA*	*2*	*4*	*NA*	*3*
Ca	845	1404		1474				34900		1224	35000		2900
Sc	0.3	13.3		7.6				57.4		4.7	46.7		16.6
Ti	31.3	3110		8660				3120		5370	6070		12310
V	374	379		586				481		443	455		469
Mn	646	1477		1665				1493		1248	1720		2330
Co	305	87.3		132.6				64.5		61.7	66.7		89.4
Ni	564	145		680				172		140	185		536
Zn	1142	87.9		443				77.3		31.0	89.4		161.9
Ga	14.5	20.1		39.0				13.8		18.4	23.6		32.6
Y	0.02	3.13		1.17				8.83		0.40	8.62		2.71
Zr	0.27	19.80		17.24				37.2		2.42	60.4		40.5
Nb	0.05	2.51		4.79				0.86		0.36	6.61		35.0
Sn	0.938	0.760		1.600				1.095		0.830	1.243		1.140
Hf	0.018	0.327		0.453				1.752		0.113	1.513		0.615
Ta	bdl	0.052		0.560				0.448		0.066	0.389		0.683
U	0.034	0.138		0.099				0.050		0.027	0.150		0.896

Table 6.6 Averaged major element (in wt% oxide) and trace element (in ppm) composition of chromite in the peridotite xenoliths. The number of analyses averaged are represented by N and values below detection limit, by "bdl". NA stands for "Not Analysed"

#Mg coupled with a decrease in #Cr (fig. 6.10). As shown in this graph, usually chromite from coarse peridotites is both enriched in Cr and Mg (magnesiochromite) with regards to that found in porphyroclastic garnet peridotites (spinel). Ti content can be up to 2.5 wt % TiO_2, whereas Si and Mn are usually low (< 0.20 wt% SiO_2 and < 0.30 wt % MnO). Zn appears in low concentration in the analysed chromite (<200 ppm), having the chromite from Spl-lherzolite the highest contents (950-1220 ppm Zn). Higher Zn content is directly correlated to lower temperature (Griffin et al., 1994), which is consistent with the equilibration of spinel at lower temperatures in the Spl-harzburgite than the chromite found in garnet-bearing peridotite.

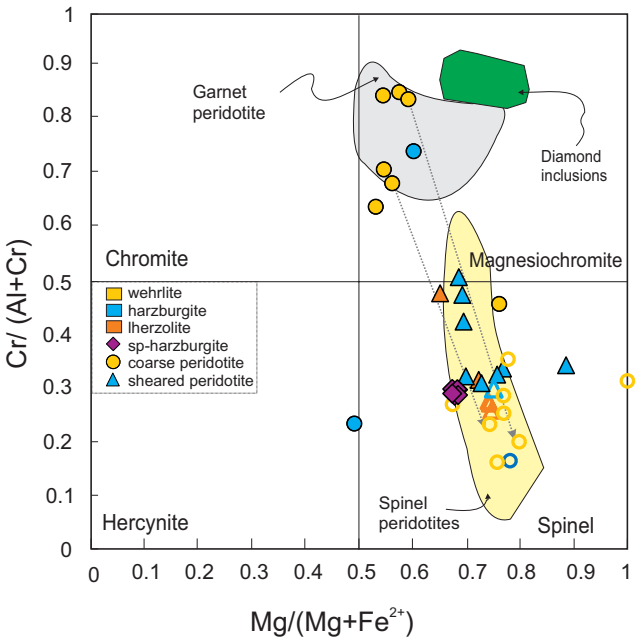

Figure 6.10 #Cr [Cr/(Al+Cr)] vs #Mg [Mg/(Mg+Fe^{2+})]. Open symbols represent the boundaries of the chromite grains, showing an enrichment in #Mg and a decrease of the #Cr rimwards. The arrows connect core and and rim of some grains.

Phlogopite

Phlogopite found as large tabular crystals in the xenoliths is highly magnesian and displays a wide range of Al contents (7.3-15.0 wt% Al_2O_3). This compositional range reflects the occurrence of three different generations of phlogopite within each peridotite xenolith (fig. 6.3). Apart from differing in their aluminium content, other significant compositional differences are found in terms of Ti, Na, Mg and Fe contents (fig. 6.11). The first generation of phlogopite is typically defined by lower Ti, Al and Fe (0.6-1.2 wt% TiO_2; 12.0-12.8 wt% Al_2O_3 and 2.7-3.6 wt% FeO) than the second generation of phlogopite (2.5-4.1 wt% TiO_2; 13.7-15.3 wt% $Al_2O_3$and 3.3-4.5 wt% FeO). These two generations of phlogopite can be also distinguished in terms of trace elements; phlogopite 2 is more enriched in Cr (<2090 ppm Cr *vs* 2000-12970 ppm Cr), Nb (<7.7 ppm vs 7.5-26 ppm Nb) and Mn (124-251 ppm vs 124-338 ppm), but poorer in Ba (873-1009ppm vs 635-928 ppm) and Cs (5.5-8.9 ppm vs 2.9-6.6 ppm). Phlogopite 1 compositions are similar to those observed in other phlogopite grains in mantle xenoliths (e.g. Grégoire et al., 2003). The third generation of phlogopite, which forms thin rims on the previously crystallised grains, could not be analysed for trace elements because of its small size. However, it is depleted in Al (7.9-9.7 wt% Al_2O_3), but has higher Fe (>6 wt% FeO), Ti (~4.3 wt% TiO_2), Na (0.38-0.54 wt% Na_2O) and Ba (up to 0.6 wt% BaO) contents than the other phlogopite generations. As shown in table 6.7, phlogopite found in the reaction rims on garnet is compositionally similar to that found as tabular crystals, although it is usually richer in Ti.

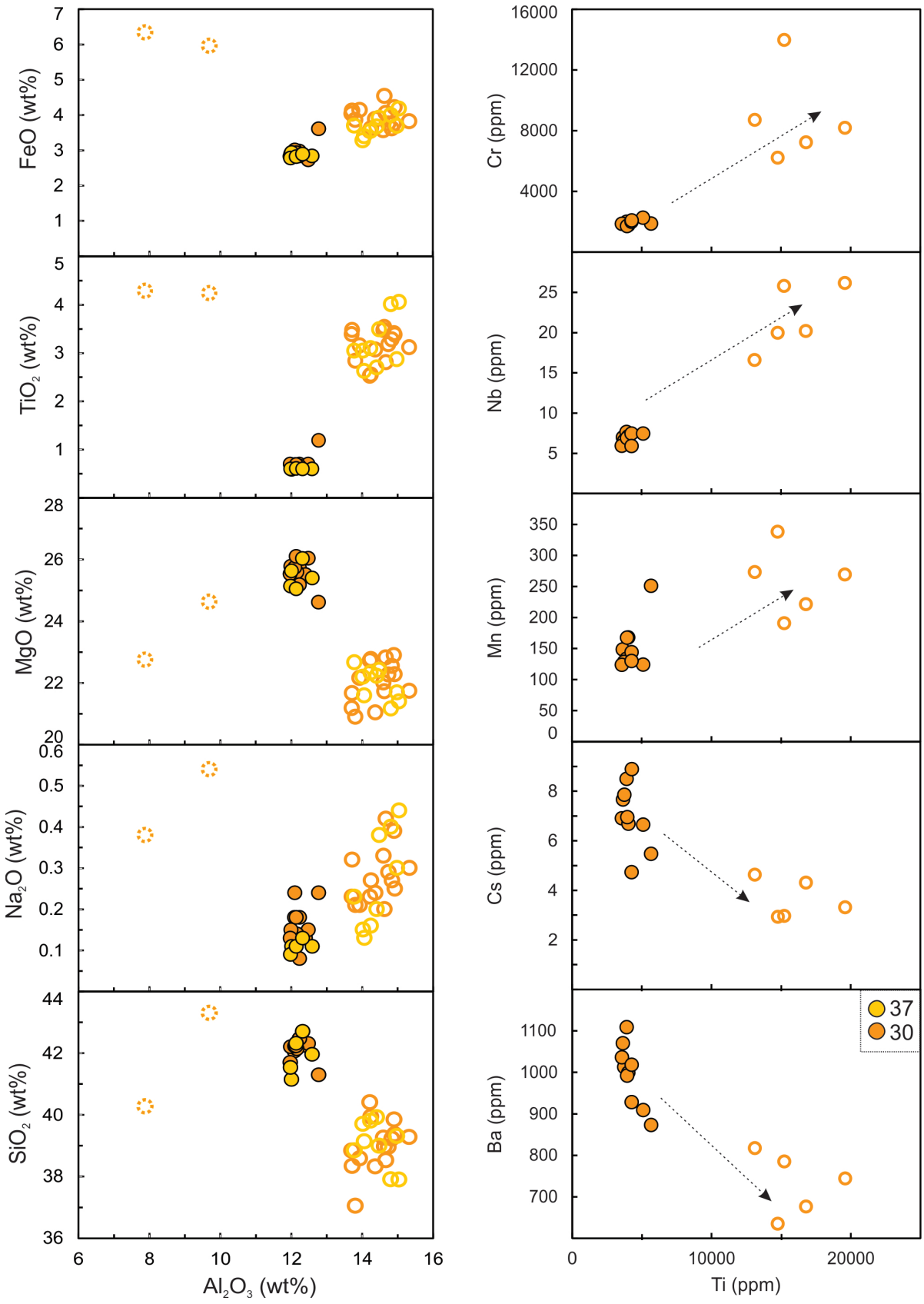

Figure 6.11 Binary diagrams of major- and trace-element compositions, showing the main compositional differences among the three generations of phlogopite found in the coarse garnet peridotites: phl_1 (circles), phl_2 (open circles) and phl_3 (open circles with dashed lines). Arrows indicate core to rim variations in samples 30 and 37.

Label	**30A**	**30A**	**30A**	**37**	**37**	**12**	**12**	**40b**	**40b**	**28**	**34**	**34**
Rock	grt-Hz	grt-Hz	grt-Hz	grt-Lhz	grt-Lhz	grt-Hz	grt-Hz	grt-Hz	grt-Hz	grt-Hz	grt-Whr	grt-Whr
Occurrence	tabular	tabular	tabular	tabular	tabular	garnet rim	garnet rim	garnet rim	garnet rim	garnet rim	garnet rim	garnet rim
zone	core	rim1	rim2	core	rim	core	rim	core	rim	core	core	rim
N	*11*	*15*	*2*	*5*	*9*	*5*	*1*	*9*	*3*	*3*	*5*	*5*
SiO_2	42.13	39.00	41.79	41.94	39.06	38.94	38.66	38.41	37.32	38.12	40.85	39.93
TiO_2	0.72	3.15	4.27	0.60	3.22	3.87	3.77	4.07	4.14	3.56	1.59	3.49
Al_2O_3	12.23	14.44	8.79	12.21	14.42	16.09	16.06	15.09	13.70	15.18	11.60	10.63
Cr_2O_3	0.34	1.56	0.10	0.90	2.64	1.93	2.28	1.98	1.40	2.74	0.08	0.06
FeO	2.95	3.90	6.15	2.85	3.71	4.16	4.18	5.23	5.63	4.40	6.40	7.89
MnO	0.02	0.04	0.06	0.02	0.01	0.04	0.05	0.04	0.02	0.03	0.02	0.05
MgO	25.59	22.05	23.69	25.45	21.97	21.70	22.22	20.86	20.72	21.16	23.95	21.33
CaO	0.01	0.04	0.04	0.03	0.02	0.01	0.02	0.02	0.25	0.01	0.01	0.01
Na_2O	0.16	0.28	0.46	0.11	0.27	0.90	0.95	0.43	0.46	0.49	0.18	0.24
K_2O	9.94	9.51	8.94	9.89	9.37	8.62	8.59	9.30	8.53	8.78	9.77	9.66
BaO	0.18	0.16	0.52	0.06	0.10	0.30	0.34	0.22	0.00	0.25	0.11	0.18
NiO	0.23	0.21	0.13	0.19	0.15	0.05	0.06	0.10	0.08	0.07	0.06	0.08
F	0.24	0.26	2.80	0.26	0.39	0.55	0.05	0.52	1.26	0.15	0.34	1.14
Cl	0.18	0.05	0.03	0.09	0.05	0.04	0.05	0.05	0.04	0.05	0.05	0.04
H_2O(c)	4.06	4.03	2.83	4.06	3.99	4.00	4.25	3.94	3.44	4.09	3.97	3.51
O=F	0.10	0.11	1.18	0.11	0.16	0.23	0.02	0.22	0.53	0.06	0.15	0.48
O=Cl	0.04	0.01	0.01	0.02	0.01	0.01	0.01	0.01	0.01	0.01	0.01	0.01
Sum Ox%	98.84	98.56	99.38	98.54	99.19	100.97	101.49	100.03	96.45	98.99	98.82	97.75
#Mg	93.92	90.95	87.25	94.10	91.34	90.30	90.40	87.66	86.80	89.57	86.98	82.80
Oct	5.95	5.81	6.33	5.97	5.81	5.78	5.83	5.78	5.91	5.81	6.12	6.12
Int	1.86	1.84	1.81	1.84	1.79	1.81	1.81	1.83	1.78	1.76	1.86	1.90
LA-ICP-MS (ppm)												
N	*10*	*5*	*NA*	*NA*	*NA*	*NA*	*NA*	*NA*	*NA*	*NA*	*4*	*NA*
Sc	2.5	5.2									1.9	
Ti	4090	12690									2120	
V	59.9	208									44.0	
Cr	1879	6940									88.6	
Mn	156.3	223									287	
Co	54.8	56.3									65.3	
Ni	1623	1381									206	
Ga	34.5	28.2									60.7	
Rb	482	495									773	
Sr	18.37	15.67									1.80	
Y	bdl	bdl									bdl	
Zr	0.24	7.93									7.17	
Nb	6.74	17.67									3.11	
Cs	7.37	4.22									4.22	
Ba	1014	785									226	

Table 6.7 Average major-element (in wt% oxide) and trace-element (in ppm) composition of phlogopite in the peridotite xenoliths. The number of analyses averaged is indicated by N and the values below detection limit, by "bdl". NA stands for not analysed

6.3. Eclogites and garnet pyroxenites

Three nearly bimineral eclogite xenoliths, two garnet-rich pyroxenites and one granulite have been recovered from drill cores of the Catoca kimberlite (fig.6.12). The presence of abundant eclogite xenoliths in this pipe and the nearby Cat115 has been previously reported by Nikitina et al. (2014).

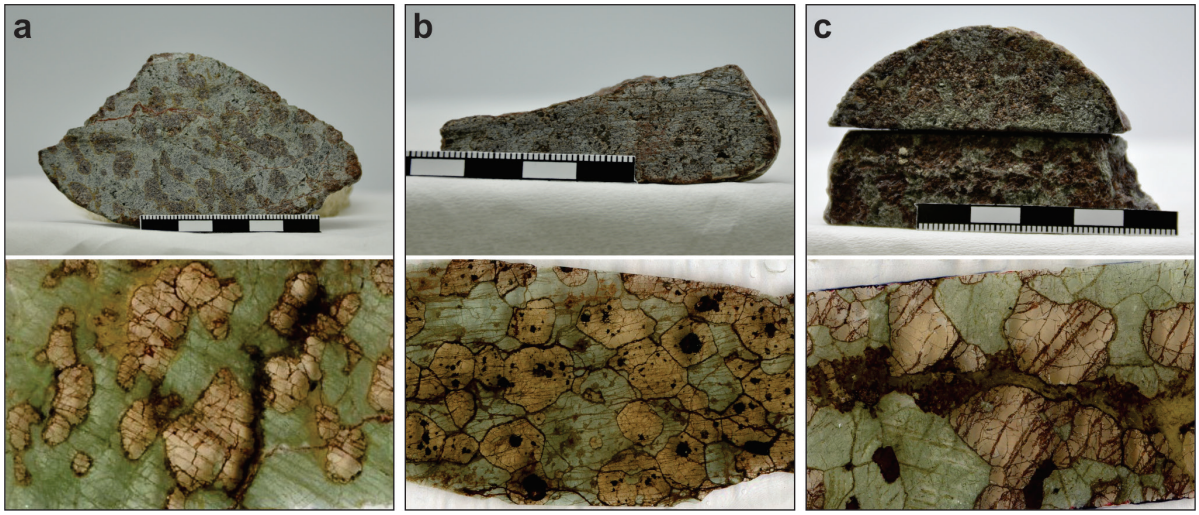

Figure 6.12 Examples of hand samples and thin sections of the eclogite and garnet-pyroxenite xenoliths. (a) Low-Mg eclogite. (b) High-Mg eclogite. Note the abundant oxide inclusions in garnet. (c) Garnet-pyroxenite with amphibole in veins and rutile .

6.3.1. Petrography

Eclogite xenoliths are composed of fresh subhedral clinopyroxene (30-50%) and garnet (45-70%). The grain size of the clinopyroxene commonly ranges from 0.5 to 3 mm and it does not show obvious exsolution of garnet. A second fine-grained (<20 μm) generation of clinopyroxene was also identified in these eclogites, usually related to grain boundaries and fractures (fig. 6.13). Garnet in these xenoliths is larger than garnet in peridotites, with diameters ranging from 2 mm to 2 cm. Garnet may contain multi-oriented rutile needles, locally with unidentified inclusions near the grain boundaries. A characteristic feature of the sample CAT-34 is the presence of large inclusions in garnet (or melt pockets). As shown in fig. 6.13c, these inclusions can be quite complex, appearing as pseudomorphs of a previous euhedral crystal, perhaps chromite. Zoning of the primary inclusions is still preserved in some cases. Additionally, some inclusions present symplectitic textures, composed of an intergrowth of iron oxides and serpentine minerals. Most of them have a very thin coating of hematite. Eclogites can have subordinate amounts of phlogopite, which can occur as vein fillings or surrounding the garnet grains. It never represents more than 2% of the whole xenolith. Sample

CAT-26 contains minor amounts of K-amphibole and euhedral crystals of Cl-apatite (<5 μm). Rutile (1mm in diameter) also occurs as an accessory phase in these eclogites. It shows very thin grid exsolution of iron oxide (fig. 6.13f), similar to those observed in eclogite xenoliths of the Catoca pipe (Nikitina et al., 2014). Based on these observations, these eclogites share features of both type I and type II eclogites found in the Roberts Victor kimberlite in the Kaapvaal craton (Gréau et al., 2011), so further chemical characterization is required to classify them.

Other bimineralic (Grt-cpx) xenoliths have been sampled by the Cat115 kimberlite. In sample MGR-13, garnet is usually significantly less abundant (up to 30%), whereas fresh clinopyroxene constitutes most of the xenolith. In contrast with garnet from eclogites, thick cryptocrystalline kelyphitic coronas are developed around the garnet grains, leaving only their cores (0.5-1 mm) well preserved. A characteristic feature of sample MGR-35, which might have been a granulite, is the presence of abundant garnet (40%), surrounding anhedral crystals of ilmenite, which may show exsolution of titanomagnetite (fig.6.13g). This garnet may contain inclusions of orthopyroxene (± quartz?), in some cases altered to serpentine. MicroRaman spectroscopy is required for the correct identification of these inclusions.

6.3.2. Mineral composition

Clinopyroxene

Eclogitic pyroxenes are omphacite (fig. 6.14a). However, significant compositional differences were found among these xenoliths, resulting in a wide range in Na, Ca, Al and Mg contents. Cpx from Low-Mg eclogites typically show higher Al and Na contents (4.1-6.9 wt% Na_2O, 8.5-12.0 wt% Al_2O_3) and lower Ca contents (13.6-18.4 wt% CaO) than high-Mg eclogite (2.6-4.8 wt% Na_2O, 4.3-5.7 wt% Al_2O_3, 16.6-20.4 wt% CaO). Fine-grained clinopyroxene (fig.6.13) is found in both suites and it is typically enriched in Mg and Ca and depleted in Na and Al relative to the first generation. Similar textures and compositions have been interpreted previously as the result of infiltration of metasomatic fluids (Hills and Haggerty, 1989), which would be consistent with the presence of some phases typically related to modal metasomatism, such as phlogopite. Both high-Mg and low-Mg suites have also been described previously in eclogites sampled by the Catoca and Cat115 kimberlites, although the second generation of clinopyroxene was only reported in the low-Mg suite (Nikitina et al., 2014). In all cases,

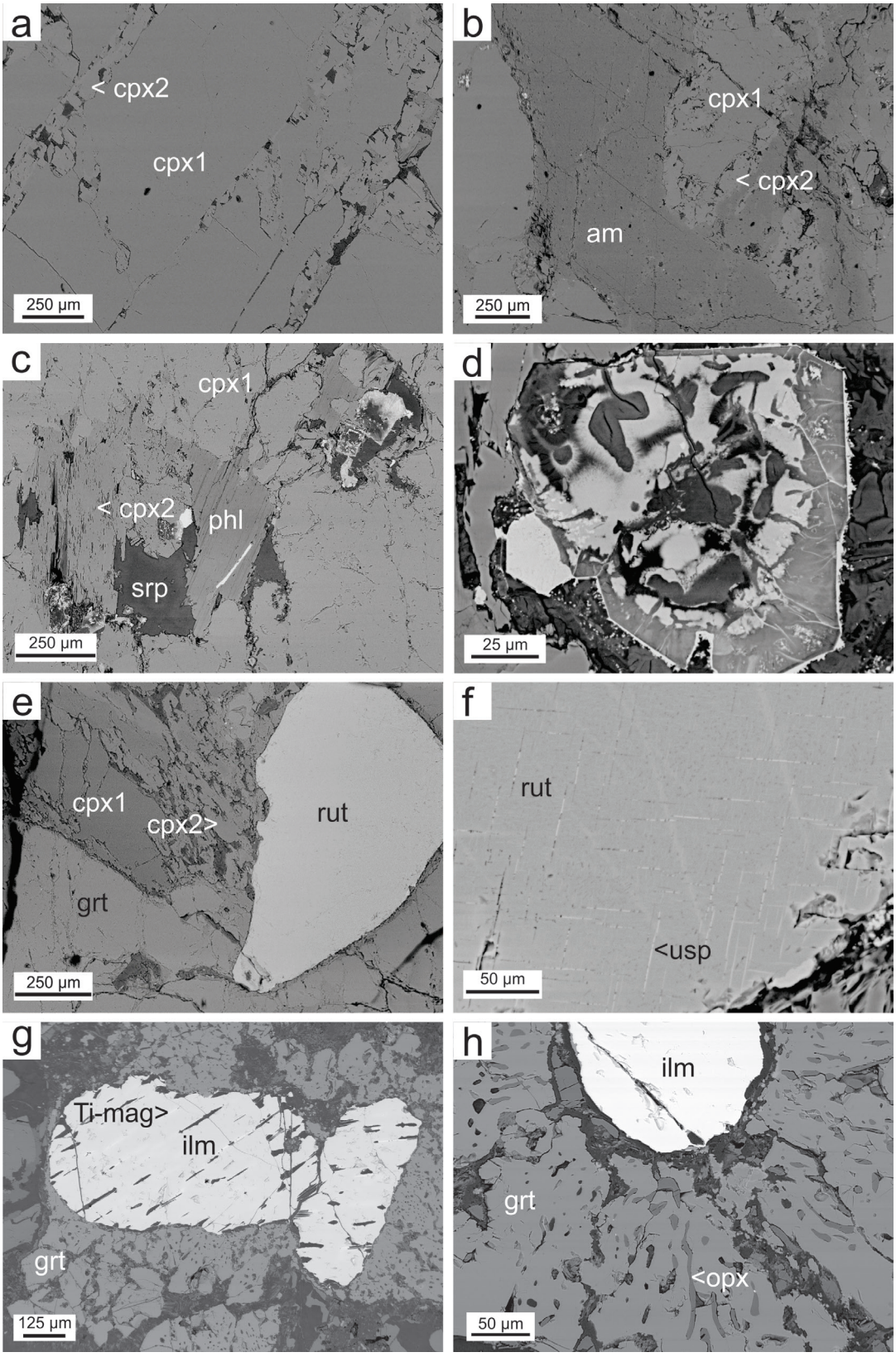

Figure 6.13 BSE images of the eclogite and garnet pyroxenite xenoliths. (a) Two generations of clinopyroxene typical of the studied eclogites (cpx1 and cpx2). (b-c) Metasomatic phases in the eclogites, including amphibole (am) veins and phlogopite (phl). (d) Totally altered melt pockets in sample CAT-26, now comprised of serpentine and iron oxides. (e) Rutile (rut) is an accessory phase and typically shows exsolved grids of iron oxide(f). (g-h). Garnet (grt) with orthopyroxene exsolution (opx) around an ilmenite with Ti-magnetite exsolutions.

the potassium content of clinopyroxene is very low (<0.1 wt% K_2O) and thus these eclogites should be classified as type II following the chemical classification of McCandless and Gurney (1989). In terms of trace elements, clinopyroxene from low-Mg eclogites has high contents of Ti (1540-1690 ppm) and low contents of Sr (48-78 ppm), Zr (11-25ppm), Nd (<2.7 ppm) and Hf (<0.8 ppm). These trace-element compositions are is similar to those observed in type II eclogites from the Roberts Victor kimberlites (Gréau et al., 2011). Conversely, clinopyroxene from the high-Mg eclogite is characterised by higher contents of Ti (1760-2130 ppm), Sr (430-520 ppm), Zr (42-91ppm), Nd (25-42 ppm) and Hf (1.56-2.34ppm), which could be closer to the composition of omphacites in type I eclogites. Compared with pyroxene from peridotites, omphacite of the low-Mg eclogites is typically depleted in HREE, thus having a steeper slope of the REE pattern (fig. 6.15). Additionally, the clinopyroxenes from these two xenoliths have subchondritic to 10x chondrite enrichment in LREE. In contrast, the clinopyroxenes from high-Mg eclogite shows a high enrichment (x100) in LREE. However, in both eclogite suites, the second generation of clinopyroxene is enriched in terms of REE, as well as in Nb, Zr and Cr (table 6.8).

Clinopyroxenes from garnet pyroxenites are diopside (fig. 6.14), with high contents of Ca (20.6-21.6 wt% CaO) and low Al and Na (1.96-2.49 wt% Al_2O_3 and ca. 1.06-1.98 wt% Na2O). However, they can be clearly distinguished by their trace element composition. Sample MGR-13 has very high Ti contents (5880-6330 ppm), but low Hf (<1.5 ppm), Zr (6.3-12.3 ppm), Nd (<6.2 ppm) and very low Sr (<1.2 ppm). In contrast, sample CAT-26 has low Ti contents (778-854 ppm), but high Sr (203-209 ppm). Zirconium (ca. 28 ppm) and Nd (ca. 9 ppm) contents are slightly higher than in the other garnet pyroxenite. Clinopyroxene in both xenoliths has upward convex chondrite-normalised REE patterns, with suprachondritic LREE (x10).

Garnet

Garnets from eclogites define a wide compositional range, being solid solutions between pyrope, almandine and grossular (fig. 6.14c). Eclogites with low-Mg pyroxene have also low-Mg garnet ($Prp_{40-44}Alm_{30-36}Gross_{18-24}$), whereas garnet in the high-Mg eclogite is significantly enriched in the pyrope end-member ($Prp_{71}Alm_{19}Gross_3$). All garnets display low contents of Na (<0.06 wt% Na_2O), Cr (< 0.2 wt% Cr_2O_3) and Fe (9.6-17.3wt% FeO). Garnets of all eclogites have #Mg>0.5 and their calcium content varies between 3.1 and 10.3 wt% CaO. As seen in fig.6.14, the chemistry of these garnets is similar to that of garnet in type II eclogites from the

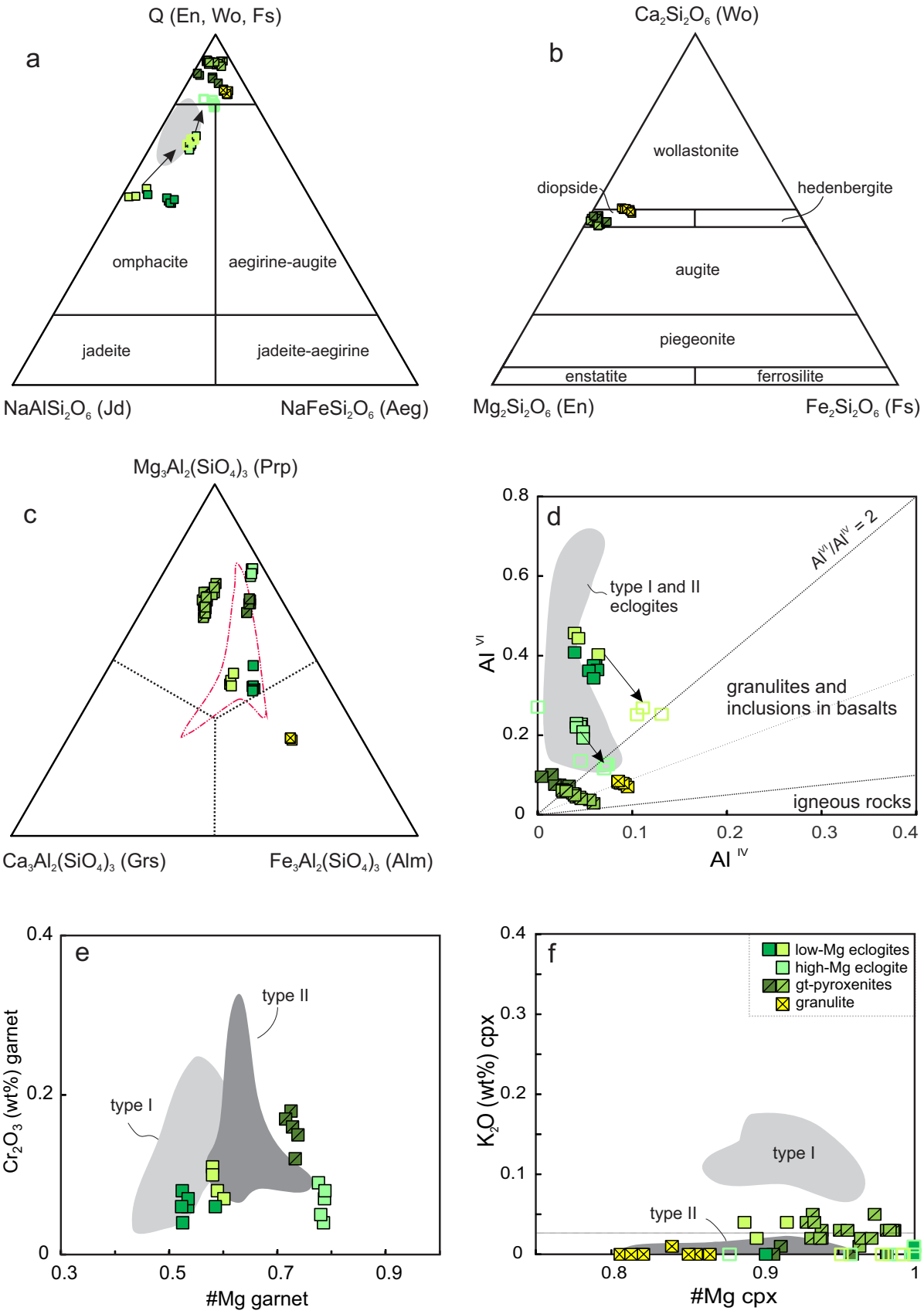

Figure 6.14 Ternary diagrams for the classification of clinopyroxene (a-b) and garnet (c) of the eclgoties and garnet clinopyroxenites. (d) Al^{VI}/Al^{IV} relation in clinopyroxenes. (e) Cr_2O_3 vs #Mg in garnet and (f) K_2O vs #Mg in clinopyroxene. The fields for type I and type II eclogites are taken from Greau et al. (2011). Dashed red line includes garnet data from Nikitina et al. (2014).

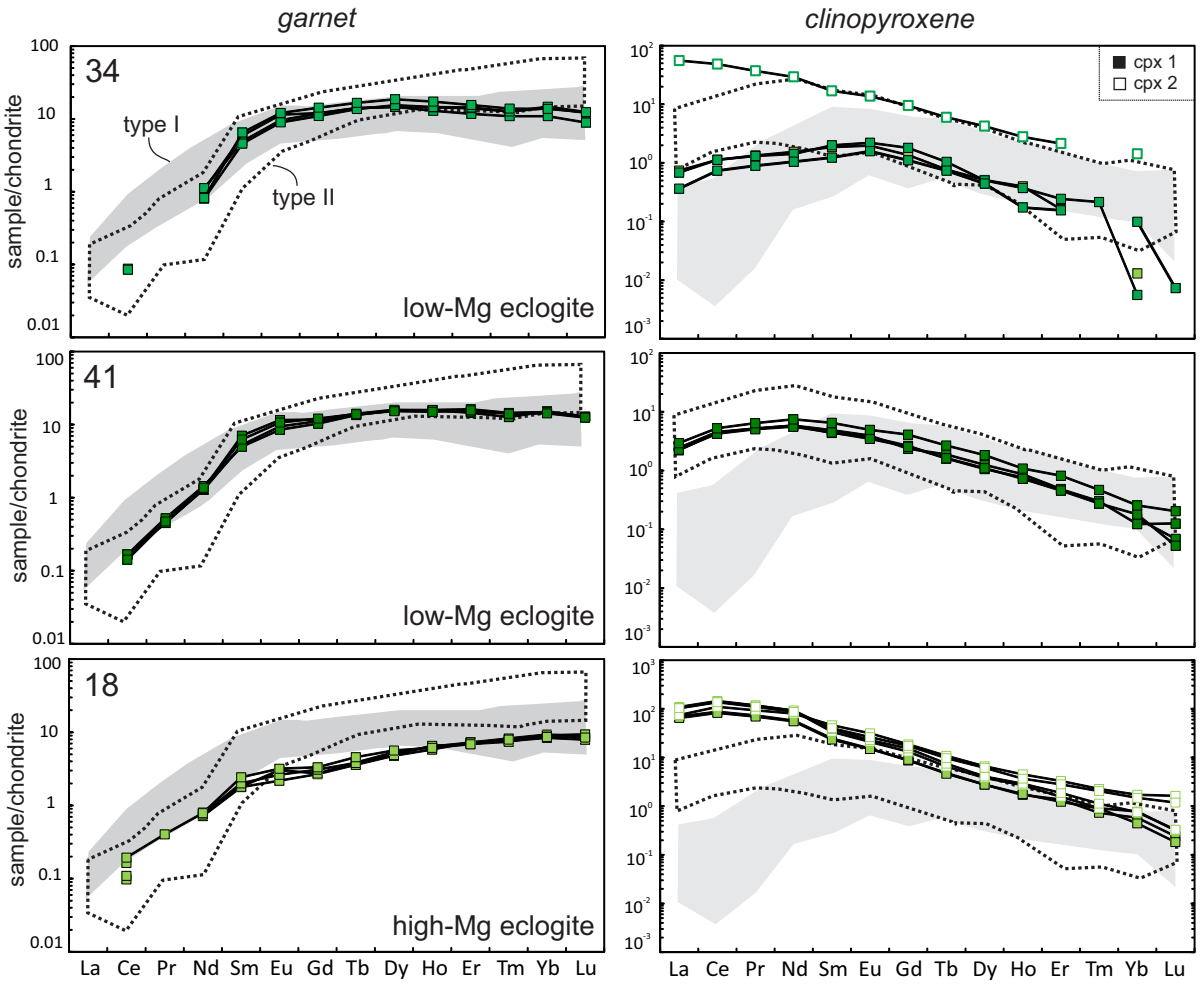

Figure 6.15 REE patterns of garnet and clinopyroxene in the eclogite xenoliths, normalised to the chondrite values of McDonough and Sun (1995). The fields for type I and type II eclogites were taken from eclogites of the Roberts Victor kimberlite (Gréau et al., 2011).

Roberts Victor kimberlite (Gréau et al., 2011). The very low Na contents of these garnets also classifies them as type II eclogites (McCandless and Gurney, 1989).

Garnets from low-Mg eclogite xenoliths show a distinctive REE pattern, characterised by very low LREE contents (below detection limit), which result in a steep positive slope from La to Sm-Eu and unfractionated (flat) MREE and HREE at x10 the chondritic values. REE pattern of garnet in the high-Mg eclogite also has very low LREE, but it is characterised by a constant positive slope towards HREE (fig.6.15). In all eclogites garnet has low contents of Sr (<0.7 ppm), Hf (<0.2 ppm), Zr (<23 ppm) Ti (330-820 ppm) and Ni (<15 ppm).

The garnets of the two garnet-pyroxenite xenoliths are very different. Although garnet from both xenoliths is mainly pyrope (Prp_{63-64}), grossular and almandine contents are very similar ($Alm_{13}Gross_{15}$) in sample MGR-13, whereas almandine clearly dominates over grossular

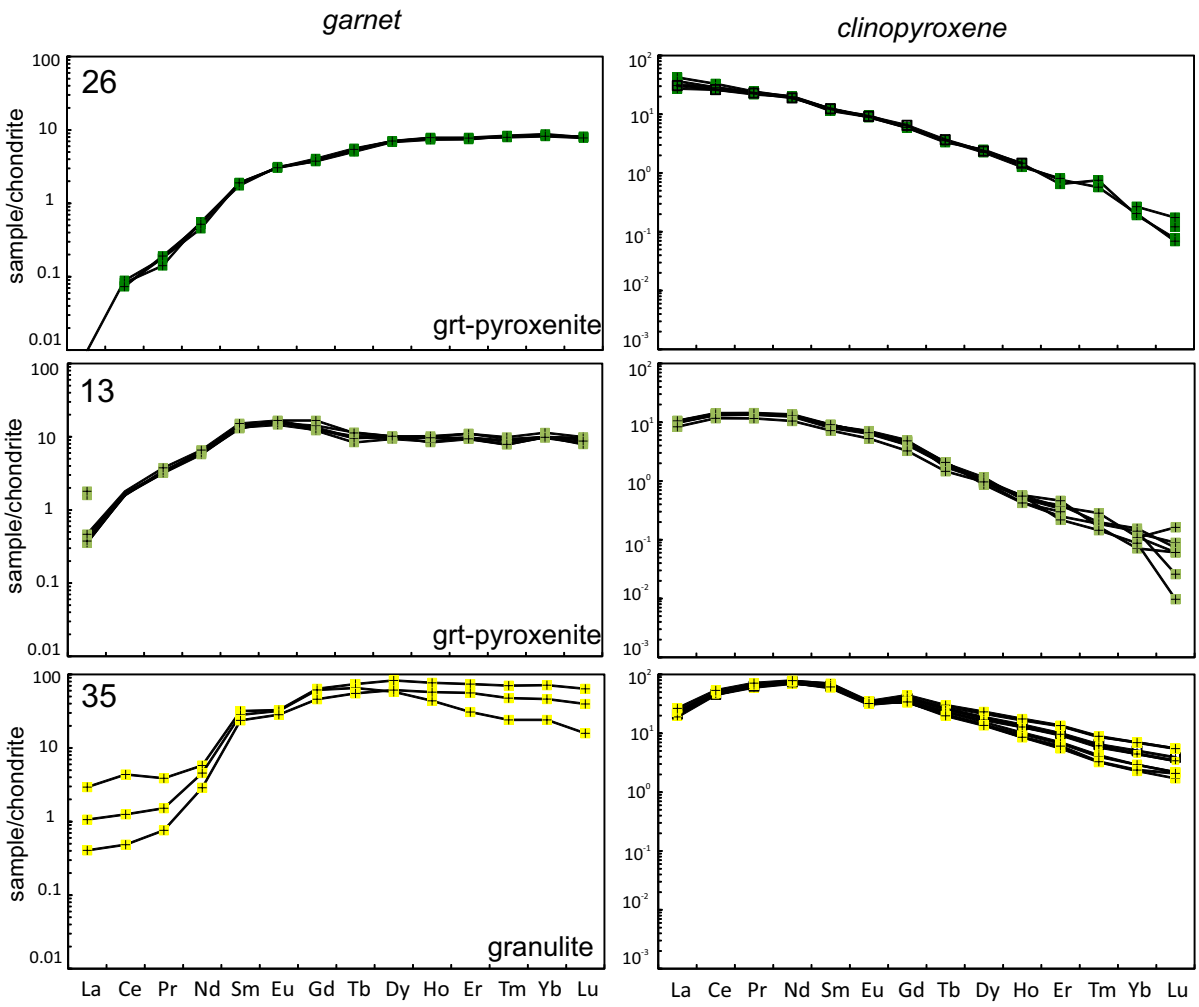

Figure 6.15 (continued) REE patterns of garnet and clinopyroxene in the garnet pyroxenites and the granulite, normalised to the chondrite values of McDonough and Sun (1995).

($Alm_{24}Gross_{8}$) in sample CAT-26. Additionally, sample MGR-13 has a characteristic hinge at Eu, followed by a flat HREE pattern at 10x chondrite values. It has also high contents of Ti, Cr and Ni (5560-6330 Ti ppm; 6620-8390 Cr ppm and 142-157 Ni ppm). Conversely, sample MGR-26 shows a constant positive slope and flat HREE and low Ti (813-986 ppm), Cr (763-811 ppm), Sr (<0.074ppm), Hf (<0.364 ppm), Zr (<24 ppm) and Ni (<33 ppm) contents.

Xenolith	CAT-18	CAT-18	CAT-34	CAT-34	CAT-41	CAT-26	MGR-13	MGR-35
Rock	high-Mg eclogite	high-Mg eclogite	low-Mg eclogite	low-Mg eclogite	high-Mg eclogite	grt-pyroxenite	grt-pyroxenite	granulite
Mineral	cpx1	cpx2	cpx1	cpx2	cpx	cpx	cpx	cpx
N	*6*	*5*	*3*	*3*	*6*	*5*	*13*	*8*
SiO_2	54.91	53.77	55.45	52.86	54.98	54.76	53.83	51.90
TiO_2	0.39	0.34	0.42	0.60	0.37	0.13	0.31	0.29
Al_2O_3	6.25	4.55	11.67	8.89	10.17	2.42	2.07	3.87
Cr_2O_3	0.10	0.10	0.10	0.11	0.08	0.08	0.19	0.03
$Fe_2O_{3(c)}$	3.65	3.95	1.39	4.23	4.98	1.79	1.69	5.45
FeO	0.00	0.37	1.87	0.52	0.05	1.73	1.41	4.34
MnO	0.04	0.11	0.03	0.08	0.05	0.08	0.04	0.08
MgO	13.59	14.51	9.39	11.47	9.70	15.99	17.04	12.19
CaO	16.88	20.06	13.77	18.11	13.63	21.15	21.40	20.17
Na_2O	4.58	2.75	6.54	4.20	6.80	1.76	1.15	2.23
K_2O	0.00	0.00	0.03	0.00	0.01	0.00	0.03	0.00
Sum Ox%	100.39	100.52	100.64	101.07	100.81	99.90	99.15	100.54
Wo(Ca)	47.17	49.49	48.68	52.52	50.19	47.28	46.31	49.78
En(Mg)	52.83	49.80	46.17	46.29	49.66	49.72	51.32	41.86
Fs(Fe^{2+})	0.00	0.70	5.15	1.20	0.15	3.00	2.37	8.35
XMg	0.99		0.94		1.00	0.94	0.96	0.83
LA-ICP-MS (ppm)								
N	*2*	*5*	*2*	*1*	*4*	*5*	*7*	*10*
Sc	17.5	22.2	10.7	10.0	14.8	24.5	16.8	114.4
Ti	2090	1875	1613	3530	1606	801	1534	1766
V	346	364	352	319	451	402	155	340
Cr	376	592	477	429	323	405	1273	110
Mn	386	541	188	931	281	424	bdl	bdl
Co	18.6	19.8	25.7	33.2	25.5	32.0	43.7	53.0
Ni	250	245	242	331	153	476	734	87
Ga	15.7	11.0	23.6	19.1	24.8	7.9	4.8	18.5
Rb	bdl	1.91	0.21	5.25	bdl	0.10	bdl	0.04
Sr	412	484	51	108	66	213	161	51
Y	2.15	3.97	0.47	4.06	0.86	1.63	0.68	14.82
Zr	43.30	66.60	11.62	24.88	17.21	27.82	3.99	152.50
Nb	0.78	11.06	0.13	24.60	0.21	0.34	0.14	0.18
Cs	bdl	0.04	0.01	0.20	bdl	0.01	bdl	bdl
Ba	0.03	30.95	0.29	15.60	0.03	1.73	0.49	0.30
La	15.97	21.63	0.17	13.20	0.43	8.02	2.347	5.23
Ce	51.90	77.38	0.69	29.70	2.14	17.48	8.22	28.98
Pr	6.615	9.708	0.123	3.450	0.379	2.143	1.256	5.945
Nd	25.70	38.56	0.68	13.38	2.09	8.96	5.77	33.84
Sm	3.550	5.778	0.286	2.510	0.552	1.792	1.269	9.274
Eu	0.851	1.418	0.118	0.772	0.179	0.513	0.366	1.852
Gd	1.750	3.182	0.315	1.890	0.429	1.207	0.871	7.308
Tb	0.171	0.309	0.033	0.216	0.053	0.128	0.068	0.849
Dy	0.682	1.268	0.125	1.041	0.237	0.586	0.246	4.104
Ho	0.095	0.188	0.021	0.152	0.034	0.074	0.028	0.641
Er	0.208	0.375	0.033	0.342	0.063	0.119	0.053	1.368
Tm	0.020	0.040	0.005	0.042	0.006	0.016	0.005	0.131
Yb	0.082	0.190	0.002	0.230	0.022	0.036	0.018	0.649
Lu	0.005	0.021	bdl	0.026	0.002	0.003	0.002	0.077
Hf	1.573	2.152	0.568	0.826	0.569	1.280	0.217	5.790
Ta	0.048	0.601	0.009	3.390	0.022	0.016	0.009	0.009
Th	bdl	bdl	bdl	bdl	bdl	bdl	0.019	0.034
U	bdl	bdl	bdl	bdl	bdl	bdl	0.002	0.002

Table 6.8 Average major-element (in wt% oxide) and trace-element (in ppm) compositions of clinopyroxene in the eclogite, garnet-pyroxenite and granulite xenoliths. The number of analyses averaged is indicated by N and the values below detection limit by "bdl".

Xenolith	CAT-18	CAT-34	CAT-41	CAT-26	MGR-13	MGR-35
Rock	high-Mg eclogite	low-Mg eclogite	high-Mg eclogite	grt-pyroxenite	grt-pyroxenite	granulite
N	*5*	*5*	*6*	*5*	*23*	*3*
SiO_2	41.43	39.89	39.63	41.44	40.91	38.59
TiO_2	0.14	0.21	0.15	0.15	0.97	0.01
Al_2O_3	23.87	22.72	22.45	23.13	20.94	21.23
Cr_2O_3	0.07	0.09	0.06	0.16	0.92	0.00
$Fe_2O_{3(c)}$	1.96	1.36	1.84	0.93	1.77	0.80
FeO	9.75	14.43	16.74	11.93	6.49	24.51
MnO	0.37	0.28	0.34	0.34	0.22	0.66
MgO	19.89	11.40	10.95	17.89	17.65	6.98
CaO	3.22	10.05	8.56	4.31	9.11	6.84
Na_2O	0.01	0.00	0.00	0.04	0.08	NA
K_2O	0.00	0.00	0.00	0.00	0.00	NA
Sum Ox%	100.74	100.45	100.77	100.32	99.01	99.63
Pyrope	71.33	42.41	41.01	64.18	63.11	27.09
Almandin	19.62	30.12	35.19	24.02	13.02	52.38
splessartine	0.75	0.58	0.73	0.70	0.45	1.46
Andradite	5.10	3.72	5.04	2.51	4.89	2.34
Uvarovite	0.19	0.25	0.18	0.44	2.69	0.00
Grossulaire	3.01	22.90	17.84	8.16	15.85	16.73
LA-ICP-MS (ppm)						
N	*5*	*4*	*4*	*4*	*7*	*3*
Sc	33.1	41.0	43.3	68.9	96.8	57.3
Ti	769	1104	848	901	6037	220
V	51.5	101.5	103.0	186	306.1	76
Cr	288	416	190	782	7250	12
Mn	2593	2079	2297	2537	NA	4688
Co	54.5	60.3	54.5	67.0	67.9	64.4
Ni	16	27	8	33	150	3
Ga	8.0	10.8	10.1	10.6	12.6	16.3
Rb	bdl	bdl	bdl	0.02	bdl	0.20
Sr	0.05	0.64	0.23	0.06	1.04	3
Y	8.4	20.5	22.0	10.52	12.8	89.87
Zr	9.0	11.8	9.3	23.63	64.7	10.68
Nb	bdl	0.06	bdl	0.02	0.49	0.01
Cs	0.000	bdl	bdl	bdl	bdl	bdl
Ba	bdl	bdl	bdl	bdl	bdl	0.29
La	bdl	0.053	bdl	0.00	0.093	0.35
Ce	0.079	0.161	0.098	0.05	1.022	1.25
Pr	0.007	0.017	0.044	0.016	0.310	0.191
Nd	0.335	0.436	0.619	0.24	2.809	2.02
Sm	0.237	0.812	0.874	0.274	2.033	4.127
Eu	0.149	0.594	0.566	0.174	0.895	1.746
Gd	0.578	2.443	2.253	0.767	2.698	11.373
Tb	0.138	0.529	0.499	0.192	0.364	2.343
Dy	1.257	3.898	3.840	1.718	2.432	16.583
Ho	0.340	0.810	0.847	0.418	0.510	3.247
Er	1.142	2.228	2.463	1.227	1.603	8.587
Tm	0.195	0.310	0.343	0.202	0.215	1.173
Yb	1.406	2.153	2.378	1.361	1.628	7.610
Lu	0.207	0.283	0.313	0.196	0.220	0.978
Hf	0.114	0.164	0.096	0.325	1.288	0.159
Ta	bdl	bdl	bdl	bdl	bdl	bdl
Th	bdl	bdl	bdl	bdl	bdl	0.036
U	bdl	bdl	bdl	bdl	0.035	0.012

Table 6.8 (continued) Average major-element (in wt% oxide) and trace-element (in ppm) compositions of garnet in the eclogite, garnet-pyroxenite and granulite xenoliths. The number of analyses averaged is indicated by N and the values below detection limit by "bdl".

6.4. Clinopyroxene megacrysts

6.4.1. Petrography

Very large (> 10cm) clinopyroxene megacrysts have been sampled by the kimberlite. These clinopyroxenes are fresh and do not contain orthopyroxene lamellae. No accessory minerals have been identified in the megacrysts. However, a second generation of very fine grained clinopyroxene was formed on the rims and fractures of the large crystals. This clinopyroxene typically shows a spongy texture (fig. 6.16). Along grain boundaries and veins, pyroxenes have undergone a late serpentinisation process.

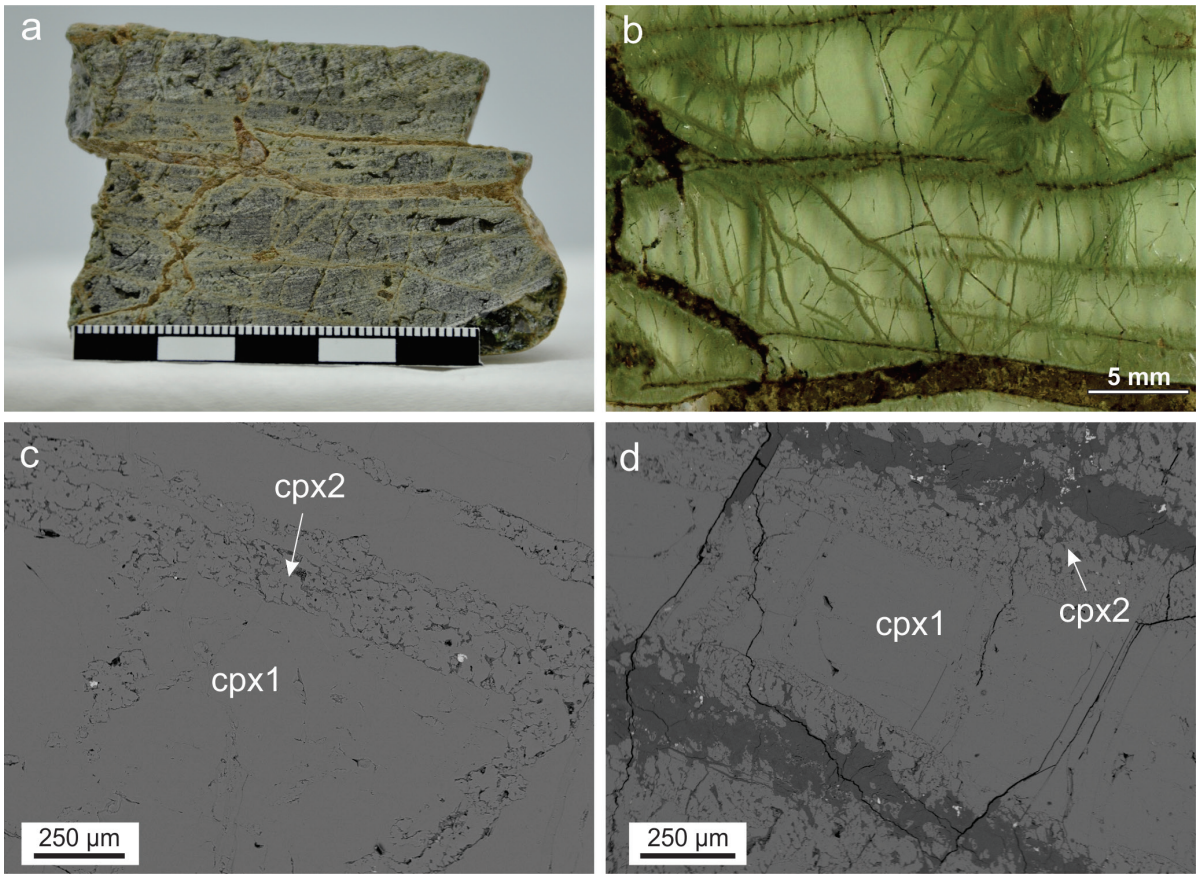

Figure 6.16 Clinopyroxene megacrysts. (a) Hand sample and thin section (b) of one of the clinopyroxene megacrysts sampled by the Cat115 kimberlite. (c-d) BSE images of the clinopyroxene megacrysts, showing the two generations of clinopyroxenes found in these rocks: primary (cpx1) and spongy clinopyroxene (cpx2).

6.4.2. Mineral composition

Most of the clinopyroxene megacrysts are classified as augite (fig. 6.17), although a few of them are slightly more enriched in Na and thus are classified as aegirine-augites. Augites are characterised by low sodium contents (0.87-2.70 wt% Na_2O) and commonly have higher Mg (15.4-20.3 wt% MgO ca. 18.0 wt% MgO) and Fe (up to 5.1 wt% FeO) than clinopyroxenes

found in xenoliths. Their aluminum content ranges from 0.34 to 3.55 wt% Al_2O_3 and their calcium, from 15.9 to 21.0 wt% CaO. Both types of megacryst show similar contents of LILE and HFSE, although the aegirine-augite megacrysts are slightly more enriched in Zr and Hf (fig. 6.18).

However, the composition of the spongy clinopyroxene is very similar in both types of megacrysts. In all cases it is defined by higher Ca contents and intermediate Mg values, coupled with enrichment in Ti and Cr and depletion in Na (fig. 6.17 and 6.18). The spongy clinopyroxene in both types of megacrysts is characterised by an enrichment in Sr, Y and HFSE relative to the first generation of clinopyroxene.

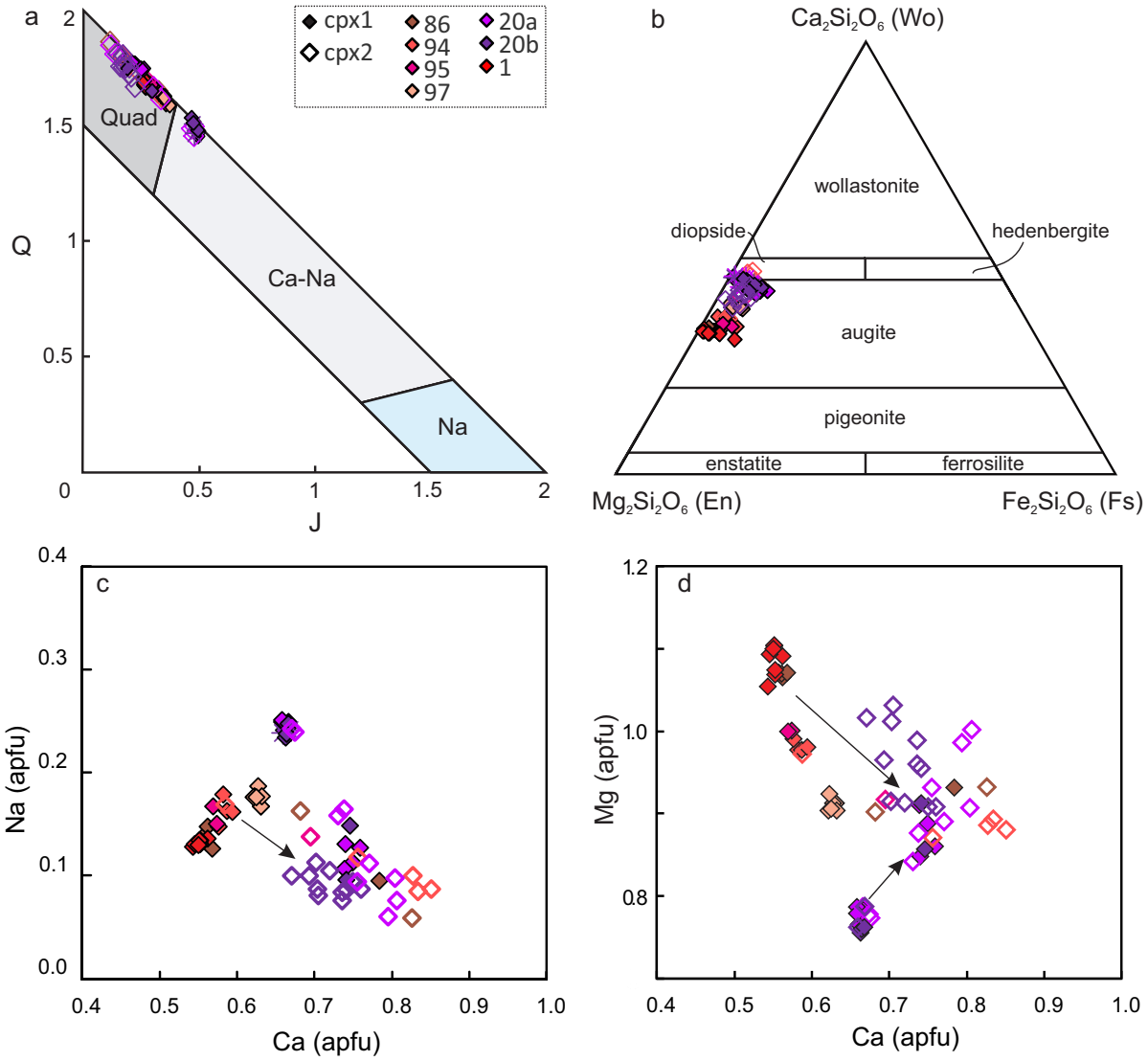

Figure 6.17 Major- element compositions of the clinopyroxene megacrysts. In these figures, filled diamonds represent the primary clinopyroxene and open diamonds, spongy clinopyroxene. Different megacrysts are represented with different colours so the correlation between both generations of clinopyroxene could be done. (a) Q-J diagram for the classification of the clinopyroxene megacrysts, where Q= Ca+Mg+Fe^{2+} and J=2Na. (b) Classification in the clinopyroxene quadrilateral based on enstatite, wollastonite and ferrosilite contents. (c-d) Na-Ca and Mg-Ca binary diagrams, where it can be seen that the composition of the spongy clinopyroxene is similar regardless of the original composition of the megacrysts .

The chondrite-normalised REE patterns are very similar in all clinopyroxene megacrysts, with a convex-upward shape and suprachondritic values (10x) for the LREE (fig. 6.19). However, in all cases the second generation of clinopyroxene is significantly more enriched in LREE (La to Nd), while the MREE are very similar and HREE contents are lower. Averaged major- and trace-element compositions are included in table 6.9.

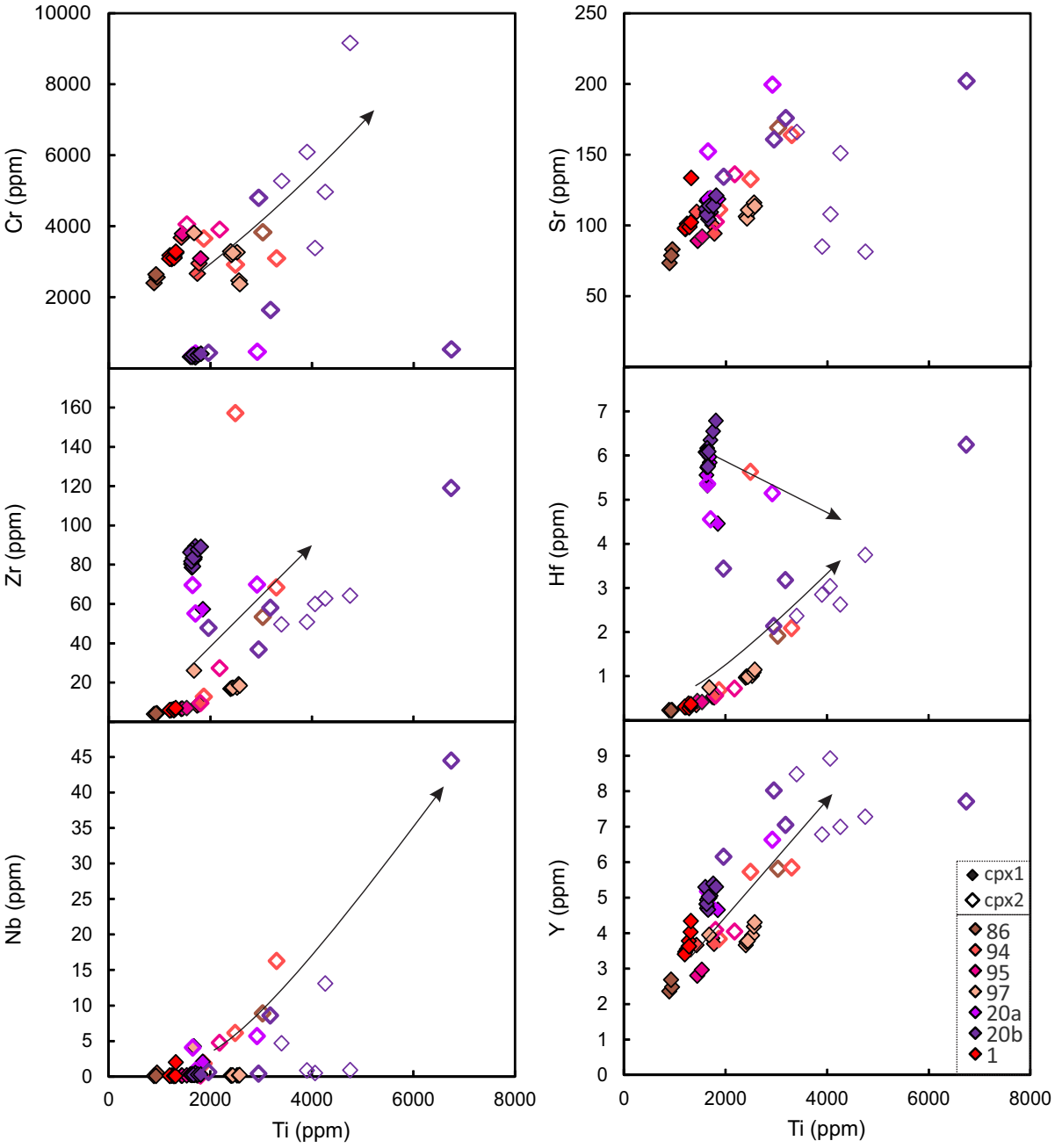

Figure 6.18 Trace-element compositions of the clinopyroxene megacrysts. As in figure 6.17, filled diamonds represent the primary clinopyroxene and open diamonds, spongy clinopyroxene. These diagrams show that the enrichment in Ti typical of the spongy clinopyroxene is coupled with an enrichment in Cr and incompatible elements. Different megacrysts are represented with different colours so the correlation between both generations of clinopyroxene could be done.

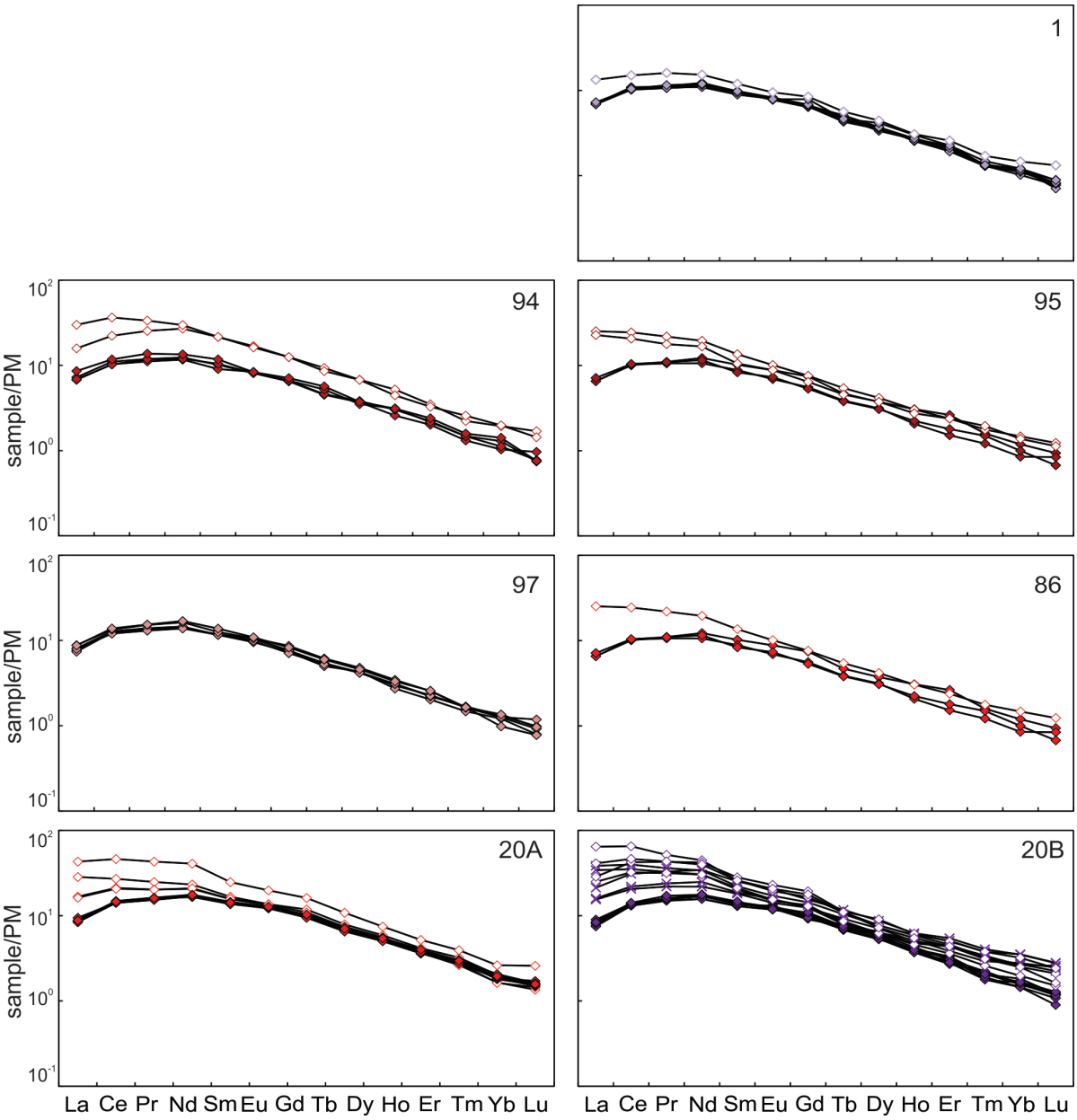

Figure 6.19 Chondrite-normalised REE patterns of the clinopyroxene megacrysts, using the chondrite values of McDonough and Sun (1995). As in previous figures, filled diamonds represent the primary clinopyroxene and open diamonds, spongy clinopyroxene, which is typically enriched in LREE relative to the primary one.

Sample	CAT-86	CAT-86	CAT-94	CAT-94	CAT-95	CAT-95	CAT-97	MGR-20A	MGR-20A	MGR-20B	MGR-20B	MGR-1
Mineral texture	coarse	fine	coarse	fine	coarse	fine	coarse	coarse	fine	coarse	fine	coarse
N	*5*	*1*	*4*	*4*	*2*	*1*	*7*	*2*	*8*	*5*	*11*	*3*
SiO_2	54.80	55.07	54.62	54.08	54.94	53.87	54.65	54.03	53.96	54.45	52.80	55.57
TiO_2	0.31	0.31	0.34	0.42	0.28	0.48	0.50	0.35	0.47	0.36	0.90	0.23
Al_2O_3	2.36	2.92	3.06	1.59	2.95	2.30	3.09	3.64	2.79	3.34	2.33	2.71
Cr_2O_3	0.59	0.63	0.47	0.51	0.63	0.62	0.48	0.07	0.20	0.05	1.03	0.54
$Fe_2O_{3(c)}$	3.20	2.24	3.06	3.00	2.46	2.58	2.92	6.14	4.52	3.95	2.37	1.74
$FeO_{(c)}$	1.80	2.20	2.37	2.61	2.71	2.70	2.76	0.58	1.51	2.52	2.52	3.18
MnO	0.12	0.13	0.13	0.15	0.13	0.17	0.13	0.12	0.10	0.12	0.18	0.12
MgO	19.59	16.90	18.35	16.72	18.75	16.89	17.01	14.54	15.75	14.41	17.69	20.14
CaO	15.86	17.77	15.21	19.42	14.90	17.80	16.30	17.19	18.81	17.48	18.53	14.44
Na_2O	1.85	2.35	2.34	1.63	2.28	1.95	2.52	3.51	2.41	3.15	1.28	1.90
K_2O	0.02	0.00	0.02	0.01	0.02	0.00	0.01	0.01	0.01	0.04	0.00	0.04
Sum Ox%	100.50	100.52	99.97	100.14	100.01	99.37	100.38	100.15	100.51	99.87	99.65	100.62
Wo(Ca)	35.54	41.34	35.72	43.28	34.57	41.00	38.69	45.39	44.93	44.25	41.09	32.14
En(Mg)	61.32	54.67	59.96	52.15	60.53	54.14	56.20	53.43	52.34	50.74	54.55	62.36
Fs(Fe^{2+})	3.14	3.99	4.32	4.57	4.89	4.86	5.10	1.18	2.74	5.01	4.36	5.49
XMg	0.95	0.93	0.93	0.92	0.93	0.92	0.92	0.98	0.95	0.91	0.93	0.92
LA-ICP-MS (ppm)												
N	*3*	*3*	*3*	*3*	*2*	*2*	*7*	*7*	*9*	*8*	*4*	*8*
Sc	12.0	26.9	17.9	30.2	17.3	18.3	22.4	41.2	57.3	43.3	39.4	15.5
Ti	923	3030	1648	2554	1626	1858	2370	1658	3166	1684	3708	1264
V	145.5	266.0	224.7	252.8	229.0	236.8	301.7	344.5	286.2	351.7	276.4	191.8
Cr	2533	3830	3097	3221	3440	3979	3091	352	3388	346	1851	3154
Mn	805	1100	1007	941	1000	956	991	NA	NA	NA	NA	NA
Co	33.08	53.60	42.60	42.63	40.20	35.10	33.52	24.91	26.34	24.92	27.47	40.33
Ni	505	680	540	593	472	432	323	49	132	64	157	602
Ga	4.86	9.96	7.11	7.03	7.08	7.59	8.47	18.27	7.94	17.29	6.63	6.16
Rb	0.20	32.10	bdl	11.94	0.03	1.89	0.32	0.06	3.80	0.11	1.01	0.73
Sr	78.3	169.0	101.4	135.9	95.8	114.1	111.7	116.3	131.1	111.2	168.2	103.9
Y	2.506	5.810	3.737	5.133	3.445	3.500	3.936	4.910	6.627	5.058	7.233	3.725
Zr	4.22	53.50	7.94	79.47	8.16	17.14	18.94	81.87	59.97	85.58	65.45	6.24
Nb	0.242	8.89	0.155	8.10	0.136	2.46	0.752	0.271	3.641	0.312	13.54	0.355
Ba	0.414	81.40	0.308	43.33	0.186	40.57	4.294	0.334	21.48	0.594	34.91	1.175
La	1.306	8.330	1.647	4.293	1.551	3.836	2.413	2.070	6.053	1.942	9.428	1.852
Ce	4.87	20.90	6.45	14.39	6.23	10.69	8.58	8.81	17.95	8.38	28.50	6.81
Pr	0.783	3.130	1.074	2.243	1.004	1.523	1.348	1.461	2.642	1.463	3.933	1.077
Nd	3.86	14.24	5.49	10.70	5.22	7.09	6.96	7.84	12.75	7.69	17.91	5.49
Sm	1.069	3.240	1.460	2.707	1.410	1.620	1.767	2.084	2.919	2.064	3.738	1.456
Eu	0.369	0.948	0.463	0.777	0.442	0.491	0.569	0.703	0.892	0.687	1.107	0.461
Gd	0.884	2.420	1.307	2.130	1.295	1.285	1.506	1.958	2.586	1.994	3.310	1.398
Tb	0.1129	0.3080	0.1723	0.2840	0.1545	0.1665	0.1949	0.2513	0.3224	0.2593	0.3768	0.1729
Dy	0.643	1.560	0.904	1.418	0.846	0.892	1.057	1.310	1.641	1.386	1.860	0.924
Ho	0.0943	0.2370	0.1590	0.2327	0.1405	0.1440	0.1669	0.2070	0.2664	0.2160	0.3005	0.1503
Er	0.217	0.511	0.340	0.489	0.332	0.334	0.372	0.468	0.635	0.482	0.702	0.345
Tm	0.0216	0.0613	0.0351	0.0526	0.0347	0.0403	0.0413	0.0470	0.0694	0.0495	0.0782	0.0344
Yb	0.121	0.293	0.185	0.286	0.165	0.199	0.201	0.255	0.395	0.256	0.410	0.190
Lu	0.0130	0.0344	0.0204	0.0319	0.0219	0.0235	0.0237	0.0280	0.0500	0.0283	0.0471	0.0216
Hf	0.231	1.920	0.469	2.803	0.502	0.572	0.994	5.700	3.797	6.231	3.753	0.329
Ta	0.007	0.532	0.007	0.487	0.008	0.144	0.043	0.035	0.237	0.038	0.618	0.015
Th	bdl	bdl	bdl	bdl	bdl	bdl	bdl	0.023	0.305	0.026	0.439	0.038
U	bdl	bdl	bdl	bdl	bdl	bdl	bdl	0.007	0.072	0.006	0.108	0.549

Table 6.9 Average major-element (in wt% oxide) and trace-element (in ppm) composition of the different generations of clinopyroxene in the clinopyroxene megacrysts. The number of analyses averaged is indicated by N and the values below detection limit, by "bdl".

6.5.Highly metasomatised xenoliths

This group includes all xenoliths which contain phases resulting from pervasive metasomatic processes and consequently, it is a miscellany of different lithologies. Their petrography is described in the following paragraphs. The composition of ilmenite in these xenoliths will be discussed in more detail in chapter 9.

The first xenolith is an ilmenite-rich pyroxenite (sample MGR-44), which only preserves part of the clinopyroxene and the interstitial ilmenite (fig. 6.20). It shows strong mineral banding, defined by an alternation of layers of highly serpentinised olivine and others of fresh clinopyroxene (40 vol %). This pyroxene is subbhedral, with diameters ranging from 0.5 to 5mm, and it is in microstructural equilibrium with anhedral olivine grains (45 vol %), which have diameters ranging between 0.5 and 3 mm. Some clinopyroxene crystals contain small (<20 μm) inclusions, most of them now replaced by serpentine minerals. Additionally, spongy clinopyroxene has been found on the boundary between clinopyroxene and ilmenite (15 vol %), which forms veinlets across the xenolith. Ilmenite locally shows evidence of recrystallisation. This texture could be similar to the sideronitic texture described by Boyd et al., 1984. This assemblage has also been described in other kimberlites (e.g. Kopylova et al., 1999), where it has been suggested that it could be a consequence of a partial melting of the original rock, which resulted in porosity, followed by a crystallization event linked with metasomatic processes. However such origin remains controversial and will be discussed in chapter 9.

Sample MGR-27 also contains abundant metasomatic minerals, which have replaced the original assemblage. Among these, the most important is a brown amphibole (kaersutite) occupying the interstitial space between serpentinised olivine and clinopyroxene (fig. 6.20). Along with amphibole, it is common to find ilmenite grains with grain sizes up to 0.5 mm. A typical feature of these ilmenites is the presence of exsolved ulvöspinel, altered to titanite. Small (<250 μm) rounded crystals of apatite occur together with amphibole (fig. 6.21). Additionally, there are significant contents of interstitial calcite, replacing altered olivine and, to a lesser extent, clinopyroxene. There are two generations of carbonate, the second one defined by very thin veinlets which crosscut the original calcite. Finally, other phases typical of a highly oxidized environment, such as barite, celestine and Sr-rich barite, are found in the serpentinised areas (fig. 6.21). These phases are interpreted as late supergene products, unrelated to the formation of the main mineral assemblage or to mantle metasomatic processes.

The third xenolith included in this group is mainly composed of euhedral-subhedral

clinopyroxene crystals (35 vol %), with diameters ranging between 0.5-1 mm. These grains are in microstructural equilibrium with other euhedral crystals that are now totally altered to serpentine, but which formerly probably were olivine (35 vol %). Some of the clinopyroxene

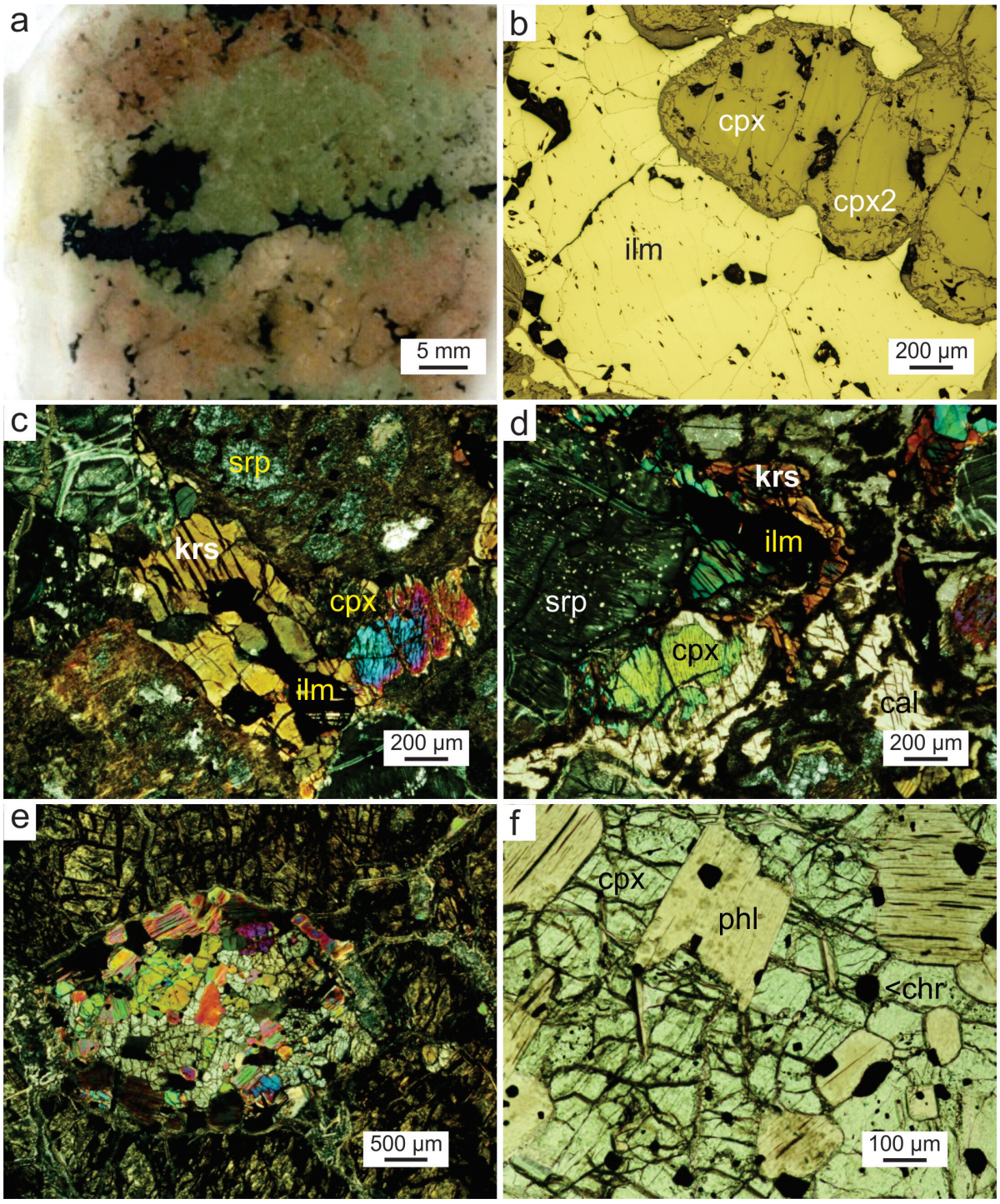

Figure 6.20 Petrographic images of the highly metasomatised xenoliths. (a) Scanned image of the thin section of sample MGR-44, showing the banding of clinopyroxene (green) and serpentinised olivine (red), with veins of ilmenite (black). (b) Interstitial ilmenite veins (ilm) in clinopyroxene (cpx), which has a spongy texture on the boundaries (cpx2 (reflected light). (c-d) Images of sample MGR-27, showing the abundance of kaersutite (krs), ilmenite and calcite (cal) between serpentinised olivine grains (srp) and clinopyroxene. (e-f) Sample MGR-24B, mainly composed of phlogopite (phl), clinopyroxene and chromite (chr).

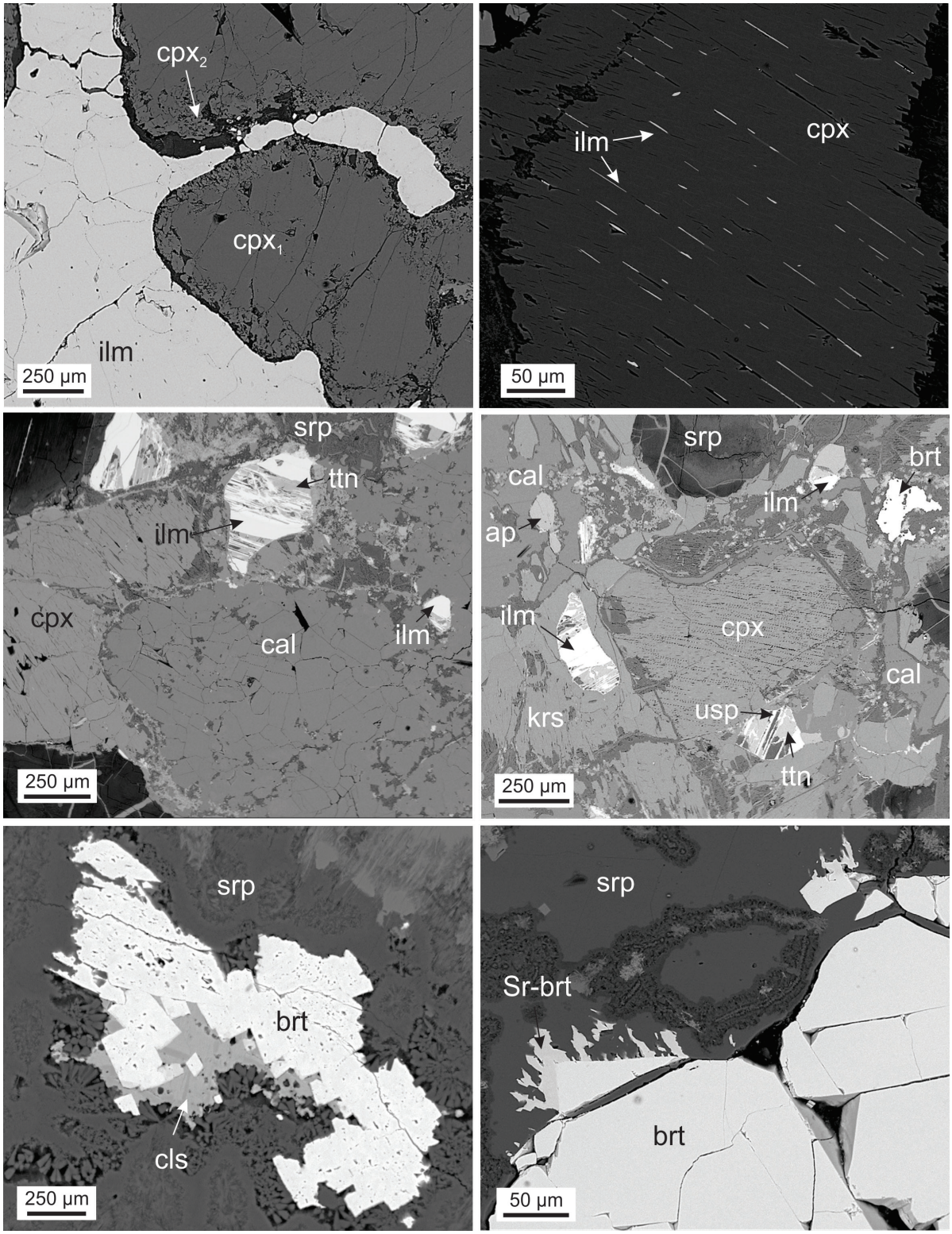

Figure 6.21 BSE images of the highly metasomatised xenoliths. (a) Interstitial ilmenite veins (ilm), showing evidence of recrystallisation, in clinopyroxene (cpx). Spongy clinopyroxene (cpx_2) occurs on the boundaries between ilmenite and clinopyroxene. (b) Ilmenite lamellae in clinopyroxene of sample MGR-42. (c-d) Images of the main mineralogical assemblage of sample MGR-27: clinopyroxene, calcite (cal), ilmenite with exsolved ulvöspinel, altered to titanite (ttn), olivine altered to serpentine (srp) and apatite (ap). (e-f) Late supergene minerals formed in the same xenolith, comprising barite (brt), celestine (cls) and late Sr-rich barite (Sr-brt).

grains contain ilmenite lamellae (fig. 6.21). Ilmenite occurs as small (< 200 μm) subhedral grains interstitial to the other mineral phases (<5% of the whole xenolith).

Finally, other examples of highly metasomatised xenoliths are samples MGR-15A and MGR-24B, in which euhedral phlogopite is the main constituent mineral. These xenoliths typically contain subordinate amounts of chromian diopside, chromite and, locally, olivine (fig.6.20g). The spinel in sample MGR-24B shows a characteristic symplectitic texture, not observed in the other xenoliths.

6.6. Preliminary conclusions

1. Cat115 and Catoca kimberlites sampled a wide variety of mantle xenoliths, including peridotites, eclogites and garnet pyroxenites. Highly metasomatised xenoliths were also brought to the surface by these kimberlitic magmas; as well as some large clinopyroxene megacrysts.

2. Two different suites of garnet peridotite were identified based on their microstructure: coarse garnet peridotites and porpyroblastic (sheared) garnet peridotites; the latter is characterised by the formation of both olivine and orthopyroxene neoblasts and deformation of the larger grains. Moreover, the composition of the mineral assemblage forming these two garnet peridotite suites differs both in terms of major- and trace-elements.

3. Eclogites sampled by the Catoca kimberlite can be subdivided in high-Mg eclogites and low-Mg eclogites, based on the composition of their garnet and omphacite. The available data indicates that features of both type I and type II eclogites can be observed in the studied eclogite xenoliths.

4. Typical metasomatic phases (phlogopite, interstitial chromian diopside, ilmenite, etc.) have been identified in several of these xenoliths. Additionally, peridotites, eclogites and clinopyroxene megacrysts all have developed spongy clinopyroxene, which is typically enriched in REE, HFSE and, in some cases, LILE.

5. Highly-metasomatised xenoliths typically include larger amounts of these metasomatic minerals, which are accompanied by the crystallisation of amphibole, apatite, chromite and rutile. Supergene alteration of some of these xenoliths is reflected in the occurrence of phases typical of oxidising environments (barite, celestine and calcite).

Chapter 7
STRUCTURE OF THE SCLM BENEATH LUNDA NORTE: A THERMOBAROMETRIC APPROACH

In this chapter, the major- and trace-element composition of the garnet peridotites and eclogites is used to determine the temperature and pressure of equilibration of the xenoliths, as well as those of garnet xenocrysts. These results are combined with the petrography and the composition of the xenoliths characterised in the previous chapter to define the structure of the SCLM in NE Angola. A layered SCLM is described, with the Spl-peridotite and coarse Grt-peridotites forming the shallow layer of the mantle (<145km). The porphyroclastic (sheared) garnet peridotites represent the deeper layer of the SCLM (>180 km) and are typically characterised by higher Ti, Cr and contents in garnet, as well as lower #Mg in both enstatite and olivine. Between these two garnet-peridotite suites, a level of low-Mg eclogites was defined. The origin of such layering and the current structure of the SCLM could be either explained by shallow subduction of an oceanic lithosphere (subduction origin) or by upwelling of an asthenospheric plume similar to that described in the Slave craton (cumulate origin).

7.1. Introduction to geothermobarometry

Geothermobarometry is the science that seeks to constrain the equilibrium temperature and pressure of a given mineral assemblage. This methodology is based on a combination of a thermometer and a barometer, defined by temperature- and pressure-dependent reactions, respectively. Although geothermobarometry is commonly applied to metamorphic rocks, it is becoming increasingly used to define the PT equilibrium conditions of igneous rocks and, in particular, mantle-derived samples.

The formula for each thermometer and barometer is usually obtained from experimental studies carried out in HP and HT laboratories, where the cation exchange within an artificial mineral assemblage is measured at increasing pressures and temperatures. In some cases

calibration may also be done using natural systems. Regardless of the approach, it is important to point out that each barometer or thermometer can only be used for the restricted range of composition, pressure and temperature for which it was originally defined. If the samples that are subject of study do not fit these parameters, the calculated PT conditions could be either over- or underestimated. Additionally, oxygen fugacity and water activity may also play a major role when defining the thermobarometers.

Historically most of the thermobarometers applicable to mantle rocks have relied on pairs of minerals, although some monomineralic thermometers and barometers have recently been developed as well. In such cases, the equilibrium between the analysed mineral and the corresponding pair is assumed from the composition of the studied phase [i.e. #Cr > 1 in clinopyroxene for the Cr-cpx thermobarometer by Nimis and Taylor (2000)].

In nature chemical reactions may take place in open systems, where different processes can affect the equilibrium between the mineral phases of the studied rocks. These processes can include mantle metasomatism, interaction with a melt of different composition, retrograde metamorphism or hydrothermal alteration. As a result, both textural and chemical equilibrium between the target minerals should be confirmed from detailed petrographic and mineral chemistry studies, which will ensure that no pervasive modification of the original equilibrium took place. For the same reason, the composition of the cores of the crystals should be preferred over the rims.

7.2. Calculation of the Angolan geotherm

Up to now thermal models of the lithosphere in Central Africa have relied only on global models (e.g., Artemieva, 2006; Begg et al., 2009), given the nonexistent coverage of measured heat flow and the scarcity of thermobarometric studies based on mantle xenoliths. Ashchepkov et al. (2012) made a first attempt to constrain the mantle conditions beneath the Lundas region from chemical analyses of garnet, clinopyroxene and ilmenite xenocrysts, although their studies lack petrographic information that is essential for the characterisation of the SCLM. A similar approach to that taken here was used by Robles-Cruz and coworkers (2012a), although these authors had only a limited suite of xenoliths and groundmass clinopyroxenes.

7.2.1. Geothermobarometry of garnet peridotites

A large number of thermobarometers that could be used to estimate the T-P equilibrium parameters in peridotites have been proposed, tested and often redesigned or reformulated through multiple linear regressions over a variety of compositions of natural and synthetic samples (e.g., Finnerty and Boyd, 1987; Brey and Köhler, 1990; Nimis and Grütter, 2010). In this thesis, different thermometers (O'Neill and Wood, 1979; Brey and Köhler, 1990; Nimis and Taylor, 2000) and barometers (MacGregor, 1974; Brey and Köhler, 1990; Nimis and Taylor, 2000) were paired to solve a system of two (non-linear) equations using an Excel spreadsheet and Mathcad. The results were consistent with those obtained by using PTXEL (provided by Dr. Thomas Stachel) and Hotstuff (provided by Prof. William L. Griffin).

The average compositions of minerals in each xenolith were taken to calculate the pressure and temperature conditions of equilibration of the garnet peridotite xenoliths. For each xenolith, only the results with low dispersion in the P-T space have been considered However, examining the reasons for this coherence or scatter is beyond the scope of this thesis, since it would require an exhaustive analysis of the basis for the each thermometer and barometer (theoretical assumptions, experimental calibration, multi-regression analyses, etc.). The thermometers based on partitioning of Na between opx-cpx and Ca-in-opx by Brey and Köhler (1990) are robust and gave the best results. Therefore, this pair was preferentially used to constrain the pressure and temperature of equilibrium of the garnet peridotites.

The resulting temperatures and pressures of equilibrium are shown in fig. 7.1 and presented in table 7.1. In the P-T diagram, it is clear that the two textural groups of garnet peridotites defined in this study also differ in terms of their equilibration PT conditions. The porphyroclastic garnet peridotites reported the highest pressures and temperatures (1280-1330^{o}C; 63-70 kbar) of this study, whereas the coarse garnet peridotites would be restricted to shallower levels (850-1080^{o}C; 38-53 kbar). All P-T points fit between the 35 and 40 mW/m^2 geotherms defined by Hasterok and Chapman (2011). These cold geotherms are consistent with the few published data from this area, calculated from monomineralic thermobarometry (Ashchepkov et al., 2012; Robles-Cruz et al., 2012b). However, these geotherms are derived from global models that may not be applied in the Congo Craton, which is thicker than other African cratons (e.g., Begg et al., 2009). The studied xenoliths show an almost linear correlation in the P-T space (fig.7.1b). Given that the geotherms calculated by Hasterok and Chapman (2011) are almost linear over this range of temperature and pressure, the equation

of the regression line [1] can be used as a preliminary approximation to the local geotherm.

$$[1] \qquad P\ (kbar) = 0.0561*T\ (^{o}C)-8.3761 \text{ (with } R^2=0.9637)$$

Subsequently Mathcad was used to develop a simplified model of the lithosphere beneath the Lunda Norte province. The calculation of the local geotherm in this area was based on a three-layer model (two different crustal layers and one lithospheric mantle layer), characterised by different heat production contributions and tectono-thermal constraints (fig.7.2). Provided that this region is devoid of seismic tomography, electrical conductivity and heat flow measurements, these parameters were compared to those reported by Artemieva (2006). The premises under which each value was chosen, as well as the description of the equations involved in the modelling, are explained in the electronic appendix.

This thesis does not aim to propose an accurate geophysical model of the SCLM in this area; more data, more accurate parameters and complex computations would be required. However, despite the uncertainties involved in our preliminary calculations, our model suggests that maybe cooler geotherms should be expected beneath the Lunda Norte province. As shown

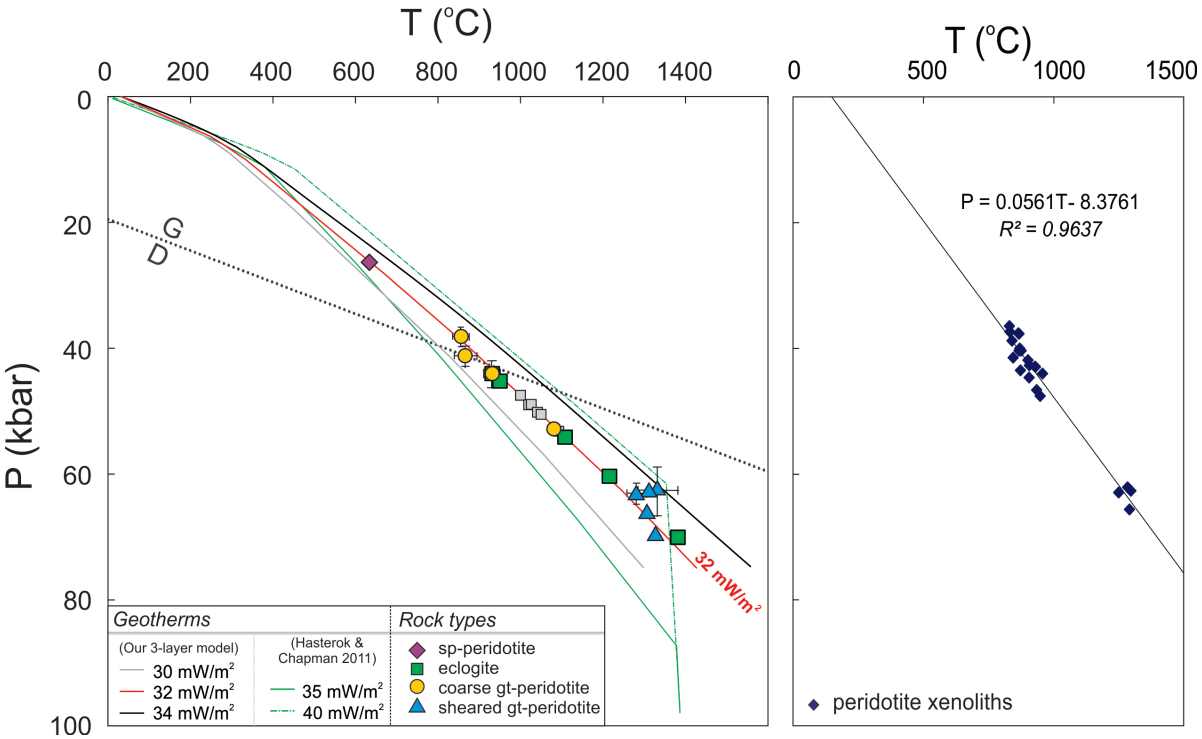

Figure 7.1 PT diagrams for the xenoliths sampled by the Cat115 kimberlite. Eclogites are located between the two garnet peridotite suites (low-T coarse Grt-peridotites and high-T porphyroclastic peridotites) and the Spl-harzburgite yield the lowest PT values. The peridotite xenoliths fit well on the 32 mW/m² geotherm calculated from the 3-layer model. The 35 and 40 mW/m² geotherms of Hasterok and Chapman (2011) are included for comparison, as well as the graphite-diamond (G-D) boundary of Kennedy and Kennedy (1976). The regression line defined by the peridotite xenoliths (right) was used as a good approximation to the local geotherm for the estimation of the pressures of eclogites and the Spl-harzburgite, as well as for the modelling.

in fig. 7.1, the peridotite xenoliths lie along the 32-34 mW/m^2 geotherms calculated by the three-layer model. These are cooler conditions than the ~37mW/m^2 geotherm of Hasterok and Chapman (2011), but are consistent with the calculated thicker lithosphere (>220-240 km). The parameters obtained for a 32 mW/m^2 geotherm are summarised in fig. 7.2.

Xenolith		**31**	**34**	**37**	**30A**	**30B**	**40**	**32B**	**10**	**28**	**24A**	**12**
Rock type		gt-hz	gt- wehr	gt- wehr	gt-lhz	gt-lhz	gt-hz	gt-hz	gt-lhz	gt-hz	gt-hz	gt-hz
Microstructure		coarse	coarse	coarse	coarse	coarse	coarse	coarse	porphyr.	porphyr.	porphyr.	porphyr.
1)	**T (BK)**	-	-	-	984	901	-	-	1268	724	-	1361
	P (BK)	-	-	-	47	21	-	-	54	26	-	60
2)	***T (BK)***	-	870	-	990	934	-	-	1290	725	-	1381
	P (MG)	-	40	-	52	47	-	-	66	28	-	71
3)	**T (NT)**	-	728	-	869	816	-	-	1218	720	-	1273
	P (NT)	-	33	-	55	39	-	-	59	39	-	60
4)	***T (NT)***	-	-	-	840	777	-	-	1196	699	-	1263
	P (BK)	-	-	-	39	16	-	-	50	25	-	56
5)	**T (BK)**	-	867	-	1003	930	-	-	1283	740	-	1369
	P (NT)	-	38	-	62	43	-	-	62	40	-	64
6)	***T (Na)***	-	830	-	897	901	-	-	1296	1679	-	1367
	P (NT)	-	36	-	57	42	-	-	63	93	-	64
7)	**T (Na)**	-	-	-	867	857	-	-	1276	1640	-	1356
	P (BK)	-	-	-	40	19	-	-	55	80	-	60
8)	***T (ca-opx)***	-	864	-	983	928	-	-	1234	1344	-	1269
	P (NT)	-	38	-	61	43	-	-	60	73	-	60
9)	**T (ca-opx)**	-	-	-	907	823	1006	-	1177	1245	1267	1243
	P (BK)	-	-	-	43	18	36	-	48	54	58	55
10)	***T (Na)***	-	832	-	873	906	-	-	1306	1670	-	1385
	P (MG)	-	37	-	43	45	-	-	67	90	-	71
11)	**T (ca-opx)**	-	875	-	926	948	1082	-	1249	1306	1326	1296
	P (MG)	-	40	-	47	48	53	-	63	66	70	65
12)	***T (ON)***	-	-	-	1688	957	-	-	1339	1878	-	1296
	P (NT)	-	-	-	101	44	-	-	65	105	-	65
13)	**T (ON)**	-	-	-	1710	966	1526	-	1374	1819	-	1296
	P (MG)	-	-	-	103	49	83	-	71	100	-	65
14)	***T (ON)***	-	-	-	1581	919	1368	-	1299	1615	-	1296
	P (BK)	-	-	-	89	22	58	-	56	78	-	65
15)	**T (NT)**	-	722	-	845	815	-	-	1223	700	-	1283
	P (MG)	-	30	-	41	38	-	-	61	26	-	64
16)	***T (NiG)***	795	770	884	906	-	1142	1216	1304	1372	1298	1434
	P (geoth)	35	34	40	41	-	56	60	66	70	66	75
T (°C)		**795 ± 13**	**856 ± 20**	**884 ± 42**	**866 ± 27**	**929 ± 44**	**1082**	**1216±12**	**1279±21**	**1306**	**1326**	**1332 ± 48**
P (kbar)		**38 ± 2**	**35 ± 1**	**40 ± 2**	**41 ± 2**	**20 ± 2**	**53**	**60 ± 1**	**63 ± 1**	**66**	**70**	**63 ± 2**

Table 7.1 Equilibration conditions (T in °C, P in kbar) of garnet peridotites sampled by the Cat115 kimberlite. Up to 6 thermometers and 3 barometers were paired to calculate the temperature and pressure of equilibrium of the xenoliths. The averaged PT values and the corresponding standard deviation of pairs showing least dispersion are included in the last row of the table. The thermometer of O'Neill and Wood (1979) tends to overestimate temperature and it has been rejected in all cases. Further explanations about the criteria used to select the best pairs is included in Appendix X. Abbreviations: Thermometers: (BK) - 2 px (Brey and Köhler, 1990); (NT) - Nimis and Taylor (2000); (Na) - partioning of Na between Opx-Cpx (Brey and Köhler, 1990); (ca-opx) - Ca in Opx (Brey and Köhler, 1990); (NiG) – Ni in garnet (Griffin et al., 1989) Barometers: (BK) - Al in coexisting Opx-Grt (Brey and Köhler, 1990); (MG) - Al in enstatite (MacGregor, 1974); (NT) – Cr in cpx (Nimis and Taylor, 2000) and P (geotherm) calculated from the local geotherm (see section 7.2.4)

Surface 0	Z0		Q0 = 0.032	T0 = 25
Upper Crust Layer 1	D1=23000	$A1 = 4.3 \cdot 10^{-7}$	K1 = 2.8	ρ1 = 2700
Surface 1	Z1=D1		Q1 = 0.022	T1 = 247
Lower Crust Layer 2	D2 = 17000	$A2 = 4 \cdot 10^{-7}$	K2 = 2.7	ρ2 = 2800
Surface 2	Z2=D1+D2		Q2 = 0.015	T2 = 365
Lithospheric mantle Layer 3	D3 = 200000	$A3 = 0.2 \cdot 10^{-7}$	K3, model	ρ3 = 3300
Surface m	Zm=D1+D2+D3		Qm = 0.0113	Tm = 1481

Figure 7.2 Results of the three-layer model used to calculate the geotherms. **Thickness:** D_1, D_2, …, D_n, with D_i the thickness (positive) between depth Z_{i-1} and Z_i (depth is computed as a positive quantity) Unit: *meters*. **Heat production:** A_i is the heat produced in layer D_i. Unit: $wat \cdot m^{-3}$ **Thermal conductivity:** K_i is the thermal conductivity in layer D_i. Unit: $wat \cdot m^{-1} \cdot C^{-1}$. For the lithospheric mantle, K_i is dependent on temperature. **Heat flow:** Q_0, Q_1, … Q_m, where Q_0 is the earth surface heat flow (level Z_0), and Q_m is the heat flow in the boundary asthenosphere-lithosphere (conventionally, the level at the intersection of the geotherm and an adiabat corresponding to 1300 °C at the surface). Q_i is then the heat flow at the base of layer "i", the sign being positive. For a three layer model (upper crust, lower crust and lithospheric mantle) four values are obtained: Q_0, Q_1, Q_2 and Q_m. Only Q_0 can be measured or fitted. Unit: $wat \cdot m^{-2}$ **Temperatures:** $T_0, T_1, \ldots T_m$ are temperatures at the surfaces limiting layers. (T_0 = 25°C), Tm>1300 °C . Unit: *°C* **Densities:** ρ_1, ρ_2, …ρ_n, are densities of layers D_1, D_2,…D_n. Unit: $kg \cdot m^{-3}$

7.2.2. Geothermobarometry of eclogites and garnet-pyroxenites

Eclogite thermobarometry is a less well-established method. The wide compositional range of garnet and clinopyroxene complicates the definition of the equation that describes the Fe-Mg exchange between these phases (e.g., Krogh, 2000). Consequently, multiple geothermometers for eclogites and garnet pyroxenites can be found in the literature (e.g., Ellis and Green, 1979; Powell, 1985; Krogh, 1988, 2000; Ai, 1994). In this thesis, the temperature of equilibrium was calculated using the thermometers of Krogh (1988) and Krogh (2000).

Additionally, no reliable barometer has been published to date. As a result, the pressure of equilibration can only be determined by the intersection of the thermometer and the local geotherm. This approach requires a good estimation of the local geotherm, since large differences in the P values can be obtained for the same xenolith depending on the chosen geotherm (fig. 7.3).

As previously seen, the peridotite xenoliths sampled by the Angolan kimberlites plot between the 35 and 40 mW/m^2 geotherms of Hasterok and Chapman (2011) in the PT space. This presents a problem, as neither of them would correctly constrain the PT conditions at which the Angolan eclogites were equilibrated. However, the equations of both geotherms are almost linear between 700 and 1200ºC and thus the equation of the regression line defined by the peridotites [1] is used here as a good approximation to the local geotherm. The results are shown in table 7.2, which also includes the data for other eclogites recovered from the Catoca and the Cat115 kimberlites (Robles-Cruz et al., 2012; Nikitina et al., 2014).

After calculating by stoichiometry the Fe^{3+}/Fe^{2+} ratios of the clinopyroxenes in pyroxenites and eclogites, some of the analyses returned very low or null Fe^{2+}. It has previously been observed that stoichiometric calculation of Fe^{3+} in low-Fe pyroxenes typically overestimates Fe^{3+}, yielding unrealistically high Fe^{3+}/Fe^{2+} ratios (e.g., Mysen and Griffin, 1973; Carswell and Griffin, 1980, 1981). This could be the case in the xenoliths studied here, since the Fe content of the clinopyroxenes in both eclogites and garnet pyroxenites is very low (table 6.8). However, this has important implications for the calculation of the temperature of equilibration of these xenoliths, since the available geothermometers involve the Fe^{2+} in clinopyroxene in the equations (e.g., Krogh, 1988, 2000).

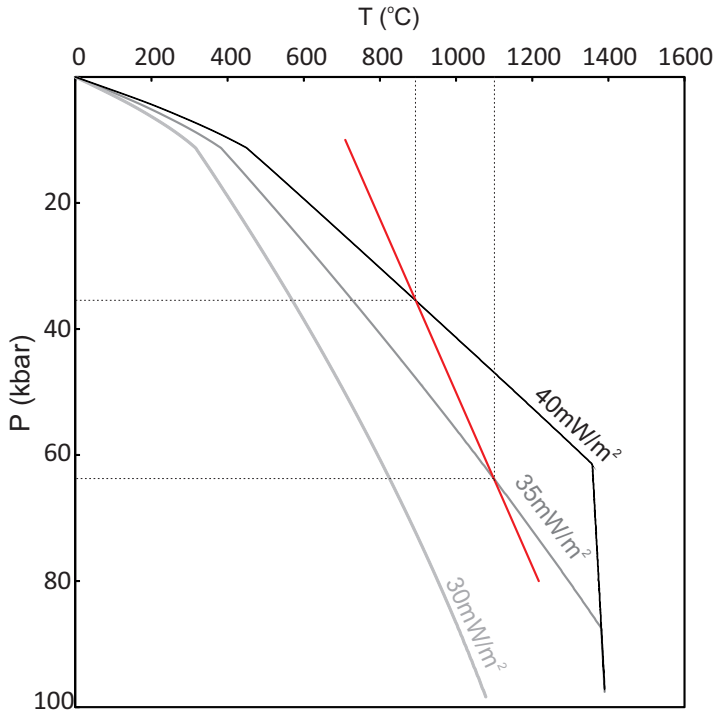

Figure 7.3 PT graph which illustrates the importance of the correct definition of the geotherm to calculate the equilibrium conditions of eclogites and Grt-pyroxenites. The intersection of the thermometer (red line) will give values differing by up to 200ºC and >25 kbar depending on the chosen geotherm. Geotherms from Hasterok and Chapman (2011).

Sample	CAT-18	CAT-34	CAT-41	CAT-26	MGR-13	MGR-35	cat-2	cat-18	cat-1	cat-3	cat-5	cat-11	cat-13	cat-15	cat-14	cat-9
Rock type	high-Mg	low-Mg	low-Mg	gt-px	gt-px	granul	high-Mg	high-Mg	low-Mg	low-Mg	low-Mg	low-Mg	low-Mg	low-Mg	high-Al	high-Al
Fe^{3+} Fe^{2+} by stoichiometry																
T (K88)	-	848	172	600	967	590	-	-	-	-	-	-	-	-	-	-
P (geoth)	-	39	1	25	46	25	-	-	-	-	-	-	-	-	-	-
T (K00)	-	777	95	550	881	590	-	-	-	-	-	-	-	-	-	-
P (geoth)	-	35	-3	23	41	25	-	-	-	-	-	-	-	-	-	-
Assuming all Fe as Fe^{2+}																
T (K88)	1131	1111	1148	889	1535	866	-	-	-	-	-	-	-	-	-	-
P (geoth)	55	54	56	41	78	40	-	-	-	-	-	-	-	-	-	-
T (K00)	1386	1110	1215	929	1697	952	-	-	-	-	-	-	-	-	-	-
P (geoth)	69	54	60	44	87	45	-	-	-	-	-	-	-	-	-	-
T (K00)	1277	1038	1139	853	no int.	890	964	1044	1063	1063	1064	1063	993	1338	1007	1016
P (H40)	57	43	49	33	no int.	35	38	43	44	44	44	44	40	59	41	41
T (N06)	-	-	-	-	-	-	1242	1356	1088	1019	1038	1089	939	1350	915	898
P (H40)	-	-	-	-	-	-	54	60	45	41	42	45	37	60	36	35

Table 7.2 Equilibration conditions (T in °C and P in kbar) of garnet-clinopyroxene assemblages from eclogites, Grt-pyroxenites and granulite. The thermometers used in these calculations are those proposed by Krogh (1988) and Krogh (2000). Pressure was obtained from the intersection of the thermometers and the local geotherm [equation [1], P(geoth)] and the geotherm 40 mW/m² of Hasterok and Chapman (2011) [P(H40)]. PT values of other eclogites sampled by the same kimberlites are included for comparison (Nikitina et al., 2014), calculated using the thermometers of Krogh (2000) and Nikitina et al. (2006).

This problem was addressed by Griffin et al. (1984), who demonstrated that for such compositions the calculated PT conditions are inconsistent with the mineralogical observations if the calculation of Fe^{2+} and Fe^{3+} in clinopyroxene is done by stoichiometry. Instead, the PT values that they obtained assuming that Fe^{3+}=0 were in good agreement with the xenolith assemblage and thus it is suggested to be a reliable basis for geothermometry.

Therefore, a new calculation of the PT conditions was done for the low-Fe pyroxene in eclogites and garnet pyroxenites sampled by the Angolan kimberlites. In these new results, we assumed that all Fe occurs as Fe^{2+}. Again, to calculate the pressure, the equation of the regression line defined by the peridotite xenoliths on the PT space is used. The PT values are compiled in table 7.2 and shown in fig. 7.4. The values obtained by assuming that Fe^{3+}=0 clearly differ from those obtained previously.

Other mantle eclogites beneath the Kasai Craton have recently been studied (Nikitina et al., 2014). These authors distinguished three different types of eclogites, based on their composition: Al-rich, kyanite-bearing eclogites, Mg-poor eclogites and Mg-rich eclogites. Using different thermometers, Nikitina and coworkers (2014) also calculated the PT conditions at which these xenoliths were equilibrated. In fig. 7.4, their results are compared with ours after obtaining pressure from the geotherm 40mW/m² of Hasterok and Chapman (2011) and

using Krogh's thermometer (Krogh, 2000). Although our data show more dispersion, they are broadly consistent with the results of Nikitina et al. (2014) and Ashchepkov et al. (2012). In the gap between the two populations of garnet peridotites, with a single exception, only eclogite and garnet pyroxenite xenoliths are found (950-1250ºC; 44-58 kbar). These results are in very good agreement with the observations made by Nikitina et al. (2014).

Both low-Mg and high-Mg eclogites were recovered from the Catoca kimberlite. Using the 40mW/m^2 of Hasterok and Chapman (2011), we could see that the two low-Mg eclogites were equilibrated at slightly lower temperatures and pressures (1040-1140ºC, 43-49 kbar) than the high-Mg eclogite (1280ºC, 57 kbar). This correlation between composition and PT conditions was also reported for other eclogite xenoliths of the same kimberlitic area. Low-Mg eclogites would be typically found at 940-1100ºC and 37-45 kbar; while high-Mg eclogites were equilibrated at >1200ºC and >50 kbar (Nikitina et al., 2014). No high-Al eclogites, common in shallower depths, were found in this study. Instead, the lowest PT values were observed in the garnet-pyroxenites and granulites (850-890ºC, ~35 kbar). The thermometer in sample MGR-13 did not intersect any of the geotherms, so no equilibrium conditions could be constrained. In this case, the PT values obtained by stoichiometric distribution of Fe^{2+} and Fe^{3+} in clinopyroxene could be used, although they should be treated with caution because of the low Fe contents in the pyroxene. The equilibration conditions of this garnet pyroxenite under this assumptions are consistent with those of the other garnet pyroxenite and the granulite.

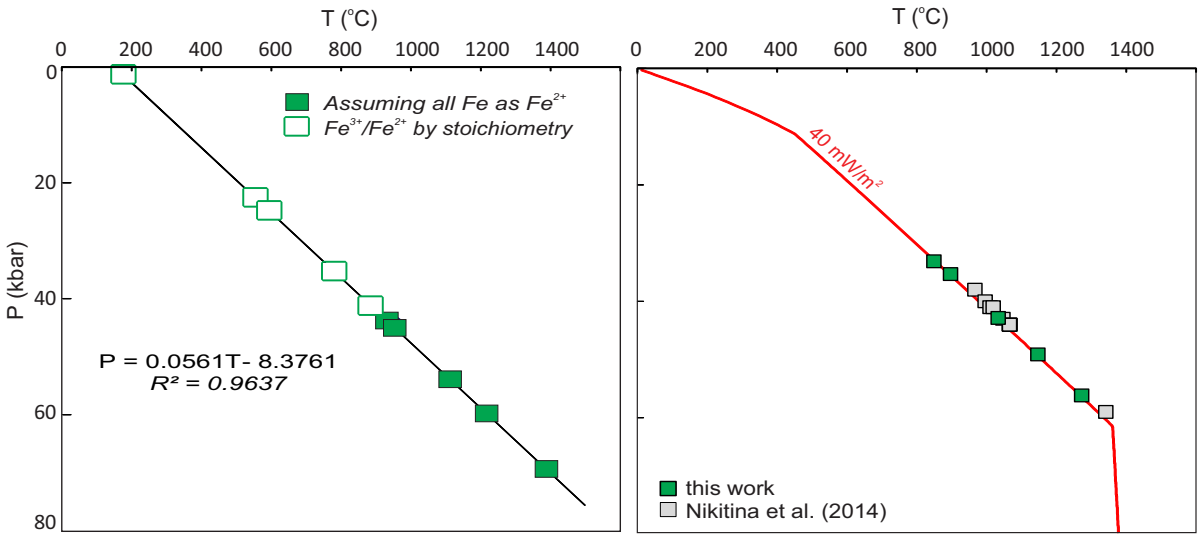

Figure 7.4 PT diagram for eclogite xenoliths from the Catoca and Cat115 kimberlites. The upper graph shows the large differences in the calculated equilibrium conditions (T and P) of the same xenoliths, depending on the Fe^{3+}- Fe^{2+} distribution in clinopyroxene (see text). Pressure was obtained from the regression line defined by the peridotite xenoliths. In the lower diagram, the same xenoliths are represented against the 40mw/m^2 geotherm of Hasterok and Chapman (2011) so they could be compared with other eclogite xenoliths sampled by the same kimberlites (Nikitina et al., 2014). In all cases, the thermometer used was that of Krogh (2000).

7.2.3. Geothermobarometry spinel-harzburgite

A similar approach was taken to constrain the pressure and temperature conditions of equilibrium in the Spl-harzburgite, which lacks clinopyroxene and garnet. In this case, the temperature of equilibrium of the xenolith was obtained using the Zn-in-spinel thermometer developed by Ryan et al (1996) and its pressure was obtained by plotting T_{Zn} against the calculated geotherm, as was done for eclogites and garnet pyroxenites. The Spl-harzburgite yield the expected lowest temperatures (630 ± 41 ºC), which corresponds to a pressure of 27 kbar (80 km).

7.2.4. Geothermobarometry of garnet xenocrysts

The Ni-in-garnet thermometer of Ryan et al. (1996) has been used to constrain the temperature of equilibration of the garnet xenocrysts derived from peridotites. This thermometer is a modification of the "Ni thermometer" of Griffin et al. (1989), which is based on the strong temperature dependence of the partitioning of this element between olivine and garnet, and the small range of Ni contents in peridotitic olivine.

Xenolith characterisation (chapter 6) showed that chromite and garnet are not in equilibrium in the garnet peridotites sampled by the kimberlites. As a consequence, pressure could not be calculated using the Cr-barometer proposed by Ryan et al. (1996), since it typically underestimates it in Cr-undersaturated rocks. Therefore, the pressure at which each xenocryst crystallised was again obtained by plotting the calculated temperature against the local geotherm defined by the xenoliths (equation [1]). However, at high temperatures garnet xenocrysts typically define a kinked geotherm which is commonly subparallel to the diamond-graphite boundary. As a consequence, pressure is likely to have been overestimated in the garnet xenocrysts with the highest Ni contents.

Representative analyses are given in table 7.3. As shown in fig. 7.5, most of the xenocrysts were sampled from the base of the lithosphere (1060-1500 ºC), with few representation of the upper lithospheric mantle, which corresponds to pressures ranging between 61 and 93 kbar.

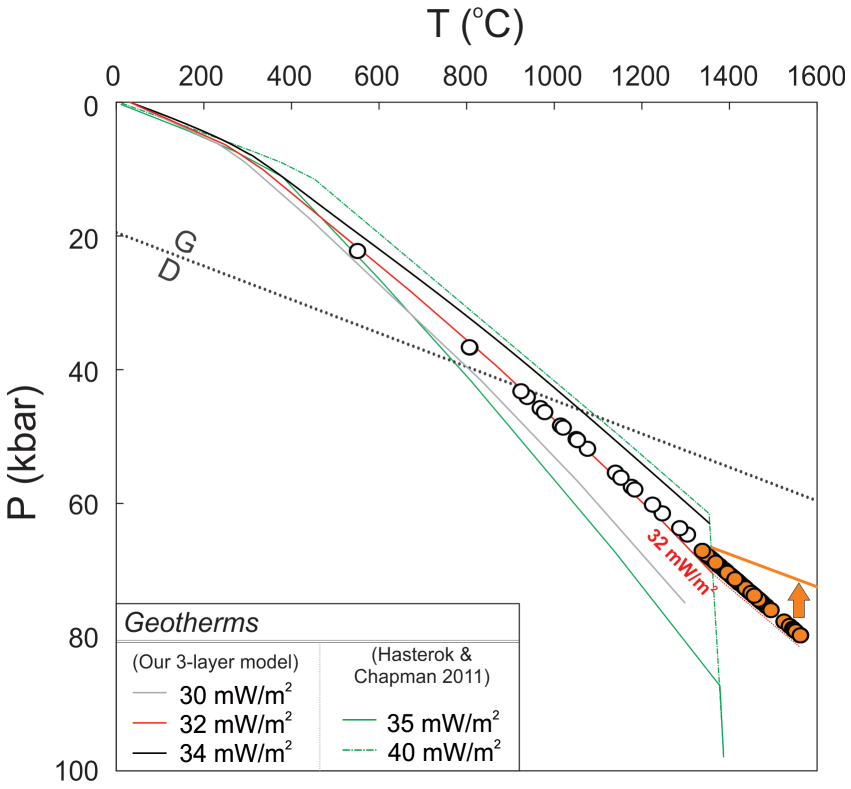

Figure 7.5 PT diagrams for the garnet xenocryst sampled by the Angolan kimberlites. Temperature was calculated using the Ni in garnet thermometer of Griffin et al. (1989) and pressure from the local geotherm (equation [1]). The geotherms 35 and 40 mW/m² of Hasterok and Chapman (2011) are included for comparison, as well as the graphite-diamond (G-D) boundary of Kennedy and Kennedy (1976). The high-T garnet xenocrysts in orange indicate that the calculated pressures might have been overestimated if a kinked geotherm was present.

7.3. Compositional structure of the lithospheric mantle

7.3.1. Thermal structure of the SCLM beneath the Lundas Norte province

The geotherm defined by the Angolan xenoliths lies between the 35 and 40 mW/m² geotherms of Hasterok and Chapman (2011). These results are consistent with those of Ashchepkov et al. (2012) and Robles-Cruz et al. (2012b) for the same kimberlitic province. These geotherms are slightly cooler than those from South Africa (Bell et al., 2003) and Namibia (Franz et al., 1996). Additionally, our three-layer model indicates that even slightly cooler conditions (30-34mW/m²) should be expected in the SCLM in NE Angola. If the approach taken in this model is valid, it would indicate that the SCLM is thicker than previously suggested (>220km), which would also be consistent with a very thick (300km) lithosphere in the core of the Congo-Kasai craton (O'Reilly et al., 2009).

The combination of the petrological and compositional data with the PT conditions reveals that the SCLM beneath the Lunda Norte kimberlitic province is layered (fig. 7.6). The

Table 7.3 Selected major- and trace-element analyses of garnet xenocrysts. Temperature was calculated using the Ni in garnet thermometer (Griffin et al., 1989). "bdl" stands for values below detection limit.

Sample	**32a_95**	**31_37**	**26_g_019**	**31_39b**	**32a_87**	**6A_g_065**	**32a_90**	**32a_97**	**32A_e_085**	**31b_16b**	**31_31b**	**32a_88**
Rock Type	Lhz	Ca-Hz	Whrl	Ca-Hz	Lhz	Low-Cr	Lhz	Lhz	Lhz	Lhz	Low-Cr	Lhz
Metasom. Type	*Depleted, low Sr*	*High Zr, low Ti, Sr*	*High Zr, low Ti, Sr*	*Depleted, low Sr*	*High Ti, Zr*	*High Ti, Zr*	*High Ti, Zr*	*High Ti, Zr*	*High Ti, Zr*	*High Ti, Zr*	*High Ti, Zr*	*High Ti, Zr*
oxides (wt%)												
SiO_2	41.88	41.60	38.38	41.92	42.42	41.04	41.32	42.34	41.23	41.35	42.79	42.26
Al_2O_3	20.42	18.42	14.36	18.77	20.37	21.39	17.12	21.20	20.9	16.33	21.80	20.79
MgO	20.46	21.25	15.13	22.12	22.45	21.21	20.49	22.81	21.33	21.03	21.98	22.28
Cr_2O_3	4.26	6.66	10.75	6.62	2.61	1.37	6.54	1.55	2.04	8.04	0.50	2.12
MnO	0.48	0.40	0.52	0.35	0.28	0.37	0.30	0.28	0.28	0.34	0.28	0.25
K_2O	bdl	bdl	bdl	bdl	bdl	0.01	bdl	bdl	0.01	bdl	bdl	bdl
CaO	4.84	4.95	9.36	4.47	4.56	3.94	5.95	4.26	4.34	5.95	4.07	4.65
Na_2O	0.06	0.05	0.09	0.05	0.09	0.13	0.07	0.10	0.1	0.09	0.16	0.09
TiO_2	0.25	0.14	0.6	0.09	0.75	0.79	0.85	0.79	0.8	1.04	1.20	0.84
FeO	8.24	7.19	9.53	6.75	7.54	9.58	8.20	7.61	8.41	6.99	8.82	7.33
NiO	bdl	bdl	0.05	bdl	bdl	0.02	bdl	bdl	0.08	bdl	bdl	bdl
Total	100.89	100.66	98.77	101.14	101.07	99.86	100.84	100.94	99.52	101.16	101.60	100.61
LA-ICP-MS (ppm)												
Li	0.391	bdl	NA	bdl	0.39	NA	bdl	0.53	NA	0.289	0.46	bdl
Be	bdl	bdl	NA	bdl	bdl	NA	bdl	bdl	NA	0.102	bdl	bdl
B	1.08	1.56	NA	1.43	1.97	NA	1.36	1.64	NA	2.65	1.75	1.73
Na	383	329	NA	275.3	720	NA	464	643	NA	590	956	559
P	108.7	233	NA	84.6	117.3	NA	170	134.6	NA	163	191	147.1
K	bdl	bdl	NA	1.74	bdl	NA	1.86	2.65	NA	1.97	bdl	111.2
Ca	31520	31500	NA	29090	24950	NA	38700	27260	NA	38500	26110	29640
Sc	89.6	116.6	126.0	128.3	81.2	71.4	88.5	70.1	62.3	145.4	60.3	75.9
Ti	1309	823	3220	525	4280	4290	4850	4380	4960	5650	6500	4680
V	212.9	208.1	191.2	283.7	195.3	191.8	302.2	216.3	213	373	253.6	232.0
Cr	25230	41200	53700	39600	11890	8190	40700	9020	12970	49100	2750	12750
Mn	3580	2986	4140	2679	2516	2170	2241	2038	2070	2280	1982	2017
Co	38.7	39.3	36.6	40.1	45.2	49.6	46.2	44.9	47.2	41.8	48.7	45.8
Ni	18.09	34.2	35.4	48.1	71.0	91.1	95.5	101.4	102.1	103.8	107.2	109.2
Cu	bdl	0.089	NA	bdl	0.496	NA	0.558	0.581	NA	0.847	0.429	0.572
Zn	9.23	8.81	NA	9.63	19.57	NA	16.61	17.90	NA	12.14	22.96	15.62
Ga	8.52	5.80	13.75	3.87	11.06	10.58	12.83	13.07	11.73	6.62	16.33	11.02
Rb	bdl	bdl	bdl	bdl	bdl	bdl	bdl	bdl	bdl	bdl	bdl	0.591
Sr	0.143	0.554	0.760	0.541	0.288	0.401	0.642	0.399	0.393	0.753	0.297	0.581
Y	15.49	15.60	37.3	1.790	17.43	16.22	21.69	17.67	13.12	15.63	24.73	16.46
Zr	19.32	64.7	157.5	20.48	43.4	45.3	87.0	50.3	46.8	102.7	80.0	68.6
Nb	0.0570	0.305	0.300	0.172	0.156	0.1140	0.412	0.224	0.226	0.382	0.397	0.197
Cs	bdl	bdl	bdl	bdl	bdl	bdl	bdl	bdl	bdl	bdl	bdl	bdl
Ba	bdl	bdl	bdl	bdl	bdl	bdl	0.0074	0.0097	bdl	bdl	bdl	0.183
La	0.0099	0.0357	bdl	0.0348	0.0087	bdl	0.0403	0.0124	bdl	0.0630	0.0212	0.0179
Ce	0.146	0.677	0.667	0.568	0.134	0.224	0.568	0.247	0.237	0.516	0.157	0.275
Pr	0.0786	0.287	0.241	0.287	0.0478	0.0820	0.200	0.0701	0.0700	0.218	0.0692	0.108
Nd	1.146	3.14	2.26	2.81	0.488	0.722	2.02	0.803	0.672	2.16	0.865	1.205
Sm	0.835	2.10	2.22	1.146	0.418	0.639	1.364	0.757	0.637	1.840	0.885	0.815
Eu	0.365	0.888	1.200	0.321	0.269	0.346	0.679	0.387	0.343	0.872	0.429	0.351
Gd	1.408	3.36	4.18	0.630	1.288	1.350	2.85	1.46	1.380	3.19	2.05	2.01
Tb	0.300	0.464	0.924	0.0879	0.241	0.319	0.507	0.338	0.274	0.590	0.484	0.367
Dy	2.21	2.87	7.34	0.298	2.62	2.64	3.80	2.96	2.23	3.42	3.79	2.84
Ho	0.571	0.574	1.529	0.0583	0.665	0.640	0.904	0.631	0.475	0.581	0.965	0.635
Er	1.727	1.530	4.05	0.250	2.196	2.09	2.374	2.13	1.490	1.441	2.87	1.813
Tm	0.256	0.207	0.551	0.0283	0.396	0.322	0.320	0.312	0.235	0.187	0.433	0.281
Yb	1.811	1.463	3.63	0.457	2.72	2.26	2.083	2.41	1.680	1.120	3.14	1.883
Lu	0.278	0.219	0.420	0.1131	0.436	0.335	0.343	0.371	0.237	0.160	0.467	0.293
Hf	0.382	0.734	2.91	0.398	1.100	1.083	2.129	1.054	1.012	2.52	1.777	1.699
Ta	bdl	0.0239	0.0236	0.0318	0.0205	bdl	0.0469	0.0200	0.01680	0.0341	0.0286	0.0245
Pb	bdl	0.015	NA	bdl	bdl	NA	bdl	0.0119	NA	bdl	bdl	bdl
Th	0.0117	0.0131	NA	0.0218	bdl	NA	bdl	0.0117	NA	0.0166	0.0087	0.0063
U	0.0166	0.0318	NA	0.0346	bdl	NA	0.0385	bdl	NA	0.0213	0.0173	bdl
T (NiG)	**770**	**919**	**929**	**1019**	**1155**	**1258**	**1279**	**1307**	**1310**	**1318**	**1333**	**1343**

Table 7.3 (continued) Selected major- and trace-element analyses of garnet xenocrysts. Temperature was calculated using the Ni in garnet thermometer (Griffin et al., 1989). "bdl" stands for values below detection limit.

Sample	32a_95	31_37	26_g_019	31_39b	32a_87	6A_g_065	32a_90	32a_97	32A_e_085	31b_16b	31_31b	32a_88
Rock Type	Lhz	Ca-Hz	Whrl	Ca-Hz	Lhz	Low-Cr	Lhz	Lhz	Lhz	Lhz	Low-Cr	Lhz
Metasom. Type	*Depleted, low Sr*	*High Zr, low Ti, Sr*	*High Zr, low Ti, Sr*	*Depleted, low Sr*	*High Ti, Zr*	*High Ti, Zr*	*High Ti, Zr*	*High Ti, Zr*	*High Ti, Zr*	*High Ti, Zr*	*High Ti, Zr*	*High Ti, Zr*
oxides (wt%)												
SiO_2	41.88	41.60	38.38	41.92	42.42	41.04	41.32	42.34	41.23	41.35	42.79	42.26
Al_2O_3	20.42	18.42	14.36	18.77	20.37	21.39	17.12	21.20	20.9	16.33	21.80	20.79
MgO	20.46	21.25	15.13	22.12	22.45	21.21	20.49	22.81	21.33	21.03	21.98	22.28
Cr_2O_3	4.26	6.66	10.75	6.62	2.61	1.37	6.54	1.55	2.04	8.04	0.50	2.12
MnO	0.48	0.40	0.52	0.35	0.28	0.37	0.30	0.28	0.28	0.34	0.28	0.25
K_2O	bdl	bdl	bdl	bdl	bdl	0.01	bdl	bdl	0.01	bdl	bdl	bdl
CaO	4.84	4.95	9.36	4.47	4.56	3.94	5.95	4.26	4.34	5.95	4.07	4.65
Na_2O	0.06	0.05	0.09	0.05	0.09	0.13	0.07	0.10	0.1	0.09	0.16	0.09
TiO_2	0.25	0.14	0.6	0.09	0.75	0.79	0.85	0.79	0.8	1.04	1.20	0.84
FeO	8.24	7.19	9.53	6.75	7.54	9.58	8.20	7.61	8.41	6.99	8.82	7.33
NiO	bdl	bdl	0.05	bdl	bdl	0.02	bdl	bdl	0.08	bdl	bdl	bdl
Total	100.89	100.66	98.77	101.14	101.07	99.86	100.84	100.94	99.52	101.16	101.60	100.61
LA-ICP-MS (ppm)												
Li	0.391	bdl	NA	bdl	0.39	NA	bdl	0.53	NA	0.289	0.46	bdl
Be	bdl	bdl	NA	bdl	bdl	NA	bdl	bdl	NA	0.102	bdl	bdl
B	1.08	1.56	NA	1.43	1.97	NA	1.36	1.64	NA	2.65	1.75	1.73
Na	383	329	NA	275.3	720	NA	464	643	NA	590	956	559
P	108.7	233	NA	84.6	117.3	NA	170	134.6	NA	163	191	147.1
K	bdl	bdl	NA	1.74	bdl	NA	1.86	2.65	NA	1.97	bdl	111.2
Ca	31520	31500	NA	29090	24950	NA	38700	27260	NA	38500	26110	29640
Sc	89.6	116.6	126.0	128.3	81.2	71.4	88.5	70.1	62.3	145.4	60.3	75.9
Ti	1309	823	3220	525	4280	4290	4850	4380	4960	5650	6500	4680
V	212.9	208.1	191.2	283.7	195.3	191.8	302.2	216.3	213	373	253.6	232.0
Cr	25230	41200	53700	39600	11890	8190	40700	9020	12970	49100	2750	12750
Mn	3580	2986	4140	2679	2516	2170	2241	2038	2070	2280	1982	2017
Co	38.7	39.3	36.6	40.1	45.2	49.6	46.2	44.9	47.2	41.8	48.7	45.8
Ni	18.09	34.2	35.4	48.1	71.0	91.1	95.5	101.4	102.1	103.8	107.2	109.2
Cu	bdl	0.089	NA	bdl	0.496	NA	0.558	0.581	NA	0.847	0.429	0.572
Zn	9.23	8.81	NA	9.63	19.57	NA	16.61	17.90	NA	12.14	22.96	15.62
Ga	8.52	5.80	13.75	3.87	11.06	10.58	12.83	13.07	11.73	6.62	16.33	11.02
Rb	bdl	bdl	bdl	bdl	bdl	bdl	bdl	bdl	bdl	bdl	bdl	0.591
Sr	0.143	0.554	0.760	0.541	0.288	0.401	0.642	0.399	0.393	0.753	0.297	0.581
Y	15.49	15.60	37.3	1.790	17.43	16.22	21.69	17.67	13.12	15.63	24.73	16.46
Zr	19.32	64.7	157.5	20.48	43.4	45.3	87.0	50.3	46.8	102.7	80.0	68.6
Nb	0.0570	0.305	0.300	0.172	0.156	0.1140	0.412	0.224	0.226	0.382	0.397	0.197
Cs	bdl	bdl	bdl	bdl	bdl	bdl	bdl	bdl	bdl	bdl	bdl	bdl
Ba	bdl	bdl	bdl	bdl	bdl	bdl	0.0074	0.0097	bdl	bdl	bdl	0.183
La	0.0099	0.0357	bdl	0.0348	0.0087	bdl	0.0403	0.0124	bdl	0.0630	0.0212	0.0179
Ce	0.146	0.677	0.667	0.568	0.134	0.224	0.568	0.247	0.237	0.516	0.157	0.275
Pr	0.0786	0.287	0.241	0.287	0.0478	0.0820	0.200	0.0701	0.0700	0.218	0.0692	0.108
Nd	1.146	3.14	2.26	2.81	0.488	0.722	2.02	0.803	0.672	2.16	0.865	1.205
Sm	0.835	2.10	2.22	1.146	0.418	0.639	1.364	0.757	0.637	1.840	0.885	0.815
Eu	0.365	0.888	1.200	0.321	0.269	0.346	0.679	0.387	0.343	0.872	0.429	0.351
Gd	1.408	3.36	4.18	0.630	1.288	1.350	2.85	1.46	1.380	3.19	2.05	2.01
Tb	0.300	0.464	0.924	0.0879	0.241	0.319	0.507	0.338	0.274	0.590	0.484	0.367
Dy	2.21	2.87	7.34	0.298	2.62	2.64	3.80	2.96	2.23	3.42	3.79	2.84
Ho	0.571	0.574	1.529	0.0583	0.665	0.640	0.904	0.631	0.475	0.581	0.965	0.635
Er	1.727	1.530	4.05	0.250	2.196	2.09	2.374	2.13	1.490	1.441	2.87	1.813
Tm	0.256	0.207	0.551	0.0283	0.396	0.322	0.320	0.312	0.235	0.187	0.433	0.281
Yb	1.811	1.463	3.63	0.457	2.72	2.26	2.083	2.41	1.680	1.120	3.14	1.883
Lu	0.278	0.219	0.420	0.1131	0.436	0.335	0.343	0.371	0.237	0.160	0.467	0.293
Hf	0.382	0.734	2.91	0.398	1.100	1.083	2.129	1.054	1.012	2.52	1.777	1.699
Ta	bdl	0.0239	0.0236	0.0318	0.0205	bdl	0.0469	0.0200	0.01680	0.0341	0.0286	0.0245
Pb	bdl	0.015	NA	bdl	bdl	NA	bdl	0.0119	NA	bdl	bdl	bdl
Th	0.0117	0.0131	NA	0.0218	bdl	NA	bdl	0.0117	NA	0.0166	0.0087	0.0063
U	0.0166	0.0318	NA	0.0346	bdl	NA	0.0385	bdl	NA	0.0213	0.0173	bdl
T (NiG)	**770**	**919**	**929**	**1019**	**1155**	**1258**	**1279**	**1307**	**1310**	**1318**	**1333**	**1343**

origin of this layering, as well as the similarities and differences with other Archean cratons will be discussed next.

The shallowest layer of the SCLM is represented in our section by the Spl-harzburgite xenolith (630ºC, 27 kbar), which is characterised by highly magnesian olivine (#Mg=92.5-93) and orthopyroxene (#Mg=92). Both clinopyroxene and garnet are absent in this xenolith, indicating that no refertilisation of the rock took place after the Archean depletion. The mineral modes and mineral composition of this layer are similar to the shallowest part of the SCLM of the Slave craton (Kopylova and Caro, 2004) (see table 7.4). In contrast, Spl-peridotites from other cratons are commonly richer in orthopyroxene (e.g., Boyd et al., 1997; Simon et al., 2007). The low PT conditions of equilibration calculated for this xenolith locate it within the graphite stability field, which rules it out as a layer of interest for diamond exploration. Therefore, it will not be included in further interpretations.

The occurrence of two distinct Grt-peridotite suites -coarse and sheared- has been documented in most of the cratons worldwide (e.g., Boyd and Nixon, 1975; Mercier and Nicolas, 1975). As in most cratons, the coarse garnet peridotites sampled by the Angolan kimberlites represent the low-T garnet peridotite suite (850-1080ºC; 38-53 kbar; 105-145km). Therefore,

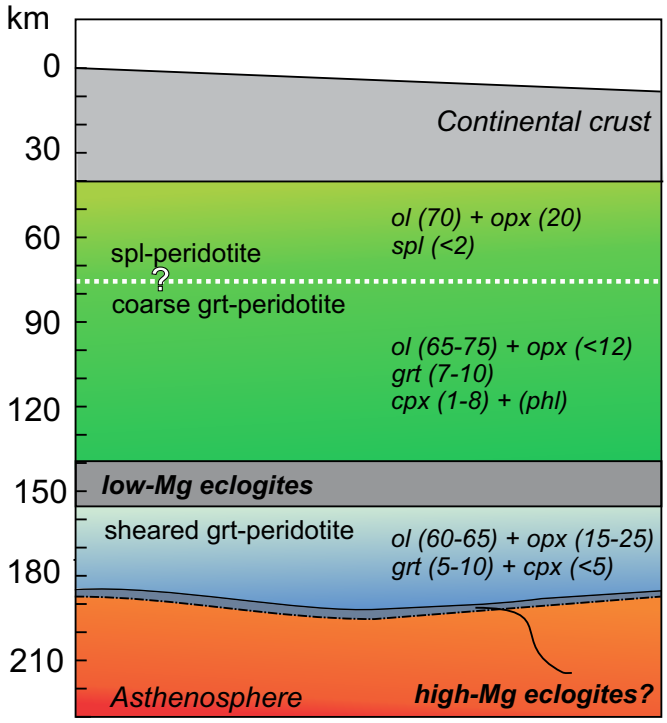

Figure 7.6 Sketch showing a synthesis of the different litotypes sampled in depth by the cat115 and Catoca kimberlites. The thickness of the porphyroclastic (sheared) peridotite layer could be less than shown, and the eclogites are more likely to occur as lenses rather than as a thick layer.

the shallow SCLM in the studied area is characterised by high olivine (65-75 vol%) and clinopyroxene (up to 10 vol%) contents, coupled with remarkably low orthopyroxene modes (commonly <10 vol%). These modal abundances are indicative of a highly depleted SCLM, probably caused by a massive partial melting episode during the Archean (Griffin et al., 2003). The porphyroclastic peridotites were equilibrated at significantly higher PT conditions (1280-1330ºC; 63-70 kbar; 180-190km). This is also consistent with the deep location of the sheared lherzolites in most cratonic areas worldwide (e.g., Nixon, 1987; Smith et al., 1993). However, the SCLM beneath the Lunda Norte province may have deeper roots (maybe >220km) than the other cratonic areas in Africa, but thinner than in Yakutia (Griffin and O'Reilly, 2007). Porphyroclastic garnet peridotites have significantly higher modes of orthopyroxene (15-25 vol%) than coarse peridotites, but almost no chromian diopside (<5 vol%). As shown in table 7.4, this modal distribution is completely different to that of the SCLM in the Kaapvaal (e.g., Boyd and Mertzman, 1987; Simon et al., 2007) and the Siberian SCLM (e.g., Boyd et al., 1997). However, it could be comparable to the modal abundances of the low-T and high-T layers of the southern Slave craton (Kopylova and Caro, 2004), but also to those typically found in abyssal peridotites (Niu et al., 1997). Two models will be proposed in the following section

	Kaapvaal	**Siberian**	**Slave**	**Lunda Norte**	**Abyssal peridotites**
	(Simon et al., 2007)	(Boyd et al., 1997)	(Kopylova and Caro, 2004)	This work	Niu et al. (1997)
Spl-peridotites					
	70.0	54.9	**78.3**	**76.1**	**73.6**
	28.3	41.9	**19.2**	**21.7**	**20.7**
	1.3	2.5	**0.6**		**4.9**
	0.7	0.7	**1.2**	**2.2**	**0.7**
Low-T Grt-peridotites					
	58.3	59	**78.8**	**73.6**	-
	30.3	36.7	**12.7**	**8.6**	-
	4.6	0.7	**3.6**	**7.5**	-
	8.3	3.4	**5.3**	**10.4**	-
	2.2	0.2	-	-	-
High-T Grt-peridotites					
	65	64.4	**71.8**	**70.2**	-
	28	30.3	**19.6**	**20.0**	-
	1.75	3	**1.9**	**2.6**	-
	8.5	2.3	**6.9**	**7.2**	-
	0.6				

Table 7.4 Comparison of the averaged mineral modes observed in each type of peridotite with its equivalent in other cratons worldwide. Please note that since there are significant heterogeneities within the blocks forming the Archean cratons, the average mineral modes shown in this table might not be totally representative of the whole craton.

to explain the observed dissimilarities between the shallow and the deep layers of the SCLM beneath the Lunda Norte province.

The vertical distribution described above also implies that there is a decrease in the #Mg of olivine with depth, coupled with a less significant decrease in #Mg of the coexisting clinopyroxene. The drastic lowering of the #Mg number in olivine in the deepest layer could be linked to the infiltration of basaltic fluids near the base of the SCLM (Smith and Boyd, 1987; Griffin et al., 2009), which is also related to strong metasomatism and introduction of garnet and clinopyroxene in the deep lithosphere (e.g., Griffin et al., 1989). Additionally, garnet in the deepest peridotites typically has higher Cr, Ti and Zr contents than that found in the shallow SCLM, whereas clinopyroxene is commonly more magnesian and has higher Cr contents in the low-T suite. These compositional variations are a common feature of most of the Archean cratons worldwide (Griffin et al., 1999b and references therein).

The occurrence of low-Mg eclogites in the gap (1040-1140ºC, 43-49 kbar; 138-155km) between the two different textural types of garnet peridotites is less common. However, our results are consistent with the eclogitic level detected by Ashchepkov et al. (2012) and Nikitina et al. (2014) between 130-170 km depth in the kimberlitic cluster. The low-T garnet pyroxenites (860-890ºC; 33-35 kbar; ~110km) described in this thesis could also be comparable to the "eclogitic" layers defined by Ashchepkov et al. (2012) at 30 kbar. The presence of another deep (>200km) eclogite level might be inferred from a high-Mg eclogite sampled by the Catoca kimberlite. Deep eclogites have also been documented at the base of the SCLM beneath the Lundas province (Ashchepkov et al., 2012; Nikitina et al., 2014) and are common in most of the world's cratons (e.g., Carswell et al., 1981; Viljoen et al., 2005; Griffin and O'Reilly, 2007).

7.3.2. Origin of the structure of the SCLM beneath the Lunda Norte province

The interpretation of the origin and evolution of the layered lithosphere in NE Angola is complex, since there is a total lack of regional geophysical data of the SCLM beneath the Lunda Norte province and this study involves only a limited set of peridotite xenoliths. Elucidating the origin and role of the eclogites in this SCLM becomes even more complicated, due to the small number of eclogite xenoliths available for this thesis. Therefore, the results published by Nikitina et al. (2014) on other eclogites of the Catoca and Cat115 will be also considered in the

following discussion.

The petrographic and chemical characterisation of garnet peridotite xenoliths suggests that the shallow peridotite layer has a different origin than the deep one. Moreover, the modal mineral abundances in the low-T and high-T peridotites indicate that their formation and evolution may differ to those previously described in the Kaapvaal or the Siberian craton. Additionally, the contrasting metasomatic signatures recorded by garnet and clinopyroxene in these layers could also be seen as an evidence of a different origin (see chapter 8). If this premise is true, two different models can be invoked to explain the current structure of the SCLM beneath the Lunda Norte province. However, in both cases constraining the origin of the eclogites found at around 140km is essential: were they part of a subducted slab, or magmatic cumulates?

The origin of the eclogite "layer(s)"

The origin of the eclogite xenoliths found in kimberlites is a controversial topic which leads to strong debate within the scientific community. Although eclogites make up less than 1% of the upper mantle (Schulze, 1989), they can provide invaluable information about the origin of the SCLM and the dynamics of the mantle. Two main models for their origin have been proposed in the literature: the "subduction model" and the "magmatic model".

The former model has been the most accepted theory over the last two decades and it considers eclogite xenoliths as samples from a subducted oceanic crust in the SCLM (e.g., Jacob, 2004; Schmickler et al., 2004). Arguments favouring this theory include the presence of coesite, quartz and/or kyanite in some eclogite xenoliths, which could not be in equilibrium with peridotites. Additionally, positive Eu and Sr anomalies and a flat HREE pattern in the reconstructed bulk composition are commonly explained by the former occurrence of plagioclase (usually known as "ghost-plagioclase signatures"). However the strongest argument for a subduction origin is the wide range of $\delta^{18}O$ reported in eclogite xenoliths, which can either be higher or lower than the homogeneous $\delta^{18}O$ signatures of the Earth's mantle (+5.5 ± 0.4 ‰; Mattey et al., 1994). This wide spectrum has been interpreted as a consequence of a differential alteration of the original oceanic crust by seawater (Jacob et al., 1994; Barth et al., 2001).

The magmatic model was strongly promoted by O'Hara and coworkers (1975) and later

by Griffin & O'Reilly (2007) and Huang et al. (2012). This model sees the eclogites as magmatic rocks crystallised and re-equilibrated at high pressure. Defenders of this model argue that in these eclogites, garnet crystallises as a consequence of exsolution and re-equilibration processes from high-Al clinopyroxenes, which in turn crystallised from mafic-ultramafic magmas in the deep mantle (Huang et al., 2012). Therefore this process eludes a strong argument against this theory (at high pressure the first mineral to accumulate would be olivine), because it implies that garnet and clinopyroxene do not crystallise at the same time. The presence of rutile exsolution in garnet and clinopyroxene is also invoked to support a magmatic origin (Huang et al., 2012).

Some preliminary considerations should be taken into account before seeking the protolith of these eclogites. It has recently been demonstrated that eclogites may experience significant modification of their chemistry and microstructure by mantle metasomatic processes, which would lead to misinterpretation of the data. Detailed petrographic studies, coupled with in situ mineral analyses, showed that type I eclogites of McCandless and Gurney (1989) could be the product of pervasive metasomatism of fresh type II eclogites (Gréau et al., 2011; Huang et al., 2012). Therefore, the study of type II eclogites should be preferred for the determination of the origin of eclogites. Major-element composition of the three eclogite xenoliths analysed in this thesis indicates that they belong to type II eclogites, which a priori would make them suitable targets to elucidate the origin of the eclogites in this area.

However, the studied eclogites also share some petrographic characteristics and trace-element signatures with the metasomatised type I eclogites in Roberts Victor kimberlite (Gréau et al., 2011). A first consequence would be that the classification used in the Kaapvaal craton may not be applicable to the mantle eclogites of the Lunda Norte province. Additional evidence for interaction with a metasomatic agent was inferred by the occurrence of spongy clinopyroxene in the low-Mg eclogites, along grain boundaries and fractures. Even if this enrichment is interpreted to have taken place at a late stage, modification of the primary omphacite by metasomatic processes should not be ruled out in the light of its enrichment in incompatible elements and its microstructure. Therefore, even if major-element composition would encourage the use of these xenoliths to constrain the origin of the eclogites, any further interpretation should be taken with caution.

The two models that could explain the occurrence of eclogites at around 140 km depth are described next and illustrated in fig. 7.7.

1. Subduction-stacking during craton assembly

The subduction-stacking model proposes that the SCLM was formed by repeated underthrusting of oceanic slabs during craton assembly, which would be accumulated beneath older continental crust (Helmstaedt and Schulze, 1989). This model could thus explain the layering observed in the NE Angolan SCLM, with occurrence of eclogites not only at the base of the SCLM (>200km), but also at intermediate levels within the lithosphere (100 km). Additionally, the similarities between the mineral modes of the deepest Grt-peridotite layer and the abyssal peridotites (Niu et al., 1997) also support an oceanic lithosphere being subducted at the base of the SCLM in the Lunda Norte province. However, it should be noted that the average spinel modes in the shallow oceanic lithosphere are too low to fully explain the formation of garnet at higher pressures, which also supports a metasomatic origin of at least part of the garnet found in the high-T peridotites (see chapter 8). The subduction-stacking model has been used to explain the formation of the current SCLM in several cratons worldwide (e.g., Pearson and Wittig, 2008; Riches et al., 2010; Tappe et al., 2011). The bulk rock chemistry of Angolan eclogites was also used to support the hypothesis of being remnants of oceanic crust (Nikitina et al., 2014). These authors argued that the compositional similarities between the Angolan eclogites and other "subduction-related" mantle eclogites worldwide were indicative of an analogous origin. Even if their results seem to be robust, the fact that

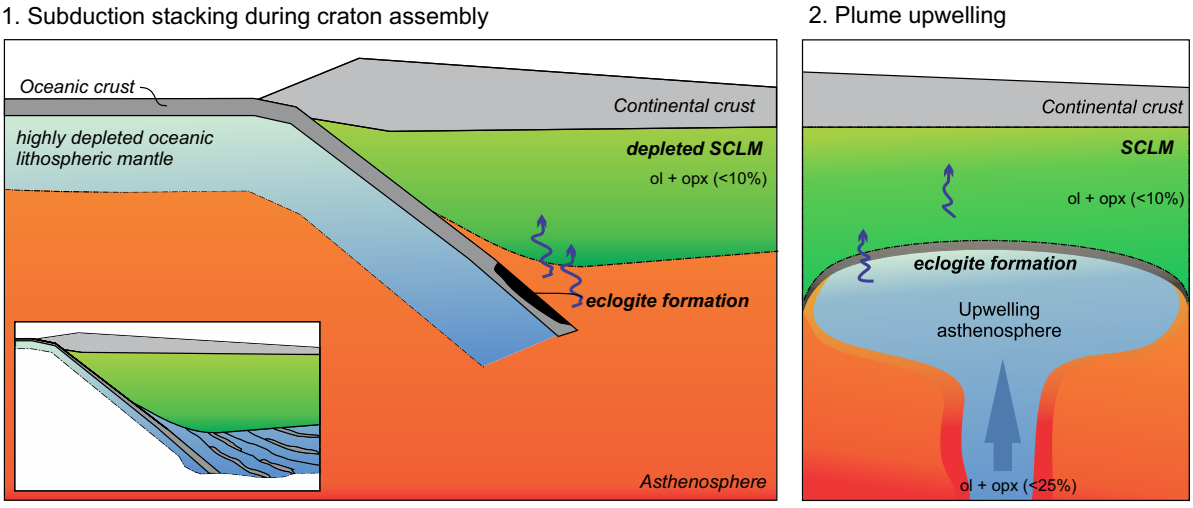

Figure 7.7 Sketch that illustrates the two possible models of formation of the current structure of the SCLM beneath the Lunda Norte province (NE Angola). Note that this model is not in scale. In the subduction stacking model (1), eclogites are formed from oceanic crust in a subducting slab. In this scenario, the high-T garnet peridotite suite would be a refertilised Archean oceanic lithospheric mantle. Progressive underthrusting of oceanic thrusts would also explain the occurrence of high-Mg eclogites below the porphyroclastic (sheared) peridotites. Alternatively, an asthenospheric plume (2) similar to that proposed by Griffin et al. (2003) in the Slave craton could be responsible for the formation of eclogite cumulates at the base of the SCLM represented by the coarse garnet peridotites. The crystallisation of the head of this plume would result in the formation of the sheared peridotites.

metasomatic modification of the composition of the eclogites could not be unambiguously ruled out, makes it necessary to take these conclusions with caution.

In any case, if this model is true, continental growth likely took place only in the Late Archean, during craton assembly, since the current steep angle of subduction of the oceanic lithosphere into the asthenosphere would not allow accumulation of oceanic lithosphere beneath the continental lithosphere (Griffin and O'Reilly, 2007). Instead, tomographic images show that oceanic slabs are nowadays delaminating and dropping deep into the asthenosphere, up to 610 km (Replumaz et al., 2004). Additionally, opponents of this model also claim that even if such shallow subduction took place during the Archean, the required thicker and depleted Archean slabs would still be denser than the hotter Archean asthenosphere, which would also prevent them from stacking (Griffin and O'Reilly, 2007 and references therein).

2. Mantle plume ascent

Alternatively, the similarities in the structure and mineral modes between the Congo-Kasai and the Slave craton could also be invoked to suggest an analogous origin in both cases. Griffin and coworkers (1999a) suggested that in the Slave craton, the shallower layer is a defined by a strongly depleted Archean lithosphere, whereas the deeper layer represents a plume head which rose from deep, more fertile, asthenosphere. Such ascent was stopped at the base of the refractory and buoyant lithosphere, causing melting at the base of the lithosphere, as well as crystallisation of basaltic melts as eclogite cumulates at the boundary of the two layers (Griffin et al., 1999a). The SCLM structure described by this process would thus be similar to that found in the Lunda Norte province and such a mechanism of formation could be also considered as a plausible option.

However, the compositions of the garnets found in the shallower layer indicate that it is not as depleted as the one described in the Slave craton, but is broadly similar to that found in the Kaapvaal craton (fig. 7.8 and 7.9). In fact, with the exception of sample MGR-37, these profiles show that the composition of garnet in both layers is very similar to the median composition of garnet in the Archean lithosphere. However, one could also argue that the silicate-metasomatism episode that affected the shallow layer of the Angolan SCLM would mask an originally ultradepleted layer (see chapter 8).

In any case, at least a subduction episode is required to explain the presence of high-Mg

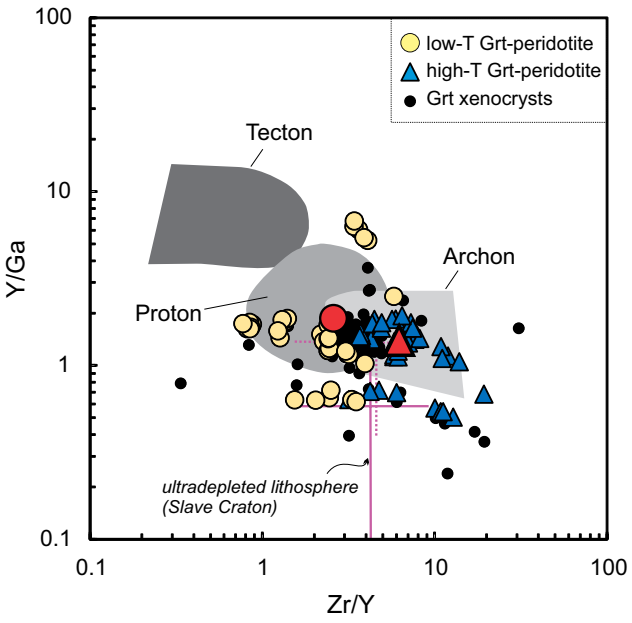

Figure 7.8 Y/Ga vs Zr/Y diagram for garnets both from xenoliths and found as xenocrysts. Fields are from Griffin et al. (1998). The secular evolution to progressively less depleted mean mantle compositions commonly results in higher Y/Ga and lower Zr/Y in garnet affected by refertilisation of an originally depleted Archean mantle (Griffin et al., 2003). In contrast with the Slave Craton (purple crosses), the mean values of the garnet peridotite suites (in red) show that compositional differences between the deeper and the shallow layer of the SCLM are not very significant in the Angolan case. Even if there is a significant spread in the Y/Ga-Zr/Y relationships of the garnets of the shallow lithosphere, they are unlikely to be indicative of an ultradepleted layer equivalent to the one defined in the Slave craton (Griffin et al., 2003), unless significant metasomatic refertilisation of this layer took place (see chapter 8).

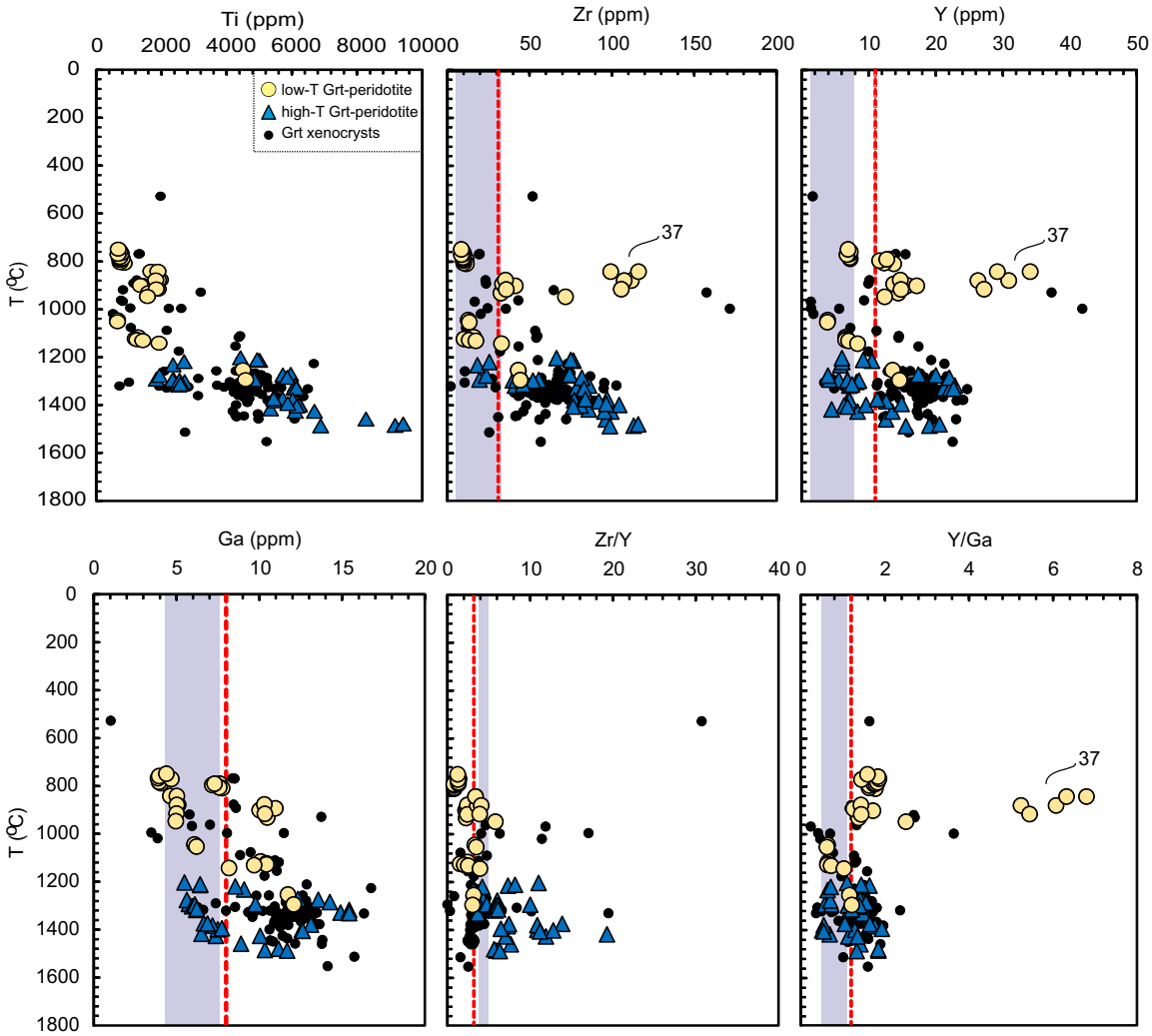

Figure 7.9 Trace-element compositions of garnet plotted against temperature (calculated using the Ni-thermometer of Ryan et al. (1996)). In purple the composition of garnets in the shallow layer of the Slave craton (Griffin et al., 1999a). This diagram also shows that compositions equivalent to the ultradepleted shallow layer of the Slave craton do not occur in the SCLM in NE Angola. The red line corresponds to the median values of garnet in Archean SCLM (Griffin et al., 1999b). The enrichment in Ti and Zr instead points to melt metasomatism.

eclogites at the base of the lithosphere, although this could be linked to late orogeny. Deep eclogites have also been described at the base of the SCLM in the Slave craton and they have been related to a late (Proterozoic) orogeny (Griffin et al., 1999a).

Given that the studied eclogites show at least some evidence of metasomatism and the limited amount of eclogite xenoliths studied, the current data are insufficient to either fully support or dismiss a subduction origin for the eclogites in the Lundas SCLM. Unfortunately, to date none of the studies on Angolan eclogites include oxygen isotope analyses, which could be a good discriminator of the source of the eclogites.

7.4. Preliminary conclusions:

1. The thermobarometric calculations for a Spl-peridotite, several Grt-peridotites and eclogites defines the following structure of the SCLM: Spl-harzburgite (630ºC; 27kbar; 75 km); coarse garnet peridotites (850-1080ºC; 38-53 kbar; 105-145 km), low-Mg eclogites (1040-1140ºC, 43-49 kbar; 138-155km), porphyroclastic (sheared) garnet peridotites (1280-1330ºC; 63-70 kbar; 180-190km) and high-Mg eclogites (>200 km).

2. This structure defines an enrichment in Ti, Cr and Zr in garnets with depth, coupled with a decrease in the Mg# of olivine. Such compositional variations, as well as the Zr/Ga-Zr/Y ratios in garnet, are similar to those defined for the Archean SCLM in most cratons worldwide. However, the mineral modes of the studied xenoliths are significantly different from those described in the Kaapvaal craton and could be comparable to those reported in the Slave craton or in oceanic peridotites.

3. Two models (subduction-stacking vs asthenospheric plume upwelling) were proposed to explain the current structure of the SCLM and the presence of eclogite levels (or lenses) between the two garnet peridotite suites. However, the current data are considered insufficient to fully support either model.

4. In the subduction-stacking model, the low-Mg eclogites were derived from shallow subduction of an oceanic crust, which was assembled at the base of the SCLM. In this scenario, the high-T garnet peridotite suite would be a refertilised Archean oceanic lithospheric mantle.

Progressive underthrusting of oceanic thrusts would also explain the occurrence of high-Mg eclogites below the porphyroclastic (sheared) peridotites. The fact that the eclogites are at least partially metasomatised makes it difficult to confirm such an origin from whole rock analyses.

5. Alternatively, an asthenospheric plume similar to that proposed by Griffin et al. (2003) in the Slave craton could be responsible for the formation of eclogite cumulates at the base of the refractory Archean SCLM. The crystallisation of the head of this plume would result in the formation of the sheared peridotites. However, the shallow SCLM in the Lunda Norte province is not as highly depleted as that in the Slave craton, which argues against this model unless significant refertilisation of this layer by metasomatism took place.

Chapter 8
MANTLE METASOMATISM IN THE SCLM IN LUNDA NORTE: A MULTI-STAGE PROCESS

This chapter aims to evaluate the effects of metasomatic processes that modified the composition of the SCLM beneath the Lunda Norte province. The compositional (major- and trace-element) and textural study of the xenoliths revealed that the current composition of this SCLM is a consequence of complex, multi-stage metasomatic processes, which affected the shallow and the deep lithospheric mantle in a different way. At the end of the chapter, a possible model of the metasomatic evolution of the SCLM is included.
The Fe-Ti rich metasomatism that led to the formation of ilmenite in the mantle is discussed in the next chapter.

8.1. Introduction to mantle metasomatism

8.1.1. Definition and types of metasomatism

Mantle metasomatism is defined as the modal and compositional changes that take place in mantle rocks as a result of their interaction with mantle-derived fluids. This process may play a major role in the modification of the original composition of the diamond indicator minerals found in the SCLM, mainly in garnet and clinopyroxene. Metasomatic fluids also are thought to be responsible for the precipitation of ilmenite in the mantle (e.g., Dawson and Smith, 1977; Grégoire et al., 2002), as well as diamond growth at high pressures within the lithosphere (e.g., Sobolev et al., 1997; Stachel et al., 2004; Malkovets et al., 2007; Araújo et al., 2009).

Historically, two main types of mantle metasomatism have been defined in the literature: modal and cryptic mantle metasomatism. Modal mantle metasomatism refers to the process that leads to the formation of minerals additional to those usually found in peridotites (Harte,

1983). The typical metasomatically-introduced phases include amphibole, mica, carbonates, apatite, sulphides, titanite, ilmenite and zircon. In contrast, cryptic mantle metasomatism causes changes in composition of the original assemblage, especially in terms of trace elements, but without crystallisation of new minerals (Dawson, 1984). However, a third type of mantle metasomatism has been recently invoked to describe the late refertilisation processes that can be observed in the lithospheric mantle. In these cases it is thought that the infiltration of metasomatic fluids may enrich the lithospheric mantle in both major elements (Ca, Al, Fe, Ti) and trace elements (Sr, Zr, REE), leading to the formation of garnet and clinopyroxene (O'Reilly and Griffin, 2013). As a consequence, despite involving the crystallisation of new phases, the mineral assemblage formed by this process is indistinguishable from that in the common peridotites. Because of its misleading nature, this type of metasomatism has been described as stealth metasomatism.

Repeated metasomatic episodes are known to be the rule rather than the exception in the Archean cratons (e.g., Griffin et al., 1996), which implies that a multi-stage process may overprint previous episodes, leading to misinterpretation of the mantle evolution. Therefore, special effort should be used to identify the origin of these processes, especially when it comes to understanding of the evolution of the diamond indicator minerals such as garnet, ilmenite and clinopyroxene.

8.1.2. Composition of the metasomatic fluids

The fluids involved in mantle metasomatism encompass a wide range of compositions, including silicate melts (mafic and ultramafic), carbonatite melts, sulphide melts, C-O-H fluids, dense brines and hydrosilicic fluids, and hydrocarbon-related fluids (O'Reilly and Griffin, 2013).

Moreover, fluids of different nature may interact and coexist even on small scales, and be miscible under certain conditions or immiscible in others. The movement of these fluids through the mantle can occur either by crack propagation or by grain-boundary infiltration. The former is registered on a lithospheric scale and it is regarded as geologically instantaneous. In xenoliths it can be recognised by the crystallisation of secondary phases such as amphibole and mica filling planar veins, as well as by the formation of planar arrays of fluid inclusions within the mineral grains affected by metasomatism. In contrast, grain-boundary infiltration

is a very slow process usually related to either cryptic or stealth metasomatism, and does not involve significant volumes of fluid. This type of movement is very effective in melts (carbonate and basaltic), but rarely occurs when H_2O-CO_2 fluids are involved.

In general, an increase in the fluid/rock ratio would result in a drift of the metasomatic fluids' composition from highly SiO_2-undersaturated, volatile, alkali-rich silicate magmas (CO_2-rich or carbonatitic magmas) towards SiO_2-saturated or SiO_2-oversaturated magmas (Coltorti and Gregoire, 2008). Additionally, metasomatic processes in an intraplate tectonic setting are dominantly driven by SiO_2-undersaturated magmas, including both alkaline-silicate (Na- and K-rich) and carbonatitic melts. In contrast, SiO_2-saturated and oversaturated magmas are the main metasomatic agents in suprasubduction and mid-ocean ridge settings (Coltorti and Gregoire, 2008).

Because of its complex nature, identifying the fluids involved in mantle metasomatism can be very complicated. However, trace elements have proved to be sensitive tracers for metasomatic and melting processes, since they typically have a wider range of crystal-fluid or crystal-melt partition coefficients than the major elements (Griffin et al., 1996). As a consequence, the study of the trace- element composition of the peridotite assemblage becomes a powerful tool to identify the processes that affected the mantle xenoliths prior kimberlite entrapment. In this sense, core-to-rim trace-element compositional variations are very commonly produced by metasomatic processes that do not involve large volumes of fluid.

Silicate metasomatism

Silicate metasomatism is thought to be mainly related to partial melting in the asthenosphere, and in some cases, the lithosphere (McKenzie, 1989). Depending on the degree of melting, the resulting melts, which usually contain large contents of dissolved oxides, can be variably enriched in incompatible elements. Subsequent interaction with the lithosphere commonly produces Fe-Ti enrichment of the original assemblage, as well as an increase in modal garnet and clinopyroxene in the peridotitic rocks near the lithosphere-asthenosphere boundary (LAB), where silicate mantle metasomatism is more extensive (Harte, 1983; Griffin et al., 1996). Several examples of this type of metasomatism can be found in the literature, as it has been described in most cratons worldwide.

Carbonatitic metasomatism

It is widely accepted that carbonatitic metasomatism results in high La_N/Yb_N ratios, as well as negative HFSE anomalies (Nb, Ta, Zr, Hf and Ti), in both peridotite xenoliths and their constituent clinopyroxenes (e.g., Rosatelli et al., 2007). Additionally modal signatures in xenoliths (orthopyroxene dissolution, trend towards wehrlite compositions and presence of apatite) are also thought to be indicative of a carbonatite metasomatic processes (e.g., Yaxley et al., 1991). However, in some cases carbonatite-metasomatised xenoliths show positive HFSE anomalies (e.g., Dalou et al., 2009; Su et al., 2010), which apparently contradict the commonly accepted influence of carbonatitic metasomatism in the lithosphere. Laurora and coworkers (2001) proposed that this anomalously high Nb, Ta, Zr and Hf contents could also a consequence of slab-derived fluids resulting from partial melting of a stagnant subducted slab within the asthenosphere at high pressures.

Experimental studies reveal that carbonatite melts are characterised by low viscosity and density (e.g., Dobson et al., 1996). As a consequence, they are more likely to percolate and spread upward in the mantle more rapidly than silicate melts (Rosatelli et al., 2007). Therefore, carbonatite metasomatism is usually more common in the shallow layers of the SCLM than in the peridotites near the base of the lithosphere.

8.2. Evidence of mantle metasomatism in the Lundas area

The petrographic description of the xenoliths sampled by the Angolan kimberlites already demonstrates that complex metasomatic processes modified the composition of the SCLM since its formation during the Archean. Mineralogical, textural and geochemical data indicate that more than one metasomatic agent affected the lithospheric mantle beneath the Lundas Norte kimberlitic province. Discrimination of these different processes is essential for the understanding of the evolution and the role of the metasomatic agents in the modification of the composition of the original mineral assemblage and thus the diamond indicator minerals.

8.2.1. Composition of the metasomatic fluids

Yttrium is usually a compatible element in garnet, although Griffin and coauthors (1999) observed that it behaves incompatibly during melt-depletion processes in the Archean

SCLM. The high Cr contents in pyrope, commonly associated with depletion in the basaltic components (Fe, Ca, Al), are negatively correlated with Y. As a consequence, the content of Y in garnet has been proposed as an indicator of the degree of depletion of the SCLM (Griffin et al., 1999b). The typical Y content of the garnets from Archean SCLM is approximately 12 ppm and, therefore, garnets having less than 8-10 ppm Y are generally assumed to derive from a depleted mantle. Other elements such as Ga, Zr, Ti and REE can also be used to constrain the degree of depletion/refertilisation of the cratonic roots, as well as the nature of the metasomatic fluid (Griffin et al., 2003). Several geochemical diagrams have been proposed in order to distinguish the source of the garnet and a possible interaction with a metasomatic fluid or melt.

For instance, the Zr-Y relationships in garnets, proposed by Griffin et al. (1999b), are commonly used to identify their source, classifying them as derived from fertile (low Zr, high Y), depleted (low Zr, low Y) or metasomatised mantle. The Zr/Y ratio also allows discrimination among types of metasomatic agent that may have changed the composition of the garnet. For example, phlogopite-related metasomatism, characterised by higher Zr contents at relatively low Y concentrations, can be distinguished from melt metasomatism, defined by intermediate Zr and Y contents.

Further characterisation of the metasomatic agent that modified the composition of both garnet and clinopyroxene can be done using the relationship between Zr/Sm_N and Ce/Yb_N in garnets. This diagram enables distinction between silicate or carbonatite metasomatic melts. The interaction of garnet with a silicate melt usually leads to an enrichment in HFSE relative to MREE, since the bulk distribution coefficients for garnet/melt and Cpx/melt are higher for Sm and Eu than for Zr and Ti (Aulbach et al., 2004a). In contrast, interaction with a carbonatitic melt results in higher LREE/HREE ratios over a limited range of HFSE/MREE values.

In order to constrain the source of the melts that produced the garnets and the role of the metasomatic agents in the modification of their composition, garnet compositions are shown in the Zr-Y and Zr/Sm_N-Ce/Yb_N diagrams (fig. 8.1). A large majority of the studied garnets have been affected by melt-related metasomatism, regardless of their texture, REE_N patterns and P-T equilibrium conditions. None of the grains come from fertile mantle and only few of them are derived from strongly depleted mantle. Only garnet from the higher temperature Grt-peridotite (1332 ^{o}C, 63 kbar) shows Zr/Y ratios typical of phl-bearing metasomatism. However, in peridotite xenoliths where large (>1mm long) phlogopite crystals occur, the equivalent garnets plot in the melt- metasomatism field, far from the field of “phlogopite”

metasomatism. As a result, it can be inferred that not only has the SCLM in the Lundas Norte province has been affected by metasomatism, but it has been a multi-stage process, with melts of different nature involved in it, each one affecting the original assemblage in a different way.

Additionally, the Zr/Sm_N-Ce/Yb_N diagram shows differences in the nature of the melt that metasomatised these garnets. Most of the garnets from coarse Grt-peridotites show high Zr/Sm_N ratios at very low Ce/Yb_N concentrations, indicating interaction with a silicate-derived melt. The only exception is given by the shallowest Grt-peridotite, which is characterised by extremely low Zr/Sm_N but intermediate Ce/Yb_N ratios and hence suggests at least some involvement of a carbonatite melt. In contrast, the Zr/Sm_N-Ce/Yb_N ratios of most of the high-T Grt-peridotites point to a mixed nature of the melt that led to the formation of these garnets, since they are characterised both by high Zr/Sm_N and Ce/Yb_N.

The Ti/Eu vs La/Yb_N discriminant diagram is commonly used to constrain the nature of the melt responsible for metasomatism in clinopyroxenes (Coltorti et al., 1999). Clinopyroxene metasomatised by a silicate melt will tend to be enriched in Ti relative to Eu, whereas its interaction with - or its crystallisation from - a carbonatite melt will led to enrichment in LREE compared to HREE. Consistent with the garnet analyses, a silicate-carbonatite melt caused the current composition of the clinopyroxene of the high-T peridotite xenoliths (fig. 8.2). However, most of the low-T garnet peridotites are characterised by high La/Yb_N ratios (30-600) at very low Ti/Eu (<1500), which would be indicative of participation of a

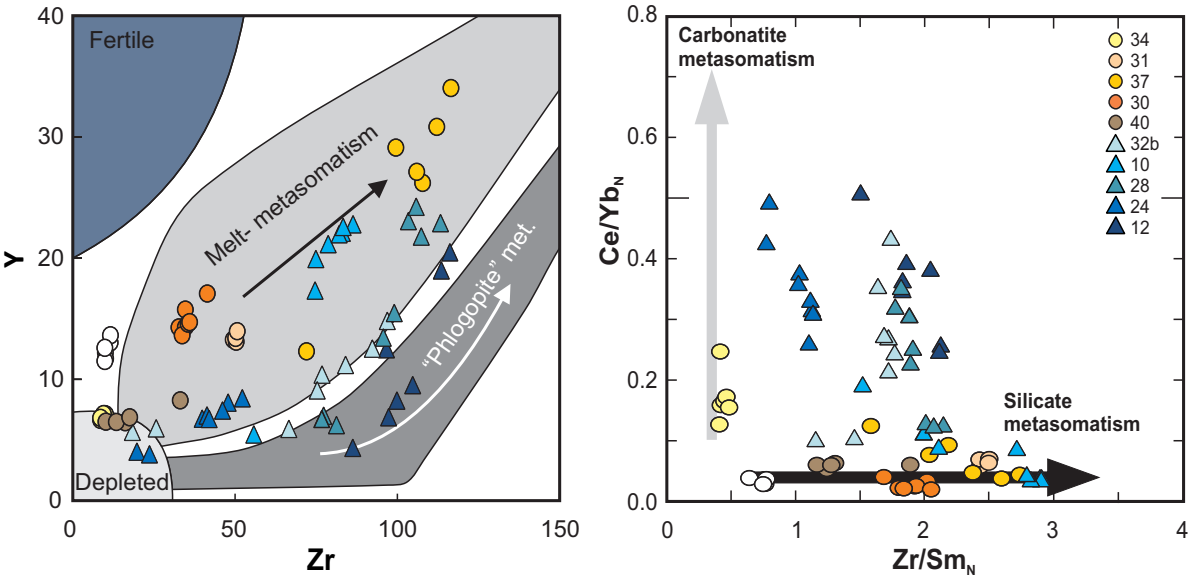

Figure 8.1 Diagrams of Zr vs Y and Zr/Sm_N vs Ce/Yb_N in garnet. Normalisation to chondritic ratios was done using the values of McDonough and Sun (1995). Garnet of coarse garnet peridotites is represented with circles, whereas the porphyroclastic (high-T) one is plotted with triangles. Different colours have been used to represent different xenoliths so they can be correlated with their equivalent clinopyroxene (fig. 8.2).

carbonatitic melt. As already suggested by Aulbach et al. (2004a), the scale of the diagram should definitely be lengthened when old metasomatised mantle xenoliths are studied. Sample 37 has slightly lower La/Yb_N (<12), although it is also coupled with low Ti/Eu and it will also register evidence of carbonatite melt metasomatism. In contrast with the effects on garnets, none of the clinopyroxene has evidence of pure silicate metasomatism, since all of the analysed grains have at least some enrichment in LREE relative to HREE (La/Yb_N> 4). These results would suggest that the crystallisation of coexisting garnet and clinopyroxene of the shallow lithospheric mantle resulted from the percolation of different metasomatic agents.

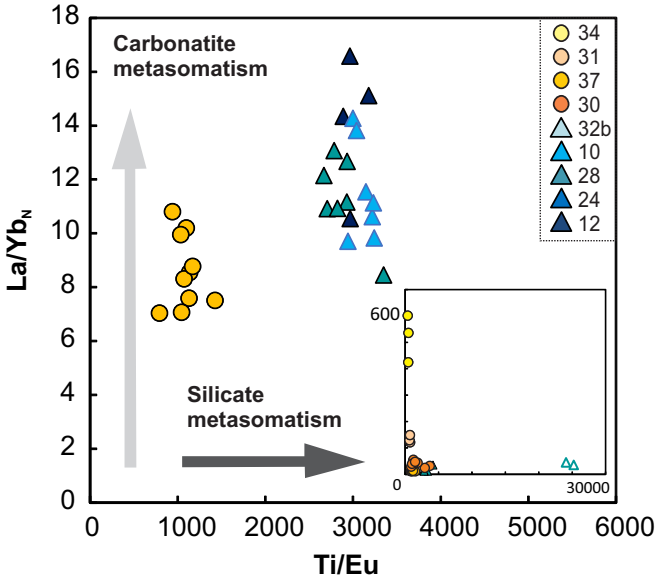

Figure 8.2 Diagram of La/Yb_N vs Ti/Eu in clinopyroxene. Normalisation to chondritic ratios was done using the values of McDonough and Sun (1995). As shown in the smaller graph, clinopyroxene from the coarse garnet peridotites (circles) has very high La/Yb_N. Clinopyroxene of porphyroclastic garnet peridotites is plotted with triangles.

To further test this hypothesis, the composition of the melt in equilibrium with garnet and clinopyroxene was calculated using the partition coefficients of van Westrenen et al. (2001) and Adam and Green (2001), respectively. The REE_N patterns of the melts in equilibrium with clinopyroxene and garnet confirm that the metasomatic agents involved in the crystallisation of these two phases in the shallow lithosphere were compositionally different (fig. 8.3). Even larger differences between both melts are found in terms of Zr, Hf and Ti. Similar conclusions were reached by Simon et al. (2003) from the study of coarse garnet peridotites in Lesotho kimberlites. In contrast, the similarity of the melts that metasomatised both garnet and clinopyroxene in the deepest xenoliths is corroborated by this figure.

Large (1-12cm) clinopyroxene megacrysts were also sampled by the Angolan kimberlites.

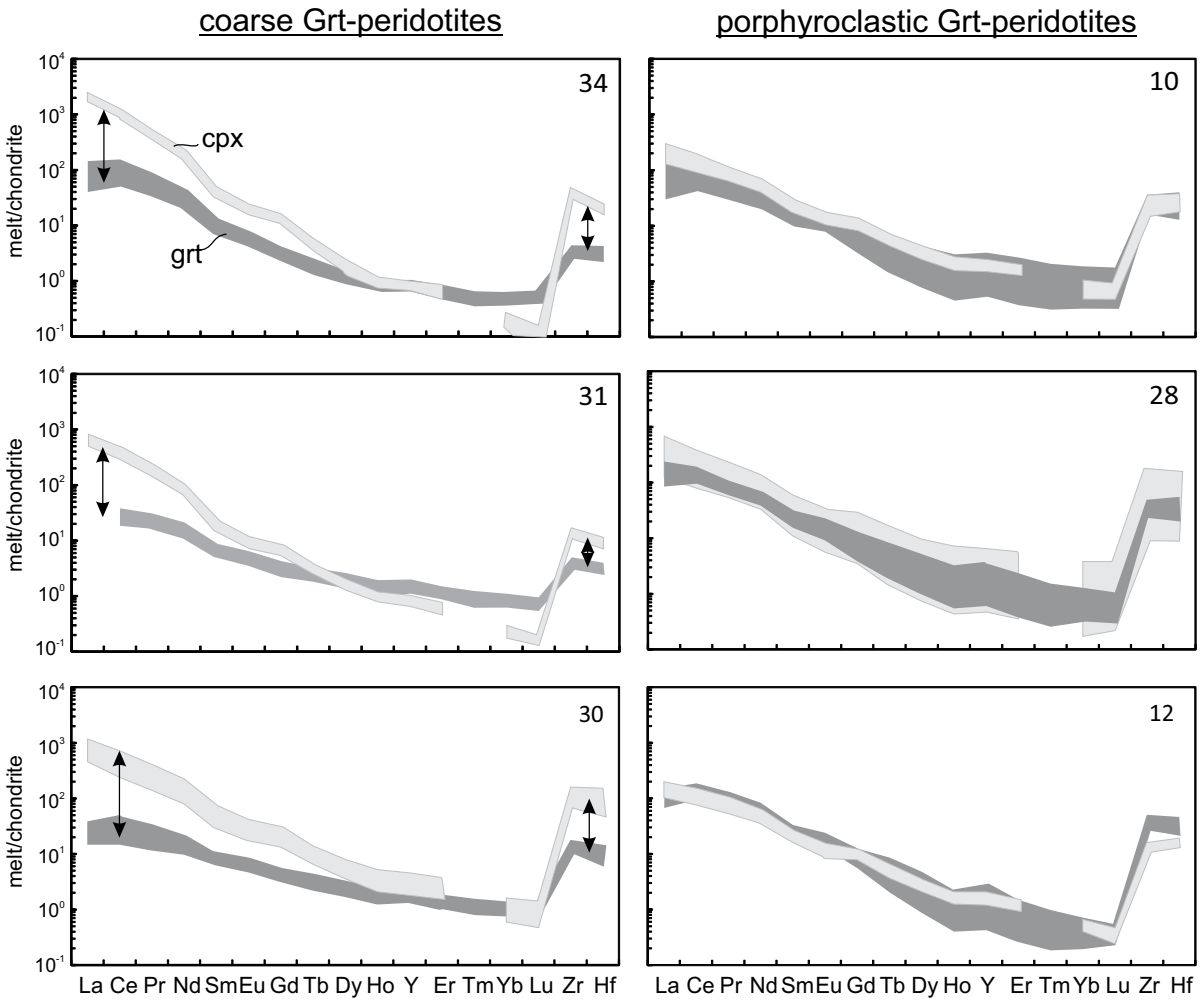

Figure 8.3 Spider diagrams of the calculated melts in equilibrium with clinopyroxene and garnet in some of the peridotite xenoliths. Note the compositional differences between these melts in the coarse garnet peridotites. The normalisation was done using the chondrite values of McDonough and Sun (1995).

The occurrence of abundant clinopyroxene megacrysts was also documented in other areas of the Congo Craton (Pivin et al., 2009), and they are very common in many other kimberlites worldwide (e.g., Bell and Moore, 2004; Kostrovitsky et al., 2004; De Bruin, 2005). However, the origin of these megacrysts has been a controversial issue. Nowadays, there is a broad consensus that clinopyroxene megacrysts and other Cr-poor megacrysts result from the crystallisation of a Ti-rich silicate melt. However, there are disputes about whether this melt was genetically linked to the parental protokimberlitic melt (e.g., Harte and Gurney, 1981; Kostrovitsky et al., 2004; Moore and Belousova, 2005), an asthenospheric melt (e.g., Nixon and Boyd, 1973; Davies et al., 2001), alkali basalts (Hops et al., 1992), or was produced by the interaction of an asthenospheric melt with the SCLM (Davies et al., 2001; Pivin et al., 2009). As observed by Pivin et al. (2009), the clinopyroxene megacrysts in the Congo craton are compositionally different to those described in other localities worldwide, and more similar to clinopyroxene

from peridotites (high #Mg, #Cr and Ti). Their trace element compositions may suggest a genetic link with a carbonatite-silicate metasomatic melt (fig. 8.4). Therefore, it could be possible that these megacrysts are the magmatic product of the partial melting of the SCLM caused by infiltration of asthenospheric melts. The presence of a second generation of fine-grained clinopyroxene, which will be related below to interaction with the kimberlite melt, suggests that the formation of clinopyroxene megacrysts results from a metasomatic episode prior to eruption.

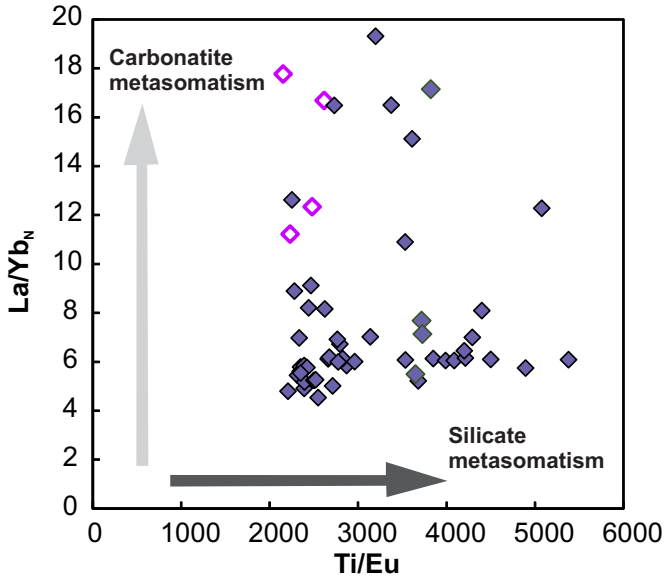

Figure 8.4 Diagram of La/Yb$_N$ vs Ti/Eu in clinopyroxene megacrysts. Normalisation to chondritic ratios was done using the values of McDonough and Sun (1995). Open symbols represent the second generation of clinopyroxene (spongy).

8.3. Metasomatism of the SCLM beneath the Lunda province: a multi-stage process

Despite the limited data available, some preliminary interpretations can be given with regards to the SCLM structure and the metasomatic processes that refertilised the depleted Archean cratonic roots in the Lunda Norte province. The evolution described below is summarised in fig. 8.5.

8.3.1. SCLM depletion by partial melting in the Archean

The predominance of harzburgite in the xenoliths sampled by the Angolan kimberlites indicates that the underlying SCLM experienced a pervasive event of high-degree partial

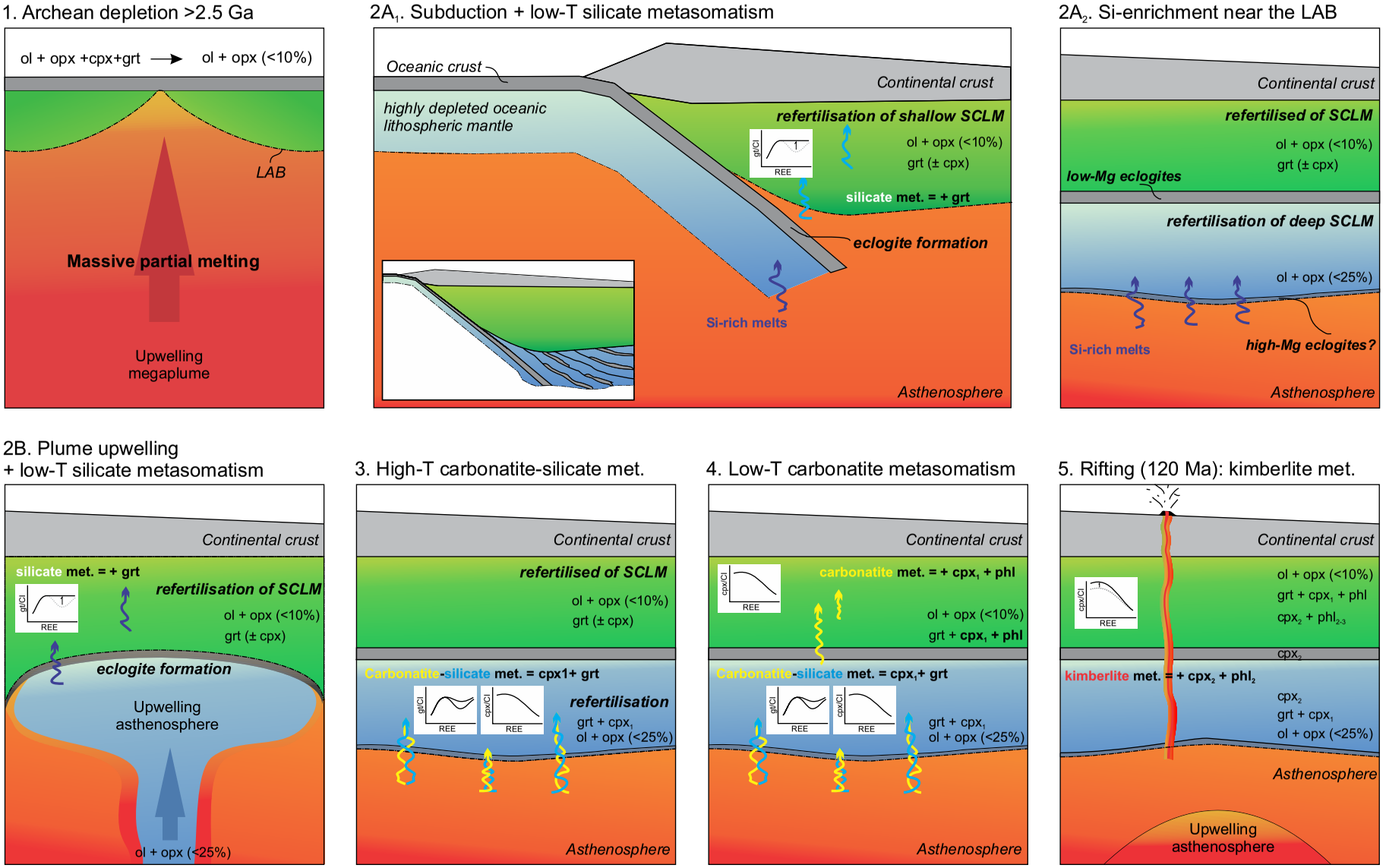

Figure 8.5 Evolution of the lithospheric mantle beneath the Lunda Norte province (NE Angola). Note that the sketch is not in scale. See text for explanation.

melting, which resulted in a highly depleted lithospheric mantle. Such depleted lithospheric roots are a very common feature in most of the cratons worldwide and probably restricted to Archean times (Griffin et al., 2003). This massive melting is thought to have involved the ascent of large volumes of the lower mantle as megaplumes ("mantle overturns"), which could only occur till 2.5 Ga, when the Earth was still hot enough (Griffin et al., 2003). Melting at high pressures caused complete elimination of both garnet and clinopyroxene from the Archean SCLM (Griffin et al., 2003). Additionally, this process would also result in a significant decrease of the Opx/Ol ratio in the mantle peridotites, although experimental calculations show that up to 10% of orthopyroxene could still be preserved in the residual peridotite (Griffin et al., 2009; Herzberg, 2012). These low contents are consistent with the modal abundances observed in the shallowest layer of the SCLM described beneath the Lunda Norte province.

8.3.2. Refertilisation of the shallow SCLM by silicate-melt metasomatism (low-T)

After the major Archean depletion, the two-layered structure of the SCLM was formed either by subduction-stacking during the Late Archean or by ascent of a mantle plume in a process similar to that described in the Slave Craton (see chapter 7). In a subduction scenario ($2A_1$), partial melting of the oceanic lithosphere would typically result in the formation of silicate melts that would infiltrate in the overlying continental lithosphere. Similarly, the ascent of an asthenospheric mantle plume (2B) would also generate large volumes of silicate melts that would interact with the overlying depleted SCLM. Either way, percolation of these silicate melts could explain the crystallisation of chemically homogeneous coarse garnets in the shallow SCLM. The REE_N patterns of these garnets, with positive slope and enrichment in MREE and HREE, are also consistent with a silicate metasomatism episode. Moreover, crystallisation of clinopyroxene could also take place during at this stage. However, in such case the composition of this clinopyroxene in the shallow SCLM would be later modified by cryptic metasomatism related to the infiltration of carbonatite melts (see section 8.3.4).

The high Opx/Ol ratios (orthopyroxene up to 25%) of the high-T peridotite suites could also be explained by subsequent infiltration of a Si-rich, asthenospheric melt through the base of the originally depleted Archean oceanic lithosphere ($2A_2$). Such refertilisation was restricted to the deepest layers of the SCLM and thus did not reach the shallow lithospheric mantle. The late addition of orthopyroxene by Si-rich fluids is very common in the Kaapvaal craton

(e.g., Boyd, 1989; Simon et al., 2007; Wittig et al., 2008), although in the studied section of the Congo craton the Opx/Ol ratio is lower than in Kaapvaal and truly lherzolitic peridotites are rare. However, if the deep SCLM was related to a head of a mantle plume, the aforementioned Opx/Ol ratios are more likely related to the composition of the plume itself.

8.3.3. Refertilisation of the base of the SCLM by carbonatite-silicate metasomatism

Subsequently, a second metasomatic event led to the crystallisation of both garnet and clinopyroxene in the high-T garnet peridotites. Such refertilisation processes are widespread in all cratonic roots (e.g., Griffin et al., 2009) and may be correlated with the so-called stealth metasomatism, which can only be identified from the study of mineral trace element compositions. In the SCLM beneath the Lunda Norte province this study revealed that the melt responsible for crystallization of clinopyroxene and garnet was of a mixed nature, having components of both a silicate- and a carbonatite-melt. The sinusoidal REE_N patterns in garnet, typical of harzburgite xenoliths, show a wide range of compositions in terms of MREE and HREE. Such zoning is indicative of disequilibrium and may suggest that the composition of the metasomatic agent has changed over time, most likely towards a more silicate-melt nature, which would have partially overprinted the original carbonatitic signature in both phases. Even if high-T peridotites are classified as harzburgites, lherzolitic garnets (G9) would be produced during this episode, since all xenoliths are Cpx-saturated. This mismatch between modal classification of the rock and composition of garnet has also been previously observed in mantle garnets from other cratons (e.g., Griffin et al., 1999a; Burgess and Harte, 2004; Su et al., 2010; Howarth et al., 2014). A mixed nature of the metasomatic fluid was also described in the Slave (e.g., Aulbach et al., 2004a), North China (e.g., Su et al., 2010) and the North African cratons (Natali et al., 2013), although in the latter the xenoliths equilibrated at low PT conditions. However, in contrast with other cratonic roots such as the Kaapvaal or the Siberian cratons, no evidence of pure silicate-melt metasomatism, usually ascribed to the ascent of asthenospheric melts, is found in garnet or clinopyroxene of the studied xenoliths.

8.3.4. Low-T carbonatite- (and Phl-) melt metasomatism

Clinopyroxenes in coarse-garnet peridotites are systematically enriched in LREE and other

incompatible elements, which is interpreted as reflecting crystallisation from -or interaction with- a carbonatitic melt. The differences in the modal abundances of clinopyroxene in the shallowest layer indicate a more localised metasomatic event, which only partially modified the composition of the shallow lithospheric mantle. Additionally, the calculation of the melts in equilibrium with garnet and clinopyroxene in these rocks confirms that two separate metasomatic episodes took place in the shallow lithospheric mantle. In contrast with garnet, clinopyroxene chemistry is mainly driven by dissolution/precipitation processes (Boyd et al., 1997; van Achterbergh et al., 2001), which makes it more susceptible to metasomatism than garnet (e.g., Misra et al., 2004; Howarth et al., 2014). Moreover, since the carbonatitic trace element signature in clinopyroxenes is easily obliterated if later interaction with a silicate melt occurs (Puziewicz et al., 2014), it can be inferred that carbonatite metasomatism took place subsequent to the silicate metasomatism that refertilised the shallow layers of the lithosphere. This is consistent with the metasomatic sequence proposed in this chapter. The fact that garnets are compositionally homogeneous would also suggest that carbonatite metasomatism took place shortly before eruption, otherwise garnet rims with sinusoidal REE patterns should be expected. In the Kaapvaal craton, it has also been interpreted that introduction of clinopyroxene into the coarse garnet peridotites happened shortly before kimberlite intrusion (<200Myr ago); whereas introduction of clinopyroxene and garnet in the high-T peridotites likely took place around 2.9 Ga (Simon et al. 2003, 2007). Although dating of garnet and clinopyroxene was not carried out in this work, it could be possible that in the Lundas province the metasomatic timing was similar to that described by Simon and coworkers (2003, 2007). Even if it is unusual to find metasomatic garnet and clinopyroxene derived from different melts within the same xenolith, examples have been reported in the Siberian craton (e.g., Doucet et al., 2013; Howarth et al., 2014), leading to a transition from harzburgitic to lherzolitic garnet (Griffin et al., 1999d).

Crystallisation of large, euhedral phlogopite laths in garnet peridotites is common during low-T metasomatism (e.g., Boyd and Mertzman, 1987; Griffin et al., 1999d). Since clinopyroxene is commonly related to the formation of phlogopite, it seems plausible that the two metasomatic phases resulted from the interaction of the peridotite with the same metasomatic agent. In fact, this paragenesis is common in metasomatised mantle xenoliths (e.g., Dawson, 2002; Grégoire et al., 2002). The fact that the garnet found in the samples containing phlogopite does not fall in the phlogopite-metasomatism field in the Zr-Y diagram (Fig. 8.1) also supports the different nature of the melts that led to the crystallisation of these phases.

However, the origin of this carbonatite melt is unclear, since the source of the carbonatite magmas and carbonatitic metasomatic agents is still debated. It has been proposed that mantle metasomatism is an evolutionary process, controlled by percolative fractional crystallisation (Burgess and Harte, 2004). This term was first introduced by Harte et al. (1993) to define the process that controls the composition of the metasomatic fluids or melts within the cratonic roots, including both fluid-rock exchange interaction and fractional crystallisation. Their model starts with the upwelling of an asthenospheric basaltic melt, which would infiltrate at the base of the SCLM and modify the composition of the sheared peridotites. As a consequence of this interaction, the residual melt is enriched in LREE, LILE and volatiles. Experimental studies have shown that these new carbonatite-bearing melts are characterised by low viscosity and density (Dobson et al., 1996). Being highly mobile, they percolate and spread faster upward in the mantle than the silicate melts (Rosatelli et al., 2007). As a result, minerals from the shallower mantle lithosphere are typically enriched in incompatible elements and new phases, such as phlogopite and amphibole, may crystallise as a consequence of increasing contents of Na and K.

Therefore, it is reasonable to suggest that crystallisation of both clinopyroxene and phlogopite in the shallow SCLM in NE Angola resulted from percolative fractional crystallisation of ascending carbonatite-silicate asthenospheric melts. This sequential interaction with a silicate melt, followed by carbonatite melt metasomatism, has already been recognized in other cratons worldwide (e.g., Aulbach et al., 2004a; Powell et al., 2004).

It has also been suggested that carbonatitic melts could result from melting of a carbonated subducting slab, with the carbonates recycled within the mantle transition zone (Grassi and Schmidt, 2011; Litasov et al., 2013; Pokhilenko et al., 2015). The new melt would be enriched in K, Ca, LREE and other incompatible elements characteristic of carbonatite-like melts (e.g., Walter et al., 2008) and could be the parental source of both carbonatite and kimberlite magmas. Such scenario could eventually be applicable for the carbonatite component found in garnet and clinopyroxene of the high-T garnet peridotite. However, further studies are required to establish any genetic link between the eclogites found at 140-155 km depth and the source of the carbonatite metasomatism that affected the shallow SCLM. Although contribution of these eclogites to the carbonatite melt should not be ruled out, it seems more likely that the low-T carbonatite metasomatism was mainly driven by percolative fractional crystallisation.

In any case, the wide variety of metasomatic phases (ilmenite, rutile, apatite, phlogopite,

clinopyroxene, amphibole and garnet), as well as the differences in the metasomatic agent that formed them, indicate that the metasomatism that affected the shallow lithosphere was complex and probably not as pervasive as the one that affected the base of the SCLM.

8.3.5. Kimberlite metasomatism

Secondary, spongy clinopyroxene occurs along fractures and foliation planes in both eclogites and clinopyroxene megacrysts. In both cases, this second generation is typically enriched in Ca, Mg, Ti, Cr and LREE, but significantly depleted in Na and Al compared to the primary clinopyroxene. Formation of Na-poor spongy clinopyroxene with similar compositions is very common in eclogites sampled by kimberlites (e.g., Misra et al., 2004; Nikitina et al., 2014). Its formation has been previously interpreted as the result of partial melting of the omphacite during –or shortly prior to- kimberlite emplacement (Spetsius and Taylor, 2002). Kimberlite metasomatism involved both partial melting and compositional changes caused by the infiltration of fluids and volatiles derived from the kimberlitic magma, under conditions of decreasing pressure. The kimberlitic fluids participating in such metasomatism are thought to be K- and H_2O-rich. The kelyphitic rims found on eclogitic and peridotitic garnets could also be explained by kimberlite metasomatism (Hunter and Taylor, 1982; Spetsius and Taylor, 2002). This type of metasomatism is consistent with the textural and compositional features of the eclogites and clinopyroxene megacrysts. Therefore it represents the latest metasomatic episode registered by the xenoliths sampled by the Angolan kimberlites.

The second generation of clinopyroxene observed in one of the high-T peridotites could also be produced by kimberlite metasomatism, since it is enriched in REE, Ca and Ti compared to the first generation of clinopyroxene, although poorer in Cr. Further evidence for its late formation is provided by its textural relationship with the orthopyroxene neoblasts. According to Mercier (1979), the disequilibrium textures observed in the sheared lherzolites could not be preserved for more than tens of years at high temperatures. Therefore, deformation and entrapment of the xenolith were almost contemporaneous (O'Reilly and Griffin, 2013). As a consequence, the fact that this clinopyroxene postdates the deformation episode that originated the neoblasts is also consistent with a metasomatic process that took place only shortly before kimberlite entrapment or during eruption.

Finally, the last evidence of kimberlite metasomatism is found in some of the low-T garnet

peridotites. In these xenoliths up to three different generations of phlogopite were described, indicating that percolation of fluids enriched in Fe, Ti, Al, Cr and Nb followed crystallisation of primary phlogopite. More than one episode of phlogopite crystallisation has also been documented in the literature (Dawson, 2002). The trace element composition of the second generation of phlogopite is very similar to that observed in kimberlitic phlogopite (e.g., Reguir et al., 2009). Therefore, it seems likely that this enrichment could be also linked to kimberlite metasomatism during kimberlite emplacement.

In the light of the complex low-T metasomatism described above, one could question if the geothermobarometric calculations carried out in the coarse garnet peridotites can yield the real temperature and pressure of equilibration of these xenoliths. However, the major-element compositions, the microstructures and the PT conditions presented in this thesis are consistent with those observed in low-T garnet peridotites worldwide. Therefore, despite the diverse origin the phases in the assemblage, it seems likely that equilibrium necessary for geothermobarometry was attained.

8.5. Chemical tomography

The concept of 4D lithospheric mapping -or chemical tomography- was introduced by O'Reilly and Griffin (1996) as a method to map the composition, structure and thermal state of the SCLM using the geochemical information from xenoliths and xenocrysts sampled by kimberlites. Ages of the kimberlite intrusions are subsequently used to correlate each chemical transect with a particular time, thus obtaining time slices that enable to investigate the formation and evolution of the SCLM roots over long periods. This method revealed that different crustal terranes within an Archean core may be underlain by distinctly different types of SCLM and thus that the crust and the underlying lithospheric mantle constitute a single block that moved jointly during craton amalgamation (Griffin et al., 1999; Griffin et al., 2003). A complex upper mantle, differing in composition, structure and type of metasomatism, is expected beneath the tectonic shields that make up each craton and the Congo Craton is not likely to be an exception.

In previous chapters, it has been shown that xenoliths contain invaluable information about the composition, structure and evolution of the metasomatism in the SCLM. However, access to xenoliths is limited and might not necessarily cover the whole mantle section. In contrast,

mantle-derived garnet xenocrysts are significantly more abundant and their study can provide additional key information about the compositional structure of the lithospheric mantle and its dynamics in the Kasai craton. All kimberlites studied in this thesis intruded around 120 Ma (see Chapter 5), so no different time slices could be obtained. However, information from garnets found in mantle xenoliths and as xenocrysts sampled by the Angolan kimberlites is combined here to provide a larger dataset which could be useful to better characterise the SCLM beneath the Lundas kimberlite province.

The major- and trace-element composition of a set of 95 garnet xenocrysts sampled by the Cat115 and Catoca kimberlites was processed using the GEOSPEED software originally developed by Oleg Belousov and described by Kobussen et al. (2009). Their Ca and Cr contents were used to determine the source rock-type, yielding a clear predominance of lherzolite (84%), with only minor amount of low-Cr (9%), Ca-harzburgitic (5%) and wehrlitic (1%) garnets. The Zr-Y and Zr/Sm_N-Ce/Yb_N diagrams were used to characterise the metasomatic style of the garnet xenocrysts (fig. 8.6).

As seen in these graphs, the vast majority of the garnet xenocrysts have intermediate Zr and Y contents, indicative of melt-related metasomatism. The few exceptions are represented by a wehrlitic garnet, which has Zr-Y ratios typical of "phlogopite metasomatism", and a minority derived from a depleted source. In contrast with what was observed in the garnets found in xenoliths, almost all garnet xenocrysts have very low Ce/Yb_N ratios and high Zr/Sm ratios, which is typical of silicate-melt metasomatism. Only harzburgitic garnets and few lherzolitic ones have slightly higher Ce/Yb_N ratios, indicating at least some contribution of a carbonatitic

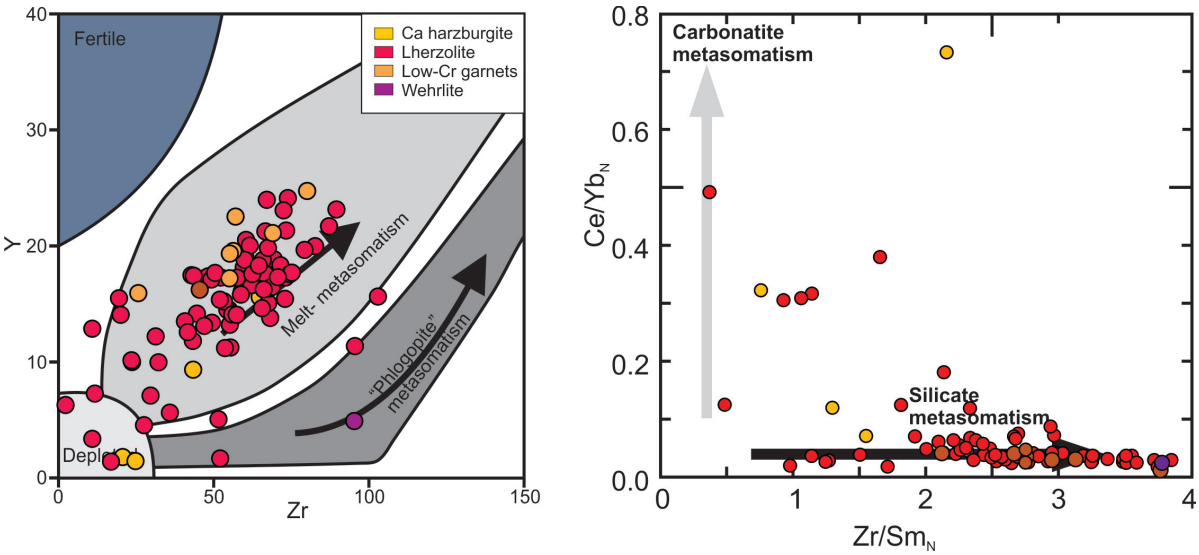

Figure 8.6 Diagrams of Zr vs Y and Zr/Sm_N vs Ce/Yb_N in garnet xenocrysts. Normalisation to chondritic ratios was done using the values of McDonough and Sun (1995).

melt in the metasomatic process.

In order to build the mantle sections, the temperature of equilibration of the xenocrysts was calculated as described in chapter 7, using the Ni thermometer (T_{Ni}) calibrated by Ryan et al. (1996). For coarse garnet peridotites, there is a good correspondence between the temperature calculated using the T_{Ni} and that calculated by two-mineral thermometers. However, it should be noted that the Ni thermometer typically yields slightly higher temperatures than those calculated from two-mineral geothermometry for high-T peridotites. Garnet equilibration temperatures are combined with their composition to obtain the mantle sections shown in fig. 8.7 and fig. 8.8.

Most of the garnet xenocrysts were sampled from the deepest layers of the SCLM, a large majority being lherzolitic. Unfortunately, the shallow SCLM is still poorly represented in these sections, but the available data confirm that depleted rocks (Ca-harzburgites) are present in this upper layer. This over-representation can be correlated with the typically higher abundance of garnet in the high-T sheared peridotites. Moreover, the study of their trace-element composition indicates that silicate metasomatism took place near the base of the lithosphere. These results may apparently contradict those obtained from the study of the mantle xenoliths, where no purely silicate-melt metasomatism was observed in the high-T peridotite suite. However,

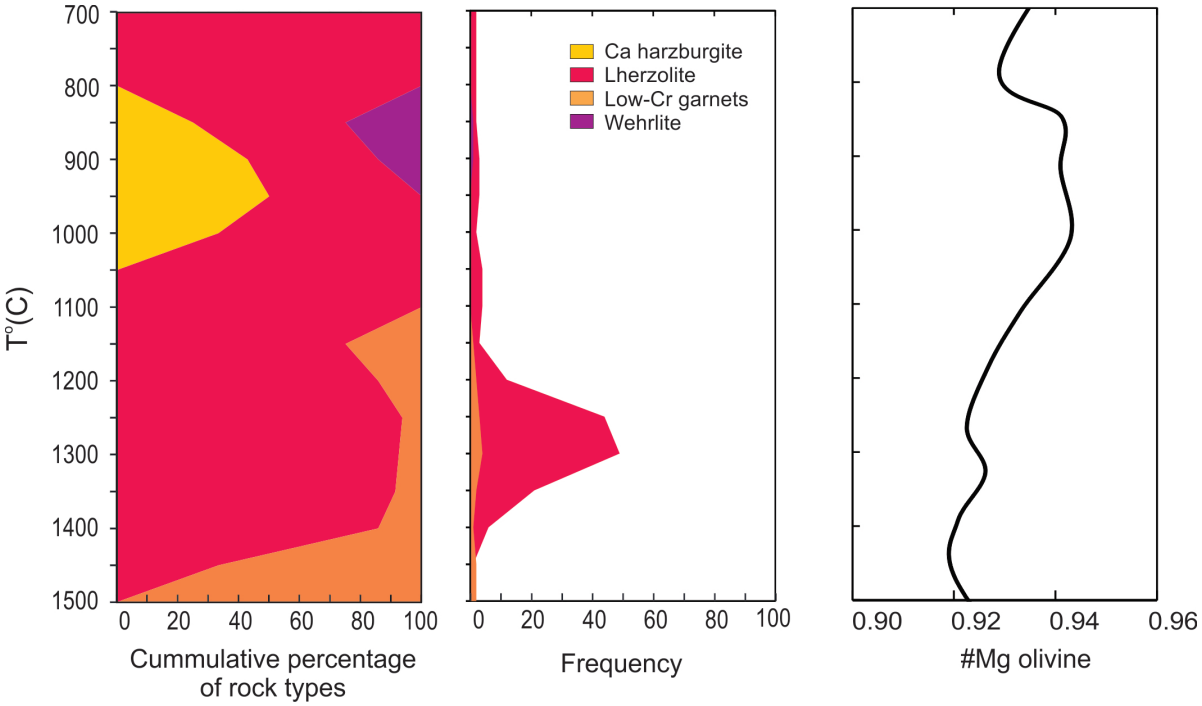

Figure 8.7 Lithosphere structure beneath the Lunda Norte province from (a) garnet classes obtained from the Cr_2O_3-CaO relationships against temperature, which was calculated using the Ni-in-garnet thermometer of Ryan et al. (1996); (b) Mg-number of olivine against temperature. The #Mg was obtained from major element composition of garnet using the formulation of Gaul et al. (2000).

the abundance of lherzolitic garnets near the LAB would be consistent with refertilisation processes caused by percolation of asthenospheric melts. As aforementioned, these melts would produce an increase in the Ca content of the garnets, moving its major composition towards more lherzolitic one (Burgess and Harte, 2004). Additionally, predominance of silicate-melt metasomatism near the base of the lithosphere is a very common feature in most of the cratonic roots worldwide. These garnets typically show a normal REE_N pattern, which is consistent with silicate-melt metasomatism.

Garnet chemistry can also be used to estimate the #Mg of the coexisting olivine (Gaul et al., 2000), which is important for the determination of the physical properties of the lithospheric mantle rocks. The #Mg profile defined by garnet xenocrysts is consistent with the composition of olivine measured in the peridotite xenoliths, showing a decrease in #Mg with depth typical of the Archean cratonic roots (Griffin et al., 2009). However, more data are required to generate profiles that could be compared with those done in central part of the Congo craton (Batumike et al., 2009) and other cratons worldwide.

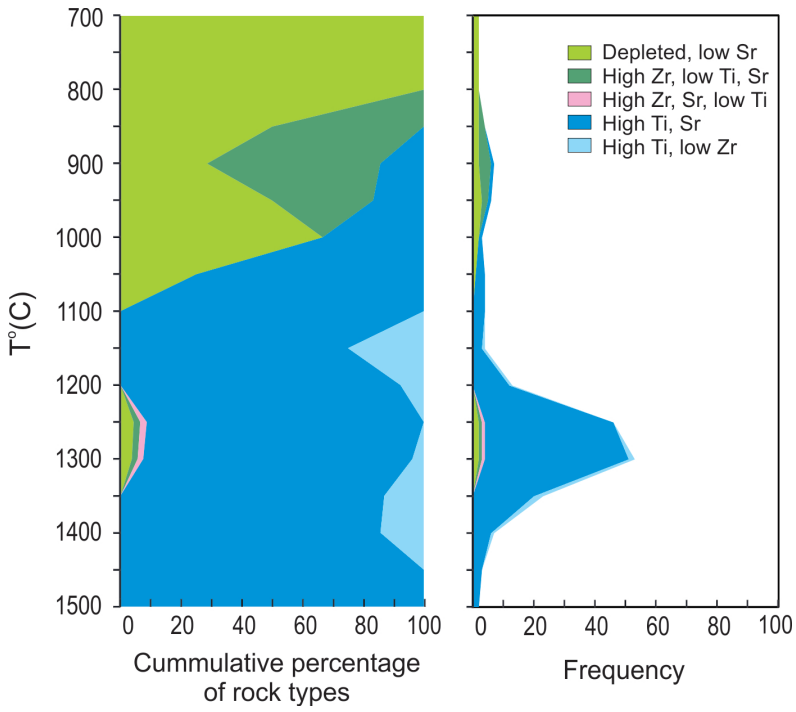

Figure 8.8 Distribution of the different types of metasomatism with temperature beneath the Lunda Norte province. Temperature was calculated from the Ni-in-garnet thermometer of Ryan et al. (1996). Metasomatism types defined as in Kobussen et al. (2009).

8.6. Preliminary conclusions:

1. Different types of mantle metasomatism could be identified in the lithosphere sampled by the kimberlite, based on mineralogical, textural and chemical features observed in the mantle xenoliths and garnet xenocrysts. Evidence of both modal metasomatism (phlogopite, ilmenite, apatite and amphibole) and cryptic/stealth metasomatism (garnet, clinopyroxene) were found in the peridotite xenoliths.

2. Complex, multi-stage metasomatic processes were identified in the SCLM beneath the Lunda Norte kimberlitic province. The study of the trace element composition of garnet and clinopyroxene revealed that the low-T and high-T garnet peridotite suites were modified by compositionally different metasomatic melts that percolated through the lithospheric mantle at different times.

3. The shallow SCLM was first affected by silicate melt metasomatism related to the ascent of asthenospheric melts, which would be linked to subduction of oceanic lithosphere or to the ascent of a mantle plume that led to the current layered SCLM. This metasomatic episode resulted in the introduction of garnet (± Cpx) into the originally depleted Archean lithosphere.

4. Subsequently a high-T metasomatic event modified the composition of the garnet peridotites located close to the new LAB. The melts involved in this process were of a mixed nature (carbonatite-silicate melts) and were responsible for the refertilisation of this layer with both clinopyroxene and garnet.

5. Percolative fractional crystallisation of these carbonatite-silicate melts would explain the late formation of clinopyroxene with a carbonatitic signature and phlogopite at the shallower layer of the SCLM. The differences in the calculated melts in equilibrium with garnet and clinopyroxene in the coarse garnet peridotites is consistent with different metasomatic events for both phases. This carbonatite metasomatism took place shortly prior to kimberlite eruption. Alternatively, if clinopyroxene was previously present, carbonatitic cryptic metasomatism would be responsible for its current composition.

6. The last metasomatic episode is defined by the crystallisation of fine-grained pyroxene along fractures and grain boundaries on eclogites, clinopyroxene megacrysts and deep Grt-peridotite. The new clinopyroxene is typically more enriched in Ti, Ca, REE and Nb, but commonly depleted in Na, and crystallises together with a second generation of phlogopite. This metasomatism has been linked to kimberlite eruption.

Chapter 9
EVOLUTION OF INDICATOR MINERALS: APPLICATIONS TO DIAMOND EXPLORATION

Diamond mining companies usually rely on indicator minerals to assess the diamond grade of the kimberlites. However, it has been proved that a good knowledge of the SCLM, as well as the evolution of the DIMs, is essential for an accurate evaluation. This chapter includes the textural and compositional characterisation of both garnet and ilmenite found in the studied Angolan kimberlites. The complex, multi-stage evolution defined for ilmenite indicates that misinterpretation of the diamond grade could take place if textural and trace-element information is disregarded. Moreover, data obtained from garnet xenocrysts, combined with the structure defined by the SCLM beneath the Lunda Norte province, suggests that the lack of G10 garnet xenocrysts should not be used to downgrade the diamond potential of a kimberlite in this area.

8.1. Kimberlites and diamond mining in Angola

Already in the beginning of the colonial era, the occurrence of alluvial diamonds in Angola encouraged the formation of the Companhia de Diamantes de Angola, devoted to kimberlite exploration. Despite all the efforts made by this company in the 20's and 30's, no kimberlite pipes could be found. Their failure can be easily explained because, unlike other diamond deposits worldwide, most of the kimberlites in Angola are buried below a thick sedimentary unit known as the Kalahari formation (Pervov et al., 2011). However, few years later diamond indicator minerals found in alluvial deposits were successfully used to discover the first kimberlitic bodies outcropping in the Lundas provinces (NE Angola). Since 1940 the development of aeromagnetic techniques for exploration, coupled with a systematic study of the DIMs, was essential to locating most of the kimberlites presently known in the country. However, the developing diamond industry was seriously hindered by the outbreak of the Independence War (1961-1975), followed by a long and devastating civil war (1975-2002).

During the latest conflict, diamond and heavy mineral deposits became strategic targets for both the government, represented by the newly created state-run diamond company (ENDIAMA), and the guerrilla armies (UNITA). This led to several battles, with foreign powers also involved.

After the armistice, systematic exploration of the Angolan diamond resources carried out by ENDIAMA, SDM, De Beers and other foreign companies resulted in a catalogue of over 2000 kimberlitic bodies, most of them buried under the sedimentary Paleogene cover. However, its recent troubled history has meant that the available information on the Angolan kimberlites is definitely very scarce.

The use of diamond indicator minerals as a prospecting tool to assess the diamond potential of the kimberlitic pipes has become routine among diamond mining companies. These companies rely on the major-element composition of mineral concentrates to discriminate between fertile and barren kimberlites. However, this approach was proved to be misleading if the textural information of the DIMs is disregarded (Robles-Cruz et al., 2009). These authors found that a significant amount of the ilmenite xenocrysts in the Catoca kimberlite are characterised by high Fe^{3+} contents, which a priori would indicate oxidising conditions in the underlying mantle and, as a consequence, poor diamond preservation (Gurney and Zweistra, 1995). In contrast, magnesian ilmenite proved to be secondary and thus any genetic link with diamond is questionable. However, Catoca is one of the largest diamond producers, which emphasizes the importance of a good characterisation of the processes that modified the composition of the DIMs for the correct evaluation of the diamond grade of a kimberlite. As a consequence, this chapter will discuss the textural and compositional information obtained from the study of garnet and ilmenite xenocrysts and its application to diamond exploration. These two minerals are particularly abundant in the studied kimberlites, which usually lack fresh xenocrysts of other DIMs such as chromite, diopside or olivine.

The Catoca kimberlite was the eighth largest diamond mine in the world in 2015, supplying over 6.5 million carats of diamond valued at 553MM US$ (Zimnisky, 2015). The nearby Cat115 kimberlite also has a diamond-rich layer at 140-160m depth, although this is 2.5 times poorer than the Catoca kimberlite (Pervov, personal communication). However, the very low erosion rates in this area have ruled it out as a potential diamond mine, since the costs of exploitation of such a deep layer made it a non-viable mine despite its diamond content. In any case, it seems reasonable to assume that the information about the mantle conditions (P, T, X, metasomatism) obtained from the DIMs sampled by this pipe are independent of

the thickness of the sedimentary cover. Therefore, in this study, the Cat115 kimberlite could be considered at least a medium-grade orebody. The compositional and textural similarities between the DIMs collected from this kimberlite and those from the Catoca diamond mine also support this assumption.

9.2. Ilmenite

9.2.1. Introduction

Ilmenite is a very common phase in kimberlites and related rocks, and as a consequence, it is one of the main kimberlite indicator minerals (KIM) used to locate new targets (e.g., Mitchell, 1986; Haggerty, 1991a; Wyatt et al., 2004). Because of its abundance in kimberlites, ilmenite has been investigated for use in diamond exploration (Gurney and Moore, 1993; Griffin and Ryan, 1995), but its use as diamond indicator mineral (DIM) has been unsuccessful to date. The major-element chemistry of ilmenite commonly used in mining exploration (Gurney and Zweistra, 1995; Wyatt et al., 2004) has proven inadequate to correctly identify the diamond potential of a prospected kimberlite (Schulze et al., 1995; Robles-Cruz et al., 2009). Recent improvements in in-situ techniques such as LA-ICP-MS have encouraged the use of trace element chemistry in DIM as a tool for assessing the diamond grade of the kimberlites, including ilmenite (Carmody et al., 2014). But to the author's knowledge, the full potential of this technique has not been applied to kimberlitic ilmenites, since no systematic in-situ study of the trace-element composition of the different ilmenite textural types has been published so far.

However, such an approach could provide key information about ilmenite petrogenesis in kimberlites, as the complex processes involved in it can only be understood by a comprehensive study of both textures and mineral compositions (e.g., Pasteris, 1980; Robles-Cruz et al., 2009). Additionally, these processes are often disregarded during the diamond exploration stage, leading to misinterpretation with a high economic cost, since potentially diamondiferous kimberlites could be discarded, and vice versa (Schulze et al., 1995; Robles-Cruz et al., 2009).

Therefore, in this study in-situ trace-element geochemistry was used to identify the processes responsible for the formation of the different textural populations of ilmenite found in the Cat115, Tchiuzo and Lucapa1 pipes. Additionally, the relationship between ilmenite and diamond, as well as the use of trace-elements as tools for diamond exploration, were evaluated.

Despite being the fourth largest diamond producer in Africa (Faure, 2010), very few studies have been published on Angolan kimberlites and their ilmenites (Robles-Cruz et al., 2009; Ashchepkov et al., 2010).

9.2.2. Ilmenite petrography

Different ilmenite populations were distinguished, including those found in a variety of mantle xenoliths sampled by the Angolan kimberlites studied here. However, the main mode of occurrence of ilmenite in these kimberlites is as individual xenocrysts within the kimberlitic matrix. Significant textural and compositional differences were observed among the ilmenite xenocrysts of a single kimberlite. Likewise, several generations of secondary ilmenite, replacing previous ilmenite grains and/or other titanium oxides, were also identified.

A. Ilmenite in mantle xenoliths

Intergranular ilmenite was found in a few mantle xenoliths, as millimetre-sized veinlets in the interstitial space between relatively fresh pyroxene and serpentinised olivine grains (fig. 9.1a). Similar metasomatic ilmenite is commonly found in xenoliths recovered from kimberlites worldwide, including MARID and PIC rocks (e.g., Dawson and Smith, 1977; Grégoire et al., 2002). This ilmenite can be polycrystalline near the contact with the silicate phases, which has been interpreted as the result of stress in the original xenolith. In some of these xenoliths, ilmenite may show a 5μm zone of Mn enrichment on the boundaries between ilmenite and the original clinopyroxene.

In one of the xenoliths, Fe^{3+}-rich ilmenite occurs as a subordinate phase that crystallised together with other metasomatic minerals such as kaersutite and apatite (fig. 9.1b). The ilmenite occurs as small (0.2-1 mm) rounded or subrounded grains. This assemblage replaces the primary clinopyroxene-olivine peridotite. This xenolith shows significant carbonatization, represented by the crystallisation of different generations of calcite. Late hydrothermal processes produced the serpentinisation of olivine and veinlets of secondary sulphates (barite and celestite). These ilmenite grains can contain exsolution lamellae of Ti-rich hematite and they might be partially altered to secondary, post-emplacement minerals such as titanite.

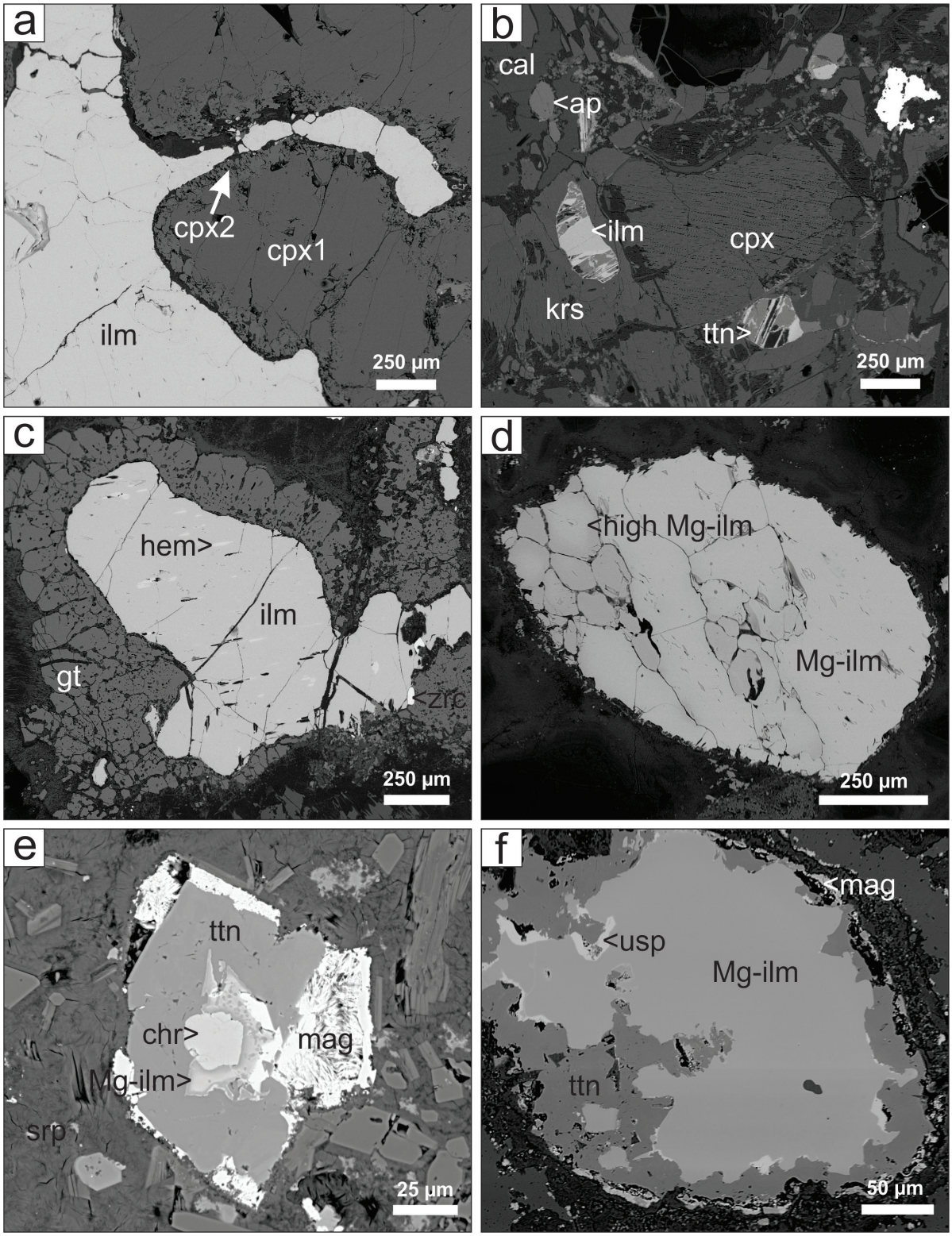

Figure 9.1 Textural types of ilmenite found in the Angolan kimberlites (BSE images). (a-c) ilmenite (ilm) in xenoliths (a) veinlets of ilmenite in clinopyroxene-olivine xenolith (cpx); (b) anhedral ilmenite, partially altered to titanite (ttn), occurring together with apatite (ap), clinopyroxene (cpx) and kaersutite (krs); (c) ilmenite with thin hematite (hem) exsolutions, surrounded by spongy garnet (gt) in granulite; (d) ilmenite nodule showing recrystallization. The difference in brightness observed in the SEM images is given by enrichment in Mg along the grain boundaries and fractures; (e) strongly zoned, Mg-rich ilmenite crystallising around chromite (chr). It contains inclusions and it has been almost completely replaced by titanite (ttn), with subsequent replacement by magnetite (mag); (f) anhedral ilmenite xenocryst found in the kimberlitic matrix, which have been differently replaced by secondary phases: titanite, ulvöspinel (usp) and magnetite (mag).

Anhedral ilmenite grains also can occur in garnet pyroxenite and granulite xenoliths, typically surrounded by garnet (fig. 9.1c). However, in contrast to the aforementioned intergranular ilmenite veins, this type of ilmenite may contain exsolved lamellae of hematite. The clinopyroxene in these garnet pyroxenites also contains very thin ilmenite lamellae (<5 µm) oriented parallel to its (010) plane. However, no further studies were performed on these thin ilmenite lamellae.

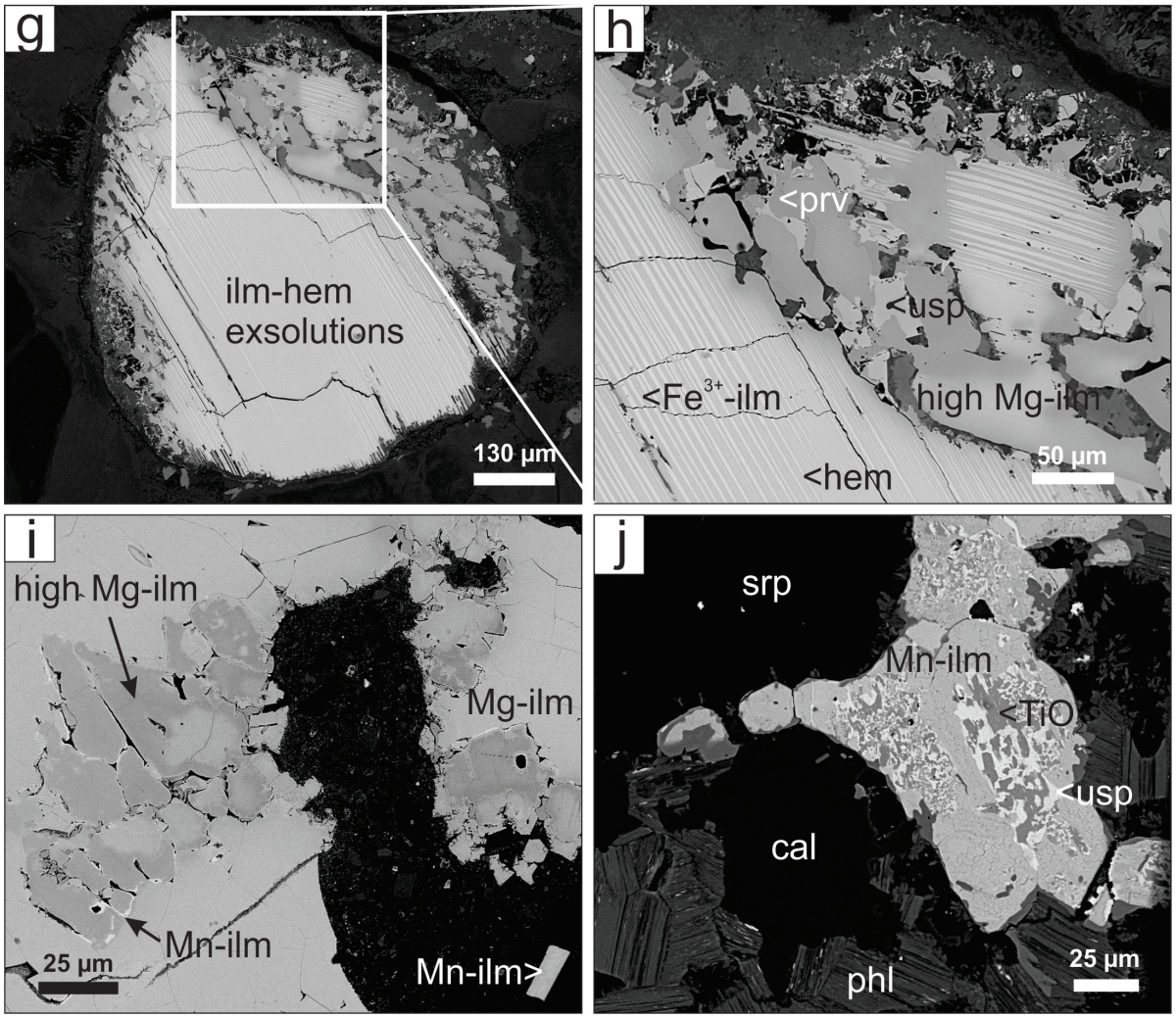

Figure 9.1 (continuation). Textural types of ilmenite found in the Angolan kimberlites (BSE images). (g) ilmenite with fine hematite exsolutions and symplectitic, darker ilmenite crystallising along fractures and grain boundaries. Detailed image (h) show the complex mineral replacement which accompanies the symplectitic ilmenite: ulvöspinel (usp), rutile (rut), magnetite, perovskite (prv) and titanite; (i) nodular ilmenite replaced by Mg- and Mn-rich ilmenite along grain boundaries of the recrystallised grains, together with tabular Mn-rich ilmenite; (j) secondary Mn-rich ilmenite, replacing previous ilmenite (dark) and ulvöspinel (bright), set in a matrix of serpentine (srp), calcite (cal) and phlogopite (phl).

B. Ilmenite xenocrysts

B_1. Nodular ilmenite

This group is composed of rounded ilmenite macrocrysts, with diameters between 0.1 and 2 cm. Nodular ilmenite is often polycrystalline and the grains typically show curved boundaries and triple points (fig. 9.1d) generated by recrystallization. A characteristic feature of the ilmenite nodules of the Lucapa kimberlite is their average smaller size (100 μm - 5 mm) and the fact that they are usually monocrystalline and compositionally homogeneous.

In contrast, some ilmenite nodules of the Tchiuzo and Cat115 kimberlites have a typical Mg-enrichment along the fractures and near the grain boundaries of the smaller grains. This replacement by more magnesian ilmenite was also observed in nodular ilmenite of the Catoca kimberlite (Robles-Cruz et al., 2009). Locally this Mg enrichment is followed by a late increase in Mn, which was also found in Catoca (Robles-Cruz et al., 2009).

Additionally, rare ilmenite nodules have been observed in the Lucapa kimberlite. In this pipe, some of the grains have inclusions of chromite, as well as smaller (<1μm) inclusions of an unidentified phase, enriched in Cr and Al (fig. 9.1e). Perovskite is commonly associated with this ilmenite, which is also a common feature in other kimberlites worldwide (e.g., Mitchell, 1986). However, the occurrence of euhedral chromite crystals as inclusions in ilmenite is much less frequent, although it has been documented in some kimberlites in South Africa (e.g., Rehfeldt et al., 2007). As shown in fig. 9.1e, this ilmenite shows a strong zoning with enrichment in Mg on the grain boundaries.

Nodular ilmenite in the Cat115 and Tchiuzo kimberlites is usually not altered or replaced by any other secondary phase. In contrast, a succession of titanite, ulvöspinel and magnetite replaces nodular ilmenite along the rims in the Lucapa pipe (fig. 9.1f).

B_2. Ferrian ilmenite xenocryst with hematite exsolutions

This type of ilmenite is common in the three studied kimberlites. The grain size of the xenocrysts ranges from 50 to 800 microns. The ilmenite is the host of lamellae of hematite that have been partially or totally altered (fig. 9.1g-h). With some exceptions, these lamellae are very thin (<5 microns width) and occupy most of the grain. However, in some cases the boundaries of the grains are lamellae-free. As observed in other ilmenite worldwide (Haggerty,

1991b), these hematitel amellae can be partially dissolved. Additionally, most of the grains are replaced by symplectitic intergrowths of Mg-rich ilmenite, perovskite, titanite and ulvöspinel along the grain boundaries (see next section).

C. Secondary ilmenite

C_1. Symplectitic ilmenite

This ilmenite typically replaces ferric ilmenite with hematite exsolutions, resulting in a symplectitic texture similar to that defined in the Catoca kimberlite (Robles-Cruz et al., 2009) (fig.9.1g). In this work, however, symplectitic ilmenite is mostly restricted to the grain boundaries of previous ilmenite xenocrysts, with only a few exceptions. This replacement is mainly driven by crystal discontinuities, exsolution planes and subgrain or grain boundaries. Symplectitic ilmenite shows significant compositional variations and it is enriched in Mg, which results in darker shades in the BSE images than the other ilmenite groups.This replacement process is often accompanied by the crystallisation of some typical kimberlitic phases, such as perovskite, as well as ulvöspinel and titanium oxides. Alteration of this assemblage resulted in the formation of late titanite and magnetite.

C_2. Tabular ilmenite

This type of ilmenite has been recognised both in the Catoca (Robles-Cruz et al., 2009) and Tchiuzo pipes. It forms small (10-50 μm) euhedral plates in the kimberlite matrix (fig. 9.1i). This ilmenite is significantly enriched in Mn. It is compositionally homogeneous and shows no alteration to any other phase.

C_3. Secondary Mn-rich ilmenite

Mn-rich ilmenite replaces earlier Ti-Fe phases, mainly ilmenite, rutile and ulvöspinel (fig.9.1i-j). This type of ilmenite occurs only in the Tchiuzo kimberlite, although similar compositions were also found at the boundaries of some ilmenite xenocrysts in the Catoca kimberlite (Robles-Cruz et al., 2009). However, in the Tchiuzo kimberlite, the replacement is significantly more important than in Catoca, and in some grains almost completely substitutes for the original xenocryst.

9.2.3. Major-element composition

Representative analyses of the major element compositions of each ilmenite type are presented in table 9.1. Although more than 430 analyses were performed, for the clarity of the graphs and the following interpretation, only a selection (197 points) was included in the figures. In order to ensure a comprehensive study, only the duplicated analyses of compositionally homogeneous grains were excluded from the graphs.

In the MgO-TiO_2 diagram (fig.9.2a) most of the grains plot within the kimberlitic field defined by Wyatt et al. (2004), which is consistent with their kimberlitic origin. The exceptions include the Mn-rich ilmenites and those found in granulites and xenoliths showing apatite-kaersutite-ilmenite metasomatism. In the ilmenite-geikielite-pyrophanite-hematite end-member ternary diagrams (fig. 9.2c), these ilmenites show compositions similar to the xenocrysts described in the Catoca diamondiferous kimberlite (Robles-Cruz et al., 2009). Negative correlations of both Ti and Mg with Fe^{3+} are observed (fig. 9.3a-b). As shown in these figures, symplectitic ilmenite is usually slightly more enriched in Mg. The major-element composition of polycrystalline ilmenite is identical to the rest of the grain or nodule (not shown), which indicates that the process that produced recrystallization was mechanical and did not involve any additional fluid. However, as already observed in the SEM images, a late enrichment in Mg occurs in some of the smaller grains along grain boundaries and fractures.

Based on these observations, four main compositional groups can be distinguished depending on their Fe^{3+}, Mg, Cr and Mn contents.

Ilmenite sensu strictu

This group is represented exclusively by the ilmenite found in the amphibole-ilmenite-apatite metasomatic association on peridotites. Its composition is close to pure ilmenite (ilm=0.73-0.82) and thus it is defined by very low abundances of Mg, Mn and Fe^{3+} (0.4-2.4 wt% MgO; < 1 wt% MnO; < 20 wt% Fe_2O_3).

Fe^{3+}-rich ilmenite

Ferric ilmenite ("hemoilmenite") compositions are observed in the grains having hematite exsolution, and to a significantly lesser extent, in exsolution-free ilmenite nodules. Although

Table 9.1 Major element analyses of ilmenite (wt %) and the calculated structural formula in atoms per formula unit (apfu) normalised to 3 oxygens

Analysis	**ilm_1**	**ilm_2**	**ilm_3**	**ilm_4**	**ilm_5**	**ilm_6**	**ilm_7**	**ilm_8**	**ilm_9**	**ilm_10**
compositional group	1	1	1	2	2	3	3	3	3	3
Texture	*granulite*	*met. 1*	*met. 1*	*exsol*	*exsol*	*met. 2*	*nodule*	*nodule*	*nodule*	*nodule*
extra info	xenolith	xenolith	xenolith	-	-	xenolith	-	-	Mg-rich	Mg-rich
analysed area	*core*	*core*	*core*	*core*	*core*	*core*	*med*	*core*	*core*	*rim*
oxides %										
SiO_2	0.01	0.12	0.05	0.00	0.10	0.08	0.03	0.02	0.04	0.04
TiO_2	43.45	43.71	44.59	37.16	30.94	47.00	50.51	45.92	50.98	52.70
Al_2O_3	0.13	0.19	0.14	0.13	0.22	0.48	0.66	0.52	0.54	0.48
Nb_2O_5	0.00	0.00	0.00	0.44	0.42	0.30	0.00	0.15	0.01	0.17
ZrO_2	0.11	0.00	0.00	0.41	0.32	0.13	0.00	0.07	0.10	0.00
Cr_2O_3	0.18	0.24	0.94	0.41	0.46	0.33	3.51	0.85	0.85	0.51
Fe_2O_3	17.88	17.12	15.55	30.06	41.51	14.66	7.49	15.80	9.78	9.26
FeO	36.49	36.91	35.58	28.52	23.69	29.16	27.44	28.18	24.33	22.09
MnO	0.08	0.31	0.27	0.12	0.08	0.27	0.35	0.24	1.65	1.28
MgO	1.33	1.13	2.35	3.03	2.63	7.42	9.85	7.25	11.11	13.52
CaO	0.00	0.07	0.01	0.00	0.07	0.01	0.01	0.02	0.09	0.04
ZnO	0.17	0.06	0.06	0.11	0.00	0.03	0.01	0.01	0.00	0.00
V_2O_3	0.00	0.00	0.00	0.00	0.00	0.00	0.00	0.00	0.00	0.00
NiO	0.07	0.09	0.07	0.00	0.05	0.08	0.10	0.16	0.06	0.10
sum	99.90	99.95	99.61	100.39	100.49	99.95	99.96	99.19	99.54	100.20
apfu (O=3)										
Si	0.000	0.003	0.001	0.000	0.002	0.002	0.001	0.000	0.001	0.001
Ti	0.787	0.792	0.808	0.673	0.560	0.851	0.915	0.832	0.923	0.955
Al	0.004	0.005	0.004	0.004	0.006	0.014	0.019	0.015	0.015	0.014
Nb	0.000	0.000	0.000	0.005	0.005	0.003	0.000	0.002	0.000	0.002
Zr	0.001	0.000	0.000	0.005	0.004	0.002	0.000	0.001	0.001	0.000
Cr	0.003	0.005	0.018	0.008	0.009	0.006	0.067	0.016	0.016	0.010
Fe^{3+}	0.324	0.310	0.282	0.545	0.752	0.266	0.136	0.286	0.177	0.168
Fe^{2+}	0.735	0.743	0.716	0.574	0.477	0.587	0.553	0.567	0.490	0.445
Mn	0.002	0.006	0.006	0.002	0.002	0.006	0.007	0.005	0.034	0.026
Mg	0.048	0.041	0.084	0.109	0.094	0.266	0.354	0.260	0.399	0.485
Ca	0.000	0.002	0.000	0.000	0.002	0.000	0.000	0.001	0.002	0.001
Zn	0.003	0.001	0.001	0.002	0.000	0.001	0.000	0.000	0.000	0.000
V	0.000	0.000	0.000	0.000	0.000	0.000	0.000	0.000	0.000	0.000
Ni	0.001	0.002	0.001	0.000	0.001	0.002	0.002	0.003	0.001	0.002
% geikielite	5.0	4.3	8.9	11.4	9.9	26.9	36.0	26.7	39.4	46.7
% hematite	17.1	16.4	14.9	28.4	39.6	13.4	6.9	14.7	8.8	8.1
% ilmenite	77.7	78.6	75.6	60.0	50.3	59.2	56.3	58.2	48.5	42.8
% pyrophanite	0.2	0.7	0.6	0.3	0.2	0.6	0.7	0.5	3.3	2.5

Abbreviations: Compositional groups: **1.** Ilmenite sensu strictu; **2.** Fe^{3+}-rich ilmenite; **3.** Mg-rich ilmenite and **4.** Mn-rich ilmenite**.** Textures: **met.1** = metasomatic ilmenite (with apatite, clinopyroxene and amphibole); **met.2** = metasomatic ilmenite (veinlets in peridotites); **exsol** = ilmenite with hematite exsolutions; **sympl** = symplectitic ilmenite; **Mg-rich** = Mg enrichment in ilmenites,usually already rich in Mg (darker areas in BSE images); **recrist.** = ilmenite nodules showing recristallisation; **with Chr** = ilmenite nodules surrounding chromite and with inclusions

Table 9.1 (continued) Major element analyses of ilmenite (wt %) and the calculated structural formula in atoms per formula unit (apfu) normalised to 3 oxygens

Analysis	**ilm_11**	**ilm_12**	**ilm_13**	**ilm_14**	**ilm_15**	**ilm_16**	**ilm_17**	**ilm_18**	**ilm_19**
compositional group	3	3	3	3	3	3	4	4	4
Texture	*nodule*	*nodule*	*nodule*	*nodule*	*sympl*	*sympl*	*tabular*	*nodule*	Mn-rich
extra info	-	recrist.	with chr	with chr	-	-	-	Mn-rich	secondary
analysed area	*core*	*core*	*core*	*rim2*	*core*	*core*	*core*	core	core
oxides %									
SiO_2	0.09	0.06	0.00	0.33	0.06	0.01	0.02	0.03	0.01
TiO_2	48.81	48.42	48.60	49.18	49.96	42.88	50.55	53.17	51.11
Al_2O_3	0.54	0.58	0.26	0.20	0.79	2.00	0.05	0.56	0.05
Nb_2O_5	0.22	0.11	0.00	0.08	0.22	0.69	0.17	0.11	0.23
ZrO_2	0.03	0.13	0.05	0.00	0.34	0.73	0.00	0.16	0.00
Cr_2O_3	1.04	2.13	2.65	0.61	1.02	1.72	0.12	0.50	0.08
Fe_2O_3	11.44	11.22	8.78	18.17	11.01	19.59	2.05	5.88	2.31
FeO	29.19	27.40	28.32	11.61	24.61	21.29	15.92	19.37	29.39
MnO	0.19	0.27	1.60	1.49	0.70	0.43	29.10	9.50	16.42
MgO	8.27	8.95	7.65	17.44	11.15	10.04	0.08	10.50	0.10
CaO	0.00	0.00	0.10	0.25	0.08	0.08	0.04	0.11	0.02
ZnO	0.06	0.01	0.01	0.10	0.06	0.00	0.03	0.05	0.01
V_2O_3	0.00	0.01	0.00	0.00	0.00	0.23	0.00	0.00	0.00
NiO	0.10	0.19	0.04	0.11	0.10	0.03	0.07	0.19	0.00
sum	99.98	99.48	98.06	99.57	100.10	99.72	98.21	100.13	99.73
apfu (O=3)									
Si	0.002	0.001	0.000	0.008	0.001	0.000	0.000	0.001	0.000
Ti	0.884	0.877	0.880	0.891	0.905	0.777	0.916	0.963	0.926
Al	0.015	0.016	0.007	0.006	0.022	0.057	0.001	0.016	0.001
Nb	0.002	0.001	0.000	0.001	0.002	0.008	0.002	0.001	0.003
Zr	0.000	0.002	0.001	0.000	0.004	0.009	0.000	0.002	0.000
Cr	0.020	0.041	0.050	0.012	0.019	0.033	0.002	0.010	0.002
Fe^{3+}	0.207	0.203	0.159	0.329	0.199	0.355	0.037	0.106	0.042
Fe^{2+}	0.588	0.552	0.570	0.234	0.496	0.429	0.321	0.390	0.592
Mn	0.004	0.006	0.033	0.030	0.014	0.009	0.593	0.194	0.335
Mg	0.297	0.321	0.275	0.626	0.400	0.360	0.003	0.377	0.004
Ca	0.000	0.000	0.003	0.006	0.002	0.002	0.001	0.003	0.001
Zn	0.001	0.000	0.000	0.002	0.001	0.000	0.001	0.001	0.000
V	0.000	0.000	0.000	0.000	0.000	0.002	0.000	0.000	0.000
Ni	0.002	0.004	0.001	0.002	0.002	0.001	0.001	0.004	0.000
% geikielite	29.9	32.8	28.7	59.3	39.6	36.9	0.3	37.2	0.4
% hematite	10.4	10.4	8.3	15.6	9.9	18.2	2.0	5.3	2.2
% ilmenite	59.2	56.3	59.6	22.2	49.1	44.0	34.3	38.5	62.2
% pyrophanite	0.4	0.6	3.4	2.9	1.4	0.9	63.4	19.1	35.2

Abbreviations: Compositional groups: **1.** Ilmenite sensu strictu; **2.** Fe^{3+}-rich ilmenite; **3.** Mg-rich ilmenite and **4.** Mn-rich ilmenite**.** Textures: **met.1** = metasomatic ilmenite (with apatite, clinopyroxene and amphibole); **met.2** = metasomatic ilmenite (veinlets in peridotites); **exsol** = ilmenite with hematite exsolutions; **sympl** = symplectitic ilmenite; **Mg-rich** = Mg enrichment in ilmenites,usually already rich in Mg (darker areas in BSE images); **recrist.** = ilmenite nodules showing recristallisation; **with Chr** = ilmenite nodules surrounding chromite and with inclusions

their Mg content is variable (2.4-9.3 wt% MgO), it is usually low (average 3.1 wt% MgO). Cr concentrations are commonly below 1.5 wt% Cr_2O_3 (fig. 9.2b). Mn contents rarely exceed 0.25 wt% MnO. In contrast, the Fe^{3+} content of these ilmenites is significantly higher (6.9-45.7 wt% Fe_2O_3, average 39 wt%) than in the other populations.

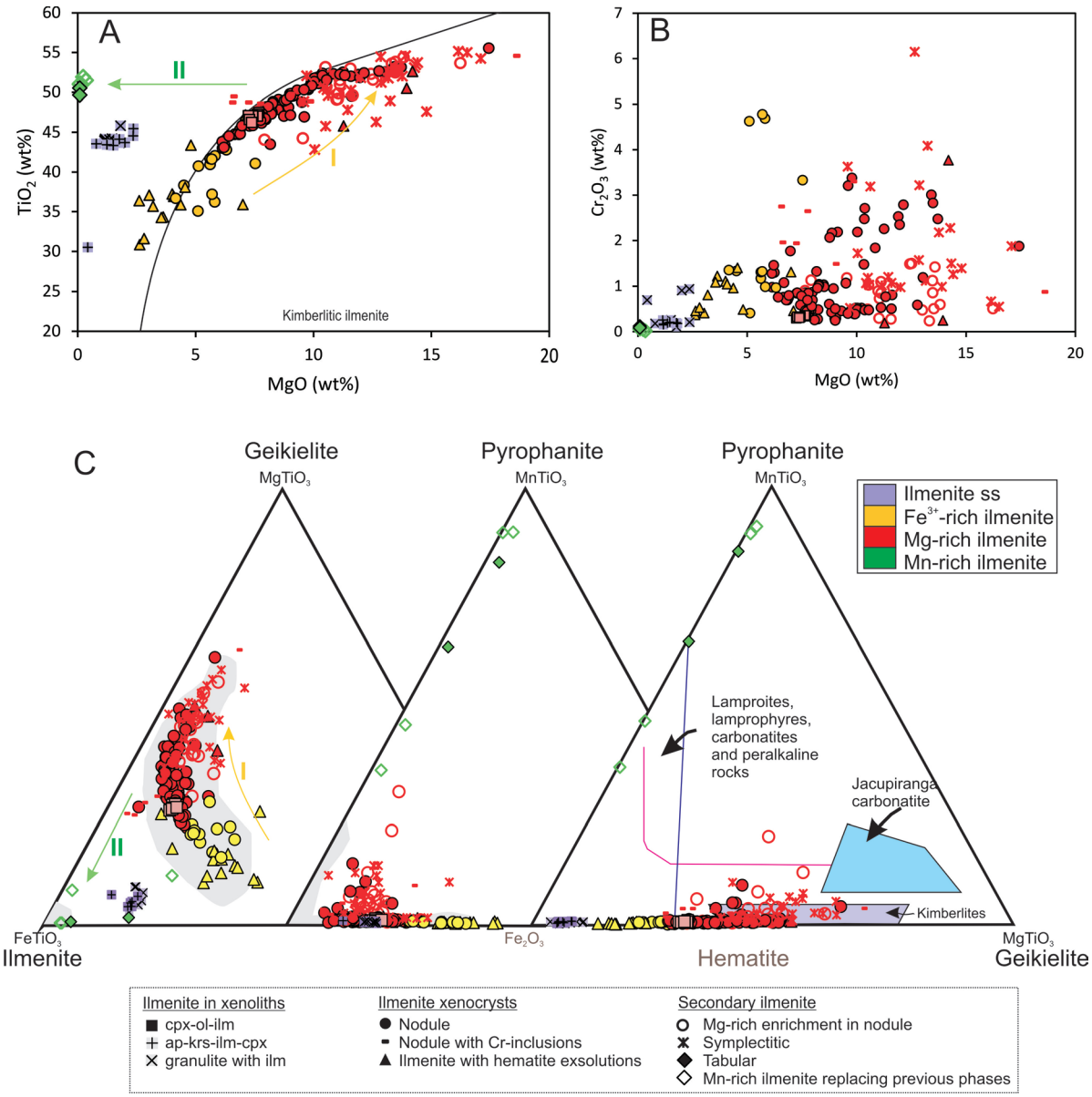

Figure 9.2. Major element chemistry of the different textural types of ilmenite of the Angolan kimberlites. (a) TiO_2-MgO, including the kimberlitic ilmenite field as defined by Wyatt et al. (2004) (b) Cr_2O_3-MgO. (c) classification of the analysed ilmenites in terms of their geikielite ($MgTiO_3$), ilmenite (FeTiO3), hematite (Fe2O3) and pyrophanite ($MnTiO_3$), after Mitchell (1979) and Tompkins and Haggerty (1985). Different colours represent different compositional groups: ilmenite sensu strictu (purple), ferric ilmenite (yellow), Mg-rich ilmenite (red) and Mn-rich ilmenite (green). In grey it is represented the composition of ilmenite xenocrysts of the Catoca kimberlite (Robles-Cruz et al., 2009). Yellow arrow (I) indicates Mg-enrichment trend, whereas the green arrow (II) shows the late Mn-ilmenite replacement trend.

Mg-rich ilmenite

Intergranular ilmenite found in xenoliths and most of the nodules of ilmenite found in this study can be defined as Mg-rich ilmenites (7.6-17.0 wt% MgO, average 12.5 wt% MgO). Ilmenites belonging to this compositional group are also often characterised by higher Cr contents (1-6.15 wt% Cr_2O_3) and lower Fe_2O_3 abundances (2.0-20.7 wt% Fe_2O_3, average 11.4 wt% Fe_2O_3). The late Mg enrichment along grain boundaries and fractures found in some of the nodules, as well as the symplectitic ilmenites, typically provides the highest Mg values, only comparable to the ilmenite nodules from the Lucapa kimberlite. Manganese contents in these textural groups are also slightly higher. Magnesium-rich ilmenite is also enriched in Cr when replacing chromite.

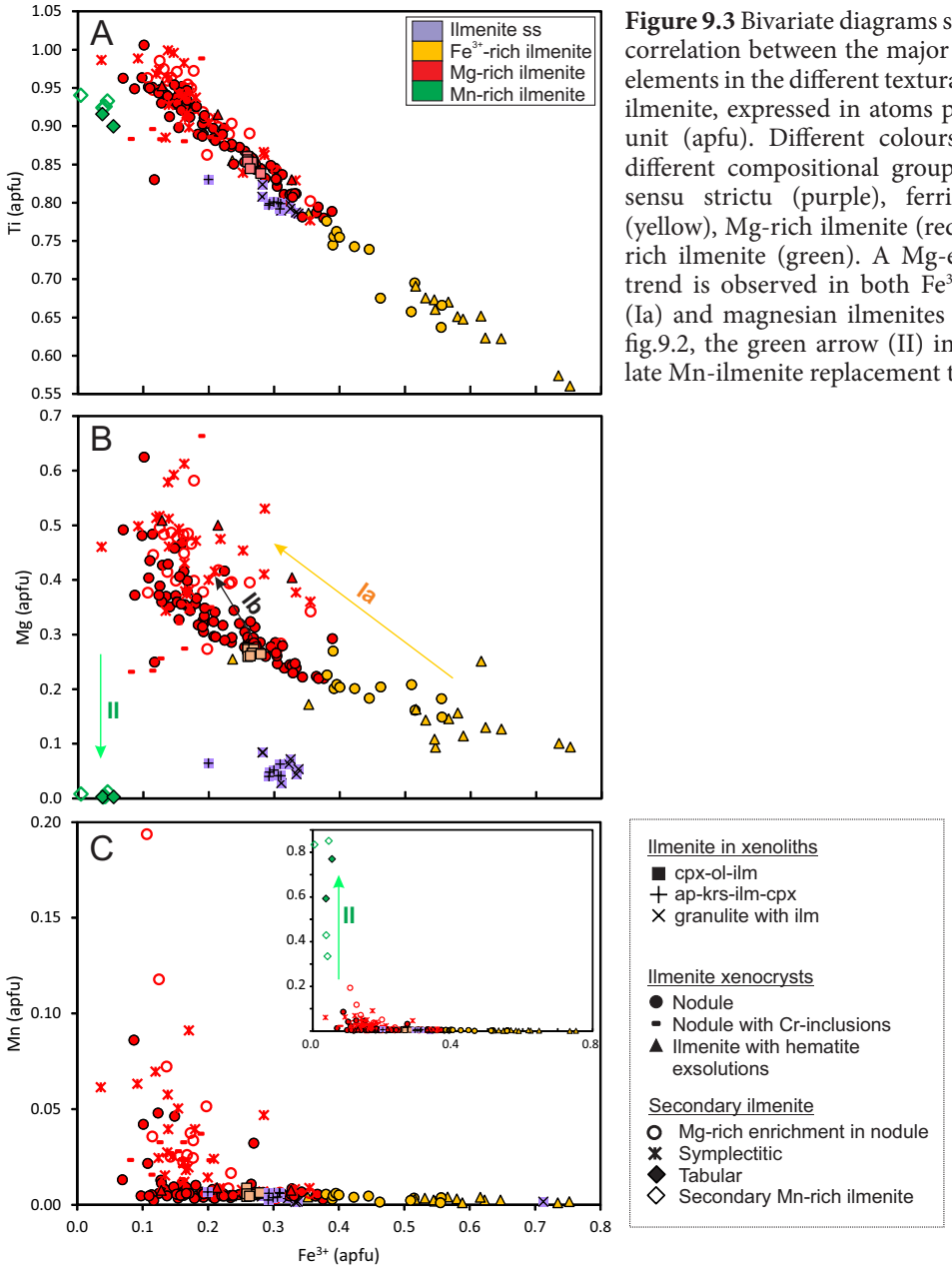

Figure 9.3 Bivariate diagrams showing the correlation between the major and minor elements in the different textural groups of ilmenite, expressed in atoms per formula unit (apfu). Different colours represent different compositional groups: ilmenite sensu strictu (purple), ferric ilmenite (yellow), Mg-rich ilmenite (red) and Mn-rich ilmenite (green). A Mg-enrichment trend is observed in both Fe^{3+} ilmenites (Ia) and magnesian ilmenites (Ib). As in fig.9.2, the green arrow (II) indicates the late Mn-ilmenite replacement trend.

Mn-rich ilmenite

This group is composed of the tabular ilmenite and the late Mn-rich ilmenites that replace earlier ilmenite xenocrysts and other Ti phases. Their manganese content is very high compared to the other ilmenites (up to 40.8 wt% MnO), especially in the secondary ilmenite, which is almost pure pyrophanite (Pph≈88) (fig 9.2c and fig.9.3c). In the MgO-TiO_2 diagram they plot in the "non-kimberlitic" field (fig. 9.2a), although they clearly have a kimberlitic origin. They are also typically poor in Mg, Cr and Nb (<0.4 wt% MgO, <0.1 wt% Cr_2O_3 and <0.3 wt% Nb_2O_5).

Although representative profiles were done in each ilmenite type, the results presented here show that most of the analysed ilmenite grains lack zoning in terms of major-element composition. The few exceptions are shown in fig. 9.4, where element profiles and maps for both symplectitic ilmenite and ilmenite with inclusions are presented. The main variations are in their Mg and Cr content.

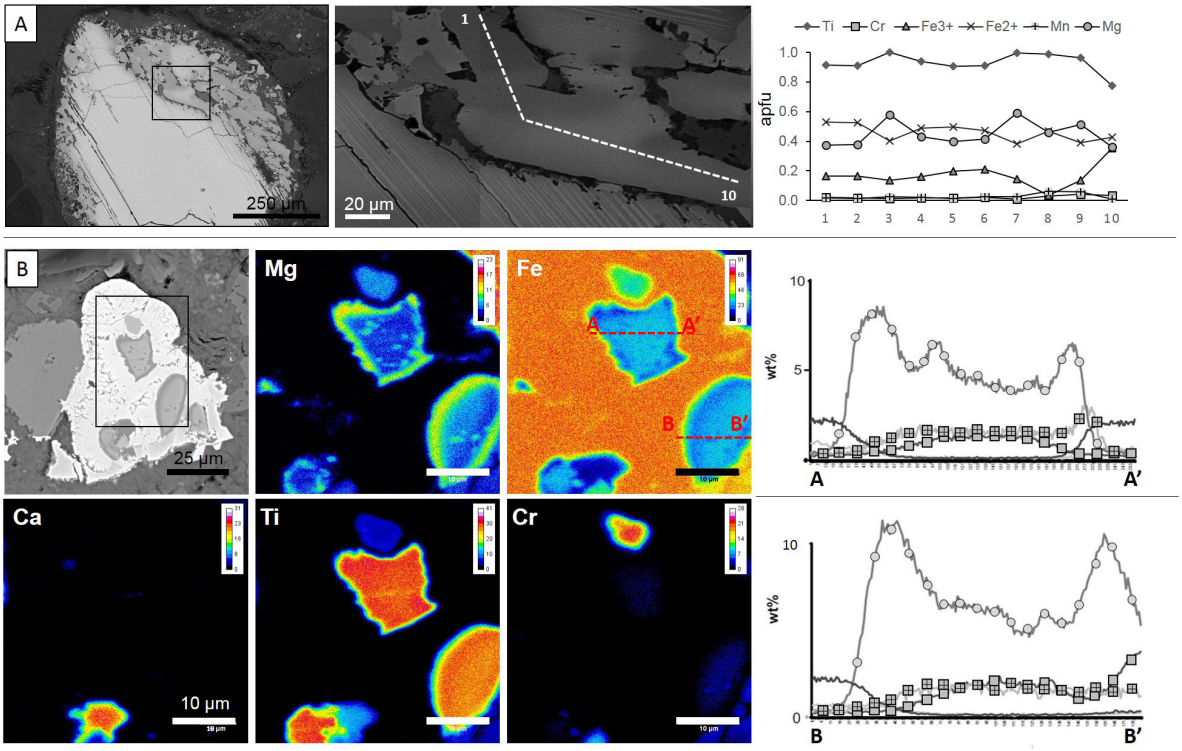

Figure 9.4 Zoning patterns in ilmenite. Except where indicated otherwise, the length of the scale bar is 10 microns. (a) BSE images and element profile of symplectitic ilmenite of the Tchiuzo kimberlite, showing that the main changes in the brightness of the BSE images are correlated with its variation in Mg; (b) BSE image, element maps and profiles of ilmenites associated with chromite and titanite in the Lucapa kimberlite. These ilmenites show strong enrichment in Mg the grain boundaries. Inclusions in ilmenite are characterised by higher Mg and Al (not shown, see table 2) and lower Fe contents.

9.2.4. Trace-element composition

The trace-element composition of the analysed ilmenites is compared with data from other kimberlitic ilmenite worldwide (fig. 9.5). Representative analyses of the trace-element composition of each ilmenite group have been included in table 9.2. Because of the fineness of the ilmenite-hematite exsolutions, it was not possible to ablate only ilmenite without analysing hematite lamellae at the same time. Therefore, in order to avoid data resulting from a mixture of both phases, trace-element analysis of this textural group was only performed in the few grains with exsolution-free areas.

Data from the Angolan kimberlites studied here are consistent with the few available trace-element analyses of ilmenite nodules from kimberlites worldwide (Moore et al., 1992; Griffin et al., 1997; Kostrovitsky et al., 2004; Kaminsky and Belousova, 2009; see fig. 9.8). Hence, ilmenite grains from the Angolan kimberlites show relative high Nb contents (310-3220 ppm) similar to those found in other kimberlites worldwide, as well as a significant enrichment in the other HSFE (45-410 Ta ppm, 10-2430 Zr and up to 100 Hf ppm). This composition clearly differs from those of ilmenites derived from other geological settings, which usually have very low contents of these elements (Jang and Naslund, 2003; Dare et al., 2012; Kryvdik, 2014). The exception is the ilmenites found in carbonatites, where the HSFE compositional range extends towards even higher values (Kryvdik, 2014).

Most of the ilmenite populations show a positive correlation between Nb and the other HFSE. This trend coincides with that found in ilmenites from carbonatites (Kryvdik, 2014). A slight covariance is also seen between Nb and V. On the contrary, there is an inverse relationship between Nb and Mg contents in the ilmenites.

The ilmenite populations with the highest Mg contents (i.e. symplectitic, secondary Mg enrichment in the ilmenite nodules) typically show significantly higher contents of HSFE, Cr and V (table 9.2) at a given Nb content, and thus diverge from the general trends described previously. In contrast, ilmenite of granulite and garnet pyroxenites is characterised by very low contents of HSFE, Cr and Sc, but has characteristically high Zn and V contents (>700 ppm Zn, > 3000 ppm V), as well as high Nb/Ta ratios (>17). These values are closer to those from non-kimberlitic rocks, where the Nb/Ta ratios are typically above 10 (Jang and Naslund, 2003; Dare et al., 2012; Kryvdik, 2014). In contrast, Nb/Ta ratios in ilmenites from kimberlites are usually lower and fall within a narrow range (5-10) (fig. 9.5).

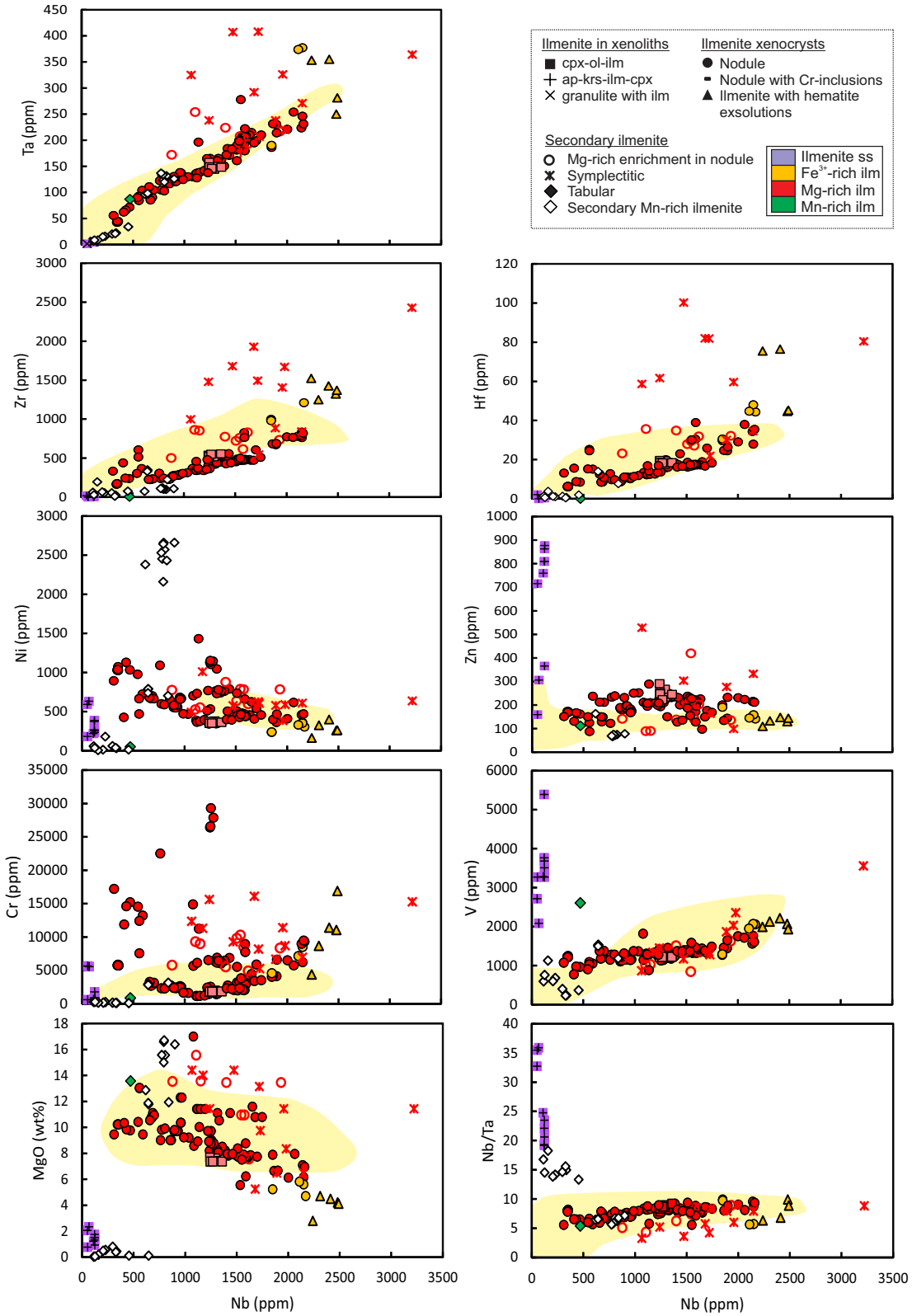

Figure 9.5 Trace-element compositional plots for the different textural groups of ilmenite found in the kimberlites of the Lunda Norte province. There is a positive correlation between Nb and the other HSFE (Ta, Zr, Hf) as well as with V. Notice the enrichment in HFSE of the Mg enrichment in ilmenite nodules and symplectitic ilmenites. Data from ilmenite inclusions in diamond (Sobolev, 1977; Kaminsky et al., 2001, 2000), as well as trace-element compositions of ilmenite xenocrysts from other kimberlites worldwide (Moore et al., 1992; Kaminsky and Belousova, 2009; Kryvdik, 2014) have been included for comparison (open diamonds and yellow field, respectively). Different colours of the symbols represent different compositional groups: ilmenite sensu strictu (purple), ferric ilmenite (yellow), Mg-rich ilmenite (red) and Mn-rich ilmenite (green).

Table 9.2 Selected trace element analyses of ilmenite (ppm)

Sample	35_c_040	42_b_155	50_2a_107	32A_g_087	6A_d_055	44_b_125	35_i_061	26_j_032	12_a_008	12_d_024	32A_l_098
Kimberlite	*Cat 115*	*Cat 115*	*Tchiuzo*	*Cat 115*	*Cat 115*	*Cat 115*	*Cat 115*	*Cat 115*	*Lucapa*	*Lucapa*	*Cat 115*
Compositional group	1	1	1	2	2	3	3	3	3	3	3
Texture	*granulite*	*met. 1*	*nodule*	*exsol**	*exsol**	*met. 2*	*nodule*	*nodule*	*nodule*	*nodule*	*nodule*
info extra	xenolith	xenolith				xenolith	Mg-ilm	Mg-ilm			
Sc	12.94	17.69	24.1	30	27.1	18.41	25.3	30.2	19.31	34.3	18.2
V	3510	2085	1292	1936	1995	1251	1363	1629	978	778	1328
Cr	861	5560	4581	16900	4380	1859	4930	8340	14590	11870	5860
Mn	1614	2480	1486	1399	962	2031	1838	2812	2493	15220	1815
Co	166	195	114.2	102.1	114.5	147.4	139.1	115.6	190.5	128.6	135.5
Ni	234.2	631	238.1	261	163.1	369	597	785	1130	427	539
Zn	810	306	191.4	144	109.3	268	202	136.1	167.3	131.4	177
Ga	17.6	4.66	13.59	13.4	21.3	15.01	19.4	23	10.34	8.97	16.24
Zr	4.69	bdl	982	1371	1523	518	831	735	244.4	441	608
Nb	122.5	67.5	1849	2490	2240	1292	1620	1930	430	409	1700
Hf	0.41	bdl	30.57	45.3	75.5	17.6	31.9	32.2	8.78	15.63	25.9
Ta	5.94	1.88	190.1	281	353	144.2	193	216.7	66.1	62.3	199
U	bdl	bdl	0.1092	0.12	bdl	bdl	bdl	0.0844	bdl	bdl	bdl
W	0.337	bdl	0.479	0.301	bdl	bdl	0.323	0.273	0.0861	bdl	bdl
Nb/Ta	20.6	35.9	9.7	8.9	6.3	9.0	8.4	8.9	6.5	6.6	8.5
Zr/Nb	0.0	-	0.5	0.6	0.7	0.4	0.5	0.4	0.6	1.1	0.4
Zr/Hf	11.4	-	32.1	30.3	20.2	29.4	26.1	22.8	27.8	28.2	23.5

Sample	618-267a_b_139	22_g_081	60A_4a_052	22_c_070	59-A2_c_057	32A_i_094	34_b_013	34_b_013	618-47_g_116	618-47_g_115
Kimberlite	*Tchiuzo*	*Cat 115*	*Tchiuzo*	*Cat 115*	*Tchiuzo*	*Cat 115*	*Cat 115*	*Cat 115*	*Tchiuzo*	*Tchiuzo*
Compositional group	3	3	3	3	3	3	3	3	4	4
Texture	*nodule*	*nodule*	*nodule*	*nodule*	*nodule*	*sympl*	*sympl*	*sympl*	*nodule*	*Tabular*
info extra		recryst.	recryst.			Mg-rich	Mg-rich	Mg-rich	Mg- Mn-ilm	Mn-rich
Sc	19.8	20.85	15.26	18.17	15.05	57.3	bdl	bdl	59.4	130
V	1374	1327	1281	1205	1108	2030	1719	1870	1021	2610
Cr	2300	6870	2325	6190	2715	11400	6950	6660	9290	840
Mn	2030	1762	2175	2052	2003	2720	2050	2240	21600	248000
Co	137	155.5	162.6	155	152.9	102.1	148	151	156	140
Ni	398	789	600	765	621	384	609	579	529	52
Zn	128	200.9	233.8	235	185.3	99.2	333	277	89.7	112
Ga	13.1	16.93	14.24	14.67	12.05	15.4	24.5	22.4	9.8	bdl
Zr	428	559	240	450	237.7	1407	841	885	864	8.4
Nb	1410	1437	774	1359	859	1958	2148	1890	1106	470
Hf	16.3	23	9.8	17.6	8.94	59.7	34.6	30.1	35.7	0.06
Ta	172	171	104.7	163	122.8	326	271	238	254	87
U	bdl	bdl	bdl	bdl	bdl	bdl	bdl	bdl	bdl	3.65
W	bdl	0.331	bdl	0.341	0.169	bdl	bdl	bdl	bdl	4.1
Nb/Ta	8.2	8.4	7.4	8.3	7.0	6.0	7.9	7.9	4.4	5.4
Zr/Nb	0.3	0.4	0.3	0.3	0.3	0.7	0.4	0.5	0.8	-
Zr/Hf	26.3	24.3	24.5	25.6	26.6	23.6	24.3	29.4	24.2	140.0

Abbreviations: Compositional groups: **1.** Ilmenite sensu strictu; **2.** Fe^{3+}-rich ilmenite; **3.** Mg-rich ilmenite and **4.** Mn-rich ilmenite. Textures: **met.1** = metasomatic ilmenite (with apatite, clinopyroxene and amphibole); **met.2** = metasomatic ilmenite (veinlets in peridotites); **exsol** = ilmenite with hematites exsolutions; **sympl** = symplectitic ilmenite; **Mg-rich** = Mg enrichment in ilmenites,usually already rich in Mg (darker areas in BSE images); **recrist.** = ilmenite nodules showing recristallisation; **with Chr** = ilmenite nodules surrounding chromite and with inclusions

9.2.5. Discussion

Ilmenite evolution

The occurrence and composition of ilmenite in the Angolan kimberlites can only be understood by integrating textural characterisation and chemical analysis of the ilmenite populations.

Textural evidence indicates a pre-kimberlite origin for most of the primary ilmenite generations. Additionally, the large compositional range shown by the ilmenite xenocrysts, as well as the textural relationships between the different populations, are also indicators of disequilibrium between the xenocrysts and the host kimberlite. Therefore, none of the ilmenite populations are considered to be kimberlitic liquidus phases.

A multi-stage model is proposed in fig. 9.6 to explain ilmenite evolution in the Angolan kimberlites. The textures and compositions observed in the ilmenite xenocrysts resulted from a combination of complex processes involving early metasomatism of mantle and crustal rocks, subsequent disaggregation of xenoliths, interaction with the kimberlitic magma(s) and late subsolidus replacement.

The textural study of the xenoliths revealed that the different types of ilmenite can be found in mantle xenoliths sampled by the kimberlite. A first example in this study would be the ilmenite-bearing granulite. In this xenolith, ilmenite shows compositions out of the kimberlite field and commonly displays evidences of hematite exsolution. It is extremely poor in elements typical of kimberlites as Mg, Cr, or HFSE, but enriched in V and Zn. Likewise, at least two types of intergranular metasomatic ilmenite have been found in the mantle xenoliths sampled by the Angolan kimberlites; one associated with amphibole and apatite (Mg-poor) and another with Cr-rich diopside (intermediate Mg, slightly enriched in HFSE). Similar ilmenite has been found in many metasomatized xenoliths in Angolan kimberlites (i.e. Robles-Cruz et al., 2009) and in other kimberlites worldwide (e.g., Dawson and Smith, 1977; Dawson, 2002). They show a wide range of compositions and mineral associations, thus suggesting a diversity of metasomatic processes reflecting the action of different types of magmas and/or environmental conditions of precipitation. Subsequent disaggregation of xenoliths during magma ascent would account for the two main compositions (Fe^{3+}-rich and Mg-rich) found in the ilmenite nodules of the Angolan kimberlites.

Most of the magnesian ilmenite nodules in the kimberlite matrix are thought to derive from

the liberation of intergranular ilmenite in metasomatised olivine-clinopyroxenite xenoliths, since both their major and trace-element compositions are similar. Although these nodules originally had relatively high Mg contents (~8.8 wt% MgO), they were often further enriched in this element (>11 wt% MgO) along grain boundaries and fractures. This Mg increase is very common in kimberlitic ilmenites (Mitchell, 1986), and it has been attributed to an interaction either with the kimberlitic magma (e.g., Pasteris, 1980), with Mg-rich metasomatic fluids (Boctor and Boyd, 1981) or with a late Mg-rich fluid not necessarily related to the kimberlitic magma (Robles-Cruz et al., 2009). In situ analysis shows that the Mg enrichment is commonly accompanied by a slight increase in the HFSE (Ta, Zr and Hf) contents in the original nodule (fig. 9.5). Consequently this enrichment is interpreted here as the product of an interaction with a carbonate-bearing kimberlite magma, which would have high contents of these elements (Kamenetsky et al., 2014; Castillo-Oliver et al., 2016).

In contrast, the available data are not enough to constrain the source of the Fe^{3+}-rich ilmenite xenocrysts. After comparing their trace-element composition with the data of all the mantle xenoliths recovered from the kimberlite, as well as with data from the literature, no clear source could be identified. However, the abundant hematite exsolutions observed in most of these xenocrysts suggests a crustal origin for this type of ilmenite. The formation of oriented hematite lamellae within an originally homogeneous ilmenite nodule has been reported in many kimberlites worldwide and it is commonly agreed that it is caused by a decrease of temperature or increase in oxygen fugacity under subsolidus conditions (e.g., Mitchell, 1986 and references therein; Haggerty, 1991a). Subsequently symplectitic ilmenite crystallised on most of these xenocrysts, replacing the original nodule along grain boundaries and/or the exsolution planes. This second generation of ilmenite is typically enriched in Mg (>10wt% MgO) and has the highest HFSE values in this study. The compositional similarities between symplectitic ilmenite and the enrichment in Mg in the magnesian ilmenite nodules suggests that the same process may have led to the crystallisation of both ilmenite types. Additionally, symplectitic ilmenite crystallises together with characteristic kimberlite phases such as perovskite (Mitchell, 1986), which further supports a kimberlitic origin for this second generation of ilmenite. The differences in the Mg content of the secondary Mg-rich ilmenites indicate variable degrees of interaction with the kimberlite magma. Consequently, this interaction probably took place during the ascent of the kimberlitic magma and not prior to entrainment, in which case more homogeneous compositions might be expected.

The next stage is represented by the crystallisation of Mn-rich ilmenite, either replacing previous generations of ilmenite or as small Mn-ilmenite plates in the kimberlitic matrix. This ilmenite type is characteristic of the Tchiuzo kimberlite and it is significantly more enriched in manganese than the Mn-rich ilmenites found in the nearby Catoca kimberlite (Robles-Cruz et al., 2009) and other pipes of the same kimberlitic cluster (Ashchepkov et al., 2012). The

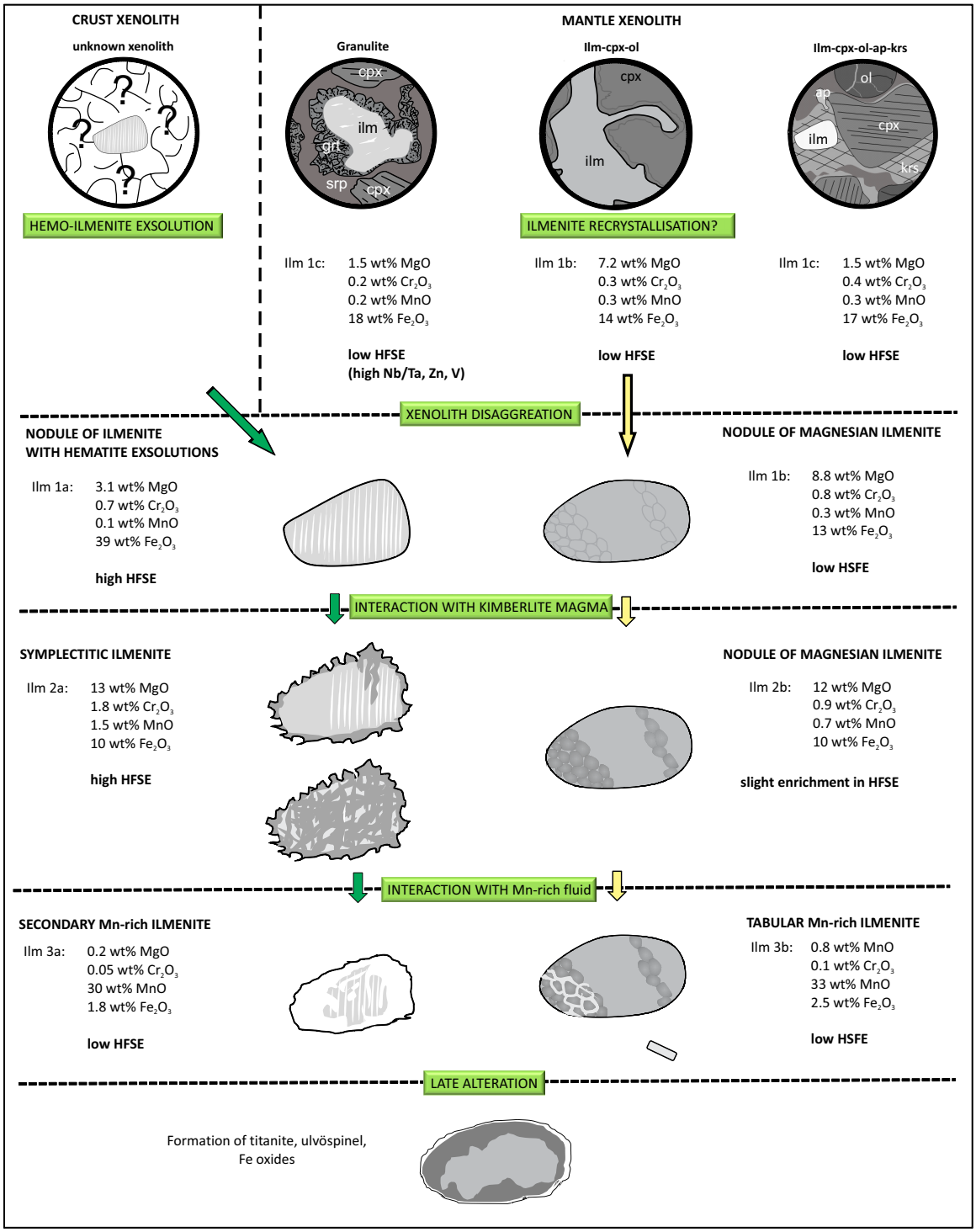

Figure 9.6 Schematic model of the multi-stage petrogenesis of ilmenite in the studied kimberlites, including the average composition of ilmenite at each stage. Mineral abbreviations: clinopyroxene (cpx), ilmenite (ilm), garnet (grt), serpentine (srp), apartite (ap), kaersutite (krs) and olivine (ol).

occurrence of manganoan ilmenites has also been reported in other kimberlites worldwide (e.g., Pasteris, 1980; Tompkins and Haggerty, 1985; Chakhmouradian and Mitchell, 1999; Robles-Cruz et al., 2009), although they are more common in carbonatite intrusions (e.g., Mitchell, 1978; Gaspar and Wyllie, 1983; Kryvdik, 2014). However, there is still a lack of consensus about the origin of the Mn-rich ilmenites in kimberlites. The processes suggested to have led to their formation include primary crystallisation under superdeep conditions (Kaminsky and Belousova, 2009), crystallisation from a late-stage fraction of the kimberlitic melt (e.g., Tompkins and Haggerty, 1985), interaction with a CO_2–rich fluid or a carbonatite-like magma (Gaspar and Wyllie, 1984; Robles-Cruz et al., 2009) and even late hydrothermal activity related to serpentinisation (Robles-Cruz et al., 2009). Manganoan ilmenite is produced at a very late stage in the mineral sequence of the kimberlite, and may replace all the other ilmenite generations. Moreover, due to the near absence of HSFE in the Mn-ilmenites studied here, it is unlikely that interaction with a late carbonatitic magma triggered their crystallisation. Therefore, in this case, this ilmenite may have been produced by late hydrothermal fluids during the serpentinisation processes.

In any case, the development of both magnesian and magnanoan ilmenites in the Angolan kimberlites cannot be ascribed to only one process; instead, it suggests the interaction of the xenocrysts with different types of kimberlitic-carbonatitic magmas. Mixing of compositionally distinct magmas within a single kimberlite has already been proposed in other Angolan kimberlites (Castillo-Oliver et al., 2016), as well as in kimberlites from other cratons (Chakhmouradian and Mitchell, 2001; Ogilvie-Harris et al., 2009).

Trace-element composition as tracer of the source of the ilmenite xenocrysts

As discussed above, ilmenite xenocrysts of different origin may eventually acquire similar major-element compositions (symplectitic ilmenite and Mg-rich ilmenite nodules). This compositional homogenisation is suggested to result from the interaction of the xenocrysts with the kimberlitic magma during entrainment, and this is supported by the co-crystallisation of ilmenite and perovskite. Although in this study symplectitic ilmenite only partially replaces previous ilmenite xenocrysts, totally replaced nodules have been found in the Catoca kimberlite (Robles-Cruz et al., 2009). As a consequence, we suggest that replacement of an originally Fe^{3+}- rich ilmenite could lead to compositionally homogeneous Mg-rich ilmenite xenocrysts by interaction with the kimberlitic magma. Therefore, caution should be taken when analysing

ilmenite concentrates without consideration of their texture and/or their trace-element composition. A high Mg content in ilmenite would not necessarily indicate the reducing conditions within the diamond stability field commonly regarded as favourable for diamond preservation. Instead, this enrichment could be a good indicator of the degree of interaction of the ilmenite with the kimberlitic magma. Trace-element chemistry is useful to constrain the source of the ilmenite xenocrysts by identifying whether the high Mg contents result from the interaction with the kimberlitic magma or earlier metasomatism. In this study, the characteristically high contents in HSFE in the Fe^{3+}-rich ilmenites clearly differ from the trace-element signatures of the other ilmenite xenocrysts found in the kimberlites. This has allowed us to follow them through the stages of their subsequent replacement during interaction with the kimberlite.

Links between diamond and ilmenite

Diamond formation is commonly agreed to occur as a consequence of complex metasomatic processes in the mantle, mainly near the base of the SCLM (Stachel et al., 2004; Malkovets et al., 2007). Infiltration of carbon-bearing fluids, enriched in Sr, Zr, Nb and LREE, is thought to be responsible for diamond growth (Sobolev et al., 1997; Araújo et al., 2009). Similarly, it is widely accepted that ilmenite is a typical metasomatic phase in the mantle (O'Reilly and Griffin, 2013), commonly found in MARID (Dawson and Smith, 1977) and related rocks (Grégoire et al., 2002).

Nevertheless, the link between ilmenite and diamond occurrence in kimberlites remains unclear. Initially it was suggested that ilmenite is a phenocryst, crystallising directly from the kimberlitic magma (e.g., Mitchell, 1973). However, subsequent work concluded that most of the ilmenite megacrysts found in the kimberlites are xenocrysts (e.g., Pasteris, 1980), even if the source rock of ilmenite was not well defined. More recently, it was proposed that ilmenite megacrysts are the product of fractional crystallisation from a mafic, picritic magma under isobaric conditions (e.g., Moore et al., 1992). Others suggested that the metasomatic ilmenite typical of some peridotites could also account for some of the xenocrysts found in kimberlitic rocks (e.g., Griffin et al., 1997; Sobolev et al., 1997). Controversy continues as recently a primary origin for the Mn-ilmenite megacrysts has been proposed (Kaminsky and Belousova, 2009).

In contrast with other DIMs, the occurrence of ilmenite inclusions in diamond is very

rare (Harris et al., 1984). However, some evidence pointing to a link between the two phases has been found, either as ilmenite inclusions in diamonds or as intergrowths with silicate phases (Meyer and Svisero, 1975; Mvuemba Ntanda et al., 1982; Jacques et al., 1989; Sobolev et al., 1997, 1999; Kaminsky et al., 2000, 2001). The composition of the ilmenite inclusions in diamond is heterogeneous, ranging from magnesian ilmenites (9-16 wt% MgO; Sobolev et al., 1997 and references therein) to Mg-poor (0.04-0.14 wt% MgO) and Mn-rich ilmenites (2-11 wt% MnO; Kaminsky et al., 2001 and references therein). Trace-element analysis of ilmenites included in diamonds from the Siberian craton showed an enrichment not only in Mg and Cr, but also in Ni, and high Nb/Zr ratios.

These compositional signatures were used to argue for a metasomatic origin of both ilmenite and diamond (Sobolev et al., 1997). Similarly, coexistence of ilmenite and lindsleyite-mathiashite (LIMA) group minerals as inclusions in diamond has been interpreted as further evidence for a common metasomatic origin (Haggerty, 1983). These phases previously have been related to low-T metasomatism and precipitation of phlogopite (Haggerty, 1983), but usually the geotherms are too hot for this process to take place at pressures high enough to be within the diamond stability field (Erlank et al., 1987). However, thermobarometry of mantle xenoliths from the Lunda Norte province reveal a geotherm significantly lower than in other cratonic areas (see chapter 7), which would be consistent with the deep roots (>300km) expected for the Congo Craton (Begg et al., 2009; O'Reilly et al., 2009). As a result, it would be possible for the metasomatism described by Haggerty (1983) to have occurred at pressures favourable for diamond formation in NE Angola. Nevertheless, the trace-element compositions of the ilmenites studied here differ from those of the Magnesian ilmenite found as diamond inclusions in other kimberlites worldwide (fig.9.5). As a consequence, additional systematic petrographic studies coupled with chemical analyses are still required to prove a genetic link between the metasomatism that led to ilmenite crystallisation and that responsible for diamond formation.

Ilmenite as diamond indicator mineral

Because of ubiquity of ilmenite in kimberlites, much effort has been expended on the characterisation of ilmenite chemistry to assess the diamond grade of targeted pipes. Even if it is now widely agreed that ilmenite is a xenocryst, and thus not directly related to the kimberlite magma, its composition has been used to constrain conditions in the mantle sampled by the

kimberlitic magma. Along these lines, Gurney and Zweistra (1995) suggested that the Fe_2O_3 - MgO diagram could be used to evaluate the diamond grade of a given kimberlite. Their results are based on the premise that ilmenite showing high Fe^{3+} contents would have crystallised from an oxidising environment and, as a consequence, diamond could not be formed or preserved. Ilmenite megacrysts from both economic and non-economic South African kimberlites could also be consistently distinguished based on this diagram (Griffin et al., 1997). However, analysis of ilmenite xenocrysts in high-grade kimberlites worldwide has revealed that this model is not universally applicable (Schulze et al., 1995 and references therein).

Recent improvement of in-situ techniques such as LA-ICP-MS has spurred the use of trace element chemistry as a tool for assessing the diamond grade of the kimberlites. The Zr/Nb ratio has been recently proposed as an additional discriminant of the diamond grade of kimberlites (Carmody et al., 2014). These authors defined a threshold value of Zr/Nb ~ 0.37; only ilmenites recovered from high-grade kimberlites have higher values. Similarly, they observed that ilmenites from barren or very low-grade kimberlites usually have Nb/Ta < 10.

In this work, for the sake of simplicity, only the ilmenite populations that could be acquired during the exploration stage (>50 microns) have been included in the Fe_2O_3- MgO and Zr/Nb-Nb/Ta discriminant diagrams shown in fig.9.7. Although all the kimberlites represented in the graphs contain diamonds, the Fe_2O_3 - MgO diagram shows no correlation between the diamond preservation of the kimberlites and the composition of their ilmenite xenocrysts. On the contrary, ilmenites from the Cat115 kimberlite, which has highest diamond grade in this study, mostly fall in the marginal preservation field. Similarly, neither the composition of ilmenite inclusions in diamond nor the data from this study support the use of the Zr/Nb vs Nb/Ta diagram to assess the diamond grade of the kimberlites. Moreover, symplectitic ilmenites typically show high Zr/Nb ratios and thus the threshold value of Zr/Nb ~ 0.37 in this case would not be linked to diamond formation, but rather indicate the degree of interaction with the kimberlitic magma.

In striking contrast with the composition of the majority of the ilmenite kimberlitic xenocrysts worldwide, manganoan (0.63-2.49 wt% MnO) ilmenite xenocrysts were found in Juina (Brasil) (Kaminsky and Belousova, 2009). Their trace-element composition clearly differs from that of the common ilmenite xenocrysts, being significantly poorer in Cr, Ca, Ni, Nb and Ta. Such compositions, however, are comparable to those of ilmenite inclusions in superdeep diamonds from the same area (Kaminsky et al., 2001; Kaminsky and Belousova, 2009). As a

consequence, these Mn-ilmenite nodules were considered as primary phases crystallized from a very deep (>670 km) magma, in a Ti-rich environment and genetically related to diamond (Kaminsky et al., 2001). These conclusions lead the author to suggest that the compositional range of the "classic" composition of DIMs should be enlarged, especially in the areas with minor amounts of the usual indicator minerals. However, the Mn-rich ilmenite found in the Angolan kimberlites is a secondary/late phase, being either a second replacement of the original ilmenite xenocrysts or crystallising as small plates from a Mn-rich fluid. Therefore, although from the geotectonic perspective a link between the Angolan and the Brasilian kimberlite fields would be reasonable, Mn-ilmenite cannot be used as a new diamond indicator unless an early origin for the Mn-ilmenite could be demonstrated in other contexts.

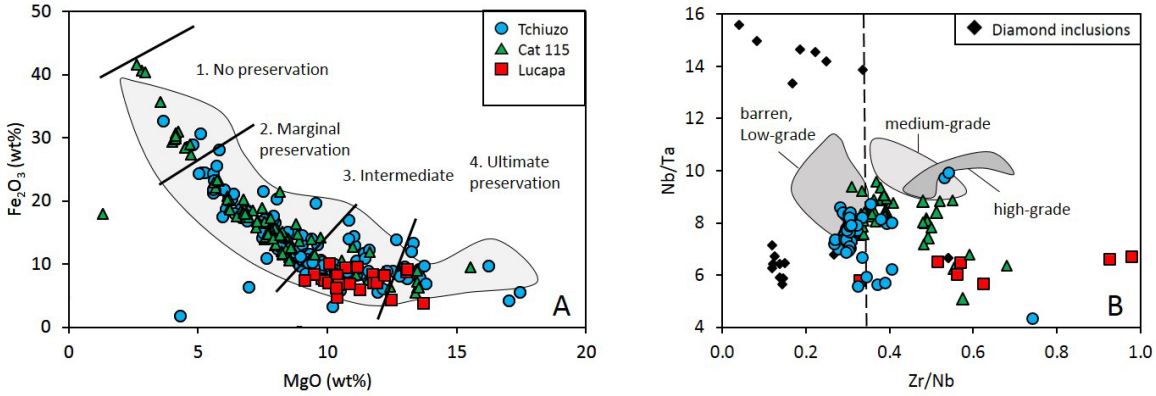

Figure 9.7 Discriminatory diagrams used to define the diamond grade of a kimberlite from the composition of its ilmenite xenocrysts. (a) Fe_2O_3 vs MgO diagram, proposed by Gurney and Zweistra (1995). All the kimberlites represented in the diagram (Lucapa, Tchiuzo and Cat115) contain diamonds. The field in grey includes data of ilmenite grains from the Catoca kimberlite (Robles-Cruz et al., 2009). (b) Zr/Nb vs Nb/Ta diagram, modified after Carmody et al. (2014). The dashed line indicates the threshold Zr/Nb ~ 0.37 that the authors proposed to assess the diamond grade of the kimberlite. The fields represented in grey were drawn after a collection of ilmenite xenocrysts of Siberian kimberlites with different diamond grade (Carmody et al., 2014). Data from ilmenite inclusions found in diamond are also represented for comparative purposes (Kaminsky et al., 2001; Sobolev et al., 1997).

9.3. Chromian pyrope

9.3.1. Introduction

Cr-rich pyrope xenocrysts derived from disaggregation of peridotite are very abundant in the mineral concentrates used for diamond exploration. Using the Cr_2O_3-CaO diagram, the source rock of the garnets can be identified (Gurney, 1984; Grütter et al., 2004). Pyrope inclusions in diamond are characterised by low Ca contents and enrichment in Cr (>5% Cr_2O_3) and usually plot in the harzburgitic (G10) field in this diagram (Gurney, 1984). As a result, a predominance or high abundance of harzburgitic garnet populations is commonly regarded as

indicative of high economic grade of the kimberlite.

However, the presence or absence of type G10 garnets is not an infallible indicator of the diamond grade of the kimberlite. As an example, it has been observed that Sommerset Island kimberlites (Canada) do not contain G10 garnets, despite being considered diamondiferous (<1CM/100t) (Jago and Mitchell, 1989). Likewise, the amount of G9 garnets in some fertile kimberlites in Colorado-Wyoming clearly exceeds the G10 garnet population (Carlson and Marsh, 1989). In contrast, both Skerring (Australia) and Zero (South Africa) kimberlites contain abundant G10 populations, but are devoid of diamond (Jacques et al., 1986; Shee et al., 1989). Other examples can also be found in the Slave craton, where non-economic kimberlites have higher contents of G10 garnets than the Ekati and Diavik diamondiferous bodies (Griffin and O'Reilly, 2005). As Mitchell (1991) concluded, the absence of G10 garnets in kimberlites only implies that harzburgite rocks similar to those found in the Kaapvaal and Anabar cratons have not been either formed in the underlying SCLM or sampled by the kimberlitic magma during its ascent towards the surface. These observations are in very good agreement with the preliminary results obtained for the Catoca kimberlite (Robles-Cruz et al., 2012b). Despite its high diamond grade, the garnet xenocrysts dominantly belong to the G9 type and only very few could be described as harzburgitic garnets.

Although significantly less abundant than peridotite garnets, eclogitic garnets have also been found as inclusions in diamond. Despite the small amount of eclogite xenoliths recovered from most kimberlite bodies worldwide - compared to the peridotite suite -, some South African kimberlites are particularly enriched in eclogites (e.g., MacGregor and Manton, 1986; Gréau et al., 2011; Huang et al., 2012). As a consequence, their composition has also been proposed as a tool to define the diamond grade of these particular kimberlites. Eclogitic garnet inclusions in diamonds have high sodium contents (>0.07% Na_2O) (Sobolev and Lavrent'ev, 1971; Gurney and Moore, 1993) and are usually poorer in Ti than Cr-poor megacrysts, with Na:Ti ratios close to unity (Reid et al., 1976). However, this Na enrichment can occur both in the graphite and diamond stability fields (Grütter and Quadling, 1999), which makes this method imperfect to distinguish between fertile and barren kimberlites.

All the results confirm that the models that could be applicable to one craton, are not necessarily useful to explain the distribution of the fertile and barren kimberlites in other cratons (Mitchell, 1991).

9.3.2. Discussion

In contrast to the complex evolution of the ilmenite xenocrysts described above, garnets are represented by a unique textural population, with no identifiable secondary generations of garnet. BSE images show that they can be partially altered along grain boundaries and fractures and some chromite and biotite may have formed in these fractures as a result of garnet breakup. The fractures are now totally replaced by serpentine and other secondary phases, such as carbonate. Additionally some garnet xenocrysts may have inclusions of apatite, quartz, iron oxides and calcite (fig. 9.8). The study of these rare inclusions was not within the scope of this thesis and thus they were not further characterised, but more work will be done on them in the future.

As shown in fig. 9.9, most of the garnet xenocrysts plot in the G9 (lherzolitic) field of Grütter et al. (2004). Their intermediate Ca and Cr contents are consistent with the main compositions of garnet grains found in the mantle xenoliths sampled by Cat115 pipe (see chapter 6). These compositions are also similar to those of garnet xenocrysts of the Catoca kimberlite (Robles-Cruz et al., 2012). As mentioned above, this kimberlite is one of the largest diamond mines in the world and thus a high abundance of G10 garnet might be expected. A larger dataset of garnet xenocrysts from several kimberlites of the same cluster was published by Aschepkov et al. (2012b). In contrast with our findings, their data includes significant amounts of G10 garnets, mainly among the garnets derived from the Catoca kimberlite. However, no trace element analyses were carried out on these mineral concentrates, making it impossible to determine their pressure and temperature of equilibration using Ni-in-garnet thermometer. However, this can be critical to correctly assess the diamond grade of any prospected kimberlite in this area.

Indeed, as seen from the characterisation of the lithospheric mantle presented in this thesis, the only xenolith containing G10 garnet was found in the shallow lithosphere, very close to the diamond-graphite boundary (880^{o}C, 40 kbar). Moreover, the chemical tomography (chapter 8) shows that the four Ca-harzburgitic garnet xenocrysts collected from the Cat115 kimberlite also yield low temperatures of equilibration (920-1020^{o}C). In contrast, the large majority of garnets within the diamond stability field were classified as lherzolitic, even if the petrographic studies revealed that the rocks that contain them are modally classified as harzburgite. As previously explained, this apparent contradiction is likely a consequence of the complex, multi-stage metasomatic episodes that took place in the SCLM beneath the Lunda

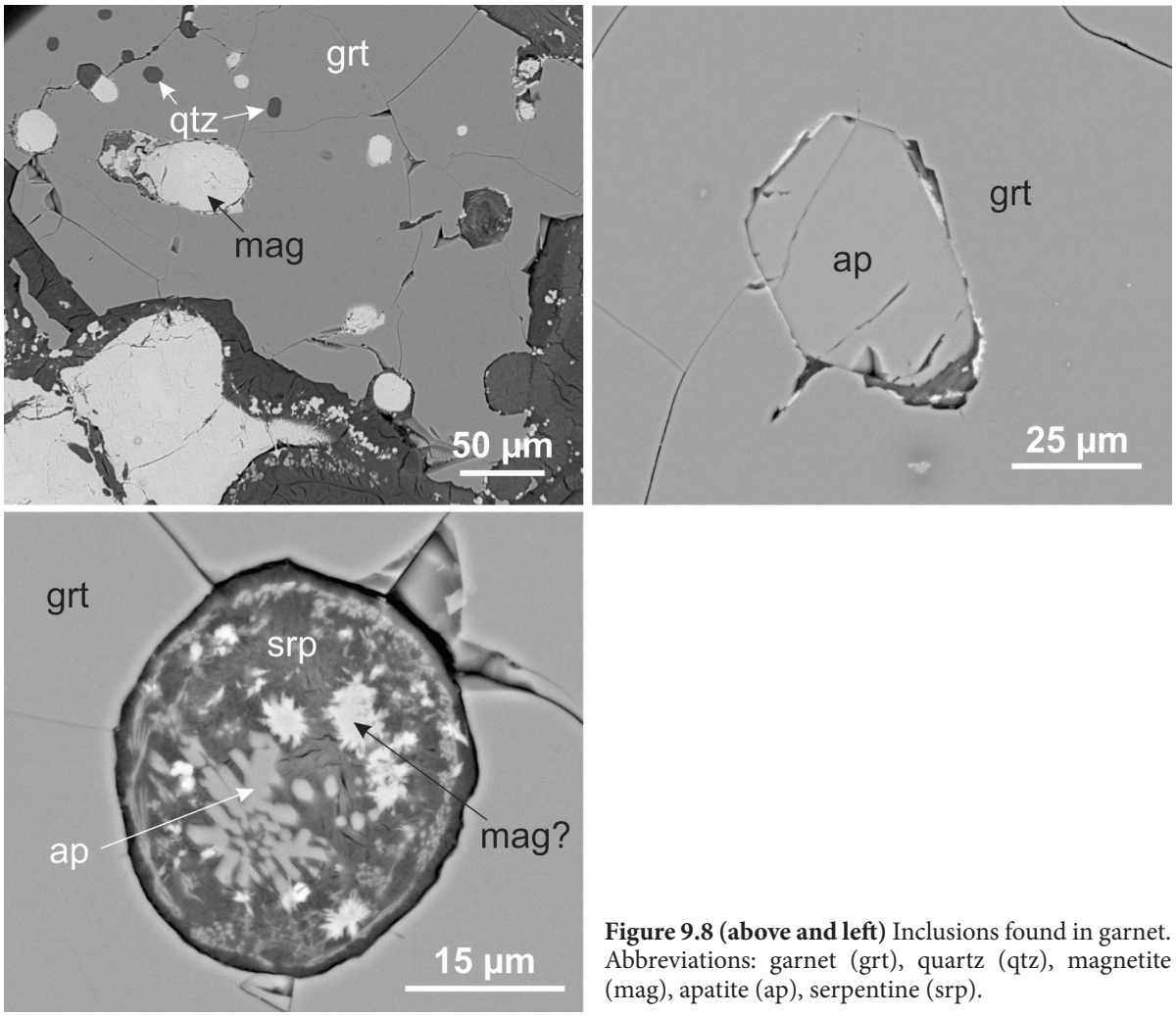

Figure 9.8 (above and left) Inclusions found in garnet. Abbreviations: garnet (grt), quartz (qtz), magnetite (mag), apatite (ap), serpentine (srp).

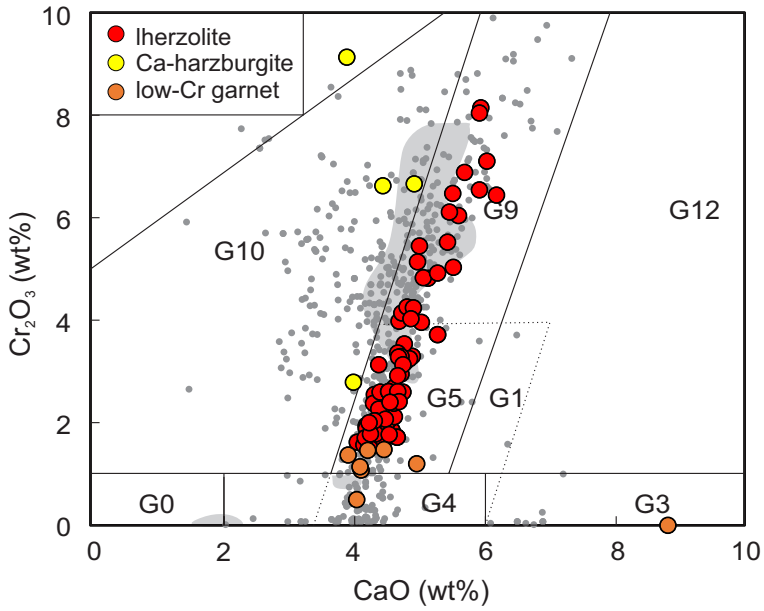

Figure 9.9 Classification of garnet xenocrysts sampled by the Cat115 and Catoca kimberlites, based on their Cr_2O_3-CaO content as proposed by Grütter et al. (2004). Additional data of garnet xenocrysts of the Catoca kimberlite are included for comparison: grey field (Robles-Cruz et al., 2012) and small grey circles (Ashchepkov et al., 2012).

Norte province. A drift from originally harzburgitic garnets towards lherzolitic compositions is a well-known result of Ca enrichment during metasomatism (e.g., Burgess and Harte, 2004; Howarth et al., 2014). Therefore, despite the currently limited amount of data, the lack of G10 garnet xenocrysts in the Lunda Norte province should not be taken as an indicator of barren kimberlites. Instead, it is possible that harzburgitic compositions are indicative of sampling of the shallow lithosphere and, as a consequence, out of the diamond stability field, as observed in the Slave craton (e.g., Griffin and O'Reilly, 2005) and the Skerring (Australia) and Zero (South Africa) kimberlites (Jacques et al., 1986; Shee et al., 1989). In any case, more data are required to either confirm or rule out this hypothesis.

A broad relationship between the grain size of the garnet xenocrysts, their composition and their crystallisation conditions was observed during this study. In general, garnet xenocrysts with grain size smaller than 1 mm were equilibrated at high PT conditions (>1200ºC), whereas larger grains are more common in the shallow lithosphere (fig. 9.10).

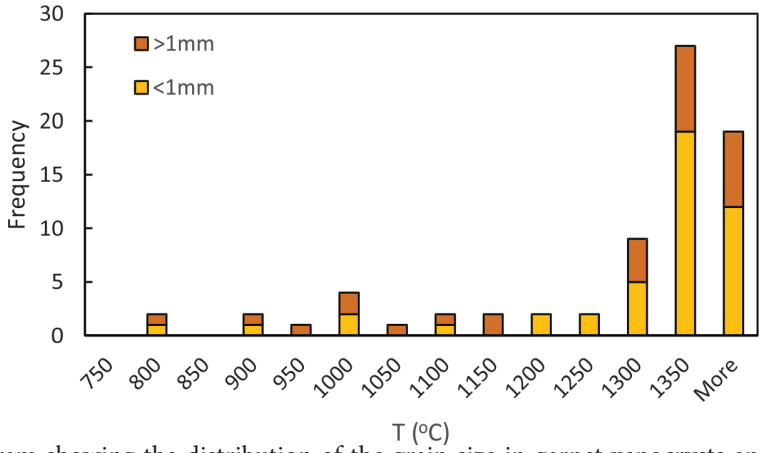

Figure 9.10 Histogram showing the distribution of the grain size in garnet xenocrysts and their equilibration temperatures, calculated by using the thermometer of Ni-in-gt of Ryan et al., (1996) (see chapter 7).

At this stage, more data are required to make a solid statement about the correlation between these three parameters (composition, PT conditions and grain size), although the current results may suggest that small garnet xenocrysts are more likely to be derived from deeper levels than those larger than 1mm. These results are consistent with the petrographic characterisation of both shallow and deep SCLM presented in chapters 6 and 7. Therefore, the small (<1mm) garnet fraction should not be neglected during the prospecting stage, since it may provide significant information on the deepest source sampled by the kimberlitic magma, within the diamond stability field.

9.4. The potential source of the diamond

Unfortunately, up to the author's knowledge no research on diamond inclusions of the Lundas kimberlite province has been carried out so far. Due to the limited information available, the identification of the potential source of diamonds in this area is thus complicated. However, the abundance of eclogitic garnet xenocrysts in the mineral concentrates of the Catoca kimberlite has been previously related to the presence of deep diamond-bearing eclogites (Ashchepkov et al., 2012). Similarly, the high-T, high-Mg eclogites described by Nikitina and coworkers (2014), were seen as a as a potential source for diamonds in the same kimberlite. The anomalously high Nb contents in rutile in these high-Mg eclogites were considered an indicator of the high productivity of the kimberlite (Nikitina et al., 2014). Such observations are consistent with the results presented in this thesis (see chapters 6 and 7). Moreover, it has been shown that the SCLM was affected by complex, multi-stage and multi-component metasomatism, which significantly modified its original depleted composition. It is also likely that these refertilisation processes could be accompanied by the crystallisation of diamond if the environmental conditions were favourable and there was a source of carbon.

9.5. Preliminary conclusions

1. The diamond mining companies commonly rely on the composition of the diamond indicator minerals (DIMs) to assess the diamond grade of a kimberlite during the exploration stage. However, it has been proven that this approach can be misleading if the textural characterisation of these minerals is disregarded. Similarly, misinterpretation of the diamond potential of a prospected kimberlite can happen if there is not enough knowledge about the structure, composition and metasomatic evolution of the SCLM sampled by the kimberlites.

2. The results presented in this chapter confirm that the current composition of ilmenite in kimberlites can only be understood through a study encompassing both textural characterisation and major- and trace-element analysis.

3. A multi-stage model is proposed to explain the evolution of ilmenite in the Angolan kimberlites, including: a) crystallisation of ilmenite in crustal domains or in metasomatized mantle sites under different conditions; b) disaggregation of xenoliths to form the corresponding populations of ilmenite xenocrysts differing in composition; c) widespread replacement of the original xenocrysts by Mg-rich ilmenite caused by interaction with the kimberlitic magma; d)

secondary replacement with a manganoan ilmenite by infiltration of a Mn-rich hydrothermal fluid and e) subsolidus alteration of the previously crystallised phases in an oxidising environment.

4. This complex sequence could thus lead to misinterpretation of the diamond potential of a kimberlitic pipe if textural and trace-element information is disregarded. The results presented in this chapter show that secondary Mg enrichment of the ilmenite xenocrysts is unrelated to reducing conditions that could favour diamond formation/preservation in the mantle. Similarly, Mn-rich ilmenite should be disregarded as a diamond indicator mineral, unless textural studies can prove its primary origin.

5. Garnet xenocyrsts sampled by the Cat115 are mostly lherzolitic and were derived from the base of the SCLM. The characterisation of the SCLM presented in previous chapters may suggest that these lherzolitic signatures are consequence of pervasive silicate melt metasomatism of harzburgites within the diamond stability field. In contrast, the few harzburgitic garnet xenocrysts collected from this kimberlite were equilibrated at low temperatures, near the graphite-diamond boundary. As a result, the lack of G10 garnet xenocrysts should not be used to downgrade the diamond potential of a kimberlite in this area. Instead, if present, it is encouraged to carry out trace-element analyses on these harzburgitic garnets, since the current results suggest that they might be derived from the shallow SLCM.

Chapter 10
CONCLUSIONS

Petrogenesis of the Angolan kimberlites: evidence of magma mingling in Cretaceous kimberlites

The petrographic characterisation of the several "kimberlitic" intrusions has shown that they have a diverse groundmass mineralogy, which may suggest that both kimberlite and other kimberlite-related rocks (meimechites) are present in the Lunda Norte province.

The study of groundmass perovskite ($CaTiO_3$) in 6 of these intrusions has constrained the timing of the eruptions, as well as the sources of the magmas. Four types of perovskite were identified, differing in texture, major- and trace-element composition, zoning patterns, type of alteration and the presence or absence of inclusions. The occurrence of these four types within the Mulepe kimberlites is interpreted as evidence of a complex, multi-stage process that involved mingling of compositionally different melts.

U-Pb dating of these perovskites yielded Lower Cretaceous ages for four of the studied kimberlites: Mulepe1 (116.2 ± 6.5 Ma), Mulepe2 (123.0 ± 3.6 Ma), Calonda (119.5±4.3 Ma) and Cat115 (133± 10 Ma). Kimberlite magmatism in NE Angola occurred due to reactivation of deep-seated translithospheric faults (>300km) during the break-up of Gondwana. Sr-Nd isotope analyses of constituent perovskite corroborated that they are Group I kimberlites.

The SCLM beneath the Lunda Norte kimberlitic province: a layered structure modified by complex metasomatic processes

The compositional structure and metasomatic evolution of the SCLM beneath the Lunda Norte kimberlitic province were defined from the characterisation of xenoliths and xenocrysts. A combined study of the composition of these xenoliths and their PT conditions revealed that the SCLM beneath these kimberlites is layered as follows:

- Spinel-harzburgite: (630ºC; 27kbar; 75 km)]
- Low-T coarse garnet-peridotites (850-1080 ºC; 38-53 kbar; 105-145 km)
- Low-Mg eclogites (1040-1140ºC, 43-49 kbar; 138-155 km)
- High-T, porphyroclastic garnet-peridotites (1280-1330 ºC; 63-70 kbar; 180-190 km)
- High-Mg eclogites (>200 km)

Compositional differences between the two Grt-peridotite suites indicates an enrichment in Ti, Cr and Zr in garnets with depth, coupled with a decrease in the Mg# of olivine and orthopyroxene. Such compositional variations, as well as the Zr/Ga-Zr/Y ratios in garnet, are similar to those defined for the Archean SCLM in most cratons worldwide. However, the mineral modes of the studied xenoliths are different from those described in the Kaapvaal and Siberian cratons, but could be comparable to those reported in the Slave craton or in oceanic peridotites.

Two different models may be proposed to explain the current structure of the SCLM and the presence of a zone rich in low-Mg eclogites between the two Grt-peridotite suites.

In a subduction-stacking model, the low-Mg eclogites would represent shallowly-subducted oceanic crust, which accumulated at the base of the SCLM during craton assembly. In this scenario, the high-T garnet peridotite suite would be a refertilised Archean oceanic lithospheric mantle. Progressive underthrusting of oceanic lithosphere would also explain the occurrence of high-Mg eclogites at the base of the lithospheric mantle.

Alternatively, an asthenospheric plume similar to that proposed by Griffin et al. (2003) in the Slave craton could be responsible for the formation of eclogite cumulates at the base of the refractory Archean SCLM. The crystallisation of the head of this plume would result in the

formation of the high-T Grt-peridotites. However, the eclogitic level in NE Angola is located at greater depths, and the shallow SCLM in the Lunda Norte province is not as ultradepleted as that of the Slave craton, which argues against this model unless significant refertilisation of this layer by metasomatism took place.

Complex metasomatic processes in the mantle were identified from the mineralogical, textural and compositional study of the mantle xenoliths and garnet xenocrysts. Modal metasomatism was identified by the addition of phlogopite, amphibole, ilmenite and rutile in some of highly metasomatised xenoliths. Additionally, trace-element analyses of garnet and clinopyroxene indicate a multi-episode metasomatic origin for these phases. Moreover, as described below, the shallow and the deep lithospheric mantle were modified by different magmas at different times.

The shallow SCLM was firstly affected by silicate melt metasomatism, which resulted in the introduction of garnet (± clinopyroxene) in the originally depleted Archean lithosphere. Subsequent to the addition of the deeper layer (either by stacking subduction or by plume upwelling), a high-T metasomatism affected the base of the lithosphere. The melts involved in this process were of a mixed nature (carbonatite-silicate melts) and were responsible for the refertilisation of this layer by introduction of both clinopyroxene and garnet. Percolative fractional crystallisation of these melts would explain: i) the late formation of clinopyroxene -or compositional modification of a previous Cpx by interaction with a carbonatitic fluid-; and ii) the crystallisation of phlogopite, in the shallower layer of the SCLM, shortly prior to kimberlite eruption. The last metasomatic episode is linked to kimberlite eruption and it is defined by the crystallisation of fine grained pyroxene along fractures and grain boundaries, as well as a second generation of phlogopite.

Use and misuse of indicator minerals in diamond exploration: ilmenite and garnet

A multi-stage model has been proposed to explain the evolution of ilmenite in the Angolan kimberlites, including: a) crystallisation of ilmenite in crustal domains or in metasomatized mantle sites under different conditions; b) disaggregation of xenoliths to form the corresponding populations of ilmenite xenocrysts differing in composition; c) widespread replacement of the original xenocrysts by Mg-rich ilmenite during interaction with the

kimberlitic magma; d) secondary replacement with a manganoan ilmenite by infiltration of a Mn-rich hydrothermal fluid and e) subsolidus alteration of the previously crystallised phases in an oxidising environment.

This complex sequence could thus lead to misinterpretation of the diamond potential of a kimberlitic pipe if textural and trace-element information is disregarded. Additionally, it has been shown that secondary Mg enrichment of the ilmenite xenocrysts in the Cat115 kimberlite is unrelated to reducing conditions that could favour diamond formation/preservation in the mantle. Similarly, Mn-rich ilmenite should be disregarded as a diamond indicator mineral, unless textural studies can prove its primary origin.

Garnet xenocyrsts sampled by the Cat115 are mostly lherzolitic and were derived from the base of the SCLM. The data obtained from the characterisation of the SCLM suggest that these lherzolitic signatures are consequence of pervasive silicate melt metasomatism of harzburgites within the diamond stability field. In contrast, the few harzburgitic garnet xenocrysts collected from this kimberlite were equilibrated at low temperatures, near the graphite-diamond boundary. As a result, the lack of G10 garnet xenocrysts should not be used to downgrade the diamond potential of a kimberlite in this area. Instead, trace-element analyses should be carried out on such harzburgitic garnets, since the current results suggest that they might be derived from the shallow SLCM.

Chapter 11
REFERENCES

Adam, J., Green, T., 2001. Experimentally determined partition coefficients for minor and trace elements in peridotite minerals and carbonatitic melt, and their relevance to natural carbonatites. Eur. J. Mineral. 815–827. doi:10.1127/0935-1221/

Ai, Y., 1994. A revision of the garnet-clinopyroxene Fe^{2+} -Mg exchange geothermometer. Contrib. Mineral. Petr. 115, 467–473.

Araújo A.G., Guimarães F. [Coords.] (1992). Notícia explicativa da Carta Geológica de Angola à escala 1:1.000.000. Serviço Geológico de Angola, Luanda, 135 pp.

Araújo, D.P., Griffin, W.L., O'Reilly, S.Y., 2009. Mantle melts, metasomatism and diamond formation: Insights from melt inclusions in xenoliths from Diavik, Slave Craton. Lithos 112, 675–682. doi:10.1016/j.lithos.2009.06.005

Arndt, N.T., Lehnert, K., Vasil'ev, Y., 1995. Meimechites: highly magnesian lithosphere-contaminated alkaline magmas from deep subcontinental mantle. Lithos 34, 41–59.

Arndt, N.T., Guitreau, M., Boullier, a.-M., Le Roex, a., Tommasi, a., Cordier, P., Sobolev, a., 2010. Olivine, and the Origin of Kimberlite. J. Petrol. 51, 573–602. doi:10.1093/petrology/egp080

Artemieva, I.M., 2006. Global 1X1 thermal model TC1 for the continental lithosphere: Implications for lithosphere secular evolution. Tectonophysics 416, 245–277. doi:10.1016/j.tecto.2005.11.022

Ashchepkov, I. V., Pokhilenko, N.P., Vladykin, N. V., Logvinova, A.M., Afanasiev, V.P., Pokhilenko, L.N., Kuligin, S.S., Malygina, E. V., Alymova, N. a., Kostrovitsky, S.I., Rotman, A.Y., Mityukhin, S.I., Karpenko, M. a., Stegnitsky, Y.B., Khemelnikova, O.S., 2010. Structure and evolution of the lithospheric mantle beneath Siberian craton, thermobarometric study. Tectonophysics 485, 17–41. doi:10.1016/j.tecto.2009.11.013

Ashchepkov, I.V., Rotman, a. Y., Somov, S.V., Afanasiev, V.P., Downes, H., Logvinova, a. M., Nossyko, S., Shimupi, J., Palessky, S.V., Khmelnikova, O.S., Vladykin, N.V., 2012. Composition and thermal structure of the lithospheric mantle beneath kimberlite pipes from the Catoca cluster, Angola. Tectonophysics 530-531, 128–151. doi:10.1016/j.tecto.2011.12.007

Ashchepkov, I.V., Vladykin, N.N., Ntaflos, T., Kostrovitsky, S.I., Prokopiev, S. a., Downes, H., Smelov, a. P., Agashev, a. M., Logvinova, a. M., Kuligin, S.S., Tychkov, N.S., Salikhov, R.F., Stegnitsky, Y.B.,

Alymova, N.V., Vavilov, M. a., Minin, V. a., Babushkina, S. a., Ovchinnikov, Y.I., Karpenko, M. a., Tolstov, a. V., Shmarov, G.P., 2014. Layering of the lithospheric mantle beneath the Siberian Craton: Modeling using thermobarometry of mantle xenolith and xenocrysts. Tectonophysics 634, 55–75. doi:10.1016/j.tecto.2014.07.017

Aulbach, S., Griffin, W.L., O'Reilly, S.Y., McCandless, T.E., 2004a. Genesis and evolution of the lithospheric mantle beneath the Buffalo Head Terrane, Alberta (Canada). Lithos 77, 413–451. doi:10.1016/j.lithos.2004.04.020

Aulbach, S., Griffin, W.L., Pearson, N.J., O'Reilly, S.Y., Kivi, K., Doyle, B.J., 2004b. Mantle formation and evolution, Slave Craton: Constraints from HSE abundances and Re-Os isotope systematics of sulfide inclusions in mantle xenocrysts. Chem. Geol. 208, 61–88. doi:10.1016/j.chemgeo.2004.04.006

Bambi, A.C.J.M. (2015): Metalogenia de las carbonatitas en dominios plutónicos, subvolcánicos y volcánicos: Tchivira, Bonga y Catanda, Angola. Unpubl. Ph.D. Thesis, Univ. Barcelona, 705 pp.

Baptiste, V., Tommasi, A., Demouchy, S., 2012. Deformation and hydration of the lithospheric mantle beneath the Kaapvaal craton, South Africa. Lithos 149, 31–50. doi:10.1016/j.lithos.2012.05.001

Barth, M.G., Rudnick, R.L., Horn, I., McDonough, W.F., Spicuzza, M.J., Valley, J.W., Haggerty, S.E., 2001. Geochemistry of xenolithic eclogites from West Africa, Part I: A link between low MgO eclogites and Archean crust formation. Geochim. Cosmochim. Acta 65, 1499–1527.

Batumike, J.M., Griffin, W.L., Belousova, E. a., Pearson, N.J., O'Reilly, S.Y., Shee, S.R., 2008. LAM-ICPMS U-Pb dating of kimberlitic perovskite: Eocene-Oligocene kimberlites from the Kundelungu Plateau, D.R. Congo. Earth Planet. Sci. Lett. 267, 609–619. doi:10.1016/j.epsl.2007.12.013

Batumike, J.M., Griffin, W.L., O'Reilly, S.Y., 2009. Lithospheric mantle structure and the diamond potential of kimberlites in southern D.R. Congo. Lithos 112, 166–176. doi:10.1016/j.lithos.2009.04.020

Becker, M., Le Roex, A.P., 2006. Geochemistry of South African on- and off-craton, group I and group II kimberlites: Petrogenesis and source region evolution. J. Petrol. 47, 673–703. doi:10.1093/petrology/egi089

Begg, G.C., Griffin, W.L., Natapov, L.M., O'Reilly, S.Y., Grand, S.P., O'Neill, C.J., Hronsky, J.M. a., Djomani, Y.P., Swain, C.J., Deen, T., Bowden, P., 2009. The lithospheric architecture of Africa: Seismic tomography, mantle petrology, and tectonic evolution. Geosphere 5, 23–50. doi:10.1130/GES00179.1

Bell, D.R., Schmitz, M.D., Janney, P.E., 2003. Mesozoic thermal evolution of the southern African mantle lithosphere. Lithos 71, 273–287. doi:10.1016/S0024-4937(03)00117-8

Bell, D.R., Moore, R.O., 2004. Deep chemical structure of the southern African mantle from kimberlite megacrysts. South African J. Geol. 107, 59–80.

Bellis, A., Canil, D., 2007. Ferric Iron in $CaTiO_3$ perovskite as an oxygen barometer for kimberlitic magmas I: Experimental calibration. J. Petrol. 48, 219–230. doi:10.1093/petrology/egl054

Beyer, C., Berndt, J., Tappe, S., Klemme, S., 2013. Trace element partitioning between perovskite and kimberlite to carbonatite melt: New experimental constraints. Chem. Geol. 353, 132–139. doi:10.1016/j.chemgeo.2012.03.025

Black, L.P., Gulson, B.L., 1978. The age of the Mud Tank carbonatite, Strangways Range, Northern Territory. J. Aust. Geol. Geophys. 3, 227–232.

Boyd, F.R., Nixon, P.H., 1975. Origins of the ultramafic nodules from some kimberlites of northern Lesotho and the Monastery Mine, South Africa. Phys. Chem. Earth 9, 431–454.

Boctor, N.Z., Boyd, F.R., 1981. Oxide minerals in a layered kimberlite–carbonatite sill from Benfontein, South Africa. Contrib. Mineral. Petr. 76, 253–259.

Boyd, F.R., Mertzman, S. a., 1987. Composition of structure of the Kaapvaal lithosphere, southern Africa. Magmat. Process. Princ. 13–24.

Boyd, F.R., 1989. Compositional distinction between oceanic and cratonic lithosphere. Earth Planet. Sci. Lett. 96, 15–26.

Boyd, F.R., Pokhilenko, N.P., Pearson, D.G., Mertzman, S. A., Sobolev, N. V., Finger, L.W., 1997. Composition of the Siberian cratonic mantle: evidence from Udachnaya peridotite xenoliths. Contrib. Mineral. Petr. 128, 228–246. doi:10.1007/s004100050305

Brey, G.P., Köhler, T., 1990. Geothermobarometry in Four-phase Lherzolites II. New Thermobarometers, and Practical Assessment of Existing Thermobarometers. J. Petrol. 38, 1353–1378. doi:10.1093/petrology/31.6.1353

Burgess, S.R., Harte, B., 2004. Tracing lithosphere evolution through the analysis of heterogeneous G9-G10 garnets in peridotite xenoliths, II: REE chemistry. J. Petrol. 45, 609–633. doi:10.1093/petrology/egg095

Cahen, L., Snelling, N.J., Delhail, J., Vail, J.R., 1984. The geochronology and evolution of Africa. Clarendon Press, London.

Canil, D., Bellis, A.J., 2007. Ferric Iron in CaTiO3 Perovskite as an Oxygen Barometer for Kimberlite Magmas II: Applications. J. Petrol. 48, 231–252. doi:10.1093/petrology/egl067

Carlson, J.A., Marsh, S.W., 1989. Discovery of the George Creek, Colorado kimberlite dikes, in: Ross, J., Jacques, A.L., Ferguson, J., D.H., G., O'Reiliy, S.Y., Danchin, R.V., Janse, A.J. (Eds.), Kimberlites Arid Related Rocks: Proceedings of the Fourth Lnternational Kimberiite Conference (2 Volumes). Geological Society of Australia, Special Publication No. 14, v. 2, pp. 1169–1178.

Carlson, R.W., Czamanske, G., Fedorenko, V., Ilupin, I., 2006. A comparison of Siberian meimechites and kimberlites: Implications for the source of high-Mg alkalic magmas and flood basalts. Geochemistry Geophys. Geosystems 7, 1–21. doi:10.1029/2006GC001342

Carmichael Ise, Nicholls J, Smith Al, 1970. Silica Activity in Igneous Rocks. Am. Mineral. 55, 246–263.

Carmody, L., Taylor, L. a., Thaisen, K.G., Tychkov, N.S., Bodnar, R.J., Sobolev, N. V., Pokhilenko, L.N.,

Pokhilenko, N.P., 2014. Ilmenite as diamond indicator mineral in the Siberian Craton: a tool to predict diamond potential. Econ. Geol. 109, 775–783.

Carswell, D.A., Dawson, J.B., Gibb, F.G.F., 1981. Equilibration conditions of upper-mantle eclogites: implications for kyanite-bearing and diamondiferous varieties. Mineral. Mag. 44, 79–89.

Carswell, D.A., Griffin, W.L., 1980. The equilibration conditions and petrogenesis of European crustal granulites. 1Lithos 13, 19–29.

Carswell, D.A., Griffin, W.L., 1981. Calculation of equilibrations conditions for garnet granulite and garnet websterite nodules in African kimberlite pipes. Tschermaks Miner. Petrogr. Mitt. 28, 229–244.

Cas, R., Porritt, L., Pittari, A., Hayman, P., 2008. A new approach to kimberlite facies terminology using a revised general approach to the nomenclature of all volcanic rocks and deposits: Descriptive to genetic. J. Volcanol. Geotherm. Res. 174, 226–240. doi:10.1016/j.jvolgeores.2007.12.018

Castillo-Oliver, M., Galí, S., Melgarejo, J.C., Griffin, W.L., Belousova, E., Pearson, N.J., Watangua, M., O'Reilly, S.Y., 2016. Trace-element geochemistry and U-Pb dating of perovskite in kimberlites of the Lunda Norte province (NE Angola): petrogenetic and tectonic implications. Chem. Geol. doi:10.1016/j.chemgeo.2015.12.014

Chakhmouradian, A.R., Mitchell, R.H., 1998. Compositional variation of perovskite-group minerals from the Khibina complex, Kola Peninsula, Russia. Can. Mineral. 36, 953–969.

Chakhmouradian, A.R., Mitchell, R.H., 1999. Niobian ilmenite, hydroxylapatite and sulfatian monazite: alternative hosts for incompatible elements in calcite kimberlite from Internatsional'naya, Yakutia. Can. Mineral. 37, 1177–1189.

Chakhmouradian, a. R., Mitchell, R.H., 2000. Occurrence, Alteration Patterns and Compositional Variation of Perovskite in Kimberlites. Can. Mineral. 38, 975–994. doi:10.2113/gscanmin.38.4.975

Chakhmouradian, A.R., Mitchell, R.H., 2001. Three compositional varieties of perovskite from kimberlites of the Lac de Gras field (Northwest Territories, Canada). Mineral. Mag. 65, 133–148.

Chakhmouradian, A.R., Reguir, E.P., Kamenetsky, V.S., Sharygin, V. V., Golovin, A. V., 2013. Trace-element partitioning in perovskite: Implications for the geochemistry of kimberlites and other mantle-derived undersaturated rocks. Chem. Geol. 353, 112–131. doi:10.1016/j.chemgeo.2013.01.007

Chalapathi Rao, N.V., Wu, F.-Y., Mitchell, R.H., Li, Q.-L., Lehmann, B., 2013. Mesoproterozoic U–Pb ages, trace element and Sr–Nd isotopic composition of perovskite from kimberlites of the Eastern Dharwar craton, southern India: Distinct mantle sources and a widespread 1.1Ga tectonomagmatic event. Chem. Geol. 353, 48–64. doi:10.1016/j.chemgeo.2012.04.023

Clement, C.., Skinner, E.M.W., 1985. A textural-genetic classification of kimberlites. Trans. Geol. Soc. South Africa 88, 403–409.

Coltorti, M., Bonadiman, C., Hinton, R.W., Siena, F., Upton, B.G.J., 1999. Carbonatite Metasomatism of

the Oceanic Upper Mantle : Evidence from Clinopyroxenes and Glasses in Ultramafic Xenoliths of Grande Comore , Indian Ocean. J. Petrol. 40, 133–165. doi:10.1093/petroj/40.1.133

Coltorti, M., Gregoire, M., 2008. Metasomatism in oceanic and continental lithospheric mantle: introduction. Geol. Soc. London, Spec. Publ. 293, 1–9. doi:10.1144/SP293.1

Corfu, F., Dahlgren, S., 2008. Perovskite U-Pb ages and the Pb isotopic composition of alkaline volcanism initiating the Permo-Carboniferous Oslo Rift. Earth Planet. Sci. Lett. 265, 256–269. doi:10.1016/j.epsl.2007.10.019

Cox, R. a., Wilton, D.H.C., 2006. U-Pb dating of perovskite by LA-ICP-MS: An example from the Oka carbonatite, Quebec, Canada. Chem. Geol. 235, 21–32. doi:10.1016/j.chemgeo.2006.06.002

Creaser, R. a., Gütter, H., Carlson, J., Crawford, B., 2004. Macrocrystal phlogopite Rb-Sr dates for the Ekati property kimberlites, Slave Province, Canada: Evidence for multiple intrusive episodes in the Paleocene and Eocene. Lithos 76, 399–414. doi:10.1016/j.lithos.2004.03.039

Dalou, C., Koga, K.T., Hammouda, T., Poitrasson, F., 2009. Trace element partitioning between carbonatitic melts and mantle transition zone minerals: Implications for the source of carbonatites. Geochim. Cosmochim. Acta 73, 239–255. doi:10.1016/j.gca.2008.09.020

Dare, S. a S., Barnes, S.J., Beaudoin, G., 2012. Variation in trace element content of magnetite crystallized from a fractionating sulfide liquid, Sudbury, Canada: Implications for provenance discrimination. Geochim. Cosmochim. Acta 88, 27–50. doi:10.1016/j.gca.2012.04.032

Davies, G.R., Spriggs, A.J., Nixon, P.H., 2001. A Non-cognate Origin for the Gibeon Kimberlite Megacryst Suite , Namibia : Implications for the Origin of Namibian Kimberlites 42, 159–172.

Davis, G.L., 1977. The ages and uranium contents of zircon from kimberlites and associated rocks, in: Extended Abstr., 2nd Int. Kimberlite Conf., Santa Fe, New Mexico.

Davis, W.J., Jones, A.G., Bleeker, W., Grütter, H., 2003. Lithosphere development in the Slave craton: a linked crustal and mantle perspective. Lithos 71, 575–589. doi:10.1016/S0024-4937(03)00131-2

Dawson, J.B., 1970. The structural setting of African kimberlite magmatism, in: Clifford, T.N., Gass, I.G. (Eds.), African Magmatism and Tectonics. Edinburgh, pp. 321–335.

Dawson, J.B., Smith, J. V., 1977. The MARID (mica-amphibole-rutile-ilmenite-diopside) suite of xenoliths in kimberlite. Geochim. Cosmochim. Acta 41, 309–323. doi:10.1016/0016-7037(77)90239-3

Dawson, J.B., 1984. Contrasting types of upper-mantle metasomatism, in: Kimberlites II. Elsevier, Amsterdam, pp. 289–294.

Dawson, J.B., 2002. Metasomatism and Partial Melting in Upper-Mantle Peridotite Xenoliths from the Lashaine Volcano, Northern Tanzania. J. Pet. 43, 1749–1777. doi:10.1093/petrology/43.9.1749

De Boorder, H., 1982. Deep-reaching fracture zones in the crystalline base- ment surrounding the west congo system and their control of mineralization in angola and gabon. Geoexploration 20,

259–273.

De Bruin, D., 2005. Multiple compositional megacryst groups from the Uintjiesberg and Witberg kimberlites, South Africa. South African J. Geol. 108, 233–246.

De Carvalho, H., Tassinari, C., Alves, P.M., Guimarães, F., Simões, M.C., 2000. Geochronological review of the Precambrian in western Angola: Links with Brazil. J. African Earth Sci. 31, 383–402. doi:10.1016/S0899-5362(00)00095-6

De Waele, B., Johnson, S.P., Pisarevsky, S. a., 2008. Palaeoproterozoic to Neoproterozoic growth and evolution of the eastern Congo Craton: Its role in the Rodinia puzzle. Precambrian Res. 160, 127–141. doi:10.1016/j.precamres.2007.04.020

Dobson, D., Jones, A., Rabe, R., Sekine, T., Kurita, K., Taniguchi, T., Kondo, T., Kato, T., Shimomura, O., Urakawa, S., 1996. In-situ measurement of viscosity and density of carbonate melts at high pressure 143. doi:10.1016/0012-821X(96)00139-2

Donnelly, C.L., Griffin, W.L., Yang, J.-H., O'Reilly, S.Y., Li, Q.-L., Pearson, N.J., Li, X.-H., 2012. In situ U-Pb Dating and Sr-Nd Isotopic Analysis of Perovskite: Constraints on the Age and Petrogenesis of the Kuruman Kimberlite Province, Kaapvaal Craton, South Africa. J. Petrol. 53, 2497–2522. doi:10.1093/petrology/egs057

Donnelly, C.L., Griffin, W.L., Yang, J., Reilly, S.Y., Li, Q., Pearson, N.J., Li, X., 2012. In situ U-Pb Dating and Sr- Nd Isotopic Analysis of Perovskite : Constraints on the Age and Petrogenesis of the Kuruman Kimberlite. J. Petrol. 0, 1–26. doi:10.1093/petrology/egs057

Donohue, P.H., Simonetti, A., Neal, C.R., 2012. Chemical Characterisation of Natural Ilmenite: A Possible New Reference Material. Geostand. Geoanalytical Res. 36, 61–73. doi:10.1111/j.1751-908X.2011.00124.x

Doucet, L.S., Ionov, D. a., Golovin, A. V., 2013. The origin of coarse garnet peridotites in cratonic lithosphere: New data on xenoliths from the Udachnaya kimberlite, central Siberia. Contrib. Mineral. Petr. 165, 1225–1242. doi:10.1007/s00410-013-0855-8

Eccles, D.R., Heaman, L.M., Luth, R.W., Creaser, R. a., 2004. Petrogenesis of the Late Cretaceous northern Alberta kimberlite province. Lithos 76, 435–459. doi:10.1016/j.lithos.2004.03.046

Egorov, K.N., Roman, E.F., Podvysotsky, V.T., Sablukov, S.M., Garanin, V.K., D'yakonov, D.B., 2007. New data on kimberlite magmatism in southwestern Angola. Russ. Geol. Geophys. 48, 323–336. doi:10.1016/j.rgg.200

Eley, R., Grütter, H., Louw, A., Tunguno, C., Twidale, J., 2008. Exploration Geology of the Luxinga Kimberlite Cluster (Angola) with Evidence Supporting the Presence of Kimberlite Lava. 9th Int. Kimberl. Conf. Ext. Abstr. 1–3.

Ellis, D.J., Green, D.H., 1979. An experimental study of the effect of Ca upon garnet-clinopyroxene Fe/Mg exchange equilibria. Contrib. Mineral. Petr. 71, 13–22.

Erlank, A.J., Waters, F.G., Hawkesworth, C.J., Haggerty, S.E., Allsopp, H.L., Rickard, R.S., Menzies, M.,

1987. Evidence for mantle metasomatism in peridotite nodules from the Kimberley pipes, South Africa, in: Menzies, M., Hawkesworth, C.J. (Eds.), Mantle Metasomatism. Academic Press, New York, pp. 221–311.

Faure, S., 2010. World Kimberlites CONSOREM Database (Version 3), Consortium de Recherche en Exploration Minérale CONSOREM, Université du Québec à Montréal [WWW Document]. www.consorem.ca.

Fedortchouk, Y., Canil, D., 2004. Intensive variables in kimberlite magmas, Lac de Gras, Canada and implications for diamond survival. J. Petrol. 45, 1725–1745. doi:10.1093/petrology/egh031

Field, M., Scott Smith, B.H., 1998. Textural and genetic classification schemes of kimberlite: a new perspective, in: Proceedings of the 7th International Kimberlite Conference. Red Roof Design, Cape Town, pp. 214–216.

Finnerty, A., Boyd, F.R., 1987. Thermobarometry for garnet peridotite xenoliths: basis for the determination of thermal and compositional structure of the upper mantle, in: PH, N. (Ed.), Mantle Xenoliths. Wiley, Chichester, pp. 381–402.

Fipke, C.E., Gurney, J.J., Moore, R.O., 1995. Diamond exploration techniques emphasising indicator mineral geochemistry and Canadian examples. Geological Survey of Canada Bulletin 423.

Francis, D., Patterson, M., 2009. Kimberlites and aillikites as probes of the continental lithospheric mantle. Lithos 109, 72–80. doi:10.1016/j.lithos.2008.05.007

Franz, L., Brey, G.P., Okrusch, M., 1996. Steady state geotherm, thermal disturbances, and tectonic development of the lower lithosphere underneath the Gibeon Kimberlite Province, Namibia. Contrib. Mineral. Petr. 126, 181–198.

Ganga, J., Rotman, A.Y., Nosiko, S., 2003. Pipe Catoca, an example of the weakly eroded kimberlites from North-East of Angola, in: The 8th International Kimberlite Conference, Extended Abstract.

Gaspar, J.C., Wyllie, P.J., 1983. Ilmenite (high Mg, Mn, Nb) in the carbonatites from the Jacupiranga Complex, Brazil. Am. Mineral. 68, 960–971.

Gaspar, J.C., Wyllie, P.J., 1984. The alleged kimberlite-carbonatite relationship: evidence from ilmenite and spinel from Premier and Wesselton mines and the Benfontein sill, South Africa. Contrib. Mineral. Petr. 85, 133–140. doi:10.1007/BF00371703

Gaul, O.F., Gri, W.L., Y, S.Y.O.R., Pearson, N.J., 2000. Mapping olivine composition in the lithospheric mantle 182, 223–235.

Gonçalves, A.O. (2007): Caracterización mineralógica, geoquímica y petroggenética de las pegmatitas graníticas de Giraúl, Nambie, Angola. Unpubl. Ph.D. Thesis, Univ. Zaragoza, 441 pp.

Goodwin, A.M., 1996. Principles of Precambrian geology. Academic Press, London.

Grassi, D., Schmidt, M.W., 2011. The melting of carbonated pelites from 70 to 700 km depth. J. Petrol. 52, 765–789. doi:10.1093/petrology/egr002

Gréau, Y., Huang, J.-X., Griffin, W.L., Renac, C., Alard, O., O'Reilly, S.Y., 2011. Type I eclogites from Roberts Victor kimberlites: Products of extensive mantle metasomatism. Geochim. Cosmochim. Acta 75, 6927–6954. doi:10.1016/j.gca.2011.08.035

Grégoire, M., Bell, D., Le Roex, a., 2002. Trace element geochemistry of phlogopite-rich mafic mantle xenoliths: their classification and their relationship to phlogopite-bearing peridotites and kimberlites revisited. Contrib. Mineral. Petr. 142, 603–625. doi:10.1007/s00410-001-0315-8

Grégoire, M., Bell, D.R., Le Roex, A.P., 2003. Garnet Lherzolites from the Kaapvaal Craton (South Africa): Trace Element Evidence for a Metasomatic History. J. Petrol. 44, 629–657.

Gregoire, M., Tinguely, C., Bell, D., Leroex, a, 2005. Spinel lherzolite xenoliths from the Premier kimberlite (Kaapvaal craton, South Africa): Nature and evolution of the shallow upper mantle beneath the Bushveld complex. Lithos 84, 185–205. doi:10.1016/j.lithos.2005.02.004

Griffin, W.L., Wass, S.Y., Hollis, J.D., 1984. Ultramafic Xenoliths from Bullenmerri and Gnotuk Maars, Victoria, Australia: Petrology of a subcontinental crust-mantle transition. J. Petrol. 25, 53–87.

Griffin, W.L., Cousens, D.R., Ryan, C.G., Sic, S.H., Suter, G.F., 1989. Mineralogy and Ni in chrome pyrope garnets : a new geothermometer 199–202.

Griffin, W.L., Ryan, C.G., Gurney, J.J., Sobolev, N.V., Win, T.T., 1994. Chromite macrocrysts in kimberlites and lamproites: Geochemistry and origin, in: Meyer, H.O.A., Leonardos, O.H. (Eds.), Kimberlites, Related Rocks and Mantle Xenoliths. Companhia de Pesquisa de Recurcos Minerais Special Publication 1/A, Brasilia, Brazil, pp. 366–367.

Griffin, W.L., Ryan, C.G., 1995. Trace elements in indicator minerals: area selection and target evaluation in diamond exploration. J. Geochemical Explor. 53, 311–337. doi:10.1016/0375-6742(94)00015-4

Griffin, W.L., Smith, D., Ryan, C.G., O'Reilly, S.Y., Win, T.T., 1996. Trace-element zoning in mantle minerals; metasomatism and thermal events in the upper mantle. Can. Mineral. 34, 1179–1193.

Griffin, W.L., Moore, R.O., Ryan, C.G., Gurney, J.J., Win, T.T., 1997. Geochemistry of magnesian ilmenite megacrysts from Southern African kimberlites. Russ. Geol. Geophys. 38, 421–443.

Griffin, W.L., O'Reilly, S.Y., Ryan, C.G., Gaul, O.F., Ionov, D.A., 1998. Secular Variation in the Composition of Subcontinental Lithospheric Mantle, in: Braun, J., Dooley, J.C., Goleby, B.R., van der Hilst, R.D., Klootwijk, C.T. (Eds.), Structure and Evolution of the Australian Continent. Geodynamic Series. Vol 26. American Geophysical Union, Washington, D. C., pp. 1–26.

Griffin, W.L., Doyle, B.J., Ryan, C.G., Pearson, N.J., Reilly, S.Y.O., Davies, R., Kivi, K., Achterbergh, E.V.A.N., Natapov, L.M., 1999a. Layered Mantle Lithosphere in the Lac de Gras Area , Slave Craton : Composition , Structure and Origin 40, 705–727.

Griffin, W.L., Fisher, N.I., Friedman, J., Ryan, C.G., O'Reilly, S.Y., 1999b. Cr-Pyrope Garnets in the Lithospheric Mantle. I. Compositional Systematics and Relations to Tectonic Setting. J. Petrol. 40, 679–704. doi:10.1093/petroj/40.5.679

Griffin, W.L., Ryan, C.G., Kaminsky, F. V., O'Reilly, S.Y., Natapov, L.M., Win, T.T., Kinny, P.D., Ilupin,

I.P., 1999c. The Siberian lithosphere traverse: Mantle terranes and the assembly of the Siberian Craton. Tectonophysics 310, 1–35. doi:10.1016/S0040-1951(99)00156-0

Griffin, W.L., Shee, S.R., Ryan, C.G., Win, T.T., Wyatt, B.A., 1999d. Harzburgite to lherzolite and back again: metasomatic processes in ultramafic xenoliths from the Wesselton. Contrib. Mineral. Petr. 134, 232–250.

Griffin, W.L., O'Reilly, S.Y., Abe, N., Aulbach, S., Davies, R.M., Pearson, N.J., Doyle, B.J., Kivi, K., 2003. The origin and evolution of Archean lithospheric mantle. Precambrian Res. 127, 19–41. doi:10.1016/S0301-9268(03)00180-3

Griffin, W.L., O'Reilly, S.Y., Natapov, L.M., Ryan, C.G., 2003b. The evolution of lithospheric mantle beneath the Kalahari Craton and its margins. Lithos 71, 215–241. doi:10.1016/j.lithos.2003.07.006

Griffin, W.L., O'Reilly, S.Y., 2005. Upper Mantle Composition: Tools for Smarter Diamond Exploration, in: GEMOC Abstracts. p. 4 p.

Griffin, W.L., OReilly, S.Y.O., 2007. Cratonic lithospheric mantle : Is anything subducted ? Episodes 30, 43–53.

Griffin, W.L., Powell, W.J., Pearson, N.., O'Reilly, S.Y., 2008. GLITTER: data reduction software for laser ablation ICP-MS, in: Sylvester, P. (Ed.), Laser Ablation–ICP–MS in the Earth Sciences. Mineralogical Association of Canada Short Course Series, pp. 204–207.

Griffin, W.L., O'Reilly, S.Y., Afonso, J.C., Begg, G.C., 2009. The composition and evolution of lithospheric mantle: A re-evaluation and its tectonic implications. J. Petrol. 50, 1185–1204. doi:10.1093/petrology/egn033

Griffin, W.L., Batumike, J.M., Greau, Y., Pearson, N.J., Shee, S.R., O'Reilly, S.Y., 2014. Emplacement ages and sources of kimberlites and related rocks in southern Africa: U–Pb ages and Sr–Nd isotopes of groundmass perovskite. Contrib. Mineral. Petr. 168. doi:10.1007/s00410-014-1032-4

Grütter, H.S., Gurney, J.J., Menzies, A.H., Winter, F., 2004. An updated classification scheme for mantle-derived garnet, for use by diamond explorers . Lithos 77, 841–857. doi:10.1016/j.lithos.2004.04.012

Grütter, H.S., Quadling, K.E., 1999. Can sodium in garnet be used to monitor eclogitic diamond potential?, in: Gurney, J., Gurney, J., Pascoe, M., Richardson, S. (Eds.), Proceedings of the 7th International Kimberlite Conference. Red Roof Design, Cape Town, pp. 314–320.

Grütter, H.S., Sweeney, R.J., 2000. Tests and constraints on single-grain Cr-pyrope barometer models: some initial results, in: GAC-MAC-GeoCanada Conference. Calgary, p. CD, not paginated.

Guiraud, R., Bosworth, W., Thierry, J., Delplanque, A., 2005. Phanerozoic geological evolution of Northern and Central Africa: An overview. J. African Earth Sci. 43, 83–143.

Gurney, J.J., 1984. A correlation between garnets and diamonds, in: Glover, J.E., Harris, P.G. (Eds.), Kimberlite Occurrence and Origins: A Basis for Conceptual Models in Exploration. Geology Department and University Extension, University of Western Australia, pp. 143–166.

Gurney, J.J., Moore, R.O., 1993. Geochemical correlations between kimberlitic indicator minerals and diamonds, in: Sheahan, P., Chater, A. (Eds.), Diamonds: Exploration, Sampling and Evaluation, Short Course Proceedings. Prospectors and Developers Association of Canada, Toronto, pp. 147–171.

Gurney, J.J., Zweistra, P., 1995. The interpretation of the major element compositions of mantle minerals in diamond exploration. J. Geochemical Explor. 53, 293–309. doi:10.1016/0375-6742(94)00021-3

Haggerty, S.E., Raber, E., Naeser, C.W., 1983. Fission track dating of kimberlitic zircons. Earth Planet. Sci. Lett. 63, 41–50. doi:10.1016/0012-821X(83)90020-1

Haggerty, S.E., 1983b. Lindseyite (Ba) and mathiasite (K): two new chromium-titanates in the crichtonite series from the upper mantle. Am. Mineral. 68, 494–505.

Haggerty, S.E., 1991a. Oxide mineralogy of the upper mantle, in: Lindsley, D.H. (Ed.), Oxide Minerals: Petrologic and Magnetic Significance. Reviews in Mineralogy, Mineralogical Society of America vol. 25, Washington, pp. 355– 416.

Haggerty, S.E., 1991b. Oxide textures; a mini-atlas, in: Lindsley, D.H. (Ed.), Oxide Minerals: Petrologic and Magnetic Significance. Reviews in mineralogy, Mineralogical Society of America, vol.25, Washington, pp. 129–219.

Hanson, R.E., 2003. Proterozoic geochronology and tectonic evolution of southern Africa. Geol. Soc. London, Spec. Publ. 206, 427–463. doi:10.1144/GSL.SP.2003.206.01.20

Harris, J.W., Hawthorne, J.B., Oosterveld, M.M., 1984. A comparison of diamond characteristics from the DeBeers pool mines, Kimberley, South Africa. Ann. Sci. Univ. Clermont Ferrand 74, 1–13.

Harte, B., Gurney, J.J., 1981. The mode of formation of chromium-poor megacryst suites from kimberlites. J. Geol. 89, 749–753.

Harte, B., 1983. Mantle peridotites and processes - the kimberlite sample, in: Hawkesworth, C.J. (Ed.), Continental Basalts and Mantle Xenoliths. Nantwich, pp. 46–91.

Harte, B., Hunter, R.H., Kinny, P.D., 1993. Melt geometry, movement and crystallization, in relation to mantle dykes, veins and metasomatism. Philos. Trans. Phys. Sci. Eng. Phys. Sci. Eng. 342, 1–21.

Hasterok, D., Chapman, D.S., 2011. Heat production and geotherms for the continental lithosphere. Earth Planet. Sci. Lett. 307, 59–70. doi:10.1016/j.epsl.2011.04.034

Hawthorne, J.B., 1975. Model of a kimberlite pipe. Phys. Chem. Earth 9, 1–15. doi:10.1016/0079-1946(75)90002-6

Heaman, L.M., 1989. The nature of subcontinental mantle from Sr-Nd-Pb isotopic studies on kimberlitic perovskite. Earth Planet. Sci. Lett. 92, 323–334.

Helmstaedt, H., Schulze, D.J., 1989. Southern African kimberlites and their mantle sample: Implications for Archean tectonics and lithosphere evolution, in: Ross, J. (Ed.), Kimberlites and Related Rocks, Vol. 1: Their Composition, Occurrence, Origin and Emplacement. Geological Society of Australia

Special Publication n14, Sydney, pp. 358–368.

Herzberg, C., Rudnick, R., 2012. Formation of cratonic lithosphere: An integrated thermal and petrological model. Lithos 149, 4–15. doi:10.1016/j.lithos.2012.01.010

Hills, D., Haggerty, S., 1989. Petrochemistry of eclogites from the Koidu Kimberlite Complex, Sierra Leone. Contrib. Mineral. Petr. 103, 397–422. doi:10.1007/bf01041749

Hops, J.J., Gurney, J.J., Harte, B., 1992. The Jagersfontein Cr-poor megacryst suite - towards a model for megacryst petrogenesis. J. Volcanol. Geotherm. Res. 50, 143–160.

Howarth, G.H., Barry, P.H., Pernet-Fisher, J.F., Baziotis, I.P., Pokhilenko, N.P., Pokhilenko, L.N., Bodnar, R.J., Taylor, L. a., Agashev, A.M., 2014. Superplume metasomatism: Evidence from Siberian mantle xenoliths. Lithos 184-187, 209–224. doi:10.1016/j.lithos.2013.09.006

Huang, J.-X., Gréau, Y., Griffin, W.L., O'Reilly, S.Y., Pearson, N.J., 2012. Multi-stage origin of Roberts Victor eclogites: Progressive metasomatism and its isotopic effects. Lithos 142-143, 161–181. doi:10.1016/j.lithos.2012.03.002

Hunter, R.H., Taylor, L.A., 1982. Instability of garnet from the mantle: Glass as evidence of metasomatic melting. Geology 10, 617–620.

Ionov, D. a., Doucet, L.S., Ashchepkov, I. V., 2010. Composition of the Lithospheric Mantle in the Siberian Craton: New Constraints from Fresh Peridotites in the Udachnaya-East Kimberlite. J. Petrol. 51, 2177–2210. doi:10.1093/petrology/egq053

Ivanikov, V. V., Rukhlov, a. S., Bell, K., 1998. Magmatic Evolution of the Melilitite-Carbonatite-Nephelinite Dyke Series of the Turiy Peninsula (Kandalaksha Bay, White Sea, Russia). J. Petrol. 39, 2043–2059. doi:10.1093/petroj/39.11-12.2043

Jacob, D., Jagoutz, E., Lowry, D., Mattey, D., Kudrjavtseva, G., 1994. Diamondiferous eclogites from Siberia: Remnants of Archean oceanic crust. Geochim. Cosmochim. Acta 58, 5191–5207.

Jacob, D.E., 2004. Nature and origin of eclogite xenoliths from kimberlites. Lithos 77, 295–316. doi:10.1016/j.lithos.2004.03.038

Jacques, A.L., Lewis, J.D., Smith, C.B., 1986. The kimberlites and lamproites of Western Australia, Geological Survey of Wester Australia, Bulletin.

Jacques, A.L., Hall, A.E., Sheraton, J.W., Smith, C.B., Sun, S.S., Drew, R.M., Foudoulis, C., Ellingsen, K., 1989. Composition of crystalline inclusions and C isotopic composition of Argyle and Ellendale diamonds, in: Ross, J., Jaques, A.L., Ferguson, J., Green, D.H., O'Reilly, S.Y., Danchin, R.V., Janse, A.J.A. (Eds.), Kimberlites and Related Rocks, Proceedings of the Fourth International Kimberlite Conference. Geological Society of Australia Special Publication n14, vol.2, pp. 966–989.

Jago, C.E., Mitchell, R.H., 1989. A new garnet classification technique: divisive cluster analysis applied to garnet populations from Somerset Island, in: Ross, J. (Ed.), Kimberlites and Related Rocks, Vol. 1: Their Composition, Occurrence, Origin and Emplacement. Geological Society of Australia, Special Publication No. 14, v. 1, pp. 298–310.

Jang, Y.D., Naslund, H.R., 2003. Major and trace element variation in ilmenite in the Skaergaard Intrusion: petrologic implications. Chem. Geol. 193, 109–125. doi:10.1016/S0009-2541(02)00224-3

Janse, a. J. a. (Bram), Sheahan, P. a., 1995. Catalogue of world wide diamond and kimberlite occurrences: a selective and annotative approach. J. Geochemical Explor. 53, 73–111. doi:10.1016/0375-6742(94)00017-6

Jelsma, H.A., Wit, M.J. de, Thiart, C., Dirks, P.H.G.., Viola, G., Basson, I.J., Anckar, E., 2004. Preferential distribution along transcontinental corridors of kimberlites and related rocks of Southern Africa. South African J. Geol. 107, 301–324.

Jelsma, H., Barnett, W., Richards, S., Lister, G., 2009. Tectonic setting of kimberlites. Lithos 112, 155–165. doi:10.1016/j.lithos.2009.06.030

Jochum, K.P., Weis, U., Stoll, B., Kuzmin, D., Yang, Q., Raczek, I., Jacob, D.E., Stracke, A., Birbaum, K., Frick, D. a., Günther, D., Enzweiler, J., 2011. Determination of Reference Values for NIST SRM 610-617 Glasses Following ISO Guidelines. Geostand. Geoanalytical Res. 35, 397–429. doi:10.1111/j.1751-908X.2011.00120.x

Johnson, S.P., Rivers, T., De Waele, B., 2005. A review of the Mesoproterozoic to early Palaeozoic magmatic and tectonothermal history of south-central Africa: implications for Rodinia and Gondwana. J. Geol. Soc. London. 162, 433–450. doi:10.1144/0016-764904-028

Kamenetsky, V.S., Kamenetsky, M.B., Sobolev, A. V., Golovin, A. V., Sharygin, V. V., Pokhilenko, N.P., Sobolev, N. V., 2009. Can pyroxenes be liquidus minerals in the kimberlite magma? Lithos 112, 213–222. doi:10.1016/j.lithos.2009.03.040

Kamenetsky, V.S., Golovin, A. V., Maas, R., Giuliani, A., Kamenetsky, M.B., Weiss, Y., 2014. Towards a new model for kimberlite petrogenesis: Evidence from unaltered kimberlites and mantle minerals. Earth-Science Rev. 139, 145–167. doi:10.1016/j.earscirev.2014.09.004

Kaminsky, F. V., Zakharchenko, O.D., Griffin, W.L., Channer, D.M.D., Khachatryan-Blinova, G.K., 2000. Diamond from the Guaniamo area, Venezuela. Can. Mineral. 38, 1347–1370. doi:10.2113/gscanmin.38.6.1347

Kaminsky, F., Zakharchenko, O., Davies, R., Griffin, W., Khachatryan-Blinova, G., Shiryaev, a., 2001. Superdeep diamonds from the Juina area, Mato Grosso State, Brazil. Contrib. Mineral. Petr. 140, 734–753. doi:10.1007/s004100000221

Kaminsky, F. V., Belousova, E. a., 2009. Manganoan ilmenite as kimberlite/diamond indicator mineral. Russ. Geol. Geophys. 50, 1212–1220. doi:10.1016/j.rgg.2009.11.019

Kennedy, C.S., Kennedy, G.C., 1976. The equilibrium boundary between graphite and diamond. J. Geophys. Res. 81, 2467–2470.

Kjarsgaard, B. a., Pearson, D.G., Tappe, S., Nowell, G.M., Dowall, D.P., 2009. Geochemistry of hypabyssal kimberlites from Lac de Gras, Canada: Comparisons to a global database and applications to the parent magma problem. Lithos 112, 236–248. doi:10.1016/j.lithos.2009.06.001

Kobussen, A.F., Griffin, W.L., O'Reilly, S.Y., 2009. Cretaceous thermo-chemical modification of the Kaapvaal cratonic lithosphere, South Africa. Lithos 112S, 886–895. doi:10.1016/j.lithos.2009.06.031

Kopylova, M.G., Russell, J.K., Cookenboo, H., 1999. Petrology of Peridotite and Pyroxenite Xenoliths from the Jericho Kimberlite: Implications for the Thermal State of the Mantle beneath the Slave Craton, Northern Canada. J. Petrol. 40, 79–104. doi:10.1093/petroj/40.1.79

Kopylova, M.G., Russell, J.K., 2000. Chemical stratification of cratonic lithosphere: Constraints from the Northern Slave craton, Canada. Earth Planet. Sci. Lett. 181, 71–87. doi:10.1016/S0012-821X(00)00187-4

Kopylova, M.G., Caro, G., 2004. Mantle xenoliths from the southeastern Slave Craton: Evidence for chemical zonation in a thick, cold lithosphere. J. Petrol. 45, 1045–1067. doi:10.1093/petrology/egh003

Kostrovitsky, S.I., Malkovets, V.G., Verichev, E.M., Garanin, V.K., Suvorova, L. V., 2004. Megacrysts from the Grib kimberlite pipe (Arkhangelsk Province, Russia). Lithos 77, 511–523. doi:10.1016/j.lithos.2004.03.014

Kotel'nikov, D.D., Zinchuk, N.N., Zhukhlistov, A.P., 2005. Stages of serpentine and phlogopite transformation in the Catoca kimberlite pipe, Angola. Dokl. Earth Sci. 403, 866–869.

Kriuchkov, A., Sarychev, I., Vouiko, V., Chipoia, B., Antoniuk, B., 2000. Kimberlite pipe of Catoca. Geology, substantial analyses of the rocks and characteristics of diamonds, in: Geoluanda. Abstract Volume. pp. 91–92.

Krogh, E.J., 1988. The garnet-clinopyroxene Fe-Mg geothermometer - a reinterpretation of existing experimental data. Contrib. Mineral. Petr. 99, 44–48. doi:10.1007/BF00399364

Krogh, E.J., 2000. The garnet – clinopyroxene Fe 2+ – Mg geothermometer : an updated calibration. J. Metamorph. Geol. 211–219.

Kryvdik, S.G., 2014. Geochemical features of ilmenites from the alkaline complexes of the Ukrainian Shield: LA-ICP-MS data. Geochemistry Int. 52, 287–295. doi:10.1134/S0016702914040041

Laurora, a, Mazzucchelli, M., Rivalenti, G., Vannucci, R., Zanetti, a, Barbieri, M. a, Cingolani, C. a, 2001. Metasomatism and melting in carbonated peridotite xenoliths from the mantle wedge: The Gobernador Gregores case (southern Patagonia). J. Pet. 42, 69–87. doi:10.1093/petrology/42.1.69

Le Bas, M.J., 2000. IUGS Reclassification of the high-Mg and picritic volcanic rocks. J. Petrol. 41, 1467–1470.

Le Pioufle, A., Canil, D., 2012. Iron in monticellite as an oxygen barometer for kimberlite magmas. Contrib. Mineral. Petr. 163, 1033–1046. doi:10.1007/s00410-011-0714-4

Le Roex, A.P., Bell, D.R., Davis, P., 2003. Petrogenesis of Group I Kimberlites from Kimberley, South Africa: Evidence from Bulk-rock Geochemistry. J. Petrol. 44, 2261–2286. doi:10.1093/petrology/egg077

Litasov, K.D., Shatskiy, a., Ohtani, E., Yaxley, G.M., 2013. Solidus of alkaline carbonatite in the deep mantle. Geology 41, 79–82. doi:10.1130/G33488.1

Llusià, R.M., Pereira, S., Melgarejo, J.C., Galiano, A., Russell, E., Kerr, P., Sebastian, P., 2005. Paleoplaceres diamantíferos aluviales de la formación Calonda del Cretácico en la zona de Muanga (Lunda Norte, Angola), in: Extended Abstract, VIII Congresso de Geoquímica Dos Países de Língua Portuguesa E XIV Sem.

Ludwig, K.R., 2003. Isoplot/Ex version 4.0: a geochemical toolkit for Microsoft Excel. Berkeley Geochronological Cent. Spec. Publ. 4, 1–70.

MacGregor, I.D., 1974. The System MgO-Al_2O_3-SiO_2: Solubility of Al2O3 in for Spinel and Garnet Peridotite Compositions. Am. Mineral. 59, 110–119.

MacGregor, I.D., Manton, W.I., 1986. Roberts Victor Eclogites: Ancient Oceanic Crust. J. Geophys. Res. 91, 14063–14079.

Malkovets, V.G., Griffin, W.L., O'Reilly, S.Y., Wood, B.J., 2007. Diamond, subcalcic garnet, and mantle metasomatism: Kimberlite sampling patterns define the link. Geology 35, 339. doi:10.1130/G23092A.1

Mattey, D., Lowry, D., Macpherson, C., 1994. Oxygen isotope composition of mantle peridotite. Earth Planet. Sci. Lett. 128, 231–241.

McCandless, T.E., Gurney, J.J., 1989. Sodium in garnet and potassium in clinopyroxene: criteria for classifying mantle eclogites, in: Ross, J., Jacques, A.L., Ferguson, J., Green, D.H. (Eds.), Kimberlites and Related Rocks. pp. 827–832.

McDonough, W.F., Sun, S.–., 1995. The composition of the Earth '. Chem. Geol. 120, 223–253.

McKenzie, D., 1989. Some remarks on the movement of small melt fractions in the mantle. Earth Planet. Sci. Lett. 95, 53–72. doi:10.1016/0012-821X(89)90167-2

Mercier, J.C.C., Nicolas, A., 1975. Textures and fabrics of upper-mantle peridotites as illustrated by xenoliths from basalts. J. Petrol. 16, 454–487.

Mercier, J.C.C., 1979. Peridotite xenoliths and the dynamics of kimberlite intrusion. Spec. Publ. 16, 197–212.

Meyer, H.O.A., Svisero, D.P., 1975. Mineral inclusions in Brazilian diamonds. Phys. Chem. Earth 9, 785–795.

Misra, K.C., Anand, M., Taylor, L.A., Sobolev, N. V., 2004. Multi-stage metasomatism of diamondiferous eclogite xenoliths from the Udachnaya kimberlite pipe, Yakutia, Siberia. Contrib. Mineral. Petr. 146, 696–714. doi:10.1007/s00410-003-0529-z

Mitchell, R.H., 1973. Magnesian ilmenite and its role in kimberlite petrogenesis. J. Geol. 81, 301–311.

Mitchell, R.H., 1978. Manganoan magnesian ilmenite and titanian clinohumite from the Jacupiranga

carbonatite, São Paulo, Brazil. Am. Mineral. 63, 544–547.

Mitchell, R.H., 1986. Kimberlites, Mineralogy, Geochemistry and Petrology. Plenum Press, New York.

Mitchell, R.H., 1991. Kimberlites and lamproites: primary sources of diamond. Geosci. Canada 18, 1–16.

Moore, R.O., Griffin, W.L., Gurney, J.J., Ryan, C.G., Cousens, D.R., Sie, S.H., Suter, G.F., 1992. Trace element geochemistry of ilmenite megacrysts from the Monastery kimberlite, South Africa. Lithos 29, 1–18. doi:10.1016/0024-4937(92)90031-S

Moore, A., Belousova, E., 2005. Crystallization of Cr-poor and Cr-rich megacryst suites from the host kimberlite magma: implications for mantle structure and the generation of kimberlite magmas. Contrib. Mineral. Petr. 149, 462–481. doi:10.1007/s00410-005-0663-x

Muller, M.R., Jones, a. G., Evans, R.L., Grütter, H.S., Hatton, C., Garcia, X., Hamilton, M.P., Miensopust, M.P., Cole, P., Ngwisanyi, T., Hutchins, D., Fourie, C.J., Jelsma, H. a., Evans, S.F., Aravanis, T., Pettit, W., Webb, S.J., Wasborg, J., 2009. Lithospheric structure, evolution and diamond prospectivity of the Rehoboth Terrane and western Kaapvaal Craton, southern Africa: Constraints from broadband magnetotellurics. Lithos 112, 93–105. doi:10.1016/j.lithos.2009.06.023

Mvuemba Ntanda, F., Moreau, J., Meyer, H.O.A., 1982. Particularités des inclusions cristallines primaires des diamants du Kasaï, Zaïre. Can. Mineral. 20, 217–230.

Mysen, B., Griffin, W.L., 1973. Pyroxene Stoichiometry and the Breakdown of Omphacite. Am. Mineral. 58, 60–63.

Natali, C., Beccaluva, L., Bianchini, G., Ellam, R.M., Siena, F., Stuart, F.M., 2013. Carbonated alkali-silicate metasomatism in the North Africa lithosphere: Evidence from Middle Atlas spinel-lherzolites, Morocco. J. South Am. Earth Sci. 41, 113–121. doi:10.1016/j.jsames.2012.06.014

Nikitina, L.P., Korolev, N.M., Zinchenko, V.N., Felix, J.T., 2014. Eclogites from the upper mantle beneath the Kasai Craton (Western Africa): Petrography, whole-rock geochemistry and UPb zircon age. Precambrian Res. 249, 13–32. doi:10.1016/j.precamres.2014.04.014

Nimis, P., Taylor, W.R., 2000. Single clinopyroxene thermobarometry for garnet peridotites. Part I. Calibration and testing of a Cr-in-Cpx barometer and an enstatite-in-Cpx thermometer. Contrib. Mineral. Petr. 139, 541–554. doi:10.1007/s004100000156

Nimis, P., Grütter, H., 2010. Internally consistent geothermometers for garnet peridotites and pyroxenites. Contrib. Mineral. Petr. 159, 411–427. doi:10.1007/s00410-009-0455-9

Niu, Y., Langmuir, C.H., Kinzler, R.J., 1997. The origin of abyssal peridotites: a new perspective. Earth Planet. Sci. Lett. 152, 251–265.

Nixon, P.H., Boyd, F.R., 1973. The discrete nodule (megacryst) association in kimberlites from Northern Lesotho, in: Nixon, P.H. (Ed.), Lesotho Kimberlites. Lesotho National Development Corporation, Maseru, pp. 67–76.

Nixon, P.H. (editor), 1987. Mantle xenoliths. John Wiley, Chichester.

Norman, M.D., Pearson, N.J., Sharma, a., Griffin, W.L., 1996. Quantitative Analysis of Trace Elements in Geological Materials by Laser Ablation ICPMS: Instrumental Operating Conditions and Calibration of NIST Glasses. Geostand. Newsl. 20, 247–261.

O'Hara, M.J., Saunders, M.J., Mercy, E.L.P., 1975. Garnet-peridotite, primary ultrabasic magma and eclogite; interpretation of upper mantle processes in kimberlite. Phys. Chem. Earth 9, 571–604.

O'Neill, H.S.C., Wood, B.J., 1979. An experimental study of Fe-Mg partitioning between garnet and olivine and its calibration as a geothermometer. Contrib. Mineral. Petr. 70, 59–70. doi:10.1007/BF00371872

O'Reilly, S.Y., Griffin, W.L., 1996. 4-D Lithosphere Mapping: methodology and examples. Tectonophysics 3–18.

O'Reilly, S.Y., Griffin, W.L., 2006. Imaging global chemical and thermal heterogeneity in the subcontinental lithospheric mantle with garnets and xenoliths: Geophysical implications. Tectonophysics 416, 289–309. doi:10.1016/j.tecto.2005.11.014

O'Reilly, S.Y., Zhang, M., Griffin, W.L., Begg, G., Hronsky, J., 2009. Ultradeep continental roots and their oceanic remnants: A solution to the geochemical "mantle reservoir" problem? Lithos 112, 1043–1054. doi:10.1016/j.lithos.2009.04.028

O'Reilly, S.Y., Griffin, W.L., 2013. Mantle metasomatism, in: Harlov, D.E., Austrheim, H. (Eds.), Metasomatism and the Chemical Transformation of Rock, Lecture Notes in Earth System Sciences. Springer Berlin Heidelberg, Berlin, Heidelberg, pp. 471–534. doi:10.1007/978-3-642-28394-9

Ogilvie-Harris, R.C., Field, M., Sparks, R.S.J., Walter, M.J., 2009. Perovskite from the Dutoitspan kimberlite, Kimberley, South Africa: implications for magmatic processes. Mineral. Mag. 73, 915–928. doi:10.1180/minmag.2009.073.6.915

Pasteris, J.D., 1980. The significance of groundmass ilmenite and megacryst ilmenite in kimberlites. Contrib. Mineral. Petr. 75, 315–325.

Paton, C., Hergt, J.M., Phillips, D., Woodhead, J.D., Shee, S.R., 2007. New insights into the genesis of Indian kimberlites from the Dharwar Craton via in situ Sr isotope analysis of groundmass perovskite. Geology 35, 1011. doi:10.1130/G24040A.1

Paton, C., Hellstrom, J., Paul, B., Woodhead, J., Hergt, J., 2011. Iolite: Freeware for the visualisation and processing of mass spectrometric data. J. Anal. At. Spectrom. 26, 2508. doi:10.1039/c1ja10172b

Paul, B., Paton, C., Norris, A., Woodhead, J., Hellstrom, J., Hergt, J., Greig, A., 2012. CellSpace: A module for creating spatially registered laser ablation images within the Iolite freeware environment. J. Anal. At. Spectrom. 27, 700–706. doi:10.1039/c2ja10383d

Pearson, G., Wittig, N., 2008. Formation of Archaean continental lithosphere and its diamonds: the root of the problem. J. 165, 895–914. doi:10.1144/0016-76492008-003

Pereira, E., Rodrigues, J., Reis, B., 2003. Synopsis of Lunda geology, NE Angola : Implications for diamond exploration. Comun. Inst. Geol. e Min. 90, 189–212.

Perevalov, O.V., Voinovsky, A.S., Tselikovsky, A.F., Agueev, Y.L., Polskoi, F.R., Khódirev, V.L., Kondrátiev, A.I., 1992. Geology of Angola: Explanatory Notes of the Geological Map at a Scale of 1:1.000.000; Geological Survey of Angola: Luanda, Angola.

Pervov, V. a., Somov, S. V., Korshunov, a. V., Dulapchii, E. V., Félix, J.T., 2011. The Catoca kimberlite pipe, Republic of Angola: A paleovolcanological model. Geol. Ore Depos. 53, 295–308. doi:10.1134/S1075701511040052

Pivin, M., Féménias, O., Demaiffe, D., 2009. Metasomatic mantle origin for Mbuji-Mayi and Kundelungu garnet and clinopyroxene megacrysts (Democratic Republic of Congo). Lithos 112, 951–960. doi:10.1016/j.lithos.2009.03.050

Platt, R.G., 1994. Perovskite, Loparite and Ba-Fe Hollandite from the Schryburt Lake Carbonatite Complex, Northwestern Ontario, Canada. Mineral. Mag. 58, 49–57. doi:10.1180/minmag.1994.058.390.05

Pokhilenko, N.P., Agashev, a. M., Litasov, K.D., Pokhilenko, L.N., 2015. Carbonatite metasomatism of peridotite lithospheric mantle: implications for diamond formation and carbonatite-kimberlite magmatism. Russ. Geol. Geophys. 56, 280–295. doi:10.1016/j.rgg.2015.01.020

Pouchou, J.L., Pichoir, F., 1984. A new model for quantitative X-ray microanalysis. Part 1. Applications to the analysis of homogeneous samples. Rech. Aerosp. (English Ed. 3, 11–38.

Powell, R., 1985. Regression diagnostics and robust regression in geothermometer / geo barometer calibration: the garnet- clinopyroxene geothermometer revisited. J. Metamorph. Geol. 33–42.

Powell, W., Zhang, M., O'Reilly, S.Y., Tiepolo, M., 2004. Mantle amphibole trace-element and isotopic signatures trace multiple metasomatic episodes in lithospheric mantle, western Victoria, Australia. Lithos 75, 141–171. doi:10.1016/j.lithos.2003.12.017

Puziewicz, J., Matusiak-Małek, M., Ntaflos, T., Grégoire, M., Kukuła, A., 2014. Subcontinental lithospheric mantle beneath Central Europe. Int. J. Earth Sci. doi:10.1007/s00531-014-1134-2

Reguir, E.P., Chakhmouradian, a. R., Halden, N.M., Malkovets, V.G., Yang, P., 2009. Major- and trace-element compositional variation of phlogopite from kimberlites and carbonatites as a petrogenetic indicator. Lithos 112, 372–384. doi:10.1016/j.lithos.2009.05.023

Reguir, E.P., Camacho, A., Yang, P., Chakhmouradian, A.R., Kamenetsky, V.S., Halden, N.M., 2010. Trace-element study and uranium-lead dating of perovskite from the Afrikanda plutonic complex, Kola Peninsula (Russia) using LA-ICP-MS. Mineral. Petrol. 100, 95–103. doi:10.1007/s00710-010-0131-9

Rehfeldt, T., Jacob, D.E., Richard, W., Foley, S.F., 2007. Fe-rich dunite xenoliths from South African kimberlites: cumulates from Karoo flood basalts. J. Petrol. 48, 1387–1409. doi:10.1093/petrology/egm023

Reid, A.M., Brown, R.W., Dawson, J.B., Whitfield, G.G., Siebert, J.C., 1976. Garnet and pyroxene

compositions in some diamondiferous eclogites. Contrib. Mineral. Petr. 58, 203–220. doi:10.1007/BF00382185

Reis, B., 1972. Preliminary note on the distribution and tectonic controls on kimberlites in Angola. 24th Int. Geollgical Congr. Montr. Section 4, 276–281.

Replumaz, A., Kárason, H., Van Der Hilst, R.D., Besse, J., Tapponnier, P., 2004. 4-D evolution of SE Asia's mantle from geological reconstructions and seismic tomography. Earth Planet. Sci. Lett. 221, 103–115. doi:10.1016/S0012-821X(04)00070-6

Riches, A.J. V, Liu, Y., Day, J.M.D., Spetsius, Z. V, Taylor, L.A., 2010. Lithos Subducted oceanic crust as diamond hosts revealed by garnets of mantle xenoliths from Nyurbinskaya, Siberia. Lithos 120, 368–378. doi:10.1016/j.lithos.2010.09.006

Robles-Cruz, S.E., Watangua, M., Isidoro, L., Melgarejo, J.C., Galí, S., Olimpio, A., 2009. Contrasting compositions and textures of ilmenite in the Catoca kimberlite, Angola, and implications in exploration for diamond. Lithos 112, 966–975. doi:10.1016/j.lithos.2009.05.040

Robles-Cruz, S.E., Escayola, M., Jackson, S., Galí, S., Pervov, V., Watangua, M., Gonçalves, A., Melgarejo, J.C., 2012a. U–Pb SHRIMP geochronology of zircon from the Catoca kimberlite, Angola: Implications for diamond exploration. Chem. Geol. 310-311, 137–147. doi:10.1016/j.chemgeo.2012.04.001

Robles-Cruz, S., Melgarejo, J., Galí, S., Escayola, M., 2012b. Major- and Trace-Element Compositions of Indicator Minerals that Occur as Macro- and Megacrysts, and of Xenoliths, from Kimberlites in Northeastern Angola. Minerals 2, 318–337. doi:10.3390/min2040318

Rosatelli, G., Wall, F., Stoppa, F., 2007. Calcio-carbonatite melts and metasomatism in the mantle beneath Mt. Vulture (Southern Italy). Lithos 99, 229–248. doi:10.1016/j.lithos.2007.05.011

Ryan, C.G., Griffin, W.L., Pearson, N.J., 1996. Garnet geotherms: Pressure-temperature data from Cr-pyrope garnet xenocrysts in volcanic rocks. J. Geophys. Res. 101, 5611–5625.

Sarkar, C., Storey, C.D., Hawkesworth, C.J., Sparks, R.S.J., 2011. Degassing in kimberlite: Oxygen isotope ratios in perovskites from explosive and hypabyssal kimberlites. Earth Planet. Sci. Lett. 312, 291–299. doi:10.1016/j.epsl.2011.10.036

Schulze, D.J., 1989. Constraints on the abundance of eclogite in the upper mantle. J. Geophys. Res. Solid Earth 94, 4205–4212.

Schulze, D.J., Anderson, P.F.N., Hearn, B.C., Hetman, C.M., 1995. Origin and Significance of Ilmenite Megacrysts and Macrocrysts from Kimberlite. Int. Geol. Rev. 37, 780–812. doi:10.1080/00206819509465427

Schmickler, B., Jacob, D.E., Foley, S.F., 2004. Eclogite xenoliths from the Kuruman kimberlites, South Africa: geochemical fingerprinting of deep subduction and cumulate processes. Lithos 75, 173–207. doi:10.1016/j.lithos.2003.12.012

Shee, S.R., Bristown, J.W., Bell, D.R., Smith, C.B., Allsopp, H.L., Shee, P.B., 1989. The petrology of

kimberlites, related rocks and associated mantle xenoliths from the Kuruman province, South Africa, in: Ross, J., Jacques, A.L., Ferguson, J., D.H., G., O'Reiliy, S.Y., Danchin, R.V., Janse, A.J. (Eds.), Kimberlites and Related Rocks, Proceedings of the Fourth International Kimberlite Conference (2 Volumes). Geological Society of Australia, Special Publication No. 14, v. 1, pp. 60–82.

Simon, N.S.C., Irvine, G.J., Davies, G.R., Pearson, D.G., Carlson, R.W., 2003. The origin of garnet and clinopyroxene in "depleted" Kaapvaal peridotites, Lithos. doi:10.1016/S0024-4937(03)00118-X

Simon, N.S.C., Carlson, R.W., Pearson, D.G., Davies, G.R., 2007. The origin and evolution of the Kaapvaal Cratonic Lithospheric Mantle. J. Petrol. 48, 589–625. doi:10.1093/petrology/egl074

Smith, C.B., Allsopp, H.L., Gravie, O.G., Kramers, J.D., Jackson, P.F.S., Clement, C.R., 1989. Note on the U-Pb perovskite method for dating kimberlites: examples from the Wesselton and De Beers mines, South Africa, and Somerset Island, Canada. Chem. Geol. 79, 137–145.

Smith, D., Boyd, F.R., 1987. Compositional heterogeneities in a high-temperature lherzolite nodule and implications for mantle processes, in: Nixon, P.H. (Ed.), Mantle Xenoliths. John Wiley, New York, pp. 551–562.

Smith, D., Griffin, W.L., Ryan, C.G., 1993. Compositional evolution of high-temperature sheared lherzolite PHN 1611. Geochim. Cosmochim. Acta 57, 605–613. doi:10.1016/0016-7037(93)90371-3

Sobolev, A. V, Sobolev, S. V, Kuzmin, D. V, Malitch, K.N., Petrunin, A.G., 2009. Siberian meimechites: origin and relation to flood basalts and kimberlites. Russ. Geol. Geophys. 50, 999–1033. doi:10.1016/j.rgg.2009.11.002

Sobolev, N. V., Lavrent'ev, J.G., 1971. Isomorphic sodium admixture in garnets formed at high pressures. Contrib. Mineral. Petr. 31, 1–12. doi:10.1007/BF00373387

Sobolev, N. V., 1977. Deep-seated inclusions in kimberlites and the problem of the composition of the upper mantle. American Geophysical Union, Washington, D. C.

Sobolev, N. V., Kaminsky, F.V., Griffin, W.L., Yefimova, E.S., Win, T.T., Ryan, C.G., Botkunov, A.I., 1997. Mineral inclusions in diamonds from the Sputnik kimberlite pipe, Yakutia. Lithos 39, 135–157. doi:10.1016/S0024-4937(96)00022-9

Sobolev, N. V., Yefimova, E.S., Koptil', V.I., 1999. Mineral inclusions in diamonds in the northeast of the Yakutian diamondiferous province, in: Gurney, J.J., Gurney, J.L., Pascoe, M.D., Richardson, S.H. (Eds.), Proceedings of the 7th International Kimberlite Conference. Red Roof Design, Cape Town, pp. 816–822.

Spetsius, Z. V, Taylor, L.A., 2002. Partial Melting in Mantle Eclogite Xenoliths: Connections with Diamond Paragenesis. Int. Geol. Rev. 44, 973–987. doi:10.2747/0020-6814.44.11.973

Stacey, J.S., Kramers, J.D., 1975. Approximation of terrestrial lead isotope evolution by a two-stage model 26, 207–221.

Stachel, T., Aulbach, S., Brey, G.P., Harris, J.W., Leost, I., Tappert, R., Viljoen, K.S., 2004. The trace element composition of silicate inclusions in diamonds: A review. Lithos 77, 1–19. doi:10.1016/j.lithos.2004.03.027

Storey, C.D., Smith, M.P., Jeffries, T.E., 2007. In situ LA-ICP-MS U-Pb dating of metavolcanics of Noorbotten, Sweden: records of extended geological histories in complex titanite grains. Chem. Geol. 163–181.

Su, B.X., Zhang, H.F., Sakyi, P.A., Ying, J.F., Tang, Y.J., Yang, Y.H., Qin, K.Z., Xiao, Y., Zhao, X.M., 2010. Compositionally stratified lithosphere and carbonatite metasomatism recorded in mantle xenoliths from the Western Qinling (Central China). Lithos 116, 111–128. doi:10.1016/j.lithos.2010.01.004

Sun, J., Liu, C.-Z., Tappe, S., Kostrovitsky, S.I., Wu, F.-Y., Yakovlev, D., Yang, Y.-H., Yang, J.-H., 2014. Repeated kimberlite magmatism beneath Yakutia and its relationship to Siberian flood volcanism: Insights from in situ U–Pb and Sr–Nd perovskite isotope analysis. Earth Planet. Sci. Lett. 404, 283–295. doi:10.1016/j.epsl.2014.07.039

Sykes, L., 1978. Intraplate seismicity, reactivation of pre-existing zones of weakness, alkaline magmatism, and other tectonic postdating continental fragmentation. Rev. Geophys. Sp. Phys. 621–688.

Tappe, S., Foley, S.F., Jenner, G. a., Heaman, L.M., Kjarsgaard, B. a., Romer, R.L., Stracke, A., Joyce, N., Hoefs, J., 2006. Genesis of ultramafic lamprophyres and carbonatites at Aillik Bay, Labrador: A consequence of incipient lithospheric thinning beneath the North Atlantic Craton. J. Petrol. 47, 1261–1315. doi:10.1093/petrology/egl008

Tappe, S., Pearson, D.G., Nowell, G., Nielsen, T., Milstead, P., Muehlenbachs, K., 2011a. A fresh isotopic look at Greenland kimberlites: Cratonic mantle lithosphere imprint on deep source signal. Earth Planet. Sci. Lett. 305, 235–248. doi:10.1016/j.epsl.2011.03.005

Tappe, S., Smart, K.A., Pearson, D.G., Steenfelt, A., Simonetti, A., 2011b. Craton formation in Late Archean subduction zones revealed by first Greenland eclogites. Geology 39, 1103–1106. doi:10.1130/G32348.1

Tappe, S., Simonetti, A., 2012. Combined U-Pb geochronology and Sr-Nd isotope analysis of the Ice River perovskite standard, with implications for kimberlite and alkaline rock petrogenesis. Chem. Geol. 304-305, 10–17. doi:10.1016/j.chemgeo.2012.01.030

Tappe, S., Kjarsgaard, B. a., Kurszlaukis, S., Nowell, G.M., Phillips, D., 2014. Petrology and Nd-Hf Isotope Geochemistry of the Neoproterozoic Amon Kimberlite Sills, Baffin Island (Canada): Evidence for Deep Mantle Magmatic Activity Linked to Supercontinent Cycles, Journal of Petrology. doi:10.1093/petrology/egu048

Tappe, S., Steenfelt, A., Heaman, L.M., Simonetti, A., 2009. The newly discovered Jurassic Tikiusaaq carbonatite-aillikite occurrence, West Greenland, and some remarks on carbonatite–kimberlite relationships. Lithos 112, 385–399. doi:10.1016/j.lithos.2009.03.002

Tappe, S., Steenfelt, A., Nielsen, T., 2012. Asthenospheric source of Neoproterozoic and Mesozoic kimberlites from the North Atlantic craton, West Greenland: New high-precision U–Pb and Sr–Nd isotope data on perovskite. Chem. Geol. 320-321, 113–127. doi:10.1016/j.chemgeo.2012.05.026

Tchameni, R., Mezger, K., Nsifa, N.E., Pouclet, A., 2000. Neoarchean crustal evolution in the Congo Craton: Evidence from K rich granitoids of the Ntem Complex, southern Cameroon. J. African Earth Sci. 30, 133–147.

Tompkins, L. a., Haggerty, S.E., 1985. Groundmass oxide minerals in the Koidu kimberlite dikes, Sierra Leone, West Africa. Contrib. Mineral. Petr. 91, 245–263. doi:10.1007/BF00413351

Van Achterbergh, E., Griffin, W.L., Stiefenhofer, J., 2001. Metasomatism in mantle xenoliths from the Letlhakane kimberlites: estimation of element fluxes. Contrib. Mineral. Petr. 141, 397–414. doi:10.1007/s004100100236

Van Westrenen, W., Wood, B.J., Blundy, J.D., 2001. A predictive thermodynamic model of garnet-melt trace element partitioning. Contrib. Mineral. Petr. 142, 219–234. doi:10.1007/s004100100285

Viljoen, K.S., Schulze, D.J., Quadling, A.G., 2005. Contrasting group I and group II eclogite xenolith petrogenesis: petrological, trace element and isotopic evidence from eclogite, garnet-websterite and alkremite xenoliths in the Kaalvallei kimberlite, South Africa. J. Petrol. 46, 2059–2090. doi:10.1093/petrology/egi047

Viljoen, F., Dobbe, R., Smit, B., 2009. Geochemical processes in peridotite xenoliths from the Premier diamond mine, South Africa: Evidence for the depletion and refertilisation of subcratonic lithosphere. Lithos 112, 1133–1142. doi:10.1016/j.lithos.2009.05.004

Walraven, F., Rumvegeri, B.T., 1993. Implications of whole-rock Pb-Pb and zircon evaporation dates for the early metamorphic history of the Kasaï craton, Southern Zaïre. J. African Earth Sci. (and Middle East) 16, 395–404. doi:10.1016/0899-5362(93)90098-B

White, S.H., De Boorder, H., Smith, C.B., 1995. Structural controls of kimberlite and lamproite emplacement. J. Geochemical Explor. 53, 245–264.

Wiedenbeck, M., Alle, P., Corfu, F., Griffin, W.L., Meier, M., Oberli, F., Von Quart, A., Roddick, J.C., Spiegel, W., 1995. Three natural zircon standards for U-Th-Pb, Lu-Th, trace element and REE analyses. Geostand. Newsl. 19, 1–23.

Williams-Jones, A.E., Hartzler, J., Francis, D., Clark, J., 2004. A geochemical approach to the classification of kimberlitic.

Wittig, N., Pearson, D.G., Webb, M., Ottley, C.J., Irvine, G.J., Kopylova, M., Jensen, S.M., Nowell, G.M., 2008. Origin of cratonic lithospheric mantle roots: A geochemical study of peridotites from the North Atlantic Craton, West Greenland. Earth Planet. Sci. Lett. 274, 24–33. doi:10.1016/j.epsl.2008.06.034

Wyatt, B. a., Baumgartner, M., Anckar, E., Grutter, H., 2004. Compositional classification of "kimberlitic" and "non-kimberlitic" ilmenite. Lithos 77, 819–840. doi:10.1016/j.lithos.2004.04.025

Yang, Y.-H., Wu, F.-Y., Wilde, S. a., Liu, X.-M., Zhang, Y.-B., Xie, L.-W., Yang, J.-H., 2009. In situ perovskite Sr–Nd isotopic constraints on the petrogenesis of the Ordovician Mengyin kimberlites in the North China Craton. Chem. Geol. 264, 24–42. doi:10.1016/j.chemgeo.2009.02.011

Yaxley, G.M., Crawford, A.J., Green, D.H., 1991. Evidence for carbonatite metasomatism in spinel peridotite xenoliths from western Victoria, Australia. Earth Planet. Sci. Lett. 107, 305–317.

Zimnisky, P., 2015. http://www.paulzimnisky.com/global-rough-diamond-production-estimates [WWW Document].

Zurevinski, S.E., Mitchell, R.H., 2004. Extreme compositional variation of pyrochlore-group minerals at the Oka carbonatite complex, Quebec: Evidence of magma mixing? Can. Mineral. 42, 1159–1168. doi:10.2113/gscanmin.42.4.1159

Chapter 12
APPENDICES